Advances in Humidity Standards

Doctoral Dissertation
Doctoral Program in Metrology (30th Cycle)

Advances in Humidity Standards

Shahin Tabandeh
* * * * * *

Supervisors
Prof. Vito Fernicola
Prof. Erkki Ikonen

Advisor
Dr. Martti Heinonen

Doctoral Examination Committee:
Prof. Francesca Romana d'Ambrosio, Referee and Commission Member, Università degli Studi di Salerno, Italy
Dr. Hisashi Abe, Referee and Commission Member, National Metrology Institute of Japan (NMIJ), Japan
Prof. José Juan Segovia, Commission Member, University of Valladolid, Spain
Dr. Wang Li, Commission Member, National Metrology Centre, Singapore

Politecnico di Torino
April 24, 2019

This doctoral thesis is conducted under a convention for the joint supervision of thesis at Aalto University (Finland) and Politecnico di Torino (Italy).

I hereby declare that, the contents and organisation of this dissertation constitute my own original work and does not compromise in any way the rights of third parties, including those relating to the security of personal data.

…….....

Shahin Tabandeh
Turin, April 24, 2019

Summary

Reliable humidity measurement is attracting an increasing interest due to its crucial role in the industry, meteorology, pharmaceutical manufacturing, electronics, food industry and air conditioning. Metrological traceability to SI through appropriate humidity standards is a key to the reliability needed in these applications. This work addresses improved humidity standards by developing new calculation methods and calibration systems and methods.

Any conversion between humidity quantities should consider a correction for the matrix effect, i.e. the interaction of water molecules with carrier gas, known as the water vapor enhancement factor. The direct measurement of the enhancement factor requires costly experiments; in contrast, current work provides a new functional equation and several sets of the coefficients by exploiting different approaches and the currently available data from the literature. The equation is founded on two mole fraction-related factors calculated based on the intermolecular potential, Helmholtz free energy, excess properties, quantum chemistry and existing experimental data. Correlations are reported for air, nitrogen, oxygen, ammonia, hydrogen, methane, argon and carbon dioxide. Four different correlations of air-water mixture exhibit a fairly good agreement within their uncertainty deviating within $4 \cdot 10^{-4}$ from the well-known Greenspan equation in the temperature range from 40 °C to 140°C and pressure up to 0.6 MPa.

Some seventh of the total energy consumption in the European Union is contributed by the industrial drying processes. Relative humidity (RH) sensors, as the most widely-used process control indicators, cannot provide traceable measurements above 100 °C due to the lack of standards causing an over dry estimated to cost 30 million euros per annum[1]. Current work introduces a

humidity generator based on SI-traceable mixing of the air and water vapor exploiting a quasi-spherical microwave resonator (QSR) as a reference for dew-point temperature up to 140 °C and pressure up to 0.6 MPa. The humidity of the generated reference flow is then defined, self-consistently, by the specific humidity estimated from the mass flow of water and air, water vapor mole fraction by exploiting the QSR and the dew-point temperature having a chilled mirror hygrometer(CMH) in its operating range. The generator is integrated into a calibration sub-chamber accommodated in a climatic temperature-controlled chamber. The expanded uncertainty (k=2) of the water vapor mole fraction is U_X=0.004 at x=0.2 increasing to U_X=0.014 at x=0.8.

Discrete steady-state calibration of RH sensors is extremely time-consuming in comparison with other physical quantities. An alternative method is introduced in this work by recovering the conventional definition of the calibration correction for the linear changes of the measurand in the second order systems based on the Laplace-domain studies. The additional uncertainty contributions are also reported for the time delay, linearity, temperature variations and differentiation of the signal. As a consequence, the calibration curves and their confidence intervals can be calculated through a data fusion method by employing the density function grids. A two-dimensional calibration strategy is also proposed. Moreover, a humidity calibrator is designed based on numerical simulations and prototyped with unique features which appropriate non-static calibration needs.

A neural network-based uncertainty algorithm (NNUA) is introduced for generic multi-input multi-output, nonlinear and computationally expensive mathematical models. The algorithm iteratively converges to the best estimate, variance and the confidence interval values guaranteed to match that of the adaptive Monte-Carlo (AMC) algorithm for the requested number of significant digits in a much more computationally efficient way. A worked example confirms that the NNUA operates 6800 times faster for an iterative simultaneous system of equations.

Acknowledgment

I have no words to express my gratitude to my loving parents; simply I would like to say thank you for your unconditional support. A special thanks goes to Parisa wholeheartedly, for helping me stay focused on the work patiently, Shahram for being such a wonderful life-coach and Sharareh for being my eternal cheerleader.

Achievements of the current work have been accomplished by an immense childish passion which redirected the academic growing path every day. Such a motivation-driven roadmap became possible as a result of the trust and belief provided by my team. I would like to thank Lucia for her continuous encouragements and sharing scientifically challenging topics with me. Thanks to Giovanni for being such an awesome officemate, Denis for his valuable knowledge in the instrumentation area, Rugiada for her collaborative spirit and Giulio for his kind availabilities. Finally, I would like to express my gratitude to Professor Fernicola for being such a supportive team leader and supervisor. Thank you for all the opportunities you gave me towards academic and professional growth.

I would like to acknowledge Roberto and Daniele for instructing me to exploit a microwave resonator in the hygrometry area. A part of chapter-2 is indebted to them since they generously lent me a well-studied cavity and an appropriate fitting-software.

With a special mention to Dr. Mikko Merimaa, Dr. Maija Ojanen-Saloranta, Dr. Richard Högström and all of my colleagues at VTT MIKES for their hospitality, in particular, I would like to thank Juho for his vital help with purchasing various components in the prototyping phase.

A very special gratitude goes to Dr. Heinonen for the fruitful discussions and his practical pieces of advice both as a project coordinator and as an advisor. I also gratefully acknowledge Professor Ikonen for his rigorous and patient follow-up and supervision.

I am grateful to Dr. Walter Bich for the useful discussions while I was mathematically deriving my uncertainty algorithm. He made me more self-confident when speaking about an alternative method for Monte-Carlo was looking too ambitious, by showing his interest to listen about the work progress even if he was extremely busy with his commitments to the revision of GUM.

I would like to thank also Dr. Allan Harvey, Dr. Jeremy Lovell-Smith and Dr. Alberto Giuliano Albo for their encouraging comments on the water vapor enhancement factor studies.

Two chapters of the current work have been carried out within the European Joint Research Project "HIT – Metrology for Humidity at High Temperatures and Transient conditions." The HIT project was co-funded within the EMPIR initiative by European Union's Horizon 2020 program and the EMPIR Participating States. I would like to express my gratitude not only to them but also to all of the partners. In particular, Mr. Peruzzi and Mr. Bosma from VSL, Dr. Cavallarin from CNR, Dr. Hudoklin from University of Ljubljana, Dr. Werhahn from PTB, Mr. Giannattasio from GBV, Dr. Wagner from TU-Darmstadt, Dr. Georgin from CETIAT and Mr. Pietari from Vaisala, for their ultimate collaborations.

With mention to Mauro and Nerina for their practical assistance and the following PoliTo and Aalto staff: Anita Bisi, Cecilia.Cappelli, Irene Gino and Marta Meniconi for the intense rounds of the negotiations.

To the most frequent signal
of my information system,
my parents and my love.

Contents

List of figures

ρ is the density, $\wp$ is the polarizability, P is pressure, T is temperature, T_dp is the dew-point temperature, q is the specific humidity, M is the molar mass, A is ampere, m is meter, kg is kilogram, s is second, K is kelvin and finally mol is mole. 83

List of tables

List of Abbreviations and Symbols

2D	Two-dimensional
ABS	Acrylonitrile Butadiene Styrene
AMC	Adaptive Monte-Carlo
AUX	Auxiliary
CFD	Computational fluid dynamics
CMH	Chilled mirror hygrometer
DUC	Device under calibration
g-MFC	Gas mass flow controller
GUF	GUM uncertainty framework
GUM	Guide to the Expression of Uncertainty in Measurement
H.E.	Heat exchanger
HIT	European Joint Research Project "HIT – Metrology for Humidity at High Temperatures and Transient conditions"
IMGC	Instituto di Metrologia Gustavo Colonetti, Torino, Italy (today INRIM)
INRIM	Istituto Nazionale di Ricerca Metrologica, Turin, Italy
INRIM-01	First primary dew/frost point generator developed at INRIM
l-MFC	Liquid mass flow controller
MCM	Monte-Carlo Method
MIKES	Centre for Metrology and Accreditation, Espoo, Finland (today VTT MIKES)
MW	Microwave
NBS	National Bureau of Standards, Gaithersburg, MD, USA (today NIST)
NNUA	Neural Network-based Uncertainty Algorithm
PDF	Probability density function
PID	Proportional–integral–derivative controller
PVC	Polyvinyl Chloride
QSR	Quasi-Spherical Resonator
RH	Relative Humidity
SI	International System of Units
TE	Transverse Electric modes
TEOS-10	Thermodynamic Equation of Seawater-2010
TM	Transverse Magnetic modes
VNA	Vector Network Analyzer
VTT	Technical Research Centre of Finland LTD

$\odot$	Hadamard product
$x^{\odot 2}$	Hadamard self production of x
$\oslash$	Hadamard division
$\varepsilon_{\mathrm{mix}}$	Relative dielectric constant
ε_{v}	Void fraction
$€$	Deviation of a random variable from its expected value
$\varepsilon/k_{\mathrm{B}}$	Well depth
$\emptyset$	Joule–Thomson coefficient
K_T	Isothermal compressibility
μ	Viscosity
$\wp$	Molar polarizability
ρ	Density
σ_{xy}	Collision diameter
$\sum$	Variance-covariance matrix
$\bar{v}_{\mathrm{c}}$	Molar volume of the condensed phase
A_{s}	Cross section area
A	Air fraction
B_{xy}	Second virial coefficient considering x and y molecules
B	Bias vector
C_{xyz}	Third virial coefficient considering x, y and z molecules
C_{p}	Pressure correction factor
C	Calibration coefficient
d_{p}	Effective particle diameter
D	Allowable numerical tolerance
$\bar{d}$	Tolerance devisor
$\hat{E}$	Error vector of the ANN
P_{ws}	Water vapor saturation partial pressure
$\mathrm{E}(x)$	Expectation of the random variable x
$(f+g)$	Average frequency corrected for its halfwidth
f	Water vapor enhancement factor
F_1	Atmospheric factor
f^{AV}	Helmholtz function of the humid air
f_i	Sub enhancement factor
F_{p}	Pressure factor
f^{V}	Helmholtz function of the water vapor
f^{w}	Helmholtz function of the condensed water
g^{AV}	Specific Gibbs function of the humid air
g^{W}	Specific Gibbs function of the condensed phase.
H	Hessian matrix
H_m^E	Excess enthalpy of the mixture
H_{n}	Hidden layer nodes

$\bar{I}_n$	n^{th} mapped input
I_n	Input nodes
I_w	Input weight vector
J	Jacobian matrix
$\bar{k}$	Training interval
k	Coverage factor
K_a	Henry's law constant
k_B	Boltzmann constant
L_w	Layer weight vector
M	Random sample size
M_A	Molar mass of air
$\dot{m}_g$	Carrier gas mass flow rate
M_g	Molar mass of carrier gas
$\dot{m}_w$	Water mass flow rate
M_w	Molar mass of water
n	Refraction index
N_A	Avogadro number
N_d	Required number of significant digits
$O^{(n_1,m_1)}$	First derivative of O_{ml} with respect to n_1^{th}
$O^{([n_1,n2],m_1)}$	Second derivative of O_{ml} with respect to n_1 and n_2
$O^{([n_1,n2,n3],m_1)}$	Third derivative of O_{ml} with respect to n_1, n_2 and n_3
O_n	Output nodes
P	Total pressure
p_c	Critical Pressure
P_i	i^{th} Pole of the transfer function
P_R	Squared of the maximum deviation of the Taylor expansion's remainder
q	Specific humidity
q_0	Transfer function constant
Q_v	Flow rate through the valve
r	Distance between molecules
R	Universal constant of the gas
s	Laplace transformation variable
S	Second order correction of the output variance
T_c	Critical temperature
t^*	Reduced dipole moment
T	Temperature
T_{dp}	Dew-point temperature
tr(x)	Trace of the x matrix
U	Expanded uncertainty
u	Standard uncertainty

u_c	Combined uncertainty
v_i	Valve number i
Var(x)	Variance of x
W	Mixing ratio
x	Water vapor mole fraction
X_{a}	Air mole fraction
Y_{high}	Upper endpoint of the 95% confidence interval of Y
Y_{low}	Lower endpoint of the 95% confidence interval of Y
Z_i	i^{th} Zero of the transfer function

Author's Contribution

The author performed the entire work presented in the manuscript unless otherwise stated below:

1. The author employed a numerical solver for Equations (1-10) to (1-12) released by Thermodynamic Equation Of Seawater - 2010 software package currently available at http://www.teos-10.org/software.htm.

2. The author did not contribute to the design and construction of the QSR and its fitting software. However, design of experiments, experimental set-up, measurements, data analysis, and validations are performed by him.

3. The author exploited an experimental setup already developed by Dr. Richard Högström for the results presented in Figure 127.

Introduction

Discussions about the presence of water in materials, i.e. humidity in gasses and moisture in solids, dated back to the earliest stage of the so-called science when Thales of Miletus who is well-known for breaking from mythology to theories and hypothesis considered water as the single material substance [2]. Some five centuries later, in China, absorption of water has been measured considering the weight gain of a charcoal cube exposed by the humid air [3]. A more recent chronological list of hygrometry starts with Nicolaus de Cusa, a German mathematician of the fifteenth century, who had a similar hygroscopic approach in wool samples [4]. In 1650, Ferdinand II, the Grand Duke of Tuscany, built a gravimetric hygrometer, i.e Figure 1, based on the weight of accumulated condensed water droplets at the reference temperature of snow [5]. In the next century, Swiss technology introduced the hair hygrometer as a turning point to the relative humidity measurements [6]. Sixteen years later, Leslie employed wet and dry thermometers to construct the first psychrometer in France and eventually, in 1854, French H.V. Regnault invented a dew-point measurement instrument which, despite the optical and electronic enhancements, still remained the base of current world-class measurements.[7,8]

Figure 1: The condensation-based hygrometer exploited by Ferdinand-II [9]

Nowadays, humidity sensing relies on different chemical and physical principles. Thus the humidity measurement instrumentation can differ from straightforward electronic devices to complicated measurement systems. Considering the humidity in the carrier gasses the most frequently used types of

hygrometer are electrical impedance devices, condensation-type devices and psychrometers [10]. The first group is founded on the changes of the electrical impedance, e.g. resistance or capacitance, of an electronic component which absorbs the water molecules. In contrast, the second group uses cooling to induce controlled condensation of water; in this case, the stable temperature in which condensation happens is indicative of the humidity level and is the dew-point temperature by definition. Psychrometers use the evaporative cooling as a measure of humidity, thus, a combination of the temperatures, after appropriate calculations, gives an indication of the humidity levels.

Humidity generators have been built under certain principles to ensure traceability of the humidity measurements. They can provide a reference humid gas flow, e.g. the dew/frost point reference temperature, or could be paired to a reference instrument (e.g. Chilled Mirror Hygrometers) and simply be used as stable sources.
The methods in which humidity standard generators operate, in principle, can be clustered as follows:

1. Two-pressure, two-temperature methods including:
   - Saturation at constant pressure and temperature, by the flow of the gas over a controlled temperature and pressure pool of water/ice based on either condensation or evaporation, e.g. [11].
   - Two-temperature method by increasing the temperature of the gas with a well-known dew-point or vapor pressure, e.g. [12,13,14].
   - Two-pressure method by expansion of the gas with a well-known dew-point or vapor pressure. , e.g. [15].
   - by combination of the previous methods, e.g. [16]
2. Dilution method by mixing the dry gas flows and humid gas flow, e.g. [17]
3. Gravimetric generator by mixing of a carrier gas and water vapor determined by weighting [18,19].
4. Coulometric method by the formation of H_2 and O_2 using the electrolytic current and recombination to water on a palladium contact. later, the recombined water is fed into dry gas stream [20]

Several humidity generators have been developed over the years. Hasegawa et al. (NBS 1976) [21], Crovini et al. (IMGC 1989)[22], Heinonen (MIKES 1999)[23], Mitter and Benyon (2008) [24] are among the best-documented works of the pioneers. The principle of such generators is mainly based on water vapor saturation either by evaporation or by condensation of a gas stream flowing, over a controlled temperature and pressure liquid water pool to cover a dew-point temperature range up to 95 °C.

Calibration of humidity sensors are performed by more than 180 industrial accredited calibration laboratories in Europe; however, none of them are capable of providing the traceability at the temperature range above 100 °C as a consequence of the lack of primary standards. The main demand arises from the

drying sector which consumes almost 15% of the overall energy in the European countries, estimated to be 30 billion euros per annum. Consequently, any tenth of percent improvement in efficiency, as a result of better humidity indication, could save some 30 million euros per year. The food industry, with a turnover of 900 billion euros per year, is the European second largest manufacturing sector and would benefit directly from any efficiency enhancements of the industrial dryers [1].

Recently, a work by Vega-Maza ad co-workers [25] introduced a method to generate a humid gas stream with water vapor amount fraction up to 0.9 at temperatures up to 200 °C. Indeed, this publication was a major step forward and benefited the second chapter of the present work, especially, at its early stage, even if this work followed a different approach to generate SI-traceable humid gas streams and to control its pressure. The main advantages of the present approach concern the ease of operation and the capability of fast transient humidity generation alongside improved measurement uncertainty, as will be discussed in chapter two. As a result of the current work, INRIM high-humidity generator provided the traceability chain for the dew-point temperature above 100 °C and pressure up to 0.6 MPa in 2016 [26], a couple of years after, in 2018, an article was published by Bosma et al. on the VSL facility for dew-points up to 150 °C [27]. The two generators have been preliminarily compared through the capacitive relative humidity sensors.

Primary calibration of humidity sensors is among the most time-consuming procedures in comparison with all the other ones measuring various physical quantities. At the moment, calibration of humidity sensing instrumentation is performed at discrete steady-state points, since the calibration systems are founded on passive sluggish phenomena, the calibration turns to be not cost-effective. Chapter-3 introduces a novel approach to calibrate industrial humidity sensors by imposing arbitrary profiles which only covers the range of interest and, simultaneously, elaborates the uncertainty as a quantity related to the mathematical approach.

Industrial humidity sensors are often calibrated using the field calibrators which, generally, compares the same type of humidity sensor as a reference. Sec 3.3 will describe design, development, prototyping and testing of such a humidity calibrator with some unique specifications. This work has been done within a European metrology project (14IND11 HIT) at the premises of VTT MIKES in Finland. In addition, most of the time, the industrial processes are achievable by the contemporaneous control of different quantities, e.g. temperature and relative humidity; this clearly highlights the necessity of the two-dimensional calibration. Sec.3.6 draws a clear picture of the method and uncertainty assessment of such calibrations.

Humidity standards also rely on the equations that relate needed quantities of the calibrant to the one realized by the generator. For instance, the water vapor enhancement factor is the major factor which takes to account the non-idealities of the humid gas mixtures at different temperatures and pressures and plays a crucial

role in the estimation of humidity-related quantities or conversion between humidity parameters. The enhancement factor is one of the most attractive topics in the humidity metrology area since reference values need to be converted from one quantity to another, a typical example is a conversion from dew-point temperature to the relative humidity during the calibration of the RH sensors.[10]

The water vapor enhancement factor estimation is typically based on complex experiments such as [28, 29, 30], however, inevitably, either there is a lack of experimental data in the whole temperature-pressure domain of interest and/or the information is incomplete in many cases. Water vapor enhancement factor is not reported in the literature for many carrier gases, or it does not cover the full range of interest. In addition, there is an increasing industrial demand for either new gases or a broader measurement range.

The groundbreaking work has been done by Hyland and Wexler in early seventies [28], later, in 1975, Greenspan published his functional equations in the Journal of Research of the National Bureau of Standards in which the water vapor enhancement factor of CO_2-free air were explicitly presented [31]. Despite the limitations in the temperature and pressure range, this formula remained the most frequently used equation for ages and the metrological effort were focused, mainly, on the experiments updating the Greenspan's coefficients and not the formula itself. Chapter-1 presents the numerical implementation of different methods to estimate the water vapor enhancement factor as well as a new functional equation for metrological applications.

Uncertainty is an inseparable part of any metrological standard and is normally considered to evaluate its value. Since uncertainty is uncertain by its nature, guides and agreed procedures have been widely used to establish a common language among the scientists. GUM [32], undoubtedly, is the most frequently used one. When the mathematical model is highly nonlinear, or the probability density functions are not necessarily Gaussian GUM supplement-I [33] where the Adaptive Monte Carlo (AMC) method has been detailed is recommended.

The AMC simulation, despite the ease of use, can be very time-consuming. This calculation time can be enormously high for computationally expensive mathematical models and especially when a confidence interval with more significant digits of the confidence interval is required. AMC is also considered as a tool to check the validity of the GUM uncertainty framework (GUF) and therefore should be counted as the most reputable reference for the uncertainty assessment.

Chapter-4 introduces a general-purpose algorithm to estimate the associated uncertainty of any mathematical model. Neural network-based uncertainty algorithm (NNUA) is an iterative algorithm aimed to propagate uncertainty and/or probability density functions in multi-input multi-output nonlinear mathematical models and is of greater value when the computation cost is high. This is worth mentioning that any mathematical model can be employed by this algorithm and this could be easily applied when an explicit form of a mathematical model is not

available or when the measurements are interpreted in a procedure and the evaluation of a mathematical model is demanding.

Chapter 1

A Novel Approach For Water Vapor Enhancement Factor Formulation

1.1 Introduction

The water vapor saturation curves represent the phase equilibrium in the absence of any carrier gas and, therefore, any conversion between humidity parameters should consider a correction for the matrix effect in the presence of other gasses. This correction is known as the water vapor enhancement factor and accounts for the increased water vapor pressure in the presence of a matrix gas.

The water vapor enhancement factor measurements were firstly reported by Hyland and Wexler on three measurement points above the room temperature [28] which combined with a new set of measurements to cover the temperature range from -20 °C to +70 °C by Hyland [34] for CO_2-free air. Later, Greenspan introduced a functional equation based on the same work by employing the Goff equation [31,35]. In 1998 Hardy released new sets of constants for the same equation based on ITS-90 formulations [36]

This chapter presents the numerical implementation of different approaches to estimate the water vapor enhancement factor as well as a new functional equation for metrological applications. Sections of this chapter are structured to describe different methods based on the examples and to provide the constants of a unique functional equation for any matrix gas under study. In a number of cases, different methods have been compared.

1.2 Estimation of the enhancement factor based on the Helmholtz function

The equations of thermodynamic equation of seawater-2010 (TEOS-10) are based on a Gibbs function formulation from which all thermodynamic properties of water, air and humid air can be derived in a thermodynamically consistent manner [37].

Considering the equilibrium between the chemical potentials in the condensed phase and the water vapor the definition of the dew-point temperature can be written as

$$g^{\mathrm{AV}} - A\left(\frac{\partial g^{\mathrm{AV}}}{\partial A}\right)_{T.P} = g^{\mathrm{W}}, \qquad (1\text{-}1)$$

Where g^{AV} is the specific Gibbs function of the humid air, A is the air fraction and g^{W} is the specific Gibbs function of the condensed phase.
The Gibbs function can be written considering total pressure, P, and the density, ρ, of the phase under consideration

$$g^{\mathrm{w}}(T,P) = f^{\mathrm{w}}(T,\rho^{\mathrm{W}}) + \frac{P}{\rho^{\mathrm{W}}}, \qquad (1\text{-}2)$$

$$g^{\mathrm{AV}}(T,P) = f^{\mathrm{AV}}(A,T,\rho^{\mathrm{AV}}) + \frac{P}{\rho^{\mathrm{AV}}}, \qquad (1\text{-}3)$$

in which

$$f^{\mathrm{AV}}(A,T,\rho^{\mathrm{AV}}) = (1\text{-A})\cdot f^{\mathrm{V}}(T,(1-A)\rho) + A\cdot f^{A}(T,A\rho) + 2A\cdot(1-A)\cdot\rho\frac{RT}{M_{\mathrm{A}}M_{\mathrm{W}}}\cdot\{B_{\mathrm{AW}}(\mathrm{T}) + \frac{3\rho}{4}\left[\frac{A}{M_{\mathrm{A}}}c_{\mathrm{AAW}}(T) + \frac{(1-A)}{M_{\mathrm{W}}}C_{\mathrm{AWW}}(T)\right]\}, \qquad (1\text{-}4)$$

where f^{AV} is the Helmholtz function of the humid air, f^{V} is the Helmholtz function of the water vapor, f^{A} is the Helmholtz function of the dry air, f^{w} is the Helmholtz function of the condensed water, R=8.31451 J $mol^{-1}K^{-1}$ is the universal constant of the gas, T is the temperature, M_{A} is the molar mass of air, M_{W} is the molar mass of the pure water, B_{AW} is the second virial cross coefficient and c_{AAW} and c_{AWW} are the third virial cross coefficients.

The first derivatives of the Helmholtz functions can be written as

$$\frac{\partial f^{F}}{\partial \rho^{w}} = \frac{P}{\rho^{\mathrm{w}2}}, \qquad (1\text{-}5)$$

and

$$\left(\frac{\partial f^{\mathrm{AV}}}{\partial \rho^{\mathrm{AV}}}\right)_{A,T} = \frac{P}{\rho^{\mathrm{AV}2}}. \qquad (1\text{-}6)$$

by substituting Equation(1-1) to (1-6) and considering infinitesimal changes in air fraction, temperature, pressure, and the two densities, Equation(1-7) to (1-9) can be derived as

$$-Af_{\mathrm{AA}}^{\mathrm{AV}}\Delta A + \left(f_{T}^{\mathrm{AV}} - f_{\mathrm{AT}}^{\mathrm{AV}} - f_{T}^{\mathrm{AV}}\right)\Delta T + \left(\frac{1}{\rho^{\mathrm{AV}}} - \frac{1}{\rho^{\mathrm{W}}}\right)\Delta P + \left(f_{\rho}^{\mathrm{AV}} - f_{\mathrm{A}\rho}^{\mathrm{AV}} - \frac{P}{(\rho^{\mathrm{AV}})^{2}}\right)\Delta\rho^{\mathrm{AV}} - \left(f_{\rho}^{\mathrm{W}} - \frac{P}{(\rho^{\mathrm{W}})^{2}}\right)\Delta\rho^{\mathrm{W}} = P\left(\frac{1}{\rho^{W}} - \frac{1}{\rho^{AV}}\right) + f^{w} - f^{AV} + Af_{A}^{AV}, \qquad (1\text{-}7)$$

$$\rho^{\mathrm{AV}} f_{\mathrm{A}\rho}^{\mathrm{AV}} \Delta A + \rho^{\mathrm{AV}} f_{T\rho}^{\mathrm{AV}} \Delta T - \frac{\Delta P}{\rho^{\mathrm{AV}}} + \left(2 f_{\rho}^{\mathrm{AV}} + \rho^{\mathrm{AV}} f_{\rho\rho}^{\mathrm{AV}}\right) \Delta \rho^{\mathrm{AV}} = \frac{P}{\rho^{\mathrm{AV}}} - \rho^{\mathrm{AV}} f_{\rho}^{\mathrm{AV}}, \quad (1\text{-}8)$$

$$\rho^{\mathrm{W}} f_{T\rho}^{\mathrm{W}} \Delta T - \frac{\Delta P}{\rho^{\mathrm{W}}} + \left(2 f_{\rho}^{\mathrm{W}} + \rho^{\mathrm{W}} f_{\rho\rho}^{\mathrm{W}}\right) \Delta \rho^{\mathrm{W}} = \frac{P}{\rho^{\mathrm{W}}} - \rho^{\mathrm{W}} f_{\rho}^{\mathrm{W}}. \quad (1\text{-}9)$$

Assume that ΔT=0, ΔP=0 and ΔA=0 for the equilibrium and rewriting the equations in terms of specific humidity a major simplification is achievable as

$$\left(f_{\rho}^{\mathrm{AV}} + f_{q\rho}^{\mathrm{AV}} - \frac{P}{(\rho^{\mathrm{AV}})^2}\right) \Delta \rho^{\mathrm{AV}} - \left(f_{\rho}^{\mathrm{W}} - \frac{P}{(\rho^{\mathrm{W}})^2}\right) \Delta \rho^{\mathrm{W}} = P\left(\frac{1}{\rho^{\mathrm{W}}} - \frac{1}{\rho^{\mathrm{AV}}}\right) + f^{\mathrm{W}} - f^{\mathrm{AV}} + (q-1) f_{q}^{\mathrm{AV}}, \quad (1\text{-}10)$$

$$\left(2 f_{\rho}^{\mathrm{AV}} + \rho^{\mathrm{AV}} f_{\rho\rho}^{\mathrm{AV}}\right) \Delta \rho^{\mathrm{AV}} = \frac{P}{\rho^{\mathrm{AV}}} - \rho^{\mathrm{AV}} f_{\rho}^{\mathrm{AV}}, \quad (1\text{-}11)$$

$$\left(2 f_{\rho}^{\mathrm{W}} + \rho^{\mathrm{W}} f_{\rho\rho}^{\mathrm{W}}\right) \Delta \rho^{\mathrm{W}} = \frac{P}{\rho^{\mathrm{W}}} - \rho^{W} f_{\rho}^{W}. \quad (1\text{-}12)$$

The simultaneous solution of the Equations (1-10) to (1-12) for a given pressure and specific humidity and iterative update of the density and the Helmholtz functions yields the dew-point temperature [38].

In order to calculate the water vapor enhancement factor based on the Helmholtz function a given amount fraction should be converted to the specific humidity considering the molar mass of the pure water and that of the dry carrier gas. Equations (1-10) to (1-12) can be used to convert the specific humidity and total pressure to the dew-point temperature. Consequently, the water vapor saturation pressure can be calculated by employing the water vapor pressure curves and eventually the enhancement factor is reachable having

$$f(P, T_{dP}) = \frac{xP}{P_{\mathrm{ws}}(T_{\mathrm{dP}})}, \quad (1\text{-}13)$$

where x is the water vapor mole fraction, P is the total pressure, P_{ws} is the water vapor saturation partial pressure, and T_{dP} is the dew-point temperature

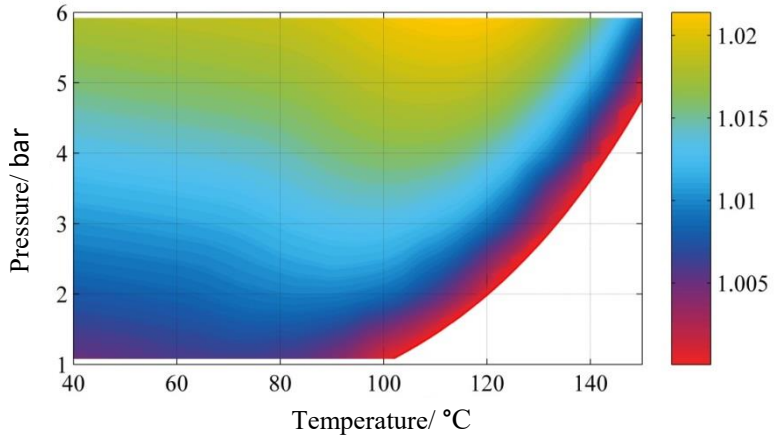

Figure 2: Water vapor enhancement factor calculations for air based on TEOS-10

Results of such calculations are presented in Figure 2. The enhancement factor equals unity for the contour on the right-hand-side, obviously, because the water mole fraction equals unity. In addition, the water vapor pressure increase is directly proportional to pressure.

1.3 Estimation of the water vapor enhancement factor based on the virial equation of state

Hyland and Wexler have derived a formulation to calculate the second virial cross coefficient of air-water mixtures [39]. This equation is rewritten in terms of sub-enhancement factors. Basically, the sub-enhancement factors are the mathematical terms of the same formulation presented by them and are considered for the sake of simplicity in the magnitude analysis of the original formulation

$$f = \prod_{i=1}^{15} f_{\mathrm{i}}\,, \qquad (1\text{-}14)$$

$$f_1 = e^{\left[(1+\mathrm{K}_T P_{\mathrm{ws}})(p-P_{\mathrm{ws}})-0.5K\left(P^2-P_{\mathrm{ws}}^2\right)\right]\frac{\bar{\mathrm{v}}_{\mathrm{c}}}{RT}}, \qquad (1\text{-}14\text{-}1)$$

$$f_2 = 1-\frac{X_{\mathrm{a}}\cdot P}{K_{\mathrm{a}}}\,, \qquad (1\text{-}14\text{-}2)$$

$$f_3 = e^{\frac{X_{\mathrm{a}}^2 P}{RT}B_{\mathrm{aa}}}, \qquad (1\text{-}14\text{-}3)$$

$$f_4 = e^{-2\frac{X_{\mathrm{a}}^2 P}{RT}B_{\mathrm{aw}}}, \qquad (1\text{-}14\text{-}4)$$

$$f_5 = e^{-\frac{P-P_{\mathrm{ws}}-X_{\mathrm{as}}^2 P}{RT}B_{\mathrm{ww}}}, \qquad (1\text{-}14\text{-}5)$$

$$f_6 = e^{\frac{X_{\mathrm{a}}^3 P^2}{(RT)^2}C_{\mathrm{aaa}}}, \qquad (1\text{-}14\text{-}6)$$

$$f_7 = e^{3\frac{X_{\mathrm{a}}^2(1-2X_{\mathrm{a}})P^2}{2(RT)^2}C_{\mathrm{aaw}}}, \qquad (1\text{-}14\text{-}7)$$

$$f_8 = e^{-3\frac{x_{\mathrm{a}}^2(1-x_{\mathrm{a}})P^2}{(RT)^2}C_{\mathrm{aww}}}, \qquad (1\text{-}14\text{-}8)$$

$$f_9 = e^{-\frac{(1+2X_{\mathrm{a}})(1-X_{\mathrm{a}})^2P^2-{P_{\mathrm{ws}}}^2}{2(RT)^2}C_{\mathrm{www}}}, \qquad (1\text{-}14\text{-}9)$$

$$f_{10} = e^{-\frac{x_{\mathrm{a}}^2(1-3x_{\mathrm{a}})(1-x_{\mathrm{a}})P^2}{(RT)^2}B_{\mathrm{aa}}B_{\mathrm{ww}}}, \qquad (1\text{-}14\text{-}10)$$

$$f_{11} = e^{-2X_{\mathrm{a}}^3\frac{(2-3X_{\mathrm{a}})P^2}{(RT)^2}\cdot B_{\mathrm{aa}}\cdot B_{\mathrm{aw}}}, \qquad (1\text{-}14\text{-}11)$$

$$f_{12} = e^{6X_{\mathrm{a}}^2\frac{(1-X_{\mathrm{a}})^2P^2}{(RT)^2}B_{\mathrm{aw}}B_{\mathrm{ww}}}, \qquad (1\text{-}14\text{-}12)$$

$$f_{13} = e^{-\frac{3X_{\mathrm{a}}^4P^2}{2(RT)^2}B_{\mathrm{aa}}^2}, \qquad (1\text{-}14\text{-}13)$$

$$f_{14} = e^{-2\,X_{\mathrm{a}}^2\frac{(1-X_{\mathrm{a}})(1-3X_{\mathrm{a}})P^2}{(RT)^2}{B_{\mathrm{aw}}}^2}, \qquad (1\text{-}14\text{-}14)$$

$$f_{15} = e^{-\frac{{P_{\mathrm{ws}}}^2-(1+3X_{\mathrm{a}})(1-X_{\mathrm{a}})^3P^2}{2(RT)^2}{B_{\mathrm{ww}}}^2}, \qquad (1\text{-}14\text{-}15)$$

where f is the enhancement factor, T is the temperature, K_T is the isothermal compressibility of the condensed phase, p_{ws} is the saturation vapor pressure, P is the total pressure, $\bar{v}_{\mathrm{c}}$ is the molar volume of the condensed phase, X_{a} is the air mole fraction, K_{a} is the Henry's law constant, B is the second virial coefficient; a refers to air and w refers to water, C is the third virial coefficient; a refers to air and w refers to water, R is the universal gas constant.

Sub-enhancement factors are not of the same order of magnitude and a magnitude analysis can cast some light to a better understanding of the enhancement factor itself, refer to Figure 3 and Figure 4.

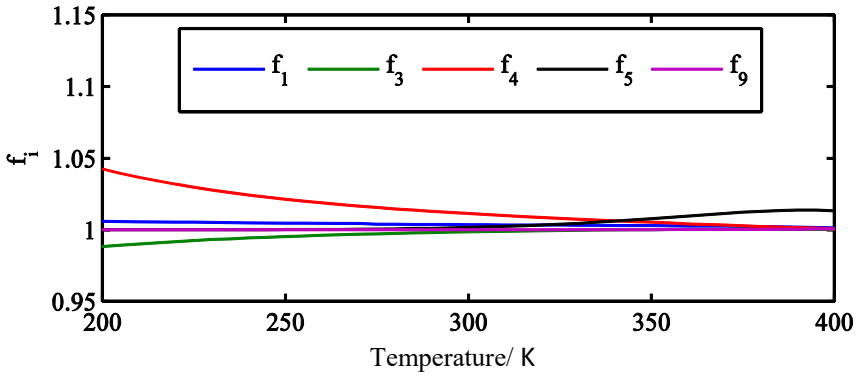

Figure 3: Major Sub-enhancement factors at 0.5 MPa for air, considering saturation with respect to liquid water and solid ice at temperatures above and below 273.15 K, respectively

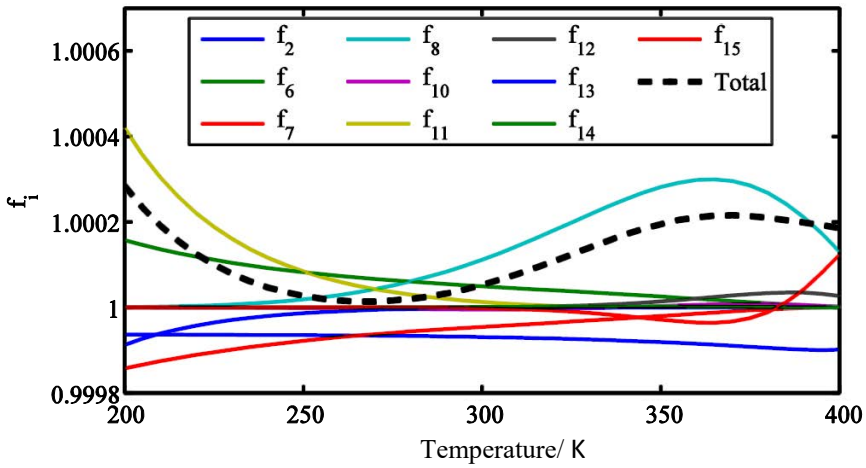

Figure 4: Minor Sub-enhancement factors at 0.5 MPa for air, considering saturation with respect to liquid water and solid ice at temperatures above and below 273.15 K, respectively, the dashed-line stands for the overall contribution of minor effects.

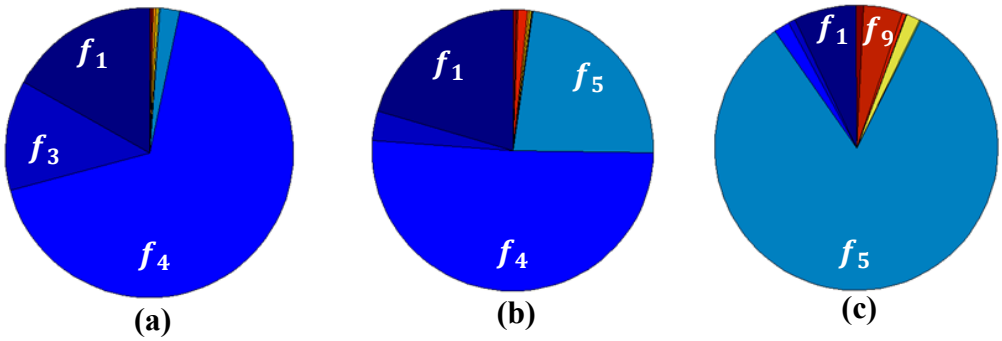

Figure 5: Major contributions to the enhancement factor for air at 0.5 MPa : (a) T=274 K (b) T=324 K and (c) T=374 K

The enhancement factor is governed by different terms considering different ranges. In the low range of water concentrations, the second cross virial coefficient contribution (i.e. f_4) is dominant; in contrast, in the high concentrations, the water vapor second virial coefficient contribution (i.e. f_5) is governing, i.e.Figure 5. This is worth mentioning that f_2 takes into account the solubility of the gasses and may contribute insignificantly for high soluble carrier gases (e.g. ammonia and carbon dioxide).

1.4 Mathematical implementation of the water vapor enhancement factor

By solving the Equation (1-14) for arbitrary pressure and temperatures in the range of interest for the water vapor and air mixture, new correlations can be formulated. These correlations give a much more clear idea about the physical meaning of the enhancement factor. Basically, due to its reduced form, the formulation can be used to map the water vapor enhancement factor for any combination of temperature and pressure for any matrix gas.

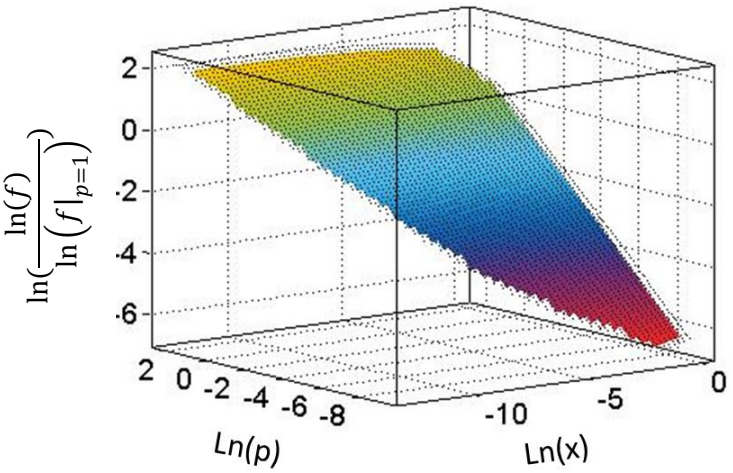

Figure 6: Pressure and amount fraction dependency of the enhancement factor. P is the normalized pressure in Pascal over 10^5, x is the water mole fraction, f is the enhancement factor and $f|_{p=1}$ is the enhancement factor at $p = 1$ bar.

Such a smooth surface of Figure 6 can yield the introduction of,

$$f = e^{(1-x)\cdot F_1 \cdot C_p}, \qquad (1\text{-}15)$$

where x is the water vapor amount fraction, F_1 is the amount fraction dependency at 0.1 MPa and will be called atmospheric factor, and C_{p} is the pressure correction factor. Consequently, the pressure correction factor is formulated as

$$C_{\mathrm{p}} = e^{\ln(P)\cdot F_{\mathrm{p}}}, \qquad (1\text{-}16)$$

where P is the normalized pressure over the reference P equals to 10^5 Pascal and F_{p} is the amount fraction dependency of C_{p} and will be called pressure factor.
The water vapor enhancement factor of any gas can be described by two sets of polynomial coefficients. One may want to write a formula based on the ratio of the enhancement factor at a given pressure and the enhancement factor at atmospheric pressure as a function of temperature which immediately fails since firstly the dew point temperature is pressure dependent and secondly, the fitting stage will not be promising.
The amount fraction dependency of the enhancement factor follows

$$F_1 = \sum_{i=0}^{6} a_i \ln(x)^i\,, \qquad (1\text{-}17)$$

and the amount fraction dependency of the pressure correction

$$F_{\mathrm{p}} = \sum_{i=0}^{4} b_i \ln(x)^i\,. \qquad (1\text{-}18)$$

The functional formulation is capable of being fitted to different calculation approaches considering all carrier gases under the study. It provides physical meaning to the parameters by employing only the water vapor mole fraction.

1.4.1 Air

Humidity in the air is, undoubtedly, the most interesting topic to start with, especially, for its applications in HVAC systems [40] and meteorology [41]. The second virial coefficients of any gas, as well as the mixtures, can be formulated in the following double exponential format

$$B_{\mathrm{xx}} = a \cdot e^{b\cdot T} + c \cdot e^{d\cdot T}, \qquad (1\text{-}19)$$

Table 1: Constants of the second virial coefficients for air

B_{xx}	*a*	*b*	*c*	*d*
B_{aa}	2.70E-06	0.003717	-0.00038	-0.01066
B_{aw}	6.02E-16	0.05386	-0.0004	-0.00883
B_{ww}	-63.01	-0.04363	-0.05117	-0.013

Table 1 summarizes the constants of the second virial coefficients which are also illustrated in Figure 7. This is considered that the coefficient of the mixture is about 2.4 % of that of water at 300 K.

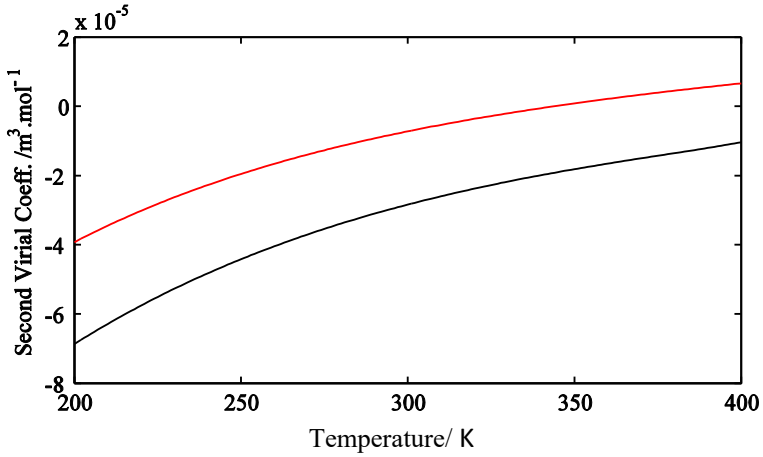

Figure 7: Second virial coefficients for air, B_{aa} in red and B_{aw} in black, obtained by employing the double exponential constants in Equation (1-19)

Considering the procedure of page 13 Coefficients of Equation (1-15) are calculated for air-water equilibrium and listed in Table 2. The polynomial is also plotted in Figure 8. The minimum occurs at about $7 \cdot 10^{-3}$ of the water mole fraction.

Table 2: Constants of Equation (1-17) for air-water equilibrium based on the experimental results of Hyland [28,34]

a_0	0.015861
a_1	0.008862
a_2	0.002837
a_3	0.000524
a_4	5.92E-05
a_5	3.70E-06
a_6	9.76E-08

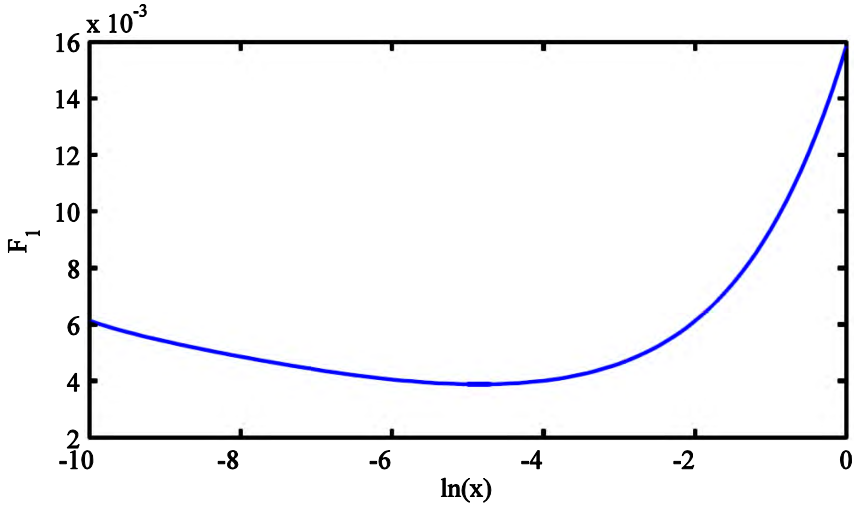

Figure 8: Atmospheric factor for air over water employing the experimental results

The pressure correction should also be considered when pressure deviates from that of the atmosphere. This is reported in Table 3 and depicted in Figure 9. The F_p value approaches to a number lower than 0.9 in the low concentrations.

Table 3: Constants of Equation (1-18) for air-water equilibrium based on the experimental results of Hyland [28,34]

b_0	0.680058
b_1	0.005049
b_2	0.018927
b_3	0.002856
b_4	1.23E-04

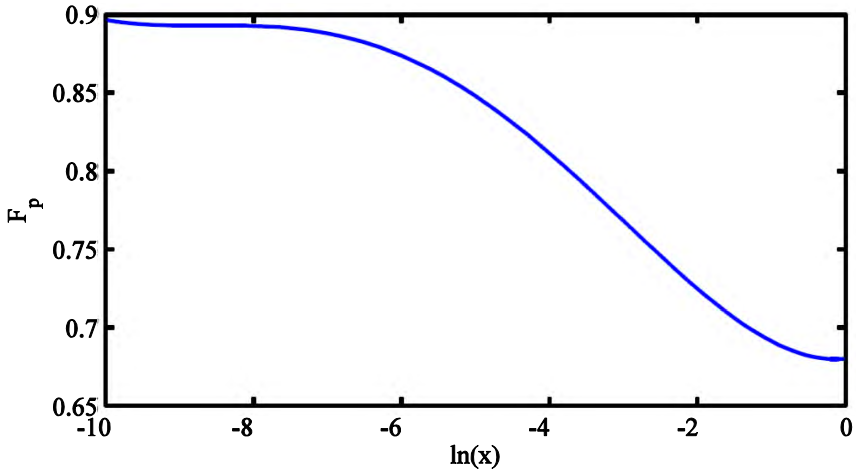

Figure 9: Pressure factor for air over water employing the experimental results

And for the equilibrium over ice:

Coefficients of Equation (1-17) are calculated for air-ice equilibrium and are reported in Table 4. A monotonic decrease of F_1 is evident in Figure 10

Table 4: Constants of Equation (1-17) for air-ice equilibrium based on the experimental results of Hyland [28,34]

a_0	0.043724097
a_1	0.031877921
a_2	0.010752927
a_3	0.001942283
a_4	1.99E-04
a_5	1.08E-05
a_6	2.44E-07

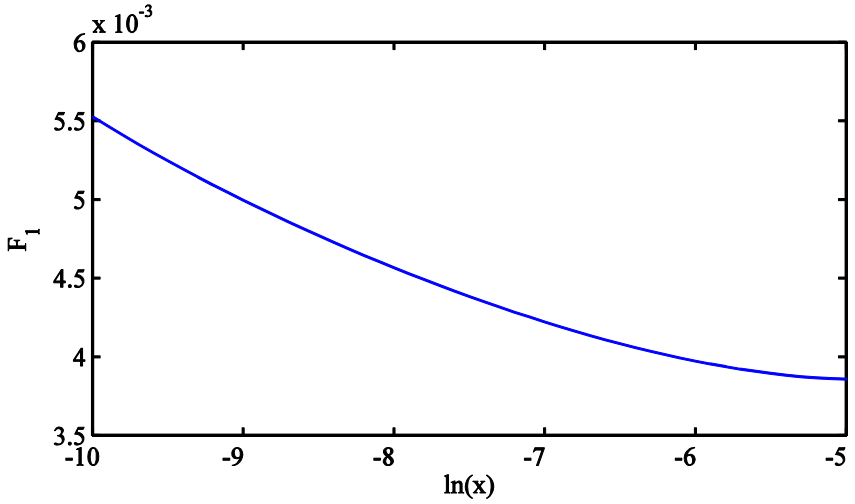

Figure 10: Atmospheric factor for air over the ice employing the experimental results

Considering the pressure factor as mentioned in Sec.1.4, the "b" values are reported in Table 5 and illustrated in Figure 11. The F_P values are slightly higher than that of Figure 9 highlighting the deviations in F_1 due to the differences in the chemical potential of ice over that of the liquid water.

Table 5: Constants of Equation (1-18) for air-ice equilibrium based on the experimental results of Hyland [28,34]

b_0	0.680058
b_1	0.005049
b_2	0.018927
b_3	0.002856
b_4	1.23E-04

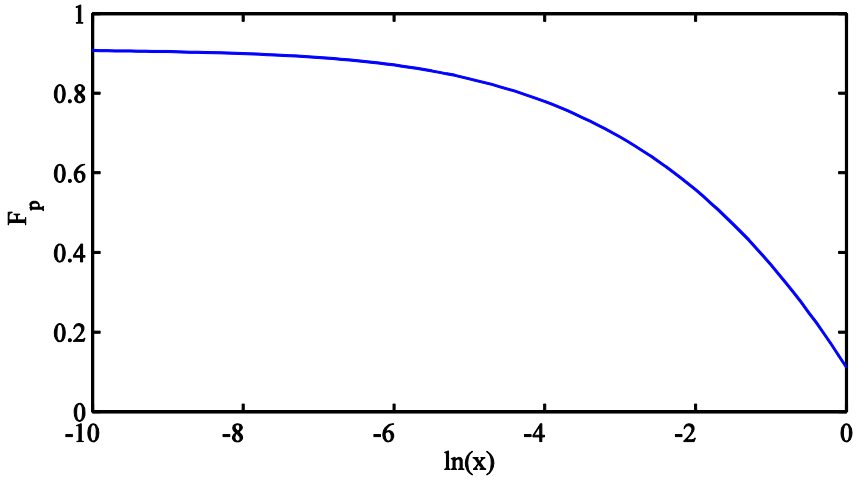

Figure 11: Pressure factor for air over ice employing the experimental results

1.4.2 Nitrogen

In order to estimate the water vapor enhancement factor for nitrogen, an alternative approach has been employed. The Lennard-Jones potential is a mathematical simplification of the interactions between the atoms[42]. The Lennard-Jones parameters of a mixture can be estimated using the so-called mixing rules listed as

$$(\varepsilon/k_B)_{12} = \sqrt{(\varepsilon/k_B)_{11}(\varepsilon/k_B)_{22}}/\xi^2, \quad (1\text{-}20)$$

$$\sigma_{12} = \frac{\sigma_{11} + \sigma_{22}}{2}\xi^{-1/6}, \quad (1\text{-}21)$$

$$\xi = 1 + 0.892\,(3a_{11}t_{22}^{*}\sqrt{\varepsilon_{22}/\varepsilon_{11}}\,/2\pi N_A{\sigma_{11}}^3), \quad (1\text{-}22)$$

by considering t_{22}^{*}=1.2 for water-water interactions the values of σ_{12} and $\varepsilon_{12}{k_B}^{-1}$ can be obtained and tabulated in Table 6.

Table 6: Lennard-Jones parameters of humid nitrogen [43]

Interacting molecules	σ/ Å	$\varepsilon.{k_B}^{-1}$ /K
N_2-N_2	3.701	95.04
N_2-H_2O	3.145	169.48

Rabinovich performed a method to calculate the second virial cross coefficient based on the Lennard-Jones potential [43]. Table 7 provides a set of constants for Equation (1-19) fitted in the calculations as illustrated in Figure 12.

Table 7: Constants of the second virial coefficients for Nitrogen

B_{xx}	*a*	*b*	*c*	*d*
B_{aa}	4.13E-06	0.003143	-0.00036	-0.01035
B_{aw}	1.42E-14	0.04698	-0.00046	-0.00883
B_{ww}	-63.01	-0.04363	-0.05117	-0.013

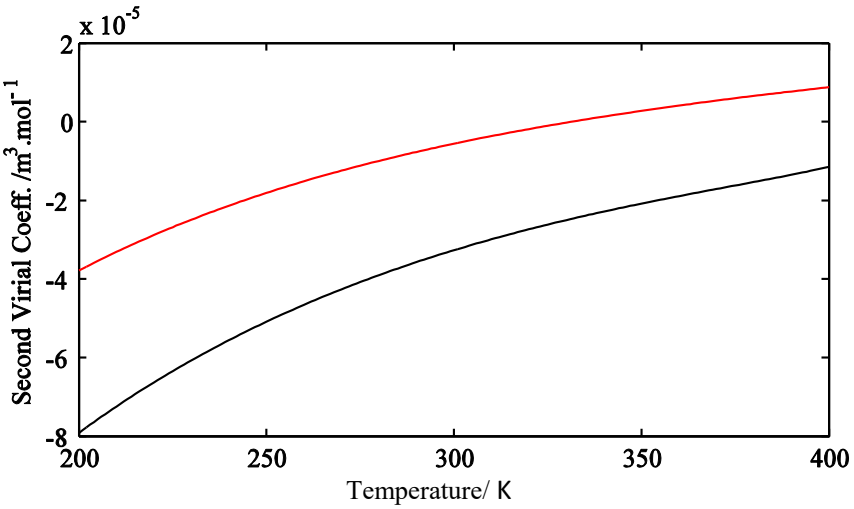

Figure 12: Second virial coefficients of nitrogen, B_{aa} in red and B_{aw} in black, obtained by employing the double exponential constants in Equation(1-19)

Coefficients of Equation (1-17) are calculated for Nitrogen-liquid water equilibrium and reported in Table 8 . Figure 13 evidences small deviations to that of air in Sec.1.4.1

Table 8: Constants of Equation (1-17) for nitrogen-water equilibrium based on B_{aw} results presented by Rabinovich

a_0	0.015882
a_1	0.008755
a_2	0.002854
a_3	0.000534
a_4	6.10E-05
a_5	3.86E-06
a_6	*1.03E-07*

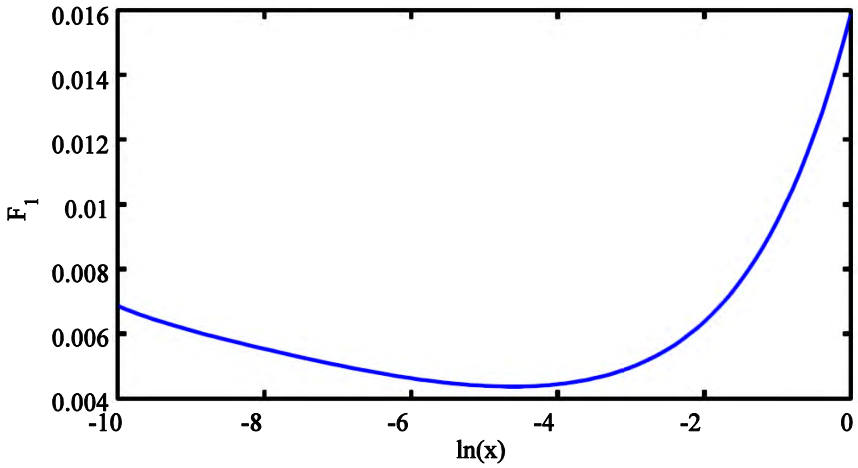

Figure 13: Atmospheric factor for nitrogen over water employing the Rabinovich values

The pressure factor should also be considered either with the following constants listed in Table 9 or values of Figure 14.

Table 9: Constants of Equation (1-18) for nitrogen-water equilibrium based on B_{aw} results presented by Rabinovich

b_0	0.679868
b_1	0.003693
b_2	0.019236
b_3	0.003025
b_4	1.36E-04

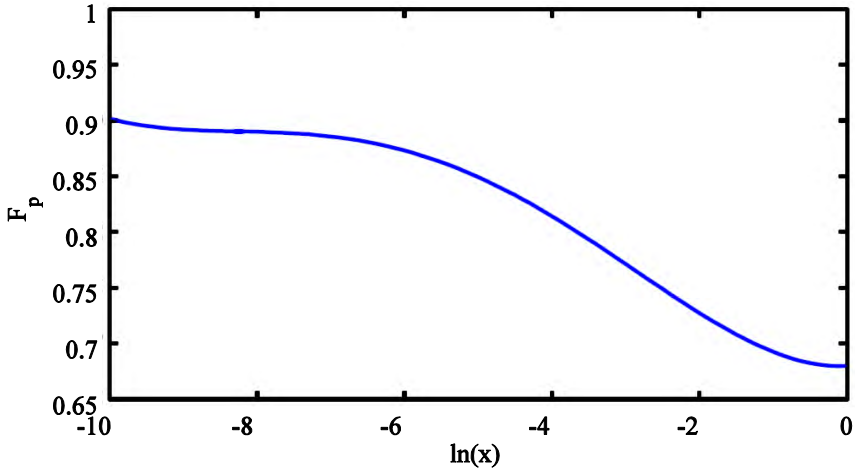

Figure 14: Pressure factor for nitrogen over water employing the Rabinovich values

For N_2 in equilibrium over ice:
As concerns the F_1 factor for nitrogen –ice equilibrium, results of Table 10 and Figure 15 shows a considerable deviation in the low water concentrations respect to that of the air.

Table 10: Constants of Equation (1-17) for nitrogen ice equilibrium based on B_{aw} results presented by Rabinovich

a_0	0.043724
a_1	0.031878
a_2	0.010753
a_3	0.001942
a_4	1.99E-04
a_5	1.08E-05
a_6	2.44E-07

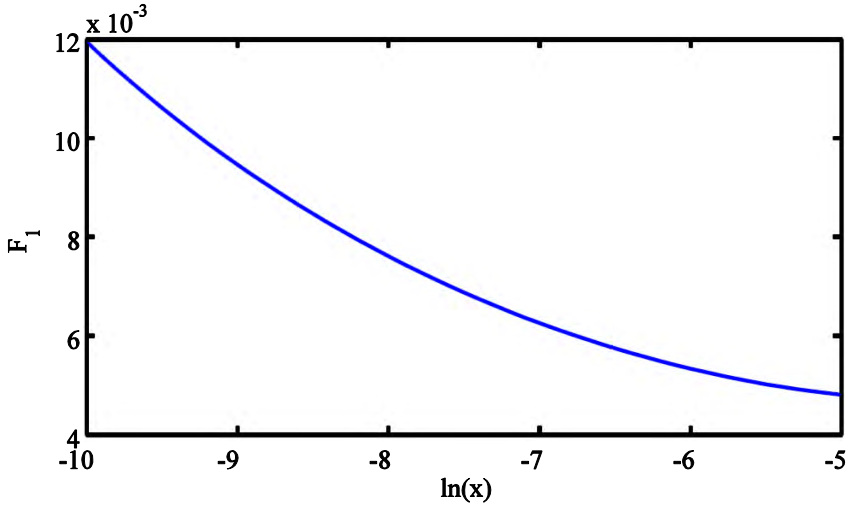

Figure 15: Atmospheric factor for nitrogen over the ice employing the Rabinovich values

Furthermore, a set of coefficients for the pressure correction are presented in Table 11 and depicted in Figure 16

Table 11: Constants of Equation (1-18) for nitrogen ice equilibrium based on B_{aw} results presented by Rabinovich

b_0	0.345025
b_1	-0.22265
b_2	-0.03284
b_3	-0.00209
b_4	-4.60E-05

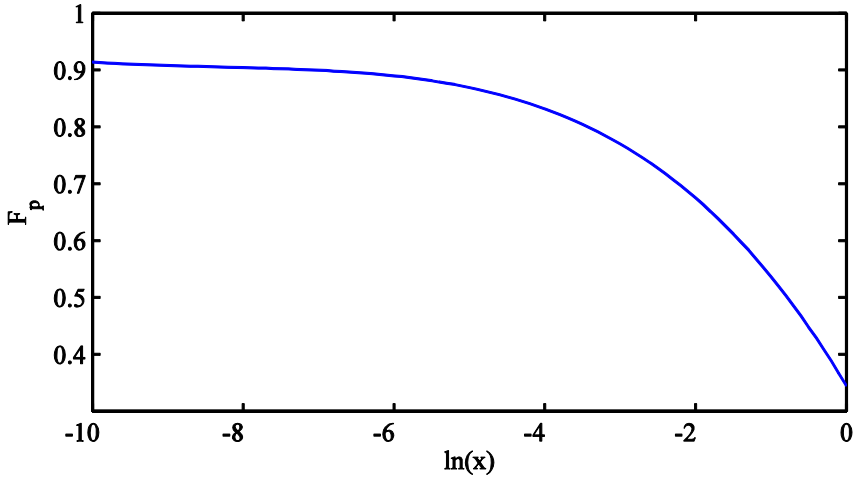

Figure 16: Pressure factor for nitrogen over the ice employing the Rabinovich values

In several metrological applications, even at the level of the primary labs, the enhancement factors for air are also employed for humid nitrogen conversions. However, this work shows that particular care should be considered at least at the uncertainty assessment stage. Basically, the differences caused by changing the carrier gas from air to nitrogen can be approximated using

$$\frac{f^{N2}}{f^{air}} = \frac{f_3^{N2} f_4^{N2}}{f_3^{air} f_4^{air}} = e^{\frac{X_a^2 P}{RT}(B_{\mathrm{NN}} - 2B_{\mathrm{NW}} - B_{AA} + 2B_{\mathrm{AA}})}, \qquad (1\text{-}23)$$

where f_3 and f_4 are that of Equation (1-14-3) and (1-14-4).

The deviation at low concentrations is much more significant because, firstly, the difference of cross virial coefficients is much greater at lower temperatures. Secondly, the water mole fraction is smaller and, eventually, the dew-point temperature is lower. The water vapor enhancement factor can be used reciprocally at relatively higher dew-point temperatures, but in the low concentrations (e.g., dew-point temperature lower than -100 °C) an uncertainty contribution of about 15%, refer to Figure 17, should be considered for the enhancement factor correction.

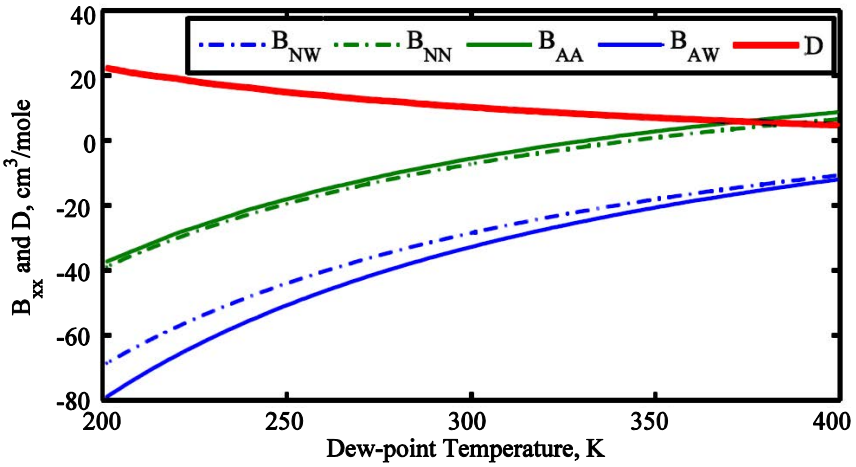

Figure 17: Second virial coefficients and the D factor as $B_{\mathrm{NN}} - 2B_{\mathrm{NW}} - B_{AA} + 2B_{\mathrm{AA}}$

1.4.3 Oxygen

Presence of water in oxygen is of interest in a number of applications including the corrosion in the gas cylinders. Considering the Lennard-Jones parameters of oxygen and water and by solving the Equations (1-20) to (1-22) the potential well depth, $\varepsilon.k^{-1}$, and the collision diameter, σ, of the mixture can be calculated and reported in Table 12.

Table 12: Lennard-Jones parameters of humid oxygen

Interacting molecules	σ/ Å	$\varepsilon.k_{\mathrm{B}}{}^{-1}$ /K
O_2-O_2	3.44	118.18
O_2-H_2O	3.016	188.67

By fitting the Rabinovich calculations to the double exponential of Equation (1-19) constants yields to Table 13 and Figure 18.

Table 13: Constants of the second virial coefficients for oxygen

B_{xx}	*a*	*b*	*c*	*d*
B_{aa}	1.82E-07	0.008666	-0.00039	-0.01025
B_{aw}	-2.25E-03	-0.02817	-0.00027	-0.00883
B_{ww}	-63.01	-0.04363	-0.05117	-0.013

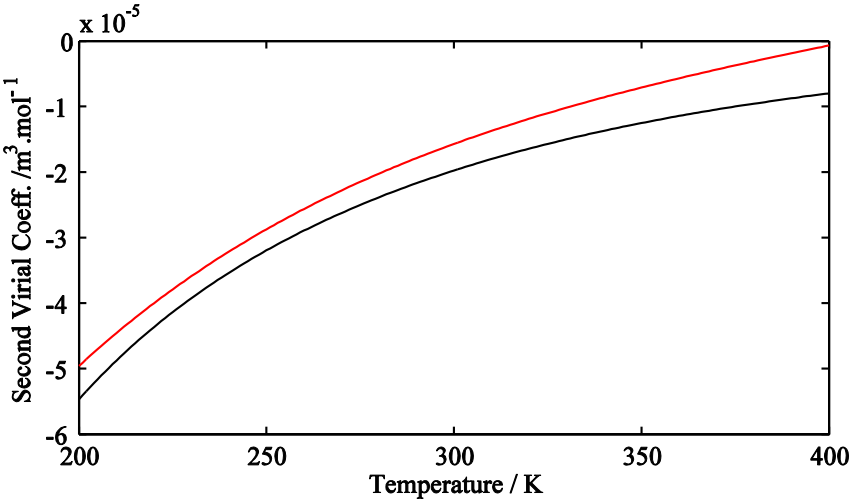

Figure 18: Second virial coefficients of Oxygen, B_{aa} in red and B_{aw} in black, obtained by employing the double exponential constants of Equation(1-19)

Coefficients of Equation (1-17) are calculated for oxygen-liquid water equilibrium and reported in Table 14. Furthermore, Figure 19 reports a minimum at about $4 \cdot 10^{-3}$ of water mole fraction.

Table 14: Constants of Equation (1-17) for oxygen-water equilibrium based on B_{aw} results presented by Rabinovich

a_0	0.015878
a_1	0.009516
a_2	0.003044
a_3	0.000572
a_4	6.52E-05
a_5	4.11E-06
a_6	1.09E-07

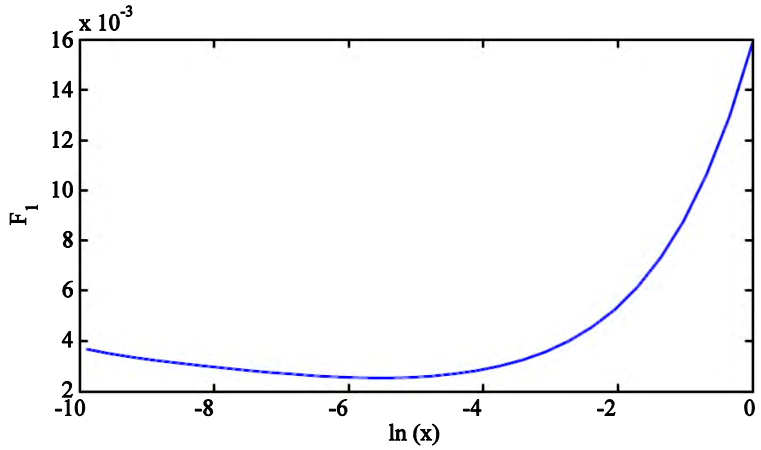

Figure 19: Atmospheric factor for oxygen over water employing the Rabinovich values

The pressure correction is applicable considering Figure 20 or by the following values for “b”:

Table 15: Constants of Equation (1-17) for oxygen-water equilibrium based on B_{aw} results presented by Rabinovich

b_0	0.680408
b_1	0.008737
b_2	0.015456
b_3	0.001895
b_4	6.3E-05

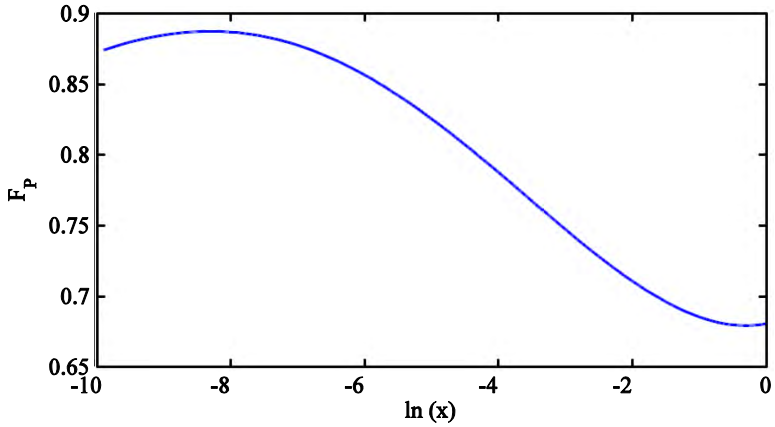

Figure 20: Pressure factor for oxygen over water employing the Rabinovich values

Further elaboration is needed for the equilibrium over ice:

Coefficients of Equation (1-17) are calculated for the equilibrium over solid water and reported in Table 16. A monotonic descending is reported by Figure 21 starting from 0.0035 at about 45 ppm of water mole fraction.

Table 16: Constants of Equation (1-17) for oxygen-ice equilibrium based on B_{aw} results presented by Rabinovich

a_0	0.015420
a_1	0.007879
a_2	0.001996
a_3	0.000274
a_4	2.20E-05
a_5	9.67E-07
a_6	1.80E-08

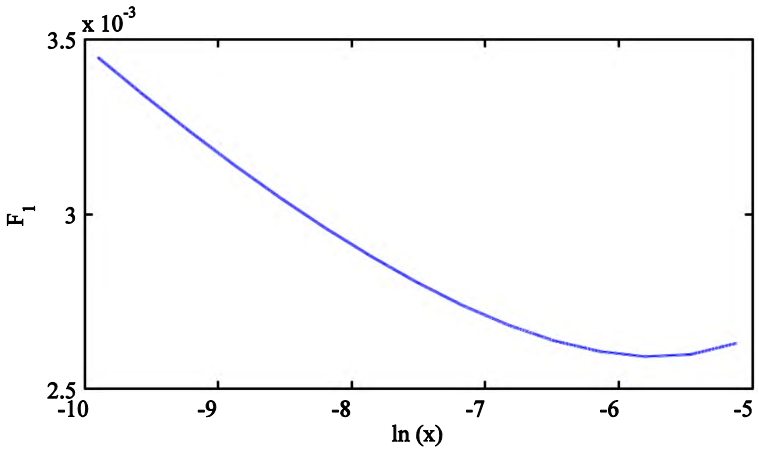

Figure 21: Atmospheric factor for nitrogen over ice employing the Rabinovich values

Moreover, a set of coefficients for the pressure factor are reported for oxygen-ice equilibrium in Table 17 and Figure 22. F_P remains in the standard shape of the previous sections considering the humid air and nitrogen.

Table 17: Constants of Equation (1-18) for oxygen-ice equilibrium based on B_{aw} results presented by Rabinovich

b_0	0.297589
b_1	-0.22496
b_2	-0.03189
b_3	-0.00204
b_4	-4.9E-05

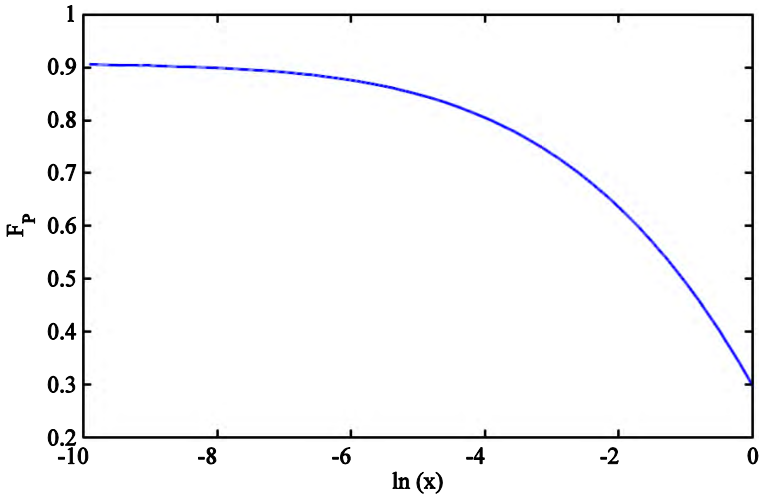

Figure 22: Pressure factor for nitrogen over the ice employing the Rabinovich values

1.4.4 **Ammonia**

Ammonia has a pyramidal molecular structure with a bond angle of 106.7° yielding to a dipole moment; thus, a strong intermolecular interaction in the water-ammonia is predictable. As an alternative method, the second virial coefficient of a mixture can be calculated using any of the excess parameters, e.g. excess enthalpy and excess density. This equation can be employed to define the

second cross virial coefficient needed for the enhancement factor elaboration using the following equation

$$B = x^2.B_{aa} + 2x(1-x)\cdot B_{aw} + (1-x)^2\cdot B_{ww}. \qquad (1\text{-}24)$$

Wormalda and Wurzberger have used the following equations to calculate the virial coefficient of the mixture for their experimental results [44]

$$H_m^E = x\cdot(1-x)\cdot p(2\emptyset_{aw} - \emptyset_{aa} - \emptyset_{ww}) - (\frac{P^2}{RT})\{B\cdot \emptyset - xB_{aa}\emptyset_{aa} - (1-x)B_{ww}\emptyset_{ww}\}, \qquad (1\text{-}25)$$

where

$$\emptyset = B - T(\frac{dB}{dT}). \qquad (1\text{-}26)$$

The second virial coefficients for ammonia has been fitted to the Equation (1-19) for the sake of uniformity and is reported in Table 18.

Table 18: Constants of the Second Virial Coefficients for air

B_{xx}	*a*	*b*	*c*	*d*
B_{aa}	-0.1754	-0.02857	-0.00192	-0.00712
B_{aw}	-25.74	-0.0406	-0.03401	-0.01179
B_{ww}	-63.01	-0.04363	-0.05117	-0.013

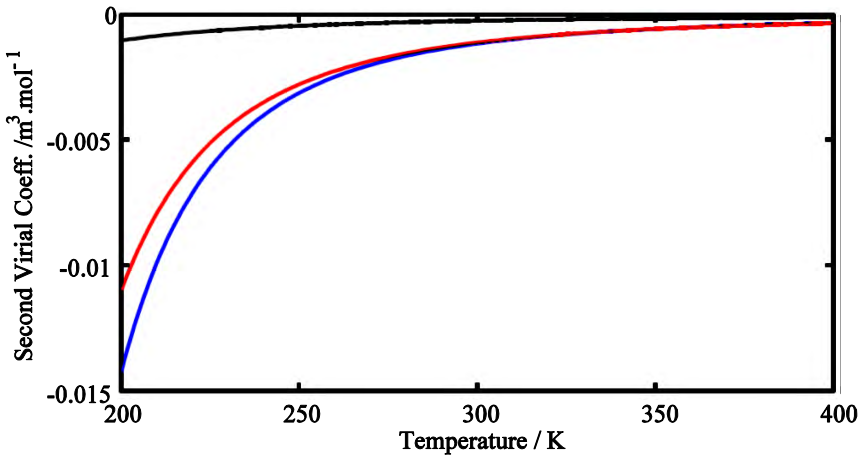

Figure 23: Second virial coefficients of oxygen, B_{aa} in red, B_{aw} in black and B_{ww} in blue, obtained by employing the double exponential constants of Equation (1-19)

Figure 23 clearly shows that the cross coefficient is at the same order as that of water and this is due to the ammonia molecular shape which provides a large intermolecular interaction with water molecules. This is worth mentioning that by applying the mixing rules for polar-polar molecules the reduced dipole moment, t^*, can be evaluated as 1.104 which represents the same order of magnitude as that of water, t_w^*=1.238. Coefficients of Equation(1-17) calculated for ammonia-water equilibrium and reported in Table 19.

Table 19: Constants of Equation (1-17) for ammonia-water equilibrium based on the excess enthalpy cross coefficient calculations presented in [44]

a_0	1.61E-2
a_1	-1.52E-2
a_2	-1.90E-4
a_3	-4.61E-4
a_4	-2.39E-5
a_5	-2.52E-6
a_6	3.80E-9

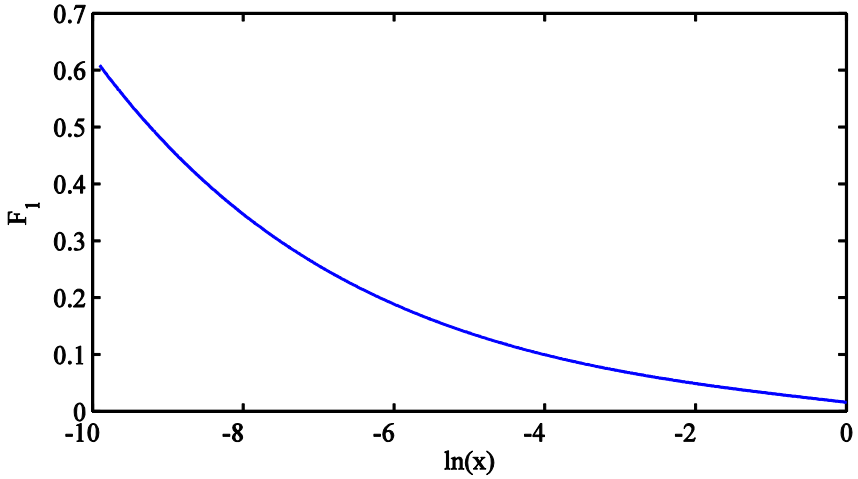

Figure 24: Atmospheric factor for ammonia over water employing the excess enthalpy measurements

Figure 24 shows an enormous value of 0.6 in the low concentrations. It remarkably highlights that for the polar molecules special care should be considered especially in the low humidity concentrations. The pressure correction should be considered in accordance with the "b" values of Table 20 in contrast with previous molecules under study, The pressure factor as depicted in Figure 25, reports a much flatter behavior in the mole fraction range.

Table 20: Constants of Equation(1-18) for ammonia-water equilibrium based on the excess enthalpy cross coefficient calculations presented in [44]

b_0	6.76E-1
b_1	-7.88E-3
b_2	-1.88E-3
b_3	-3.69E-4
b_4	-1.25E-5

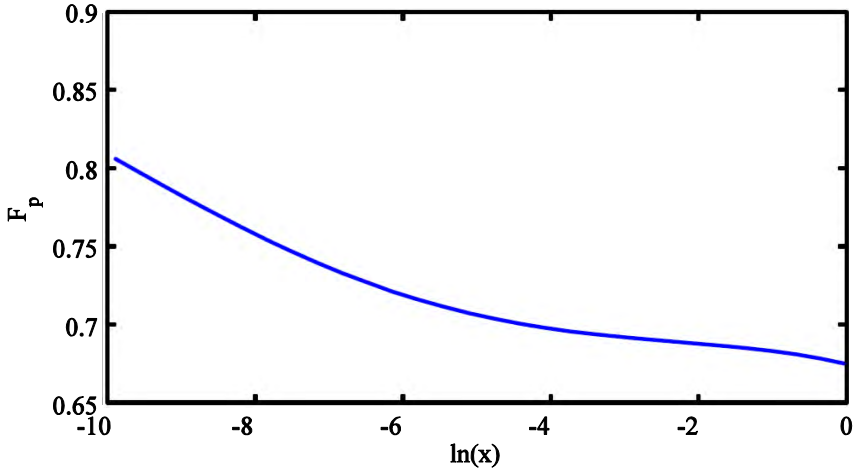

Figure 25: Pressure factor for ammonia over water employing the excess enthalpy measurements

As regards NH_3 in equilibrium over ice, Coefficients of Equation (1-17) are calculated for ammonia-water equilibrium and reported in Table 21 and finally illustrated in Figure 26.

Table 21: Constants of Equation (1-17) for ammonia-ice equilibrium based on the excess enthalpy cross coefficient calculations presented in [44]

a_0	0.028766
a_1	-0.01012
a_2	0.002193
a_3	0.000178
a_4	5.49E-05
a_5	3.27E-06
a_6	1.53E-07

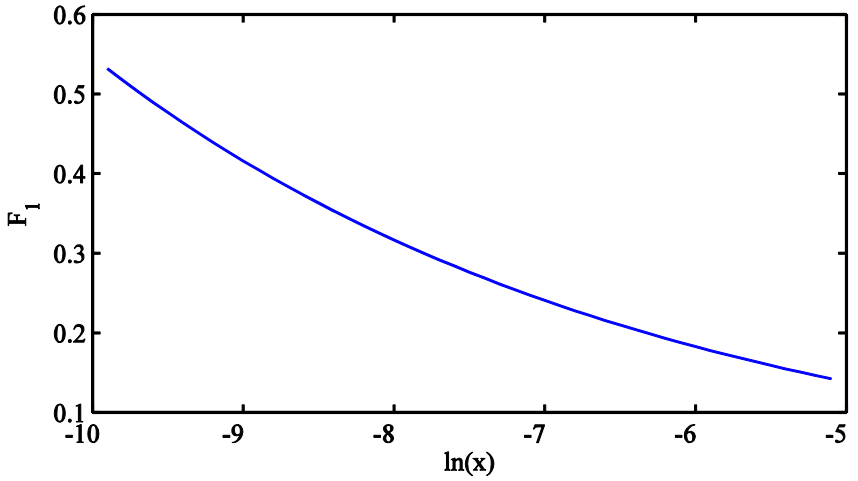

Figure 26: Atmospheric factor for nitrogen over water employing the excess enthalpy measurements

And a set of coefficients for the pressure correction should be found in Table 21. Apparently, F_p exhibits a very flat behavior in Figure 27 :

Table 22: Constants of Equation (1-18) for ammonia-ice equilibrium based on the excess enthalpy cross coefficient calculations presented in [44]

b_0	-1.3673
b_1	-1.2877
b_2	-2.903E-1
b_3	-2.837E-2
b_4	-1.003E-3

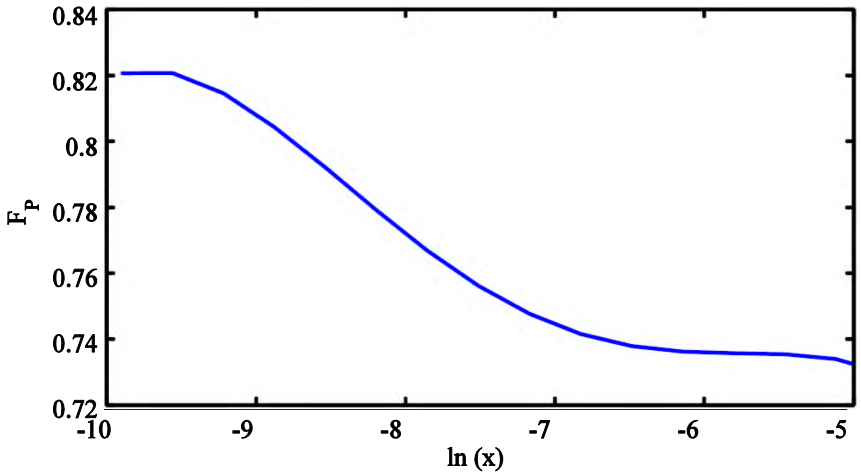

Figure 27: Pressure factor for nitrogen over water employing the excess enthalpy measurements

1.4.5 **Hydrogen**

Considering the nature of hydrogen molecules, the potential parameters are subject to the quantum corrections yielding to Table 23. By considering the Equations (1-20) to (1-22), the cross interaction parameters can be calculated and tabulated in the same table.

Table 23: Lennard-Jones parameters of humid nitrogen

Interacting molecules	σ/ Å	$\varepsilon.k_B^{-1}$ /K
H_2-H_2	2.918	32.88
H_2-H_2O	2.744	93.78

And, consequently, the Rabinovich calculations can be fitted in (1-19) to single out the parameters of Table 24.

Table 24: Constants of the second virial coefficients for nitrogen

B_{xx}	*a*	*b*	*c*	*d*
B_{aa}	1.59E-05	9.43E-05	-5.24E-05	-0.01253
B_{aw}	1.81E-06	0.003085	-0.00014	-0.0104
B_{ww}	-63.01	-0.04363	-0.05117	-0.013

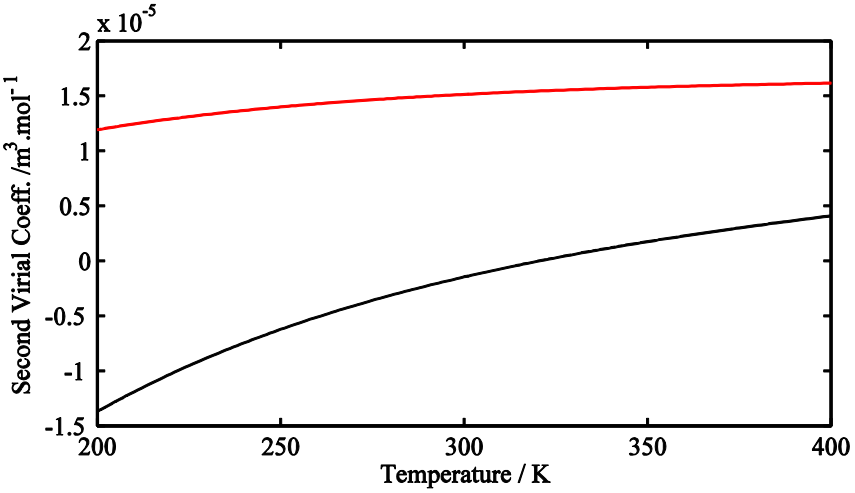

Figure 28: second virial coefficients of Hydrogen, B_{aa} in red and B_{aw} in black, obtained by employing the double exponential constants in Equation(1-19)

B_{aw} values, as reported in Figure 28, are relatively smaller than that of air, for instance, this is 20 times lower than air at 300 K. Atmospheric factor is calculated for hydrogen-water equilibrium (see Table 25) and is plotted in Figure 29.

Table 25: Constants of Equation (1-17) for hydrogen-water based on B_{aw} results presented by Rabinovich

a_0	0.015851
a_1	0.009654
a_2	0.003096
a_3	0.000585
a_4	6.69E-05
a_5	4.22E-06
a_6	1.12E-07

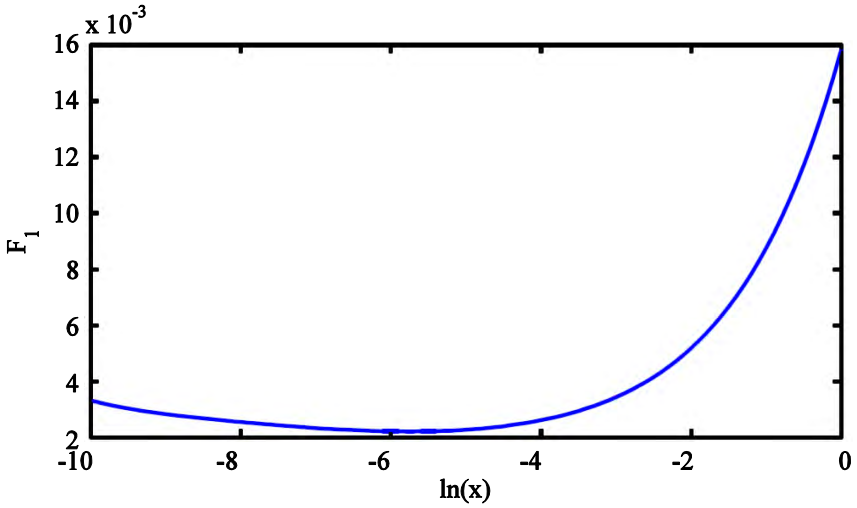

Figure 29: Atmospheric factor for hydrogen over water employing the Rabinovich values

The pressure factor is obtained and "b" values are listed in Table 26. Slight reduction of F_p appears in Figure 30 for the lowest range of water mole fraction (i.e., lower than 300 ppm)

Table 26: Constants of Equation (1-18) for hydrogen-water based on B_{aw} presented by Rabinovich

b_0	0.680581
b_1	0.010204
b_2	0.014616
b_3	0.001549
b_4	3.85E-05

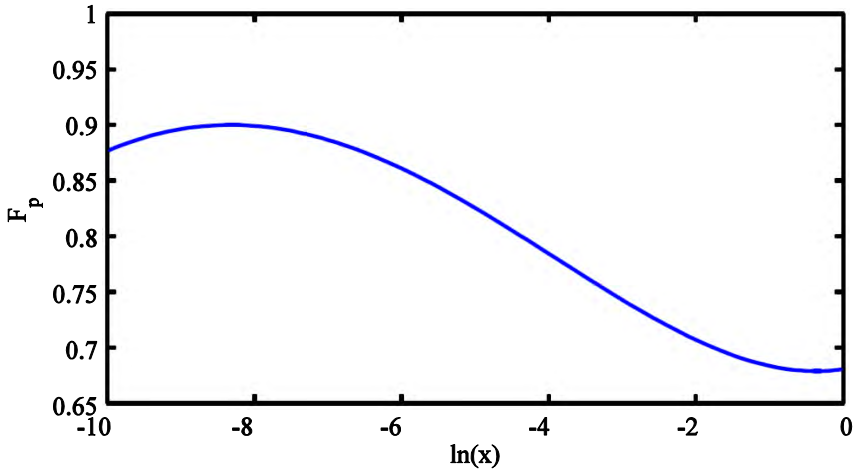

Figure 30: Pressure factor for hydrogen over water employing the Rabinovich values

A similar procedure should also be considered for the equilibrium over crystalized water. This is reported in Table 27 and illustrated in Figure 31

Table 27: Constants of Equation (1-17) for hydrogen-ice equilibrium based on B_{aw} results presented by Rabinovich

a_0	-0.00223
a_1	-0.00746
a_2	-0.00355
a_3	-0.00078
a_4	-8.95E-05
a_5	-5.25E-06
a_6	-1.25E-07

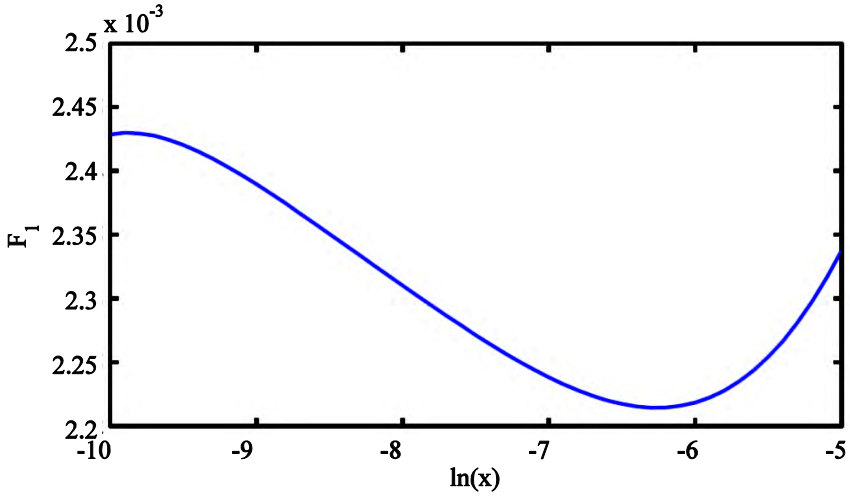

Figure 31: Atmospheric factor for hydrogen over ice employing the Rabinovich values

Pressure factor should be found by polynomial constants of Table 28 and Figure 32 in which a maximum of 0.91 is reported in the lowest range.

Table 28: Constants of Equation (1-18) for hydrogen-ice equilibrium based on B_{aw} results presented by Rabinovich

b_0	0.561505
b_1	-0.04746
b_2	0.010494
b_3	0.002188
b_4	1.02E-04

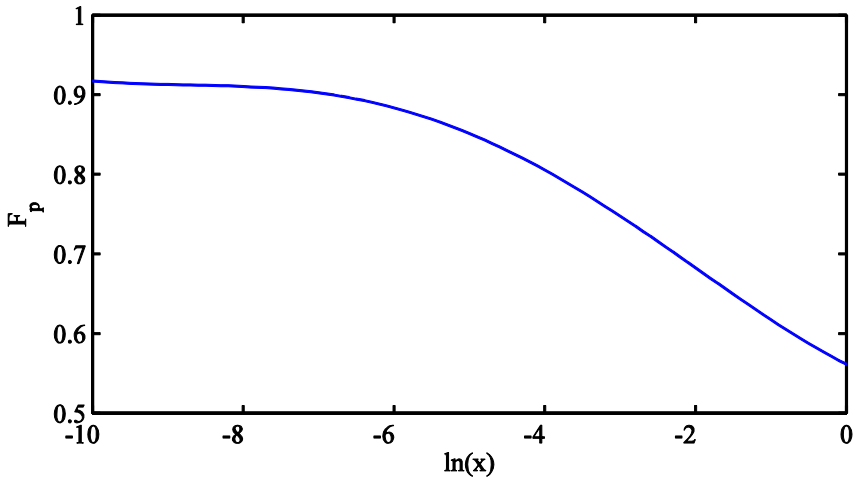

Figure 32: Pressure factor for hydrogen over the ice employing the Rabinovich values

1.4.6 **Methane**

Methane as the major component of the natural gas attracts interests in the field of humidity[45]. Experimental setups have been exploited at INRIM [29] and VTT MIKES [30] to measure the water vapor enhancement factor. Alternatively, considering the Lennard-Jones parameters of methane and water and by

employing the Equations (1-20) to (1-22) the potential well depth and the collision diameter of the mixture can be calculated (i.e. Table 29)

Table 29: Lennard-Jones parameters of humid nitrogen

Interacting molecules	σ/ Å	$\varepsilon.k_B^{-1}$ /K
CH_4-CH_4	3.816	146.1
CH_4-H_2O	3.2	280.11

By following the aforementioned method, the double exponential constants of Equation (1-19) can be achievable. This is worth mentioning that B_{aw} of CH_4 is as double as that of the air at 300 K. Figure 33 compares the values of $B_{aa}$and B_{aw} in the range 200 K to 400 K.

Table 30: Constants of the second virial coefficients for methane

B_{xx}	*a*	*b*	*c*	*d*
B_{aa}	-2.418E-03	-3.463E-2	-6.160E-4	-8.990E-3
B_{aw}	-1.12	-0.06209	-0.000630	-0.00801
B_{ww}	-63.01	-0.04363	-0.05117	-0.013

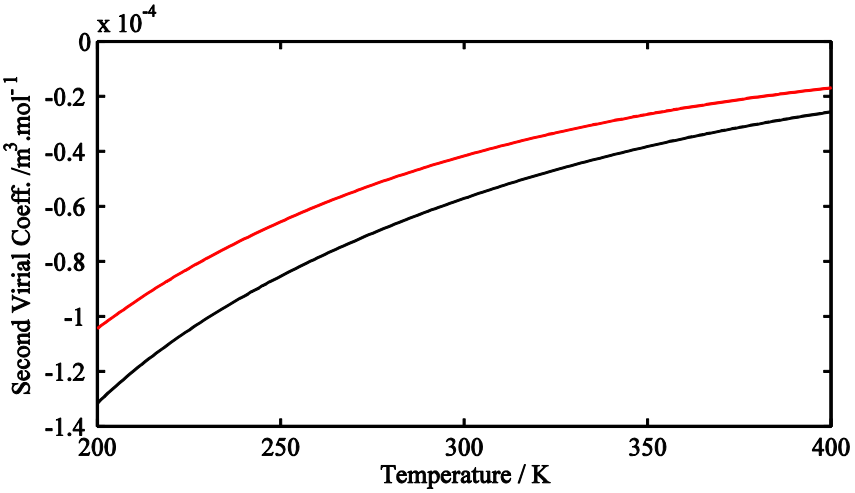

Figure 33: second virial coefficients for methane, B_{aa}in red and B_{aw} in black, obtained by employing the double exponential constants in Equation(1-19)

Methane-Water equilibrium will result in the constants of Table 31. The minimum value of the atmospheric factor, as figured in Figure 34, takes place at x=0.18.

Table 31: Constants of Equation (1-17) for methane-water equilibrium based on B_{aw} results presented by Rabinovich

a_0	0.015863112
a_1	0.008616886
a_2	0.002852687
a_3	0.000531018
a_4	6.03E-05
a_5	3.79E-06
a_6	1.00E-07

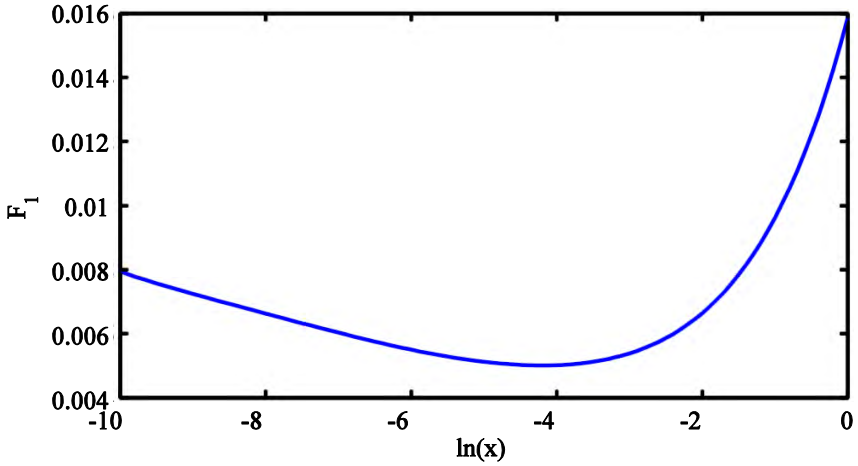

Figure 34: Atmospheric factor for methane over water employing the Rabinovich values

The pressure factor constants are detailed in Table 32. It is noticeable that despite having big differences in potential parameters. F_P remaines, with minor deviations, within the standard shape of non-polar carrier gases, refer to Figure 35.

Table 32: Constants of Equation (1-18) for methane-water equilibrium based on B_{aw} results presented by Rabinovich

b_0	0.679257979
b_1	0.002078918
b_2	0.018817622
b_3	0.003050555
b_4	1.42E-04

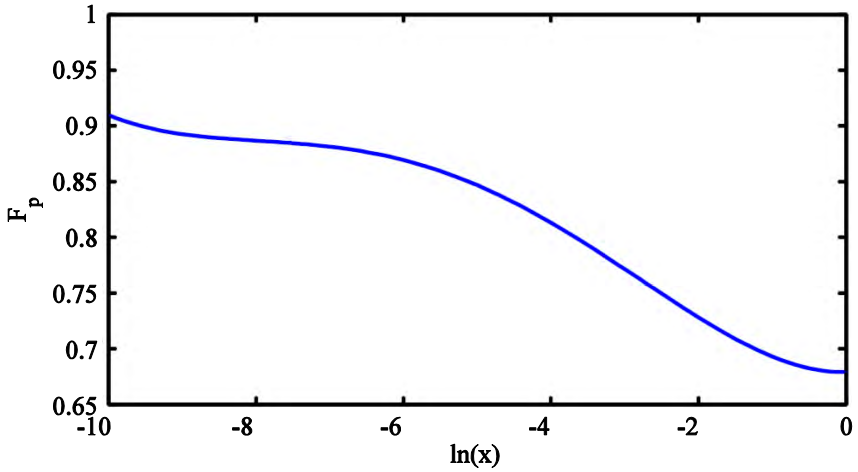

Figure 35: Pressure factor for methane over water employing the Rabinovich values

Likewise, Coefficients of Equation (1-17) are calculated for air-ice equilibrium, reported in Table 33 and depicted in Figure 36.

Table 33: Constants of Equation (1-17) for methane-ice equilibrium based on B_{aw} results presented by Rabinovich

a_0	0.015735834

a_1	0.007175095
a_2	0.001892257
a_3	0.000258561
a_4	2.07E-05
a_5	9.10E-07
a_6	1.71E-08

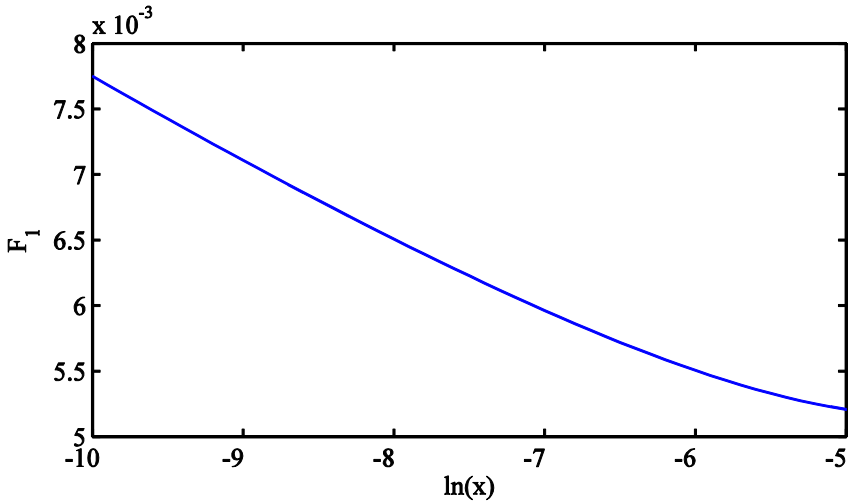

Figure 36: Atmospheric factor for methane over ice employing the Rabinovich values

Eventually, Figure 37 and Table 34 confirm that the pressure correction remains in the same shape as the other non-polar gas molecules.

Table 34: Constants of Equation (1-18) for methane-water based on B_{aw} results presented by Rabinovich

b_0	0.226302505
b_1	-0.30306364
b_2	-0.05238212
b_3	-0.00406957
b_4	-1.17E-04

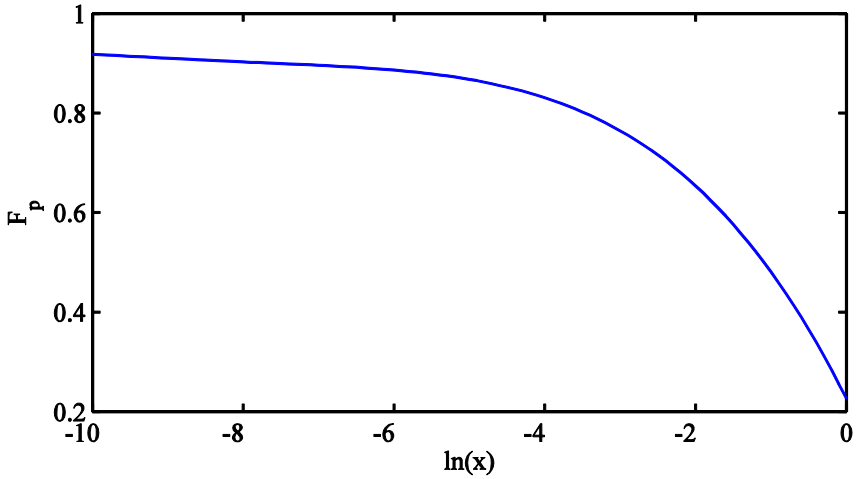

Figure 37: Pressure factor for methane over ice employing the Rabinovich values

1.4.7 **Argon**

Argon as a noble gas has the third most significant contribution to the earth's atmosphere. Lennard-Jones coefficients for Argon employing Equations (1-20) to (1-22) can be estimated in Table 35

Table 35: Lennard-Jones parameters of humid argon

Interacting molecules	σ/ Å	$\varepsilon.k_B^{-1}$ /K
Ar—Ar	3.327	121.08
Ar—H_2O	2.957	188.57

Parameters of Equation (1-19) can be fitted using the Rabinovich approach (i.e., Table 36). As illustrated in Figure 38 the second virial cross coefficient of argon is at the same order as the humid air.

Table 36: Constants of the second virial coefficients for argon

B_{xx}	*a*	*b*	*c*	*d*
B_{aa}	8.92E-05	-0.00497	-1.15E-17	0.070517
B_{aw}	0.00023	-0.00626	-8.43E-18	0.07064
B_{ww}	-63.01	-0.04363	-0.05117	-0.013

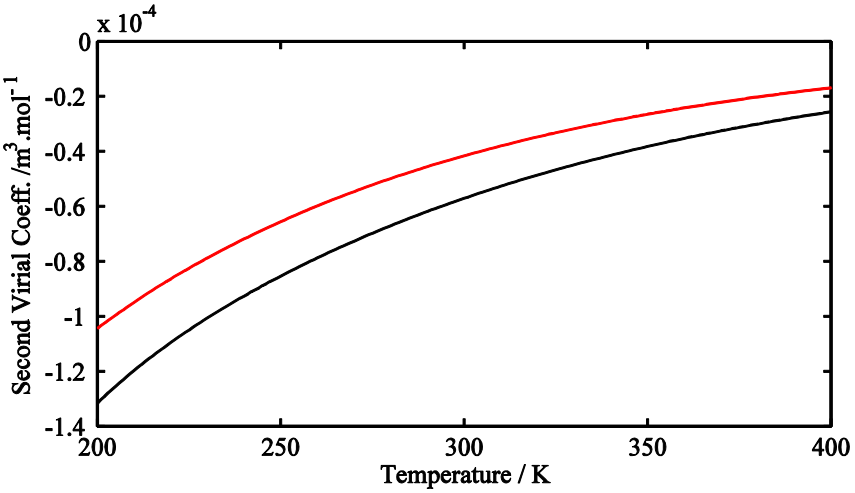

Figure 38: Second virial coefficients of argon, B_{aa} in red and B_{aw} in black, obtained by employing the double exponential constants in Equation(1-19)

In order to have the same functional equation, coefficients of Equation (1-17) are calculated for the equilibrium over liquid water equilibrium, listed in Table 37 and illustrated in Figure 39.

Table 37: Constants of Equation (1-17) for Argon-water equilibrium based on B_{aw} results presented by Rabinovich

a_0	0.015857
a_1	0.009175
a_2	0.002998

a_3	0.000562
a_4	6.42E-05
a_5	4.05E-06
a_6	1.07E-07

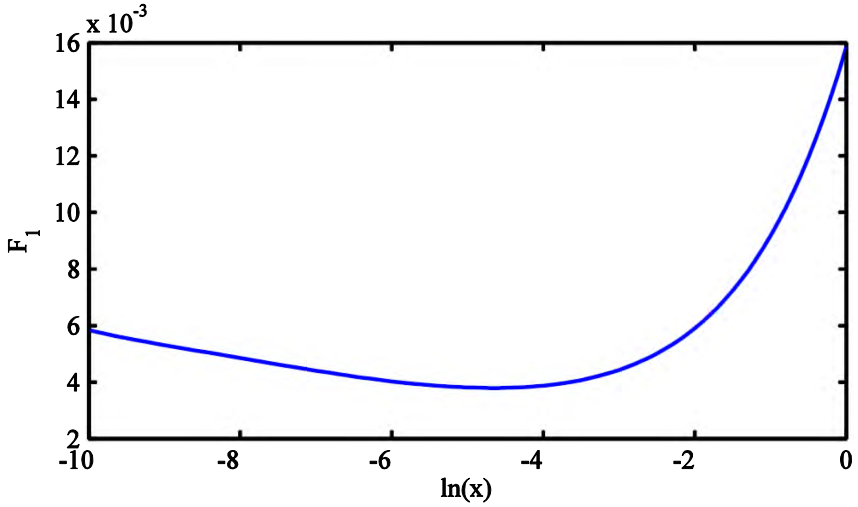

Figure 39: Atmospheric factor for argon over water employing the Rabinovich values

The pressure factor of argon should be considered according to Table 38 and Figure 40.

Table 38: Constants of Equation (1-18) for Argon-water equilibrium based on B_{aw} results presented by Rabinovich

b_0	**0.680208**
b_1	0.008304
b_2	0.018226
b_3	0.002668
b_4	1.14E-04

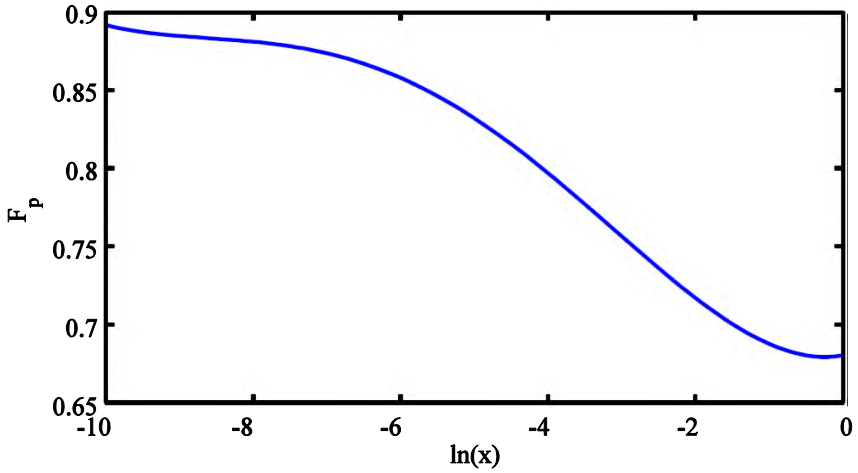

Figure 40: Pressure factor for argon over water employing the Rabinovich values

And for the equilibrium over ice:

Atmospheric factor should be applied using either Figure 41 or the polynomial of Equation (1-17) and constants of Table 39. It decreases monotonically from a value of about 5.4 which is slightly lower than that of equilibrium over water.

Table 39: Constants of Equation (1-17) for argon-ice equilibrium based on B_{aw} results presented by Rabinovich

a_0	0.015504
a_1	0.007558
a_2	0.001957
a_3	0.000268
a_4	2.15E-05
a_5	9.46E-07
a_6	1.76E-08

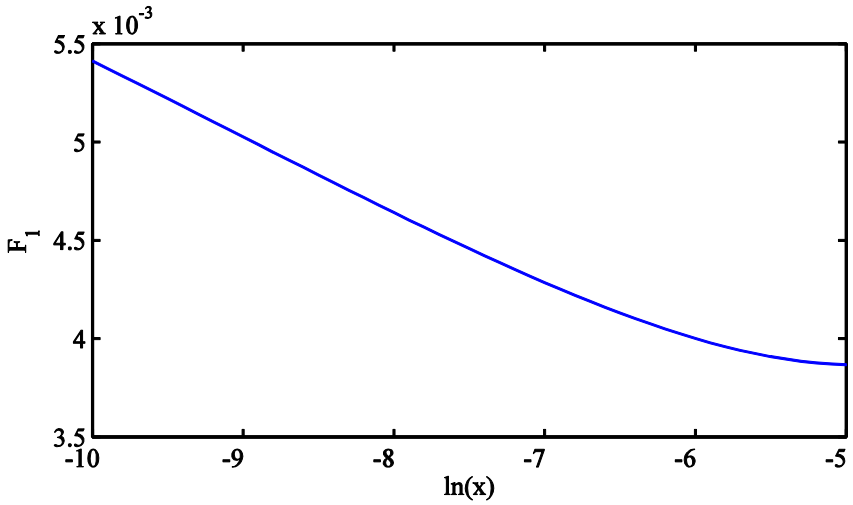

Figure 41: Atmospheric factor for argon over water employing the Rabinovich values

Similarly, a set of coefficients for the pressure correction considering Figure 42 or Table 40.

Table 40: Constants of Equation (1-18) for argon-ice equilibrium based on B_{aw} results presented by Rabinovich

b_0	0.403353
b_1	-0.17268
b_2	-0.02056
b_3	-0.00083
b_4	4.90E-07

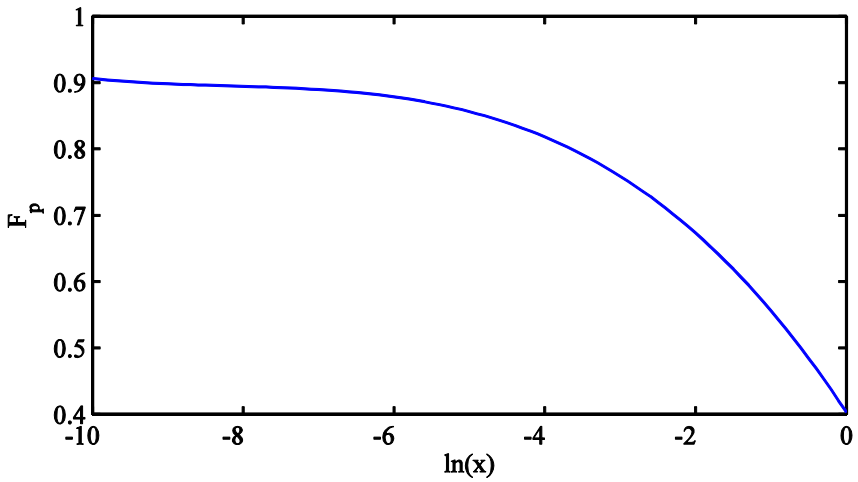

Figure 42: Pressure factor for argon over water employing the Rabinovich values

1.4.8 **Carbon dioxide**

The enhancement factor formulations released by pioneers has been carried out for CO_2-free air; however, a few decades later, the enhancement factor of CO_2-H_2O mixture has been discussed by Meyer and Harvey[46]. In order to calculate the enhancement factor theoretically, the Lennard-Jones coefficients of carbon dioxide are reported in Table 41 based on the Equations (1-20) to(1-22)

Table 41: Lennard-Jones parameters of humid carbon dioxide

Interacting molecules	σ/ Å	$\varepsilon.k_B^{-1}$ /K
CO_2-CO_2	4.306	202.8
CO_2-H_2O	3.456	257.37

The second virial coefficients can be fitted in the Equation (1-19) which results in Table 42.

Table 42: Constants of the second virial coefficients for Carbon monoxide

B_{xx}	*a*	*b*	*c*	*d*
B_{aa}	-4.62E-02	-0.03186	-9.36E-04	-0.00686
B_{aw}	-9.89E-03	-0.02702	-1.50E-03	-0.00683
B_{ww}	-63.01	-0.04363	-0.05117	-0.013

As depicted in Figure 43, the second virial cross coefficient of humid carbon dioxide is remarkably higher than that of CO_2-free air, e.g. 6 times higher at 200 K and 9 times bigger at 400 K.

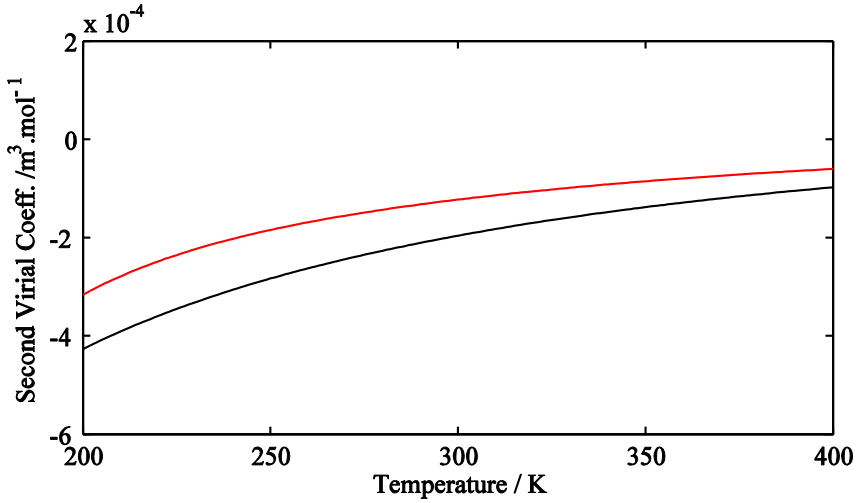

Figure 43: Second virial coefficients of carbon dioxide, B_{aa} in red and B_{aw} in black, obtained by employing the double exponential constants in Equation(1-19)

Table 43: Constants of Equation (1-17) for carbon dioxide-water equilibrium based on the results of $\boldsymbol{B_{aw}}$ presented by Rabinovich

$\boldsymbol{a_0}$	0.015888
$\boldsymbol{a_1}$	0.004712
$\boldsymbol{a_2}$	0.001908
$\boldsymbol{a_3}$	0.00033
$\boldsymbol{a_4}$	3.63E-05
$\boldsymbol{a_5}$	2.25E-06
$\boldsymbol{a_6}$	5.90E-08

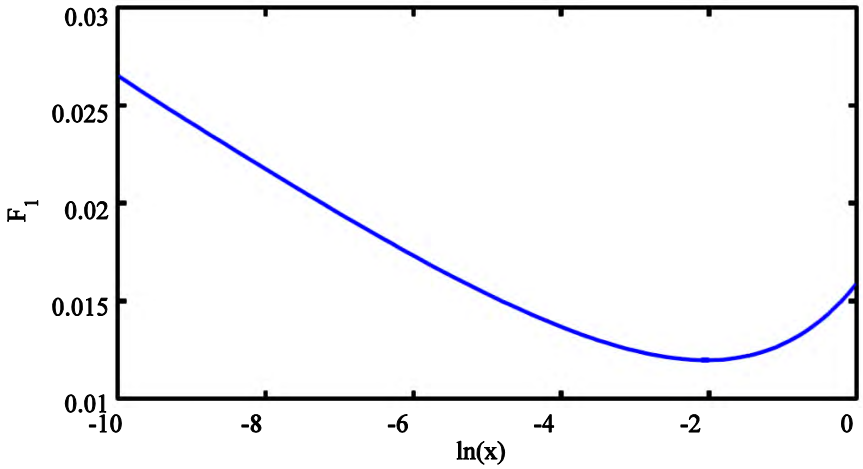

Figure 44: Atmospheric factor for carbon dioxide over water employing the Rabinovich values

Coefficients of Equation (1-17) are calculated for CO_2-water equilibrium and reported in Table 43. Consequently, Figure 44 shows that F_1 has a maximum of more than 0.025 which is enourmously higher than humid air. In addition to that, the pressure corecction should be considered with following constants of the polynomial in Equation (1-18). Figure 45 highlights an abnormal increase of 5% at the lowest range of the water mole fraction.

Table 44: Constants of Equation (1-18) for carbon dioxide-water equilibrium based on B_{aw} results presented by Rabinovich

b_0	0.674091
b_1	-0.04333
b_2	0.005234
b_3	0.001767
b_4	1.09E-04

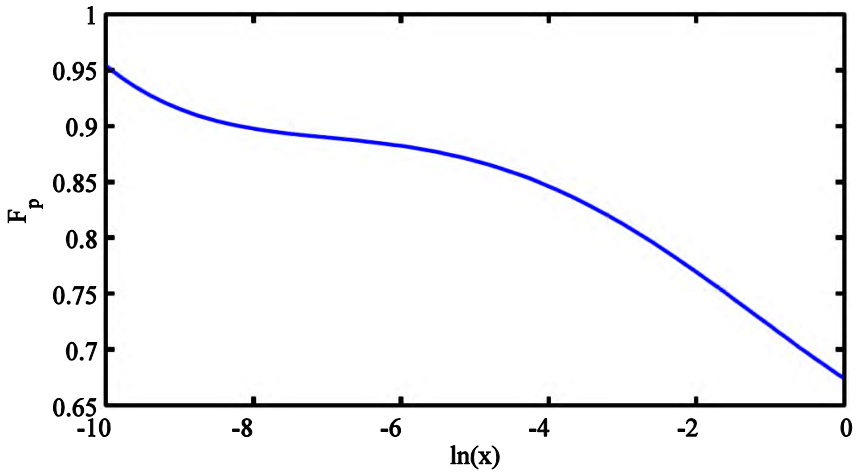

Figure 45: Pressure factor for carbon dioxide over water employing the Rabinovich values

And similarly for ice:

Coefficients of Equation (1-17) are calculated for CO_2-water equilibrium and reported in Table 45. Slight deviations from Figure 43 are due to the difference in the solid water chemical potential over that of the liquid water in Equation (1-14).

Table 45: Constants of Equation (1-17) for carbon dioxide-ice equilibrium based on the mixing rules presented in [43]

a_0	0.017484
a_1	0.00526
a_2	0.001944
a_3	0.000309
a_4	2.98E-05
a_5	1.59E-06
a_6	3.59E-08

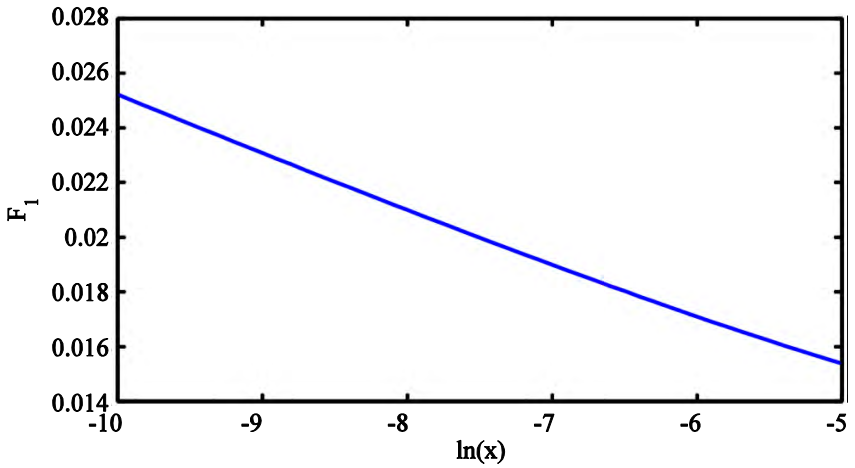

Figure 46: Atmospheric factor for carbon dioxide over water employing the Rabinovich values

A set of coefficients for the pressure correction is reported, the pressure factor remains at slightly lower levels comparing to the lowest part of equilibrium over the supercooled water (refer to Figure 47).

Table 46: Constants of Equation (1-18) for carbon dioxide-ice equilibrium based on B_{aw} results presented by Rabinovich

b_0	-0.14197
b_1	-0.55722
b_2	-0.11386
b_3	-0.01034
b_4	-3.45E-04

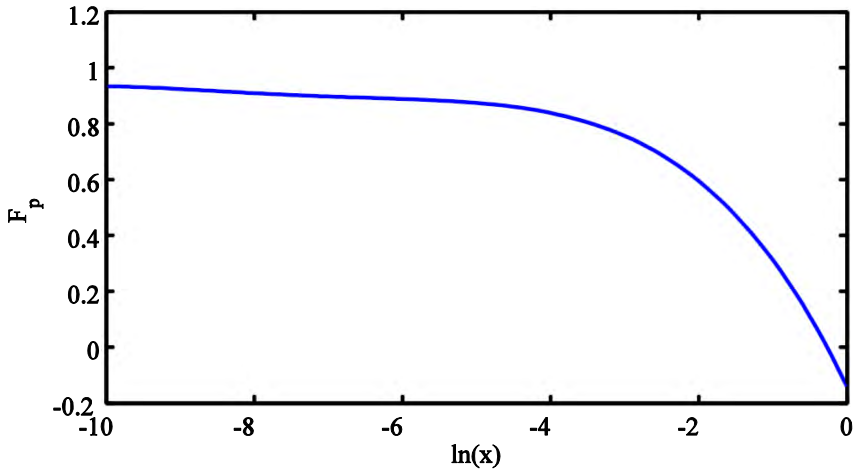

Figure 47: Pressure factor for carbon dioxide over water employing the Rabinovich values

1.5 The enhancement factor based on first-principles calculations

Recent theoretical work (e.g. [47]) together with the new hardware facilities turned computational quantum chemistry to one of the most useful tools in thermodynamics. In this section, the second virial coefficient, as reported by Harvey and Huang [48] has been considered for calculating the water vapor enhancement factor. The uncertainties of such results are better than several experimental-based correlations, and they remain valid for a broader range of temperature.

1.5.1 Nitrogen

For the sake of similarity, the original equation of Harvey and Huang [48] is rearranged to the double exponential form of the B values, i.e., Equation.(1-19). The coefficients of Table 47 indicate small deviations in the entire range (i.e. Figure 48).

Table 47 Constants of the second virial coefficients based on first-principles calculations for nitrogen according to [48]

B_{xx}	*a*	*b*	*c*	*d*
B_{aw}	7.62E-09	0.009717	-0.00057	-0.00959

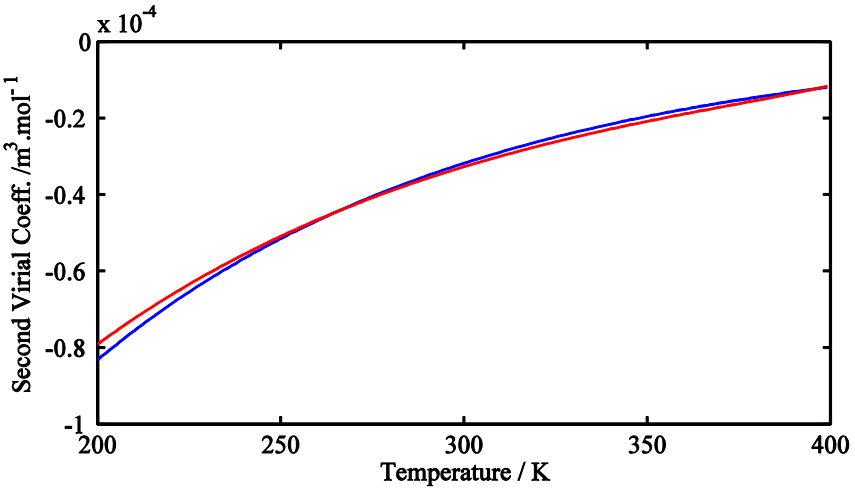

Figure 48: Second virial cross coefficients of nitrogen B_{aw}, blue stands for the correlation of Harvey [48] and red is according to Rabinovich [43]

The atmospheric factor is calculated for nitrogen-water, equilibrium in both condensed phases and reported in Table 48.

Table 48: Constants of Equation (1-17) for nitrogen-water and nitrogen-ice equilibrium based on the first-principles calculations

a_i	Liquid water	Solid water

a_0	0.015901	0.041551
a_1	0.008852	0.030026
a_2	0.002902	0.010081
a_3	0.000546	0.001814
a_4	6.29E-05	1.85E-04
a_5	3.99E-06	1.00E-05
a_6	1.07E-07	2.26E-07

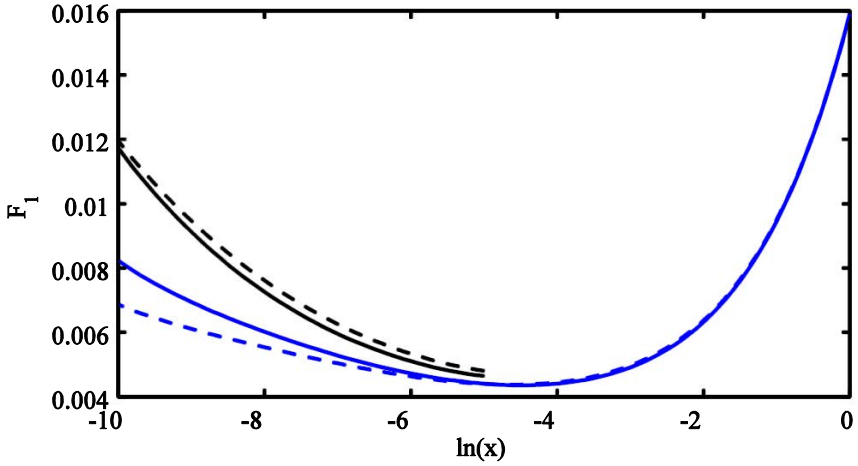

Figure 49: Atmospheric factor for nitrogen over water (in blue) and ice (in black) employing quantum chemistry calculations. Dashed lines are the results of section 1.4

Figure 49 shows negligible differences in higher concentrations for nitrogen-water equilibrium and higher differences in the lower range for nitrogen- supercooled water. Moreover, the deviation of nitrogen-ice remains within the uncertainty of calculations. Coefficients of Equation (1-18) are tabulated below in Table 49.

Table 49: Constants of Equation (1-18) for nitrogen-water and nitrogen-ice equilibrium based on the first-principles calculations

b_i	Liquid water	Solid water
b_0	0.67877	0.386255
b_1	0.002213	-0.2022
b_2	0.018055	-0.0298
b_3	0.002857	-0.0019
b_4	1.29E-04	-4.25E-05

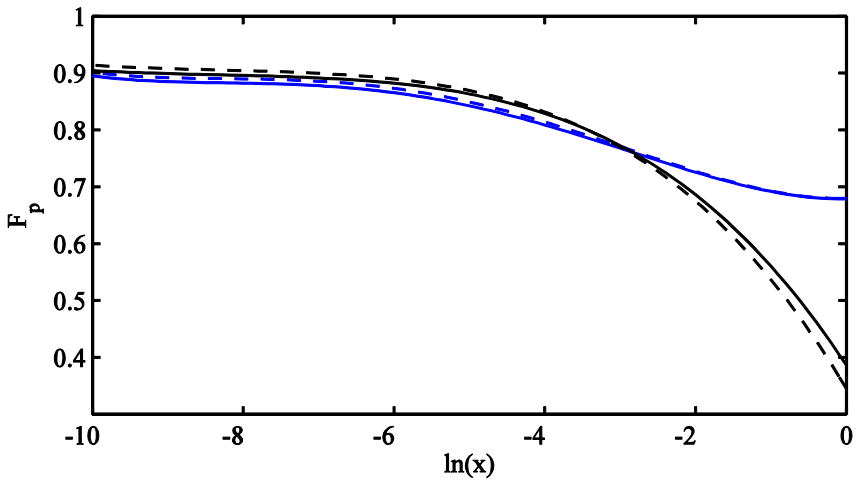

Figure 50: Pressure factor for nitrogen over water (in blue) and ice (in black) employing quantum chemistry calculations. Dashed lines are the results of section 1.4

Figure 50 reports an excellent agreement between F_P values for both water phases. The overall deviation of these calculations deviates from that of Sec.1.4.2 within only 3 % of the enhancement correction (i.e. *f*-1), refer to Figure 51.

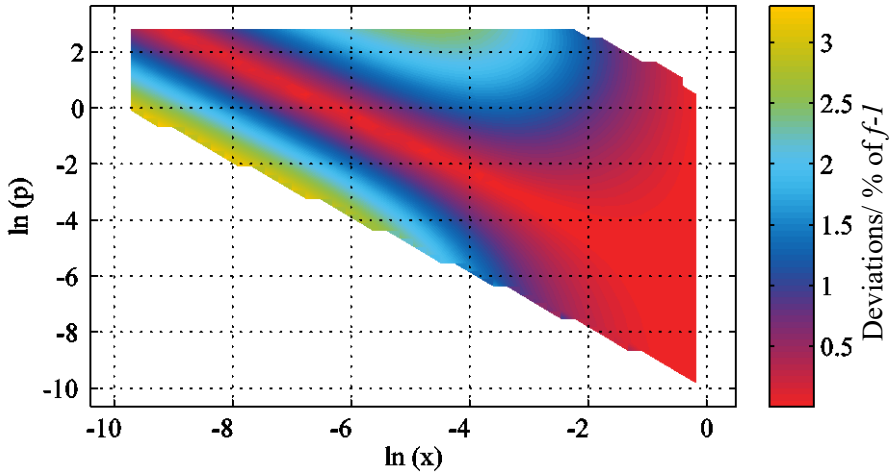

Figure 51: Overall discrepancies of results of this section with that of sec.1.4.2

1.5.2 **Argon**

The original equation of Harvey and Huang is fitted in the universal Equation (1-19) and corresponding constants are reported in Table 50. Actually, the deviation remains small in the entire range as it can be seen in Figure 52.

Table 50: Constants of the second virial coefficients based on first-principles calculations for argon

B_{xx}	*a*	*b*	*c*	*d*
B_{aw}	3.88E-15	0.04891	-0.00037	-0.00892

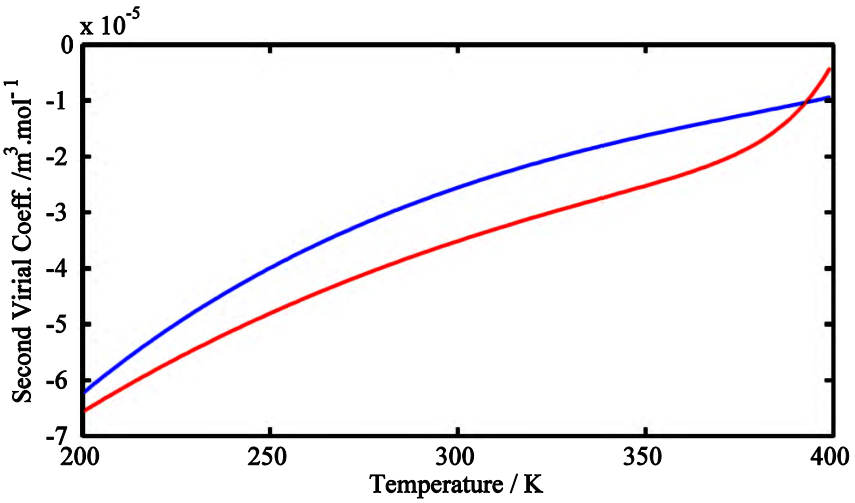

Figure 52: Second virial cross coefficients of argon B_{aw}, blue stands for the correlation of Harvey [48] and red is according to Rabinovich [43]

Coefficients of Equation (1-17) are calculated for air-water (in both phases) equilibrium and reported in Table 51. Results are illustrated in Figure 53 shows considerable deviations of about $1 \cdot 10^{-3}$ for F_1.

Table 51: Constants of Equation (1-17) for argon-water and argon-ice equilibrium based on the first-principles calculations

a_i	Liquid water	Solid water
a_0	0.0159	0.015485
a_1	0.009347	0.007687
a_2	0.003038	0.001968
a_3	0.000574	0.000271
a_4	6.58E-05	2.17E-05
a_5	4.16E-06	9.52E-07
a_6	1.10E-07	1.77E-08

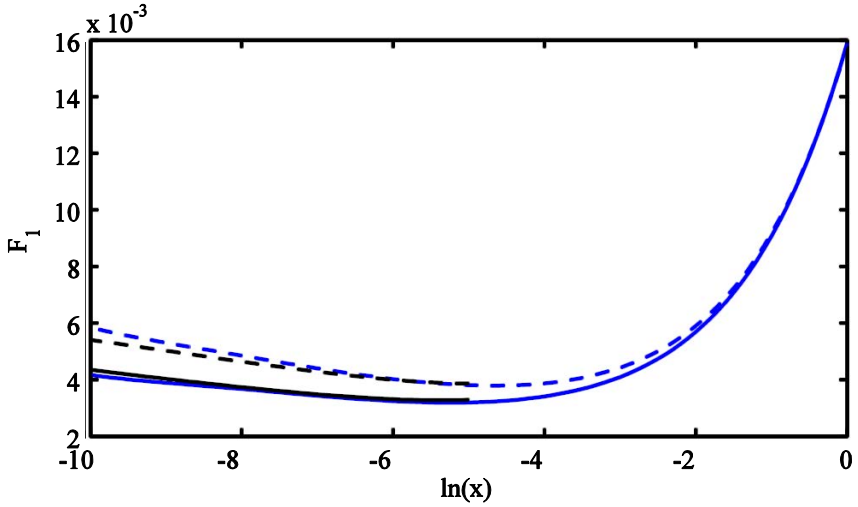

Figure 53: Atmospheric factor for argon over water (in blue) and ice (in black) employing quantum chemistry calculations. Dashed lines are the results of section 1.4

Likewise, coefficients of Equation (1-18) are tabulated in Table 52 for humid argon over both phases of water. Figure 54 illustrates the differences within the uncertainty.

Table 52: Constants of Equation (1-18) for argon-water and argon-ice equilibrium based on the first-principles calculations

b_i	Liquid water	Solid water
b_0	0.679458	0.351478
b_1	0.007567	-0.2017
b_2	0.017397	-0.02672
b_3	0.002395	-0.00147
b_4	9.45E-05	-2.53E-05

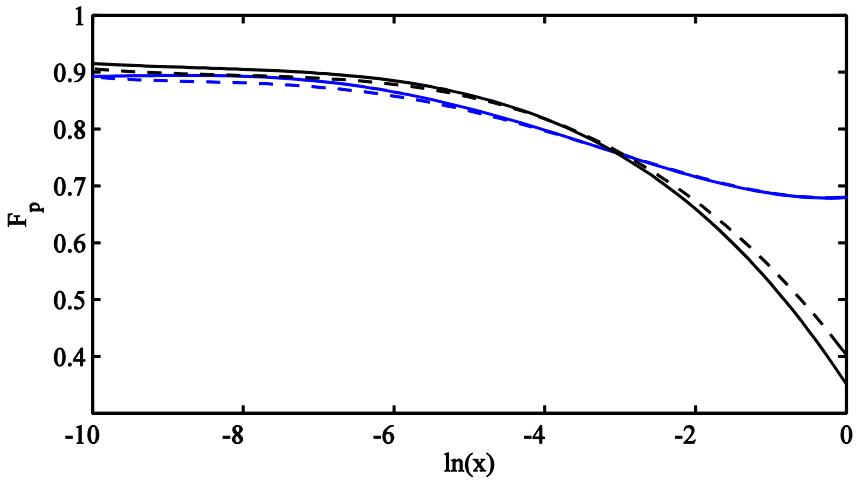

Figure 54: Pressure factor for argon over water (in blue) and ice (in black) employing quantum chemistry calculations. Dashed lines are the results of section 1.4

The deviation of the new elaboration deviates from that of sec.1.4.7 increases by decreasing the water mole fraction up to more than 25 % of the enhancement correction (i.e., *f*-1), as depicted in Figure 55.

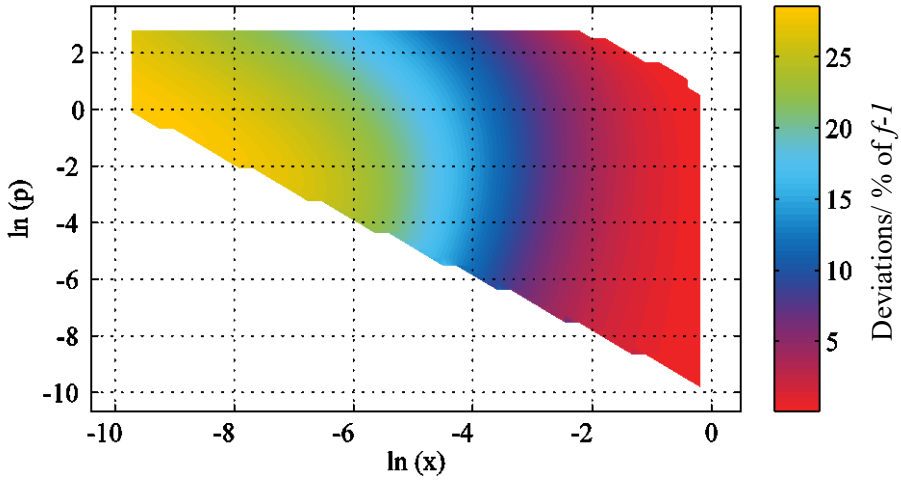

Figure 55: Overall discrepancies between results of this section and that of sec.1.4.2

1.5.3 **Oxygen**

The correlation reported by Harvey [48] is fitted in Equation (1-19) results in the constants of Table 53. B_{aw} values tend to have slight differences in the higher range of temperature (refer to Figure 56)

Table 53: Constants of the second virial coefficients based on first-principles calculations for oxygen

B_{xx}	a	b	C	d
B_{aw}	3.92E-09	0.01652	-0.0004	-0.00975

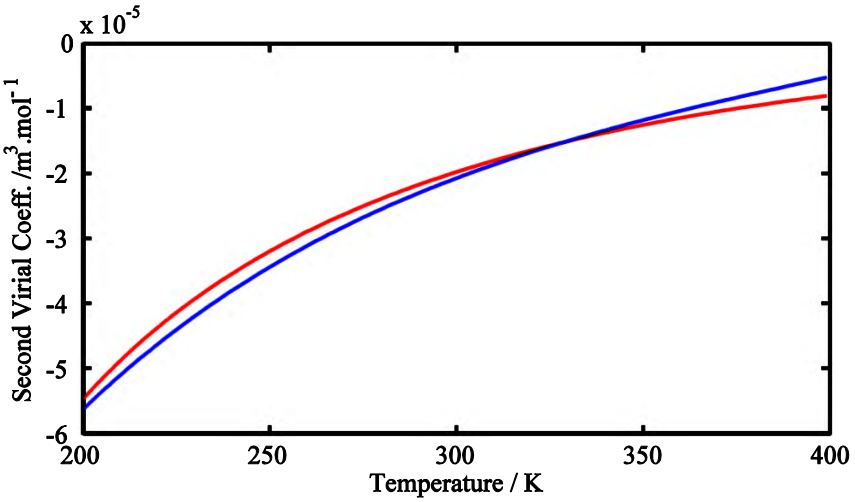

Figure 56: Second virial cross coefficients of nitrogen B_{aw}, blue stands for the correlation of Harvey [48] and red is according to Rabinovich [43]

Accordingly, coefficients of the atmospheric factor are calculated and listed in Table 54. As a consequence, Figure 57 reports a fairly good agreement in the higher range and slight deviations in the lowest range.

Table 54: Constants of Equation (1-17) for oxygen-water and oxygen-ice equilibrium based on the first-principles calculations

a_i	Liquid water	Solid water
a_0	0.015877	0.015335
a_1	0.009605	0.007821
a_2	0.003123	0.001994
a_3	0.000593	0.000274
a_4	6.83E-05	2.20E-05
a_5	4.33E-06	9.68E-07
a_6	1.15E-07	1.80E-08

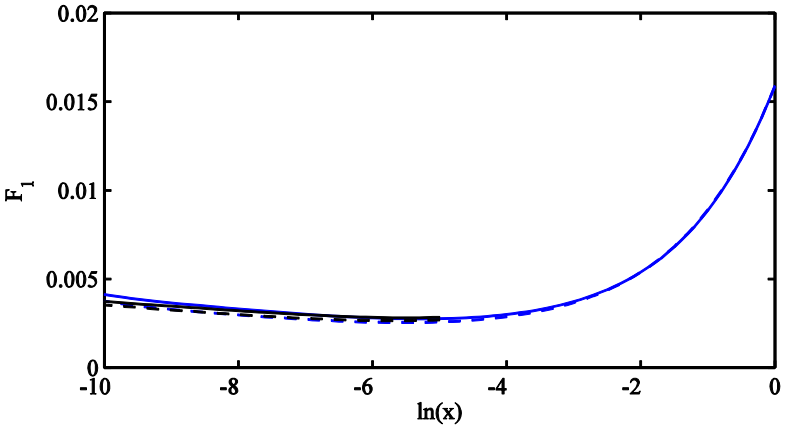

Figure 57: Atmospheric factor for oxygen over water (in blue) and ice (in black) employing quantum chemistry calculations. Dashed lines are the results of section 1.4

F_P values as illustrated in Figure 58 are reporting small deviations in the lowest concentrations. The pressure factor constants are listed in Table 55

Table 55: Constants of Equation (1-18) for oxygen-water and oxygen-ice equilibrium based on the first-principles calculations

b_i	Liquid water	Solid water
b_0	0.679398	0.389608
b_1	0.009239	-0.1656
b_2	0.015689	-0.01768
b_3	0.001953	-0.00056
b_4	6.77E-05	6.86E-06

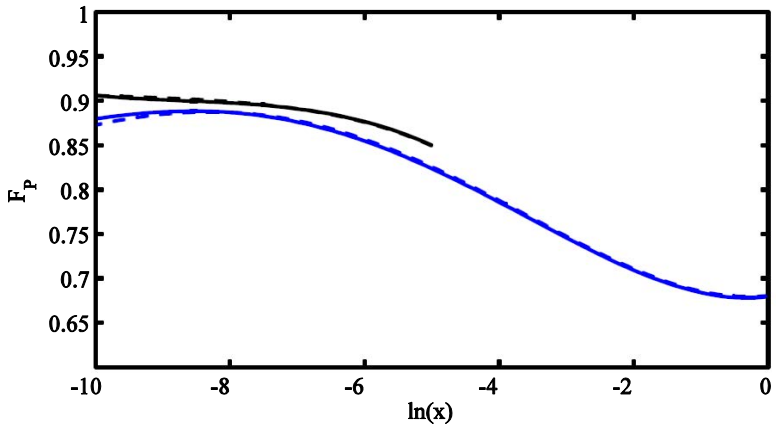

Figure 58: Pressure factor for oxygen over water (in blue) and ice (in black) employing quantum chemistry calculations. Dashed lines are the results of section 1.4

The calculations deviate by about 8% of the enhancement correction, i.e. Figure 59, from that of Sec. 1.4 at about 50 ppm of water mole fraction decreasing to lower than 1 % in higher concentrations.

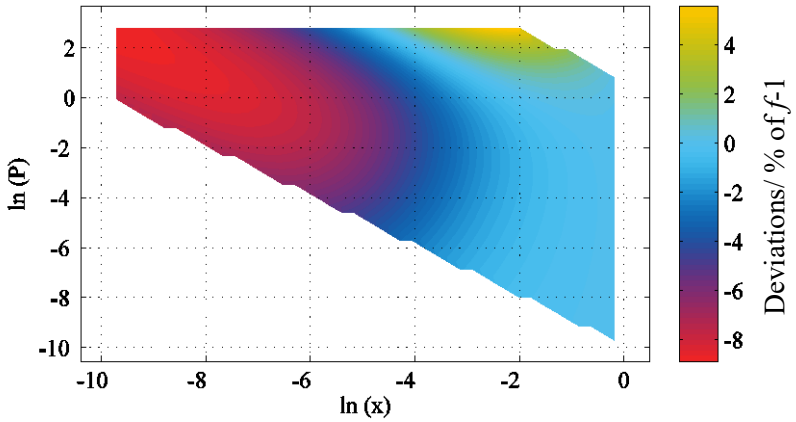

Figure 59: Overall discrepancies of results of this section with that of sec. 1.4.3

1.5.4 **Air**

Considering the standard air composition (i.e., 0.78135 mole fraction for nitrogen, 0.20948 for oxygen, and 0.00917 for argon) and employing the *B* values reported in sec 1.5.1 to 1.5.3 the double exponential constants of Equation (1-19) are calculated and listed in Table 56.

Table 56: Constants of the second virial coefficients based on first-principles calculations for air

B_{xx}	a	b	c	d
B_{aw}	3.26E-11	0.02563	-0.00054	-0.00968

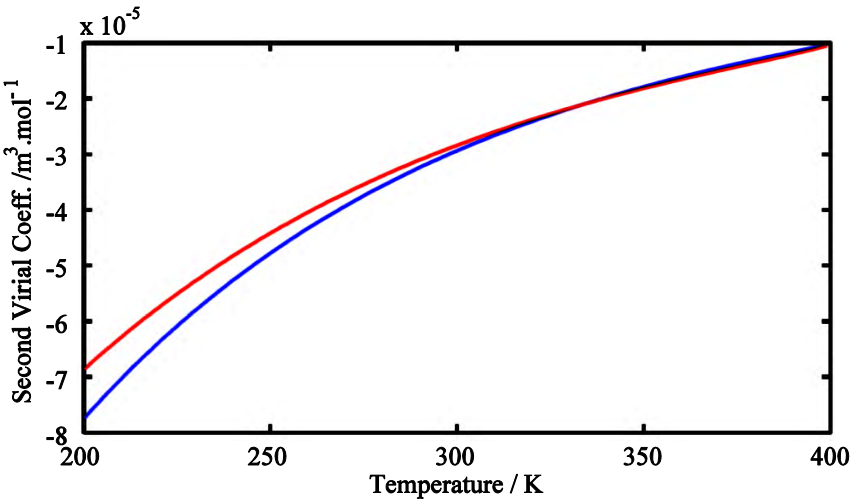

Figure 60: Second virial cross coefficients of air B_{aw}, blue stands for the correlation of Harvey [48] and red is in accordance with the experimental correlation of Hyland and Wexler [28]

Figure 60 shows a good agreement in the high-temperature range and a growing deviation by decreasing the temperature. The maximum relative deviation, i.e., at 200 K, is roughly 13%.
The atmospheric factor, Equation (1-17), is calculated for air-water equilibrium, i.e. Figure 61, and constants of the polynomial are reported in Table 57.

Table 57: Constants of Equation (1-17) for air-water and air-ice equilibrium based on the first-principles calculations

a_i	Liquid water	Solid water
a_0	0.015851	0.015737
a_1	0.00886	0.007523
a_2	0.002846	0.001942
a_3	0.000525	0.000266
a_4	5.92E-05	2.13E-05
a_5	3.70E-06	9.35E-07
a_6	9.74E-08	1.74E-08

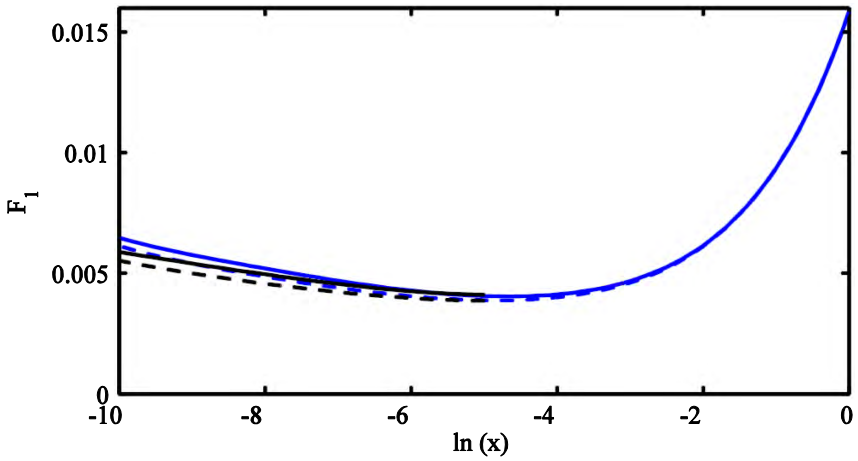

Figure 61: Atmospheric factor for air over water (in blue) and ice (in black) employing quantum chemistry calculations. Dashed lines are the results of section 1.5

And coefficients for the Equation.(1-18) are tabulated below, this is also illustrated in Figure 62.

Table 58: Constants of Equation (1-18) for air-water and air-ice equilibrium based on the first-principles calculations

b_i	Liquid water	Solid water
b_0	0.678765	0.456482
b_1	0.003248	-0.1574
b_2	0.017888	-0.01975
b_3	0.002764	-0.00095
b_4	0.000122	-9.77E-06

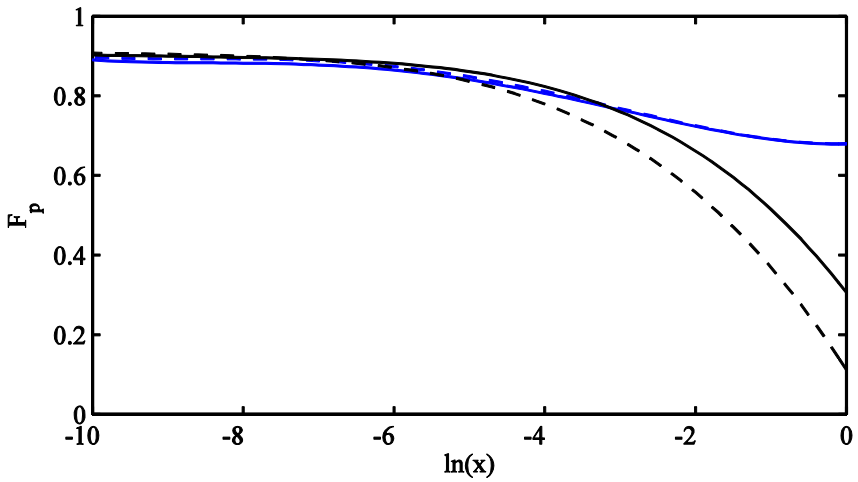

Figure 62: Pressure factor for air over water (in blue) and ice (in black) employing quantum chemistry calculations. Dashed lines are the results of section 1.4

Eventually, this is high time to look at the overall deviations of the results obtained in this section to similar results in Sec.1.4.1. Significant differences are evident for the range in which the experimental data were extrapolated by Hyland and Wexler. In the lowest range discrepancies can be as high as 10 % of the enhancement correction, refer to Figure 63.

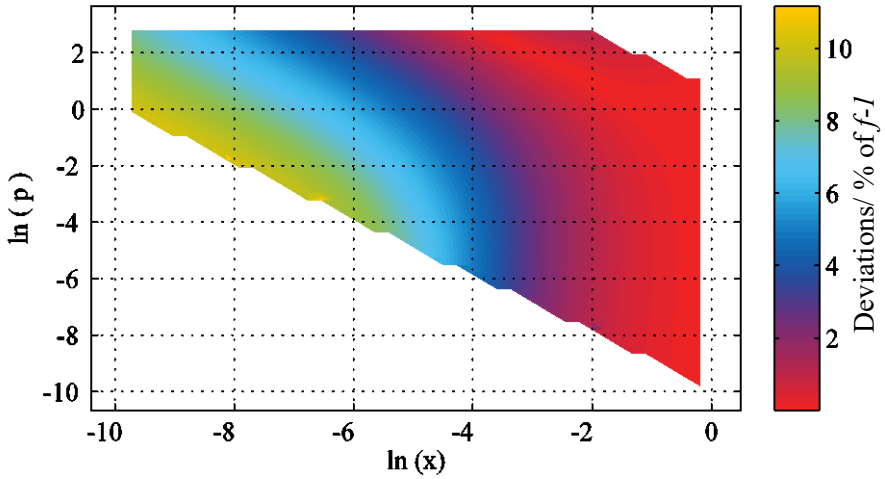

Figure 63: Overall discrepancies between results of this section and that of sec. 1.4.1

1.6 Uncertainty analysis

The uncertainty levels of the water vapor enhancement factor for air-water mixture can be estimated by considering the uncertainties of the input parameters and, later, by the propagation of the input uncertainties into the mathematical model described in Section 1.4. a similar approach can also be adopted for all the other equations under discussion in this chapter.

The uncertainty of the isothermal compressibility, molar volume and Henry's law constant contribute negligibly. The most important contributions are propagated from the second virial coefficients as reported in Table 59 as follows:

Table 59: Uncertainty of the second virial coefficients against temperature [49]

T / K	$\sigma_{B_{aa}}$	$\sigma_{B_{aw}}$	$\sigma_{B_{ww}}$
200	1.00E-6	8.30E-6	5.60E-3
250	1.00E-6	5.60E-6	7.10E-4
300	1.00E-6	4.20E-6	1.20E-4
350	1.00E-6	3.40E-6	5.80E-5
400	1.00E-6	2.80E-6	5.00E-6

Considering a normal probability distribution for the available standard uncertainty of the input parameters [49] adaptive Monte-Carlo simulations can be performed. An example of such simulation and the resulting normal probability distribution is plotted in Figure 64.

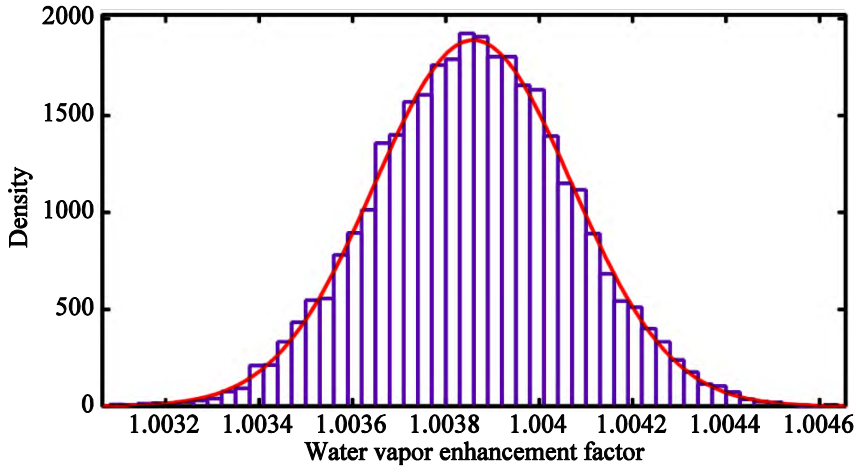

Figure 64: Example of a probability distribution function for the output parameter, this is calculated for T=273.15 and P=0.1 MPa for air over liquid water

The simulation has been repeated successively for several points at 0.1 MPa and results are listed in Table 60

Table 60: Water vapor enhancement factor standard uncertainty levels at atmospheric pressure

Ln (x)	u_f
-9.90	3.80E-4
-7.60	2.73E-4
-5.31	2.20E-4
-3.01	1.97E-4
-0.71	4.10E-4
-0.07	2.97E-4

-0.01	2.50E-4
-7E-04	2.10E-4
-7E-05	2.69E-4
-0.23	3.27E-4
-0.20	3.44E-4
-0.46	3.83E-4
-1.98	2.98E-4

Considering the enhancement factor at atmospheric pressure as a number close to unity at this stage

$$\ln(f) = f\text{-}1, \qquad (1\text{-}27)$$

thus,

$$u_f = (1\text{-x})\, u_{F_1}. \qquad (1\text{-}28)$$

Figure 65 shows the standard uncertainty levels for (1-x) u_{F_1}

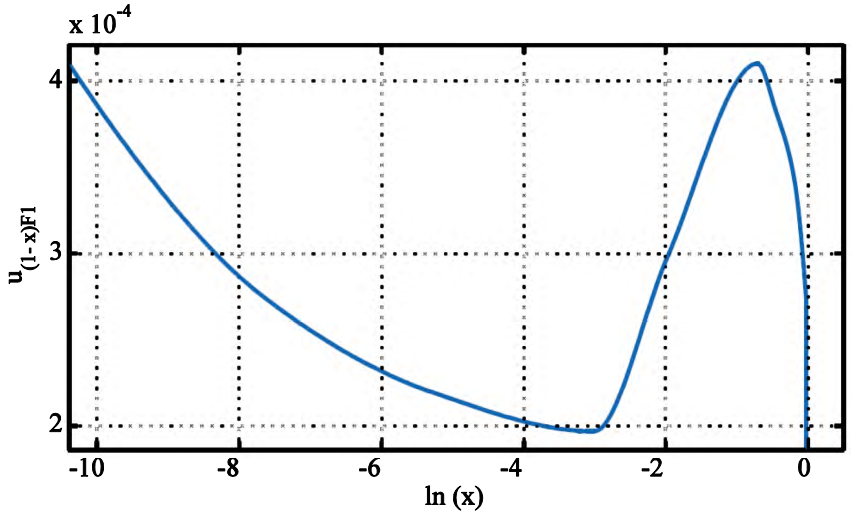

Figure 65: Standard uncertainty of the enhancement factor at atmospheric pressure.

The lowest standard uncertainty of the water vapor enhancement factor is obtained at about x = 0.05. However, the uncertainty remains reasonable in the entire range.

Adaptive Monte-Carlo simulations are also performed to evaluate the uncertainty of the pressure correction as well. Table 61 shows the results of such calculations in details.

Table 61: Standard uncertainty of the pressure correction factor at different pressures

ln(*p*)	ln (x)	u_{C_p}
-6.90	-2.99	0.15
-6.90	-0.69	0.14
-6.90	-0.07	0.12
-6.90	-0.01	0.11
-6.90	0.00	0.12
-0.69	-7.60	0.10
-0.69	-5.30	0.08
-0.69	-2.99	0.06
-0.69	-0.07	0.05
-0.69	0.00	0.04
0.69	-9.20	0.09

ln(*p*)	ln (x)	u_{C_p}
0.69	-6.90	0.08
0.69	-2.30	0.06
0.69	-0.02	0.02
0.69	0.00	0.02
1.61	-9.20	0.09
1.61	-6.90	0.09
1.61	-4.60	0.07
1.61	-2.30	0.06
2.99	-9.90	0.10
2.99	-5.29	0.08
2.99	-2.99	0.06

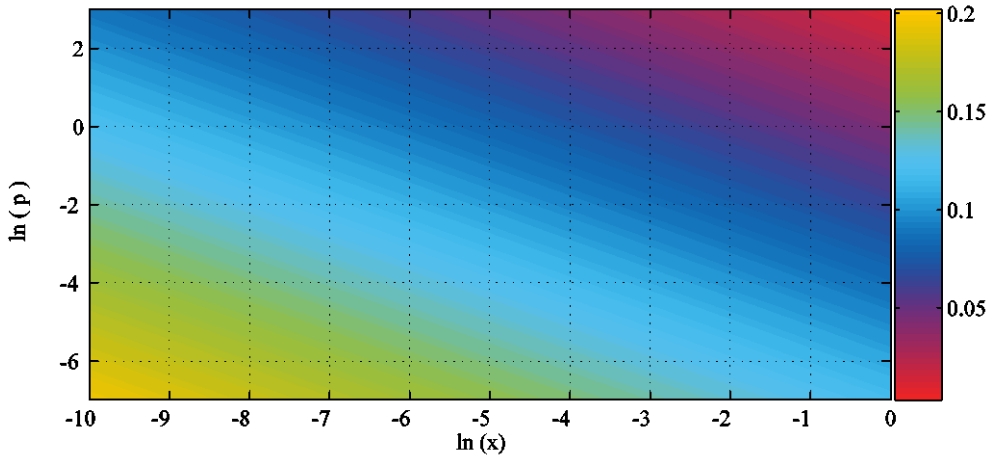

Figure 66: Standard uncertainty of Cp

Uncertainty of the enhancement factor should be considered using the law of propagation of uncertainty through Equation(1-15) taking to account

$$u_c = (1-x)\cdot f \cdot c_{\mathrm{p}} \sqrt{{u_F}^2{}_1 + [\log(p)\cdot F_1 \cdot u_{F_{\mathrm{p}}}]^2}, \qquad (1\text{-}29)$$

in which the values of u_{F_1} and $u_{\mathrm{F_p}}$ can be considered using Figure 65 and Figure 66. For instance, the combined standard uncertainty associated with the water vapor enhancement factor for the air-water mixture at 740 kPa and x=0.1 is estimated to be $u_c = 2.9\cdot 10^{-3}$ at f = 1.0226 which is more than 12 times bigger than that of atmospheric pressure(i.e. $u_c = 2.3\cdot 10^{-4}$ at f = 1.005.

1.7 Discussion on the numerical integration on the intermolecular Potentials

The Lennard-Jones potential can be converted into the virial coefficients as described in 1.4.2; alternatively, it can be solved by employing the numerical integration of Equation (1-29) as

$$B(T) = 2\pi N_A \int_0^{\infty} (1 - e^{\frac{-u(r)}{K_B T}}) r^2 dr, \qquad (1\text{-}29)$$

where N_A is the Avogadro number, K_B is the Boltzmann constant and r is the distance between molecules. This can be used to consider interactions between two particles of the carrier gas, i.e. B_{aa}, as well as the interactions between the carrier gas and water vapor molecules, i.e. B_{aw}.

This method is in a good agreement with that of sec. 1.4 for some cases hydrogen is a good example of that. Considering the Equation(1-29) hydrogen potential parameters of Table 23 can be employed to calculate the second virial coefficients. As a next step, Equation(1-14) should be used to calculate the enhancement factor and, finally, coefficients of Equation (1-17) are calculated for hydrogen-water equilibrium and are reported in Table 62, as well as Figure 67.

Table 62: Constants of Equation (1-17) for hydrogen-water and hydrogen-ice equilibrium based on the direct integration over the Lennard-Jones potential

a_i	Liquid water	Solid water
a_0	0.015897	0.015274
a_1	0.009745	0.007915
a_2	0.003148	0.001998
a_3	0.0006	0.000275
a_4	6.93E-05	2.21E-05
a_5	4.41E-06	9.72E-07
a_6	1.17E-07	1.82E-08

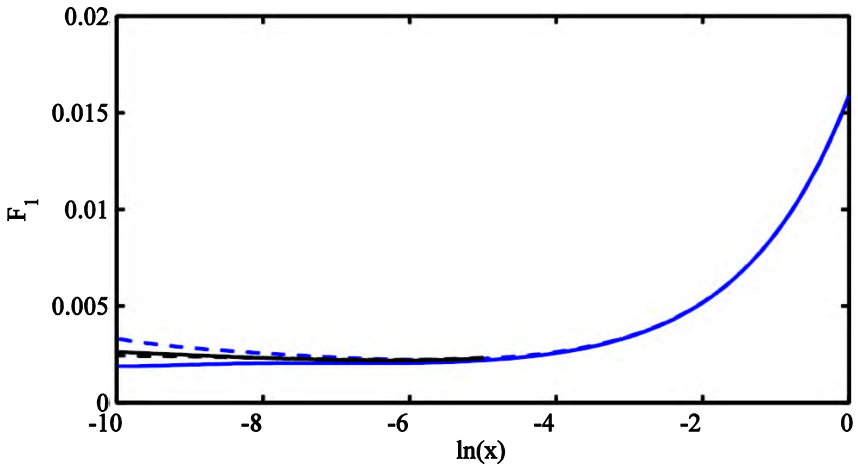

Figure 67: Atmospheric factor for hydrogen over water (in blue) and ice (in black) employing direct integration over Lennard-Jones parameters. Dashed lines are the results of section 1.4

By following the same approach coefficients of Equation (1-18) are presented below in Table 63. A fairly good agreement is reported in Figure 68.

Table 63: Constants of Equation (1-18) for hydrogen-water and hydrogen-ice equilibrium based on the direct integration over the Lennard-Jones potential

b_i	Liquid water	Solid water
b_0	0.679591	0.573122
b_1	0.009011	-0.04213
b_2	0.014192	0.011144
b_3	0.001501	0.002196
b_4	3.72E-05	1.01E-04

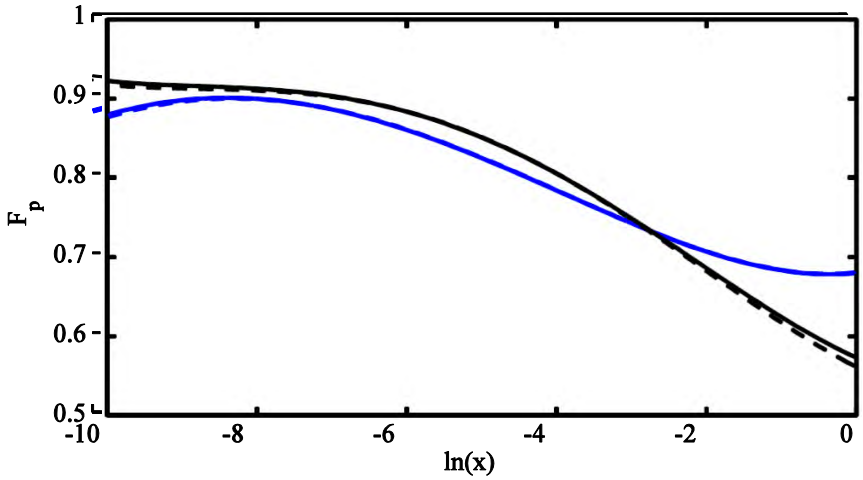

Figure 68: Pressure factor for hydrogen over water (in blue) and ice (in black) employing direct integration over Lennard-Jones parameters. Dashed lines are the results of section 1.4

1.8 Discussion on the fitting problems in a particular case

Numerical fitting of the data is considerably challenging when the enhancement factor of a gas mixture is small and the pressure dependency is small as well.

Helium is a good example of that. Figure 69 shows the C_p values based on the B_{aw} results of Robinovich.

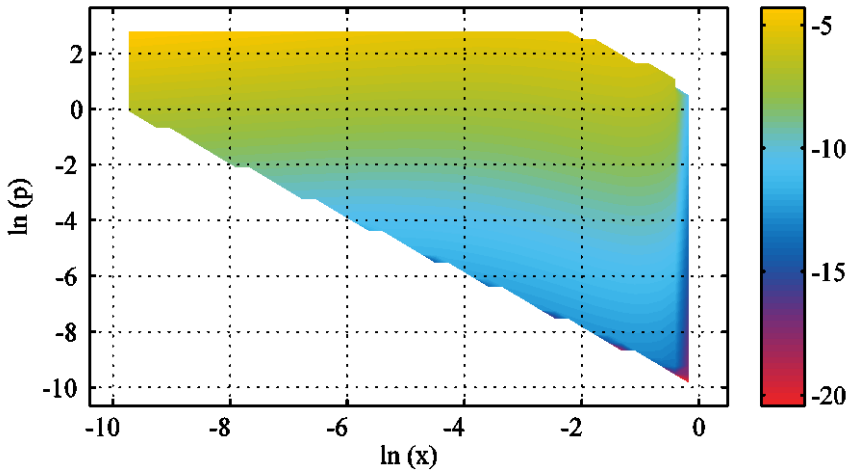

Figure 69: Results of C_p calculations based on the second virial coefficients reported by Robinovich

The pressure dependence of the enhancement factor remains well below the uncertainty levels; therefore, F_p cannot be obtained precisely. The situation is even worse considering the equilibrium over ice, i.e. Figure 70. In this case, corrections are even smaller and function does not exhibit the typical smooth behavior. Figure 71 reports the mal-conditioned F_p function for water and ice.

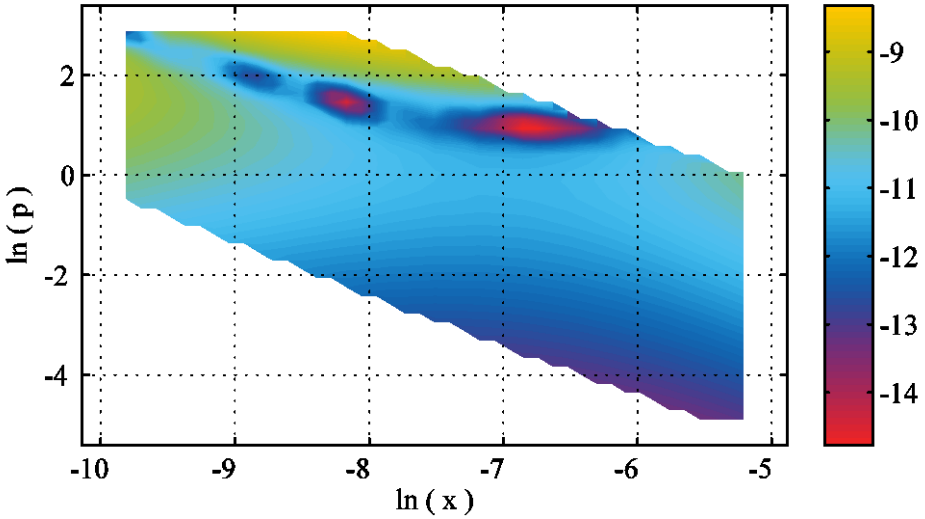

Figure 70: Results of C_p calculations based on the second virial coefficients reported by Robinovich

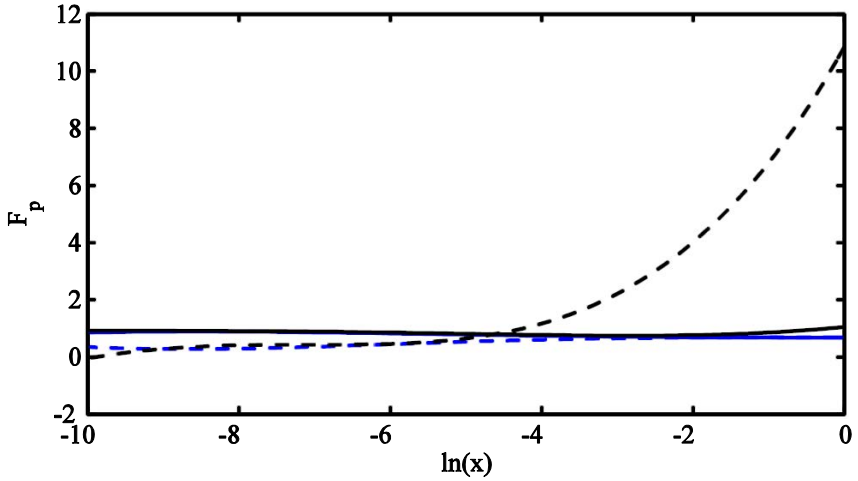

Figure 71: Atmospheric factor for hydrogen over water (in blue) and ice (in black) employing direct integration over Lennard-Jones parameters. Dashed lines stand for the implementation of the $B_{aw}re$ported by Rabinovich

As it is observable in Figure 71, F_{P} calculations result to an unacceptable curve. Let us try the second approach of having direct integration explained in the page(55) Lennard-Jones coefficients for Helium are reported in Table 64.

Table 64: Lennard-Jones parameters of humid helium

Interacting molecules	σ/ Å	$\varepsilon.k_{\mathrm{B}}{}^{-1}$ /K
He-He	2.584	8.24
He-H_2O	2.587	48.68

Coefficients of Equation (1-17) are calculated for air-water equilibrium and reported in Table 65. The atmospheric factor of helium, especially at the lower range exhibits a monotonic decrease by decreasing the amount fraction (refer to Figure 72).

Table 65: Constants of Equation (1-17) for hydrogen-water and hydrogen-ice equilibrium based on the direct integration

a_i	Liquid water	Solid water
a_0	0.015895	0.015078
a_1	0.010246	0.008222
a_2	0.003306	0.002061
a_3	0.000635	0.000285
a_4	7.36E-05	2.29E-05
a_5	4.69E-06	1.01E-06
a_6	1.25E-07	1.88E-08

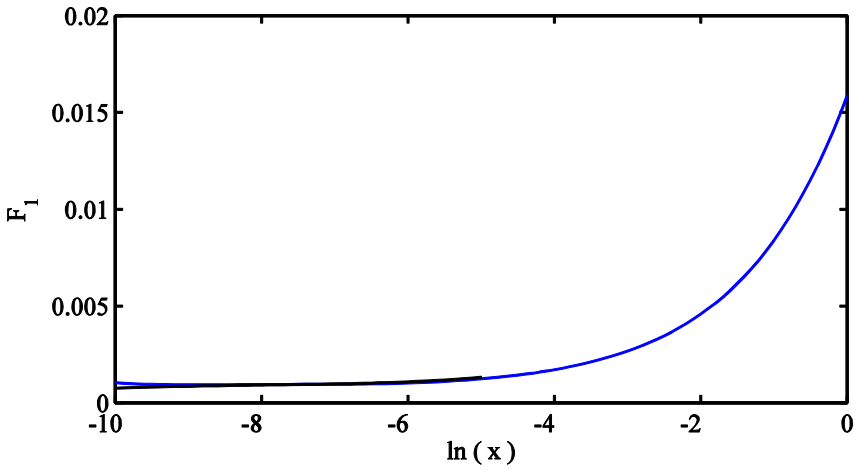

Figure 72: Atmospheric factor for hydrogen over water (in blue) and ice (in black) employing direct integration over Lennard-Jones parameters.

Moreover, coefficients for the Equation (1-18) are tabulated in Table 66. Figure 73 reports a peak at about 180 ppm of water mole fraction which is not commonly observed in the other mixtures.

Table 66: Constants of Equation (1-18) for hydrogen-water and hydrogen-ice equilibrium based on the direct integration

b_i,	Liquid water	Solid water
b_0	0.678092	1.050372
b_1	0.002374	0.261307
b_2	0.003516	0.074192
b_3	-0.00064	0.007602
b_4	-7.95E-05	2.67E-04

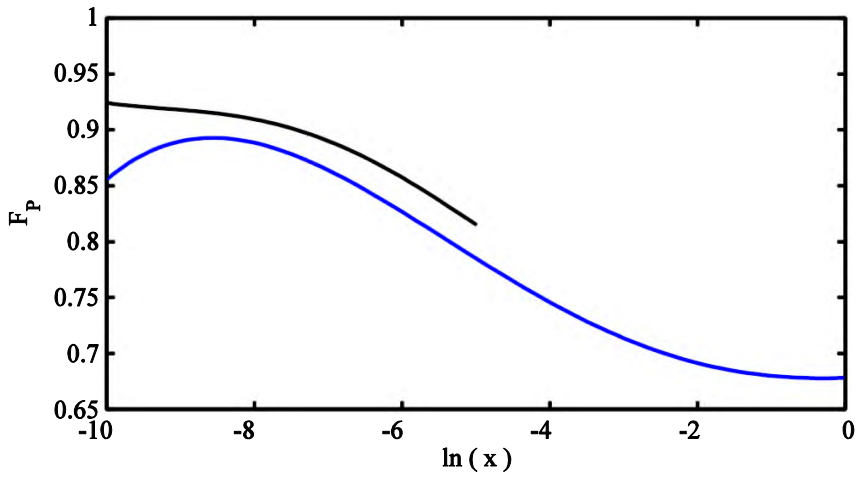

Figure 73: Atmospheric factor for hydrogen over water (in blue) and ice (in black) employing direct integration over Lennard-Jones parameters

1.9 Comparison of the water vapor enhancement factor formulations for air

The air-water mixture is, undoubtedly, the most frequently needed equation by science and industry. Let us recall all the calculations that have been done for air in this chapter and add the constants of Equation (1-17) for the results of the method discussed in sec 1.2. In addition, the same approach of page(61) can be employed to calculate the atmospheric factor and pressure factor from the following potential information of Table 67. This is summarized in Table 68 and Figure 74.

Table 67: Lennard-Jones parameters for air

Interacting molecules	σ/ Å	$\varepsilon.k_B^{-1}$ /K
Air-Air	3.653	100.01
Air-H_2O	3.112	173.64

Table 68: Constants of Equation (1-17) for air-water equilibrium based on different approaches

a_i	Sec. 1.4.1	Sec.1.2	Table 67	Sec.1.5.4
a_0	0.015861	0.01617	0.015902	0.015851
a_1	0.008862	0.009302	0.008648	0.00886
a_2	0.002837	0.00317	0.002794	0.002846
a_3	0.000524	0.000642	0.00052	0.000525
a_4	5.92E-05	8.11E-05	5.92E-05	5.92E-05
a_5	3.70E-06	5.73E-06	3.72E-06	3.70E-06
a_6	9.76E-08	1.71E-07	9.86E-08	9.74E-08

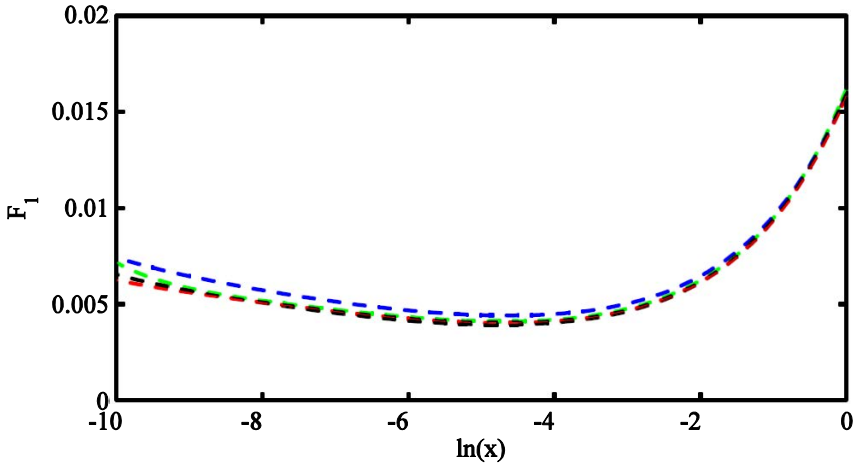

Figure 74: Atmospheric factor for air over water using different methods: black indicates sec.1.4.1, green for Sec.1.2, blue for Table 67 and red for sec1.5.4

The same results are reported for the “b” values in Table 69.

Table 69: Constants of Equation (1-18) for air-water equilibrium based on different approaches

b_i	Sec. 1.4.1	Sec.1.2	Table 67	.Sec1.5.4
b_0	0.680058	0.675029	0.678853	0.678765
b_1	0.005049	0.006038	0.000726	0.003248
b_2	0.018927	0.021342	0.018933	0.017888
b_3	0.002856	0.003513	0.003005	0.002764
b_4	1.23E-04	0.000168	0.000135	0.000122

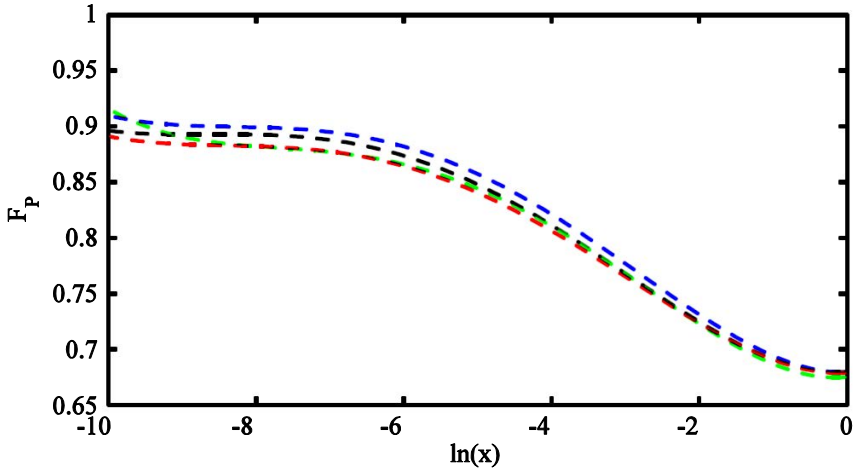

Figure 75: Pressure factor for air over water using different methods: black indicates sec.1.4.1, green for Sec.1.2, blue for Table 67 and red for sec1.5.4

Likewise, Figure 75 reports also fairly good agreements for pressure factor. The enhancement factor has also been formulated for CO2-free air by Greenspan. He suggested a set of constants for equilibrium over ice, subzero dew-point temperatures and the dew-point temperatures between 0 °C and 100 °C these constants are tabulated in Table 70 [31].

$$f = e^{[\alpha\left(1-\frac{P_{ws}}{P}\right)+\beta\left(\frac{P}{P_{ws}}-1\right)]}, \qquad (1\text{-}30)$$

$$\alpha = \sum_{i=1}^{4} A_i t^{(i-1)}, \qquad (1\text{-}30\text{-}1)$$

$$\beta = e^{\sum_{i=1}^{4} B_i t^{(i-1)}}. \qquad (1\text{-}30\text{-}2)$$

Table 70: Greenspan constants

	Water	Water	Ice
	-50 °C to 0 °C	0 °C to 100 °C	-100 °C to 0 °C
A1	3.62183E-04	3.53624E-04	3.64449E-04
A2	2.60553E-05	2.93228E-05	2.93631E-05
A3	3.86501E-07	2.61474E-07	4.88635E-07
A4	3.82449E-09	8.57538E-09	4.36543E-09

B1	-1.07604E+01	-1.07588E+01	-1.07271E+01
B2	6.39725E-02	6.32529E-02	7.61989E-02
B3	-2.63416E-04	-2.53591E-04	-1.74771E-04
B4	1.67254E-06	6.33784E-07	2.46721E-06

Figure 76 shows the deviation between the Greenspan equation and the estimation of the enhancement factor using the Helmholtz function. Unexpectedly, this is evident that the Greenspan equation remains acceptable even for the dew-point temperatures above 100 °C using the set of constants for the 0 °C to 100 °C range.

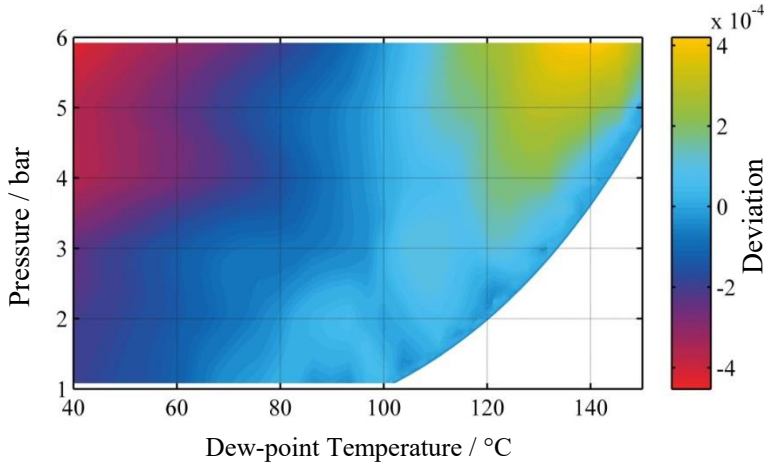

Figure 76: Greenspan and TEOS-10 comparison

1.10 Concluding remarks

This chapter concludes by arguing a summary and the validity of the water vapor enhancement factor functional formulation for different carrier gases. Initially, the possibility of using the Helmholtz-based calculations has been studied in Sec.1.2 and the numerical implementation of this approach has been presented in Sec.1.9. Likewise, in Sec.1.3 the water vapor enhancement factor has been estimated using the virial equation of estate by introducing the sub-enhancement factors and their magnitude analysis for mixtures with adequate experimental knowledge of their second cross virial coefficients. Sec.1.9 reports such calculations for air. Moreover, for polar gases, e.g. ammonia, the experimental results of the excess parameters, e.g. excess enthalpy, have been considered for calculating the enhancement factor (refer to sec 1.4.4).

Likewise, the mixing rules of the Lennard-Jones potential have been employed to calculate B_{aw} of other gas-water vapor mixtures which yield to the estimation of the enhancement factor. Such calculations have been presented in other subsections of sec 1.5. An alternative method has also been discussed for applying the direct numerical integration over the Lennard -Jones parameters of the carrier gas and that of the mixture in Sec.1.7

Besides, the enhancement factor of air components have been studied based on available second virial cross coefficients, B_{aw}, calculated by quantum chemistry. Such calculations of first-principals are valid in a wider range of temperature with competitive uncertainty levels. Results have been compared over the estimated values of Sec.1.4 for each component and the air-water vapor mixtures. (refer to Figures 50, 54, 58 and 62). These calculations are also confronted with the results of Sections 1.2, 1.4.1 and the method of sec 1.7 by the consideration of Table 67.
A new functional formula has been introduced and its coefficients were discussed in different sections. The formula is founded on two factors, F_1which is called the atmospheric factor and F_{P} which is the pressure factor. These factors are functions of the water mole fraction, this is evident that temperature and pressure do not influence that. Eventually, as a result of this chapter, the water vapor enhancement factor is available for helium, nitrogen, oxygen, ammonia, hydrogen, argon and methane for the temperature range from 200 K to 400 K and pressure from 100 Pa to 0.1 MPa with an extension for air up to 473 K.

It has been found that the water vapor enhancement factor depends strongly on the molecular structure of the carrier gas. For instance, the deviation of the water vapor enhancement factor from unity for the equilibrium over a planar water pool at 4 °C has been reported to be 2.3, 2.6, 3.8, 4.3 and 5 parts in 10^3 respectively for hydrogen, oxygen, argon, nitrogen and methane increasing to 15 parts in 10^3 for carbon dioxide and eventually 138 parts in 10^3 for ammonia.

Chapter 2

A Humidity Generator for Dew-Point Temperatures above 100 °C

Humidity plays a crucial role in controlling drying processes in many industrial applications and its measurement accuracy directly affects the efficiency of energy and production. Drying and baking are key processes in the food industry. They may particularly benefit from this work. Besides temperature, water content of a sample - which is often monitored by the relative humidity of the surrounding ambient air as a proxy - is an essential factor in determining the properties of a wide range of food products, along with that, humidity process control is a major parameter in controlling the product quality [50].

On the other hand, the reliability of industrial humidity sensors directly affects the drying efficiency where significant savings are predictable by any advancement in the existing humidity sensor testing and calibration procedures. Drying is estimated to cost European industry some 30 billion euros per annum in the energy sector. Thus a 0.1 % improvement in drying efficiency due to a better process control could save around 30 M€/year. Monitoring humidity at temperatures above 100°C is a vital factor in controlling drying processes.

The European Directive 2012/27/EU reported the importance of energy efficiency as a valuable mean to improve the Union's security of supply by reducing the primary energy consumption [51]. It reduces greenhouse emissions cost-effectively and thereby to mitigate climate change. Indeed, the targeted advances in energy efficiency through better humidity monitoring in the drying process would result in a significant reduction in the carbon dioxide emissions, enhancements in process control and reduction in the waste material.

The ceramic manufacturing industry often exploits the TGDA dryer test method to evaluate the drying quality (e.g. shrinkage and weight loss) for a ceramic part by applying a controlled temperature, humidity, and air circulation [52]. Relative humidity is one of the most critical parameters that should be controlled to optimize measurements in the testing process. The initial temperature for such a process is above 120 °C with a high relative humidity.

In the wood industry, especially in non-refractory woods, elevated process temperatures are used [53] but, if not dried rapidly, the samples may develop discoloration (blue stain) and mold on the surface. Examples are softwoods and low-density timbers such as pinus radiate. Most softwood lumber kilns operate at

around 115 °C. Precision humidity measurements would be of great significance for product quality. However, humidity sensors of such processes are not yet calibrated at the process conditions.

In food processing, over-drying at high temperature causes energy waste in one hand and negatively affect the food quality (e.g., mass shrinkage, browning and burnt flavor defects) and its cost on the other hand. In contrast, insufficient dehydration yields to the growth of bacteria, yeasts, and mold consequently reducing the shelf life of the final product.

A target application of this work concerns industrial food processing in drying tunnel ovens where the critical process parameters, e.g. for drying and roasting processes, are time, temperature and humidity. For instance, in hazelnuts drying and roasting mild processing consists of 45-50 minutes baking at 140 °C to ensure good product quality as well as small residual water content (<1 %), lipid oxidation content and color are concerned. Alternatively, a fast drying can be performed where the nuts are heated up to 180°C for 20 minutes. A typical process temperature profile in a tunnel oven is represented in Figure 77. With a production rate in excess of 300 kg/h, energy-efficient management of such a high throughput line is crucial for process performance and productivity. Similar processes are reported by [54]

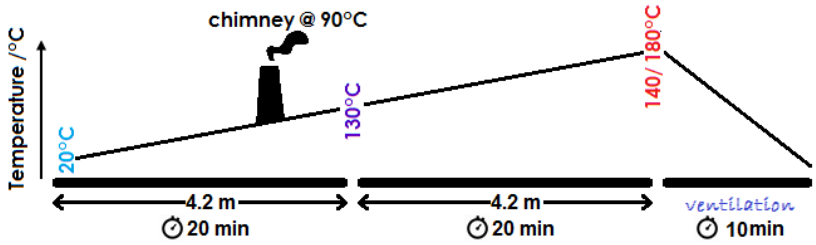

Figure 77: Process temperatures in a drying and roasting tunnel oven used in the food processing industry.

Although the most relevant part of the drying process and associated humidity monitoring takes place above 100 °C, humidity sensors are usually not calibrated at temperatures above 100 °C and seldom the calibration equipment available in the industry operates in that range. Therefore, calibration corrections are often extrapolated in the extended range and the estimated uncertainty consequently increased [55].

2.1 Generator principles and governing equations

The INRIM high humidity generator is based on a gravimetric approach where a controlled SI-traceable mixing of a water mass flow is evaporated into a dry air mass flow. It provides traceability to humidity measurements at

temperatures up to 180 °C, dew-point temperatures up to 140 °C and absolute pressures up to 0.6 MPa. Equivalently, the generator operates over a wide range of specific humidity from 0.03 kg/kg at atmospheric pressure to approximately 0.5 kg/kg at 0.6 MPa, which corresponds to an absolute humidity range from 25 g/m^3 at atmospheric pressure to approximately 1000 g/m^3 at 0.6 MPa.

In order to exploit the generator as a standard for sensors working on different principles, the conversion between different humidity parameters is necessary. The mixing ratio and specific humidity should be calculated considering Equations (2-1) and (2-2); furthermore, the mole fraction should also be considered in accordance with the molar mass of water and the carrier gas considering,

$$W = \frac{\dot{m}_w}{\dot{m}_g}, \qquad (2\text{-}1)$$

$$q = \frac{\dot{m}_w}{\dot{m}_g + \dot{m}_w}, \qquad (2\text{-}2)$$

$$x = \frac{\dot{m}_w / M_w}{\dot{m}_g / M_g + \dot{m}_w / M_w}, \qquad (2\text{-}3)$$

$$p_{ws} = \frac{x_w \cdot P}{f}, \qquad (2\text{-}4)$$

where W is the mixing ratio, q is the specific humidity, $\dot{m}_w$ and $\dot{m}_g$ are the mass flow rates for water and the carrier gas, M_w and M_g are the molar mass of water and that of the carrier gas, x is the mole fraction, P is the total pressure, f is the water vapor enhancement factor and p_{ws} is the saturation water pressure.

The saturation vapor pressure is measured by the experimental setups and is reported in a number of articles in the literature. The most frequently used ones are reported by Sonntag [56], Wexler and Hyland [57]. However, the Wagner and Pruss [58] equation appears to be the best correlation for dew-point temperatures above 100 °C. Figure 78 shows the deviation of abovementioned equations from Wagner and Pruss equation,

$$\ln\left(\frac{P_{ws}}{P_c}\right) = \frac{T_c}{T}[a_1\tau + a_2\tau^{1.5} + a_3\tau^3 + a_4\tau^{3.5} + a_5\tau^4 + a_6\tau^{7.5}], \qquad (2\text{-}5)$$

where T_c=647.096 K, p_c=22.064 MPa,τ=1-$\frac{T}{T_c}$ and $a_i$is a set of coefficients as reported in Table 71.

Table 71: Coefficients of the water vapor pressure of Equation (2-5) as reported by Wagner and Pruss

a_1	-7.85952

a_2	1.844083
a_3	-11.7866
a_4	22.68074
a_5	-15.9619
a_6	1.801225

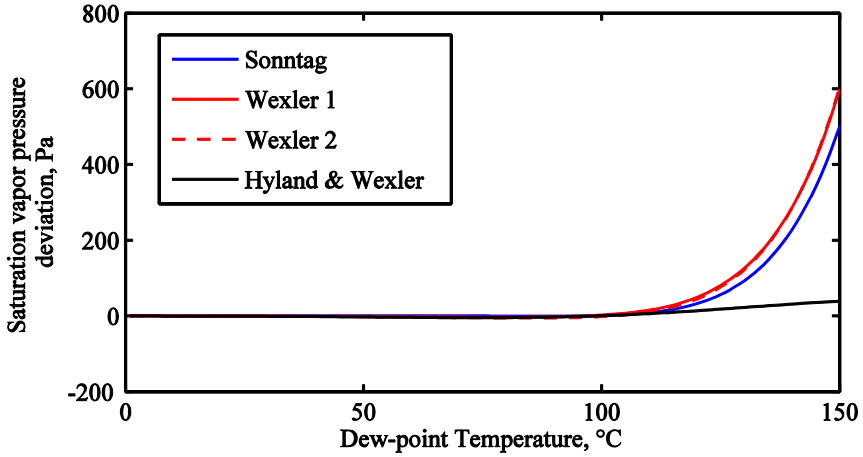

Figure 78: Deviation of saturation pressure curves from Equation (2-5)

The humidity generator output was validated through independent measurements of water vapor amount fraction in the gas phase by means of microwave-based hygrometry and by comparison against the INRIM primary humidity standard in the relevant dew-point temperature range.

2.2 Generator: design, constructing features, operating principle development

Figure 79 depicts a detailed schematic of the experimental setup. The first stage comprises the liquid water (blue) line and the compressed air (mustard) line of the generator. A displacement gear pump sucks water from a reservoir and delivers pressurized water to a pair of check valves whose trip point is set in such a way a small fraction is delivered to a calibrated liquid mass flow controller (*l*-MFC) and a larger fraction is bypassed back to the reservoir. Such a passive control strategy helps to filter down pressure fluctuations associated with the gear pump operation. Compressed air is delivered through pressure regulators to a calibrated gas mass flow controller (*g*-MFC). Mass-based humidity generation is then achieved by PID-controlling the flow mixing through a nozzle mixer which controls the water mass ratio evaporated into a high-temperature heat exchanger (steam evaporator) to the dry air mass at the same pressure.

The humid gas flow is further delivered via heated hoses (red lines) to a chilled mirror hygrometer (CMH) and a microwave quasi-spherical resonator (QSR) hygrometer, refer to Figure 80, which measures humidity in terms of dew-point temperature and water vapor amount fraction, respectively. The system pressure is measured by a precision capacitive sensor which was calibrated at

several temperature points inside a thermal chamber. A PID-driven solenoid valve acts as a back-pressure controller of the system by controlling the dry gas pressure after a cold steam trap.

As a first step, instruments were installed and connected to a CMH to carry out preliminary tests at atmospheric pressure. In order to characterize the generator, different quantities were monitored in the system.

This strategy helps to smooth down pressure fluctuations associated with the gear pump operation. Compressed air is delivered through pressure regulators to a calibrated gas mass flow controller (*g*-MFC). Mass-based humidity generation is then achieved by PID-controlling the flow mixing through a nozzle mixer which controls the water mass ratio evaporated into a high-temperature heat exchanger (water evaporator) to the dry air mass at the same pressure.

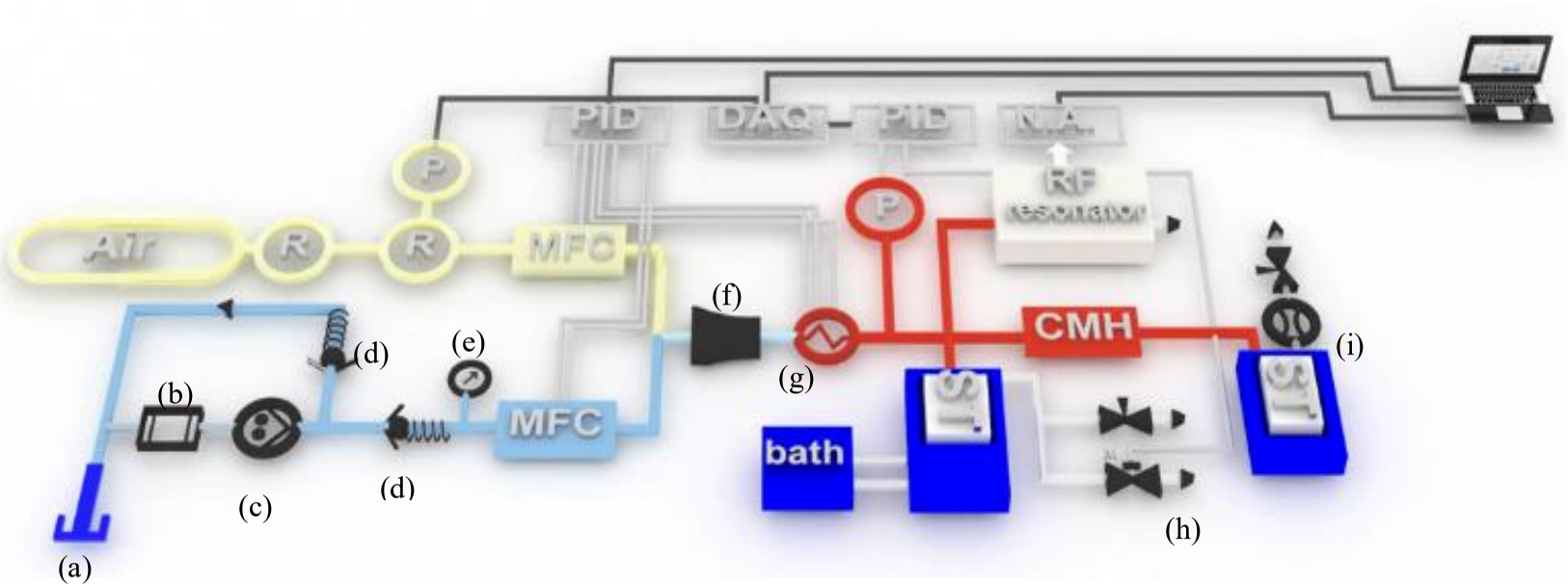

Figure 79: Schematic diagram of the high-temperature dew-point generator

(a) Water reservoir
(b) Filter
(c) Gear pump
(d) Check valve
(e) Barometer
(f) Mixing nozzle
(g) Heat exchanger
(h) Solenoid valve
(i) Mass Flow Meter

(R) Pressure regulator
(p) Pressure gage
(MFC) Mass Flow Controller
(CMH) Chilled Mirror hygrometer
(ST) Steam trap
(N.A.) Network Analyzer
(DAQ) Data Acquisition Unit

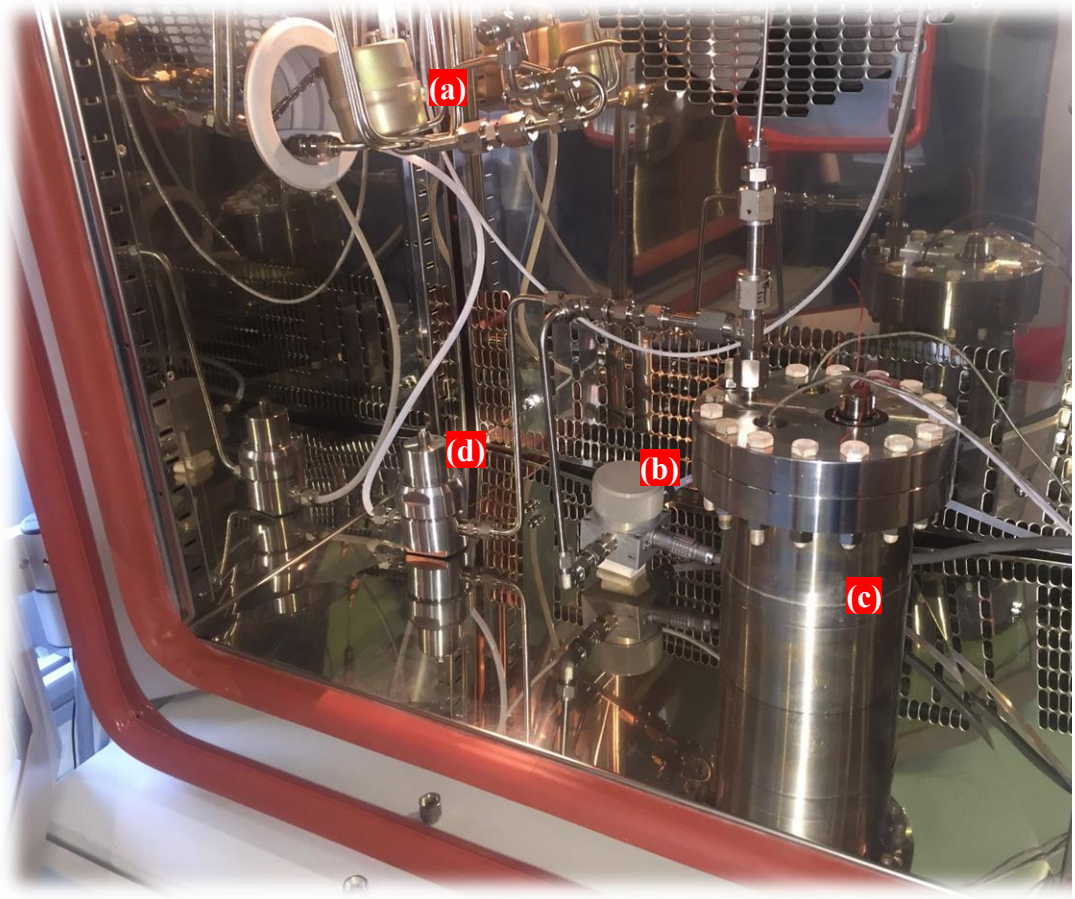

Figure 80: Thermal chamber
(a) Pressure transducer (b) Chilled mirror hygrometer (c) Vessel of the QSR (d) Mechanical pressure regulator.

2.2.1 **Mass flow rate control stability**

The generator is operated by keeping constant the gas mass flow rate at the desired operating pressure while setting the water mass flow rate to cover the intended humidity range. Two forward pressure regulators are cascaded to ensure a stable pressure at the *g*-MFC inlet, and a relative control stability of the gas flow rate of better than 0.05 % was achieved.

The initial control stability of the *l*-MFC was way more challenging, as shown in Figures 81 to 83, where for some flow rates it was unacceptably high. After an investigation, the instability was attributed to tiny air bubbles entrained in the liquid which caused pressure instability and, consequently, flow instability. Both pressure and flow fluctuations, albeit correlated, contributes to the uncertainty of the generated humidity quantities.

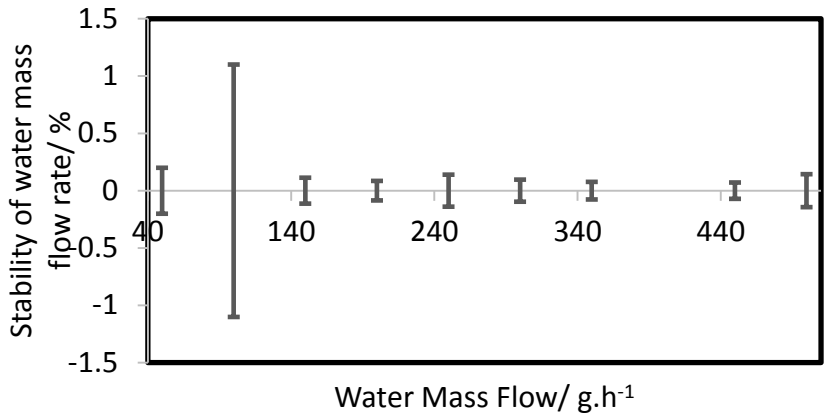

Figure 81: Preliminary tests, stability of water mass flow rate

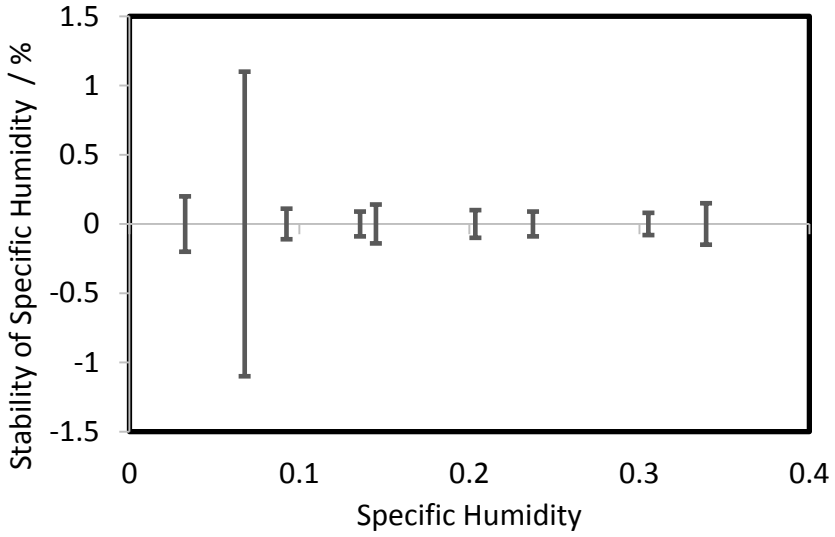

Figure 82: Preliminary tests, stability of the specific humidity

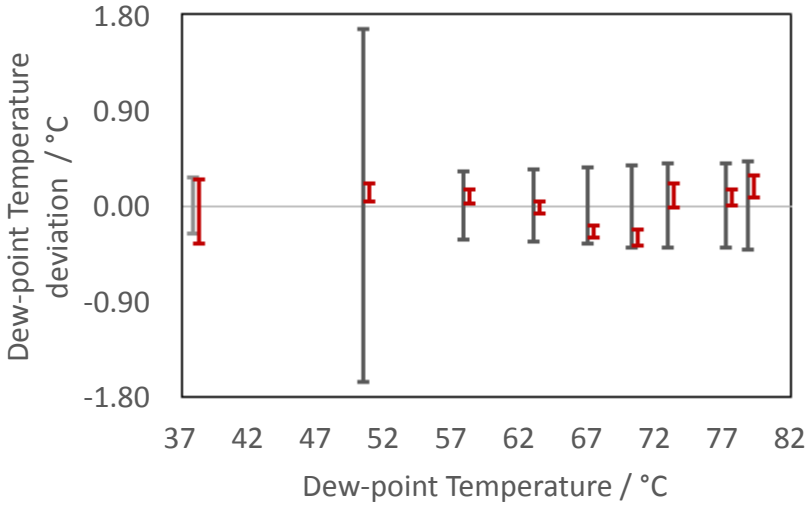

Figure 83: Preliminary tests, Dew-point Temperature stability, conversion of the generated mixing ratio in black and CMH measurement in red, uncertainty bars are indicative of the expanded uncertainty and shifted horizontally for the sake of visualization

Few attempts were carried out to filter out the air bubbles, the insertion of a standard arterial line filter with a conical micro-mesh strainer before the pump resulted in being the most effective. Water enters tangentially (top left) to the filter which encourages any possibly entrained bubbles to rise to the top where they are vented out (see Figure 84).

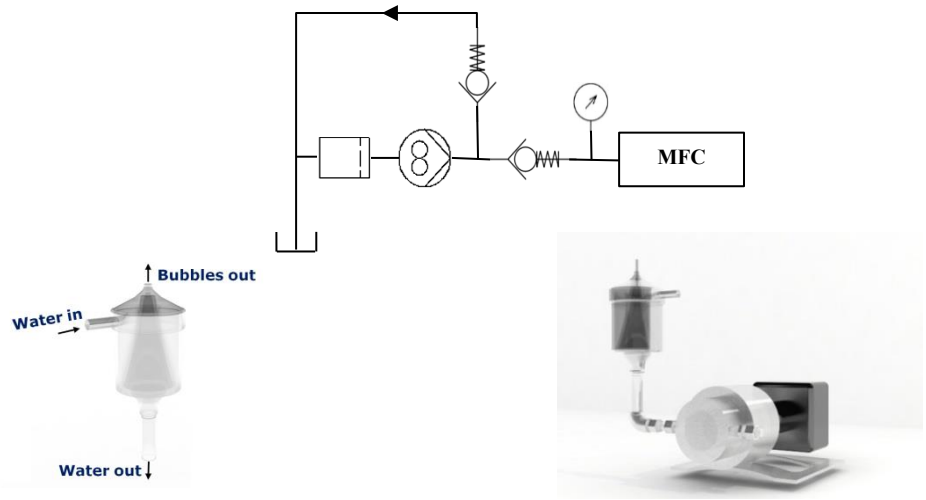

Figure 84: Introduction of a bubble filter trap to remove entrained air bubbles in the liquid.

2.2.2 **Pressure control stability**

Pressure control plays a major role in the performance of the generator; its importance is even more critical when the measurands are the dew-point temperature and the relative humidity. In preliminary tests, it was estimated that a relative pressure instability of about four parts in 10^3 contributed to about 70 % of the combined uncertainty in the dew-point temperature. To improve the relative stability to better than 10^{-3} a combination of techniques were exploited. The most effective was to minimize the lag time between the pressure sensing device and the electro-valve actuator, to develop a software cascade controller that continuously tracks and adjusts the set point of the analog PID controller and to integrate a high-temperature mechanical pressure regulator into the thermal chamber closer to the QSR vessel, as depicted in Figure 85.

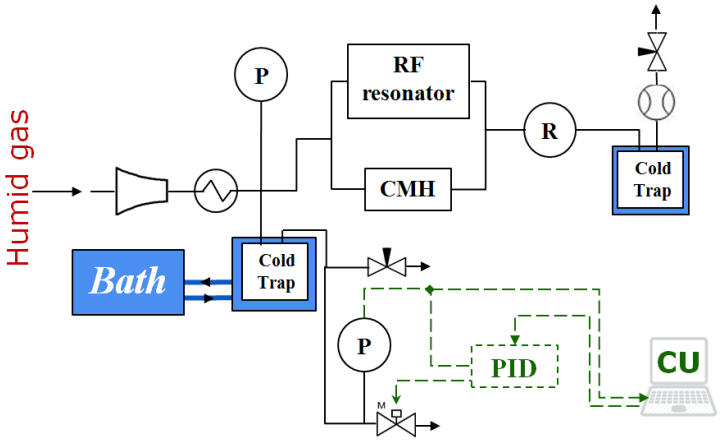

Figure 85: Block diagram of the multilayer pressure control strategy

2.2.3 Evaporation efficiency

The efficiency of a high-temperature steam evaporator directly affects the overall performance of the system. Ideally, perfect evaporation is expected, in fact, few tiny water droplets entrained in the humid gas stream would largely affect the operation of the optical detection in a CMH and the resonance frequencies in the microwave resonator, thus causing large measurement errors.

The initial experiments were aimed at the correlation between the evaporator temperature and the dew-point temperature, as detected by a CMH, when the generator was operated at a constant specific humidity value.

Although, an increase in the measured dew-point with the evaporator temperature is recorded (i.e. at the millikelvin level) which could be a symptom of a non-ideal evaporator operation, even if it is within the standard deviation of the measurements, a more rigorous and sensitive method was used to further assess the evaporation efficiency, based on measurement of the resonance frequencies in a microwave resonator employing the TE_{11} mode. Indeed, even small droplets can strongly affect the resonance triplets, but no changes were observed in the resonance waveforms in the whole range of evaporator set point temperatures. It clearly means that such a small increase in T_{dp} should be interpreted as the temperature elevation disturbance on the mirror. However, as a safe approach, we decided to set the evaporator temperature from 30 °C to 60 °C higher than the expected dew-point temperature.

2.3 Basic principles of microwave hygrometry using resonant cavities

The relative dielectric constant of a gas sample can be considered as an intensive thermodynamic quantity, depending, in a first approximation, on the gas (or gas mixture) molar density as

$$\varepsilon_{\mathrm{mix}} = \frac{2\rho_{\mathrm{mix}}\wp_{\mathrm{mix}} + 1}{1 - \rho_{\mathrm{mix}}\wp_{\mathrm{mix}}}, \qquad (2\text{-}6)$$

where $\wp_{mix}$ is the gas mixture molar polarizability, $\varepsilon_{\mathrm{mix}}$ is the relative dielectric constant and ρ_{mix} is the density of gas mixture.

By measuring the dielectric constant and one of the two variable, *P* or *T*, the missing thermodynamic quantity determination is possible; If the gas is a binary mixture, a contemporaneous measurement of pressure, temperature and dielectric constant gives the composition in terms of the molar fraction of the two components. In practice, this technique is effective only in the case of great difference in the molar polarizability between the two components, for example, a carrier inert gas, e.g. standard air, nitrogen, argon, together with water vapor.

In the following, the molar polarizability $\wp_{\mathrm{mix}}$ of a humid mixture is expressed using the mixing rule $\wp_{\mathrm{mix}} = x\ \wp_{\mathrm{w}} + (1\text{-}x)\ \wp_{\mathrm{d}}$, where $\wp_{\mathrm{w}}$ is the molar polarizability of pure water vapor, $\wp_{\mathrm{d}}$ is the molar polarizability of the pure carrier gas, i.e. the dry fraction, and *x* is the water vapor mole fraction. To single out the water vapor mole fraction, i.e. *x*, from Equation (2-6), it is necessary to provide an approximated equation of state for the humid mixture, in the form of a relationship between the thermodynamic quantities involved as a function of temperature, pressure and mole fraction. Considering the global uncertainty target of the present work, a truncated virial expansion is appropriated as

$$\rho_{mix} = \frac{\rho_0}{(1 + B_{\mathrm{mix}}\cdot\rho_0)}, \qquad (2\text{-}7)$$

$$\rho_0 = \frac{P}{R\cdot T}, \qquad (2\text{-}8)$$

$$B_{mix} = x^2\, B_{ww} + 2xB_{\mathrm{aw}} + (1 - x)^2 B_{\mathrm{aa}}, \qquad (2\text{-}9)$$

where B_{ww} and B_{aa}, are the temperature-dependent second virial coefficients of water vapor and dry fraction, respectively; B_{aw} is an interaction term characteristic of the mixture. When ε_{r}, *P*, *T*, are experimentally determined quantities, Equations (2-6) to (2-9) can be solved for *x* and the system operates as a hygrometer [[59], and references therein].

Oscillating electric field techniques are based on the following relation between the refraction index of a non-magnetic gas and the relative dielectric constant, far from possible absorption bands [60],

$$n^2 = \varepsilon_r, \qquad (2\text{-}10)$$

Where *n* is the refraction index and

$$n^2 = \left[\frac{(f_{l,m,n} + g_{l,m,n})|_{p=0}}{(f_{l,m,n} + g_{l,m,n})|_p (1 - \mathrm{K}_T P/3)}\right]^2, \qquad (2\text{-}11)$$

should be considered for the microwave resonators where $f + g$ is the average frequency (corrected for its halfwidth) of a microwave mode, identified by the indexes (*l, m, n*), measured in vacuum and at a pressure *P* at the same temperature *T*; K_T is the isothermal compressibility of the metal comprising the resonator, at the temperature *T*.

Microwave QSRs have a series of advantages over possible competing techniques:

- they have been successfully employed in a variety of primary metrology experiments and very refined models are available for correcting the experimental frequencies and reducing the type-B uncertainty components;
- a sturdy construction: resonators can be employed without modification of the original design from cryogenic temperatures up to 1000 K and up to several MPa of pressure, depending only on the mechanical resistance of the external pressure vessel;
- it is possible to use the same resonator as a molar fraction measuring device or a condensation hygrometer [61]; the working principles of the device are theoretically well-founded.

2.4 Microwave apparatus and measurement procedure (as used in this work)

The core of the microwave (MW) apparatus used for molar fraction determinations is a quasi-spherical resonator (QSR), *i.e.* a triaxial ellipsoidal cavity obtained from two blocks of maraging steel and plated with a 10 μm thick layer of gold. The three semi-axes of the ellipsoid are parametrized by *a*, *a* (1 + ε_1) and *a* (1 + ε_2), with *a* = 25.4 mm, ε_1 = 0.001, and ε_2 = 0.003. The small deviation of this geometrical surface from that of a sphere justifies the name of the device, QSR. The resonator is equipped with four 2.3 mm diameter holes, two for MW antennas mounting and two for gas inlet and outlet tubing. The gold plating ensures outstanding chemical resistance and greatly enhances the quality factors of the resonant MW modes. Since The MW resonator is not gas tight, it is enclosed in a stainless steel pressure vessel provided with electrical feedthrough for MW signals and temperature sensors; a stainless steel gas manifold, connected to the inner resonator by 1/8” diameter PTFE short pipes, allows the usage of the pressure vessel as an in-line device, with the sample gas continuously flowing through the QSR out to different measuring instruments. In the actual set-up, two non-calibrated capsule platinum resistance thermometers (PRT) are used; two massive copper blocks keep them in good thermal contact with the outer surface of the resonator. The pressure in the vessel is inferred from the pressure transducer installed at the head of the measuring line and described in the previous sections, neglecting the losses due to gas mixture flowing in the gas manifold.

A (VNA) operates MW frequency sweeps in a set of frequency windows containing selected resonance modes of the cavity in the range from 5 GHz to 12 GHz; the MW spectra are recorded by a computer and fitted with a combination of complex Lorentzian functions [60] to assess a very precise estimation of the Eigen-frequencies. Due to VNA limitations, three modes (TM_{11}, TE_{11}, and TM_{12}) are available. In order to follow the rapid variations of gas composition the apparatus undergoes during the humidity generator tests, we chose to analyze only the TM_{11} mode (the scan-and-fit sequence is time-consuming, if a good signal-to-noise ratio, i.e. 10^8, is to be preserved during frequencies measurement).

2.5 Humidity generator validation

Validation is the most critical aspect of developing standards and is performed, initially, by using two different chilled mirror hygrometers. These hygrometers are calibrated against INRIM-01 primary standard [22] and therefore are representatives of the existing Italian humidity standards. The initial observation shows that pressure stability is more critical at higher humidity levels (e.g. relative pressure stability estimated to be about 0.02% at $T_{\mathrm{dp}} = 56$ ℃ up to 0.11% at $T_{\mathrm{dp}} = 89$ ℃). On the contrary, by increasing the dew-point temperature, the specific humidity stability enhances. (e.g. 0.4% at $T_{\mathrm{dp}} = 56$ ℃ down to 0.02% at $T_{\mathrm{dp}} = 89$ ℃) and the main reason, clearly, is due to the improved relative stability of the mass flow controllers in the mid-range, especially in the liquid branch.

Figure 86 illustrates the deviation between the generation phase and the measurement phase by employing a high pressure chilled mirror hygrometer. The uncertainty levels remain almost the same in the generation, intercepting accordingly with that of the measurements.

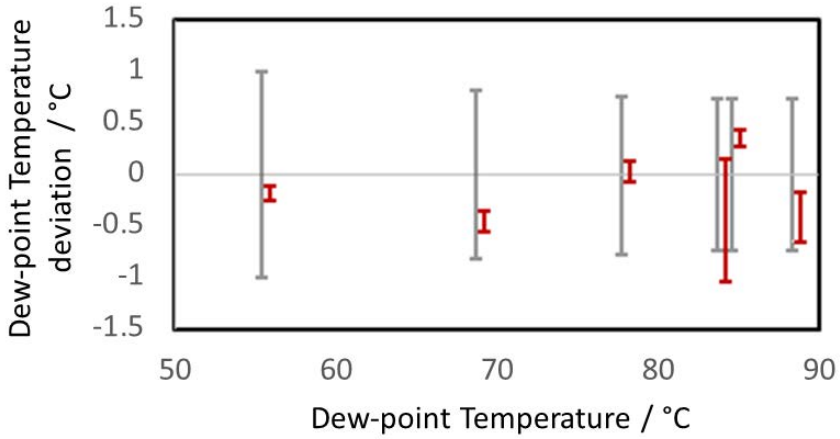

Figure 86: Validation against INRIM-01 at elevated pressures, conversion of the generated mixing ratio in black and CMH measurement in red, uncertainty bars are indicative of the expanded uncertainty and shifted horizontally for the sake of visualization

As a next step, the generator has been employed to compare the results of the chilled mirror hygrometer, as a representative of the existing Italian humidity standard, with that of a quasi-spherical resonator. The QSR is an integrated part of the humidity generator and its operation and calculation approaches should be validated. A fairly good agreement has been achieved in the entire operating range of the CMH as is observable in Figure 87. This is evident that the uncertainty levels for QSR increase by increasing the humidity and is always greater than that of a CMH; however, QSR approaches much faster to the final stable values.

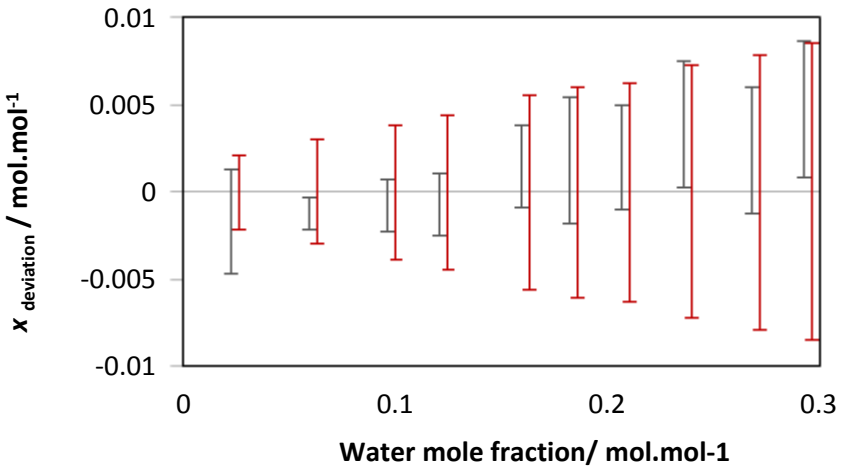

Figure 87: Confronting CMH in black vs. QSR in red, the measurements have been performed at the atmospheric pressure; uncertainty bars are indicative of the expanded uncertainty and shifted horizontally for the sake of visualization

The mole fraction stability is also reported in Figure 88 which never exceeds $4 \cdot 10^{-3}$ of the average value.

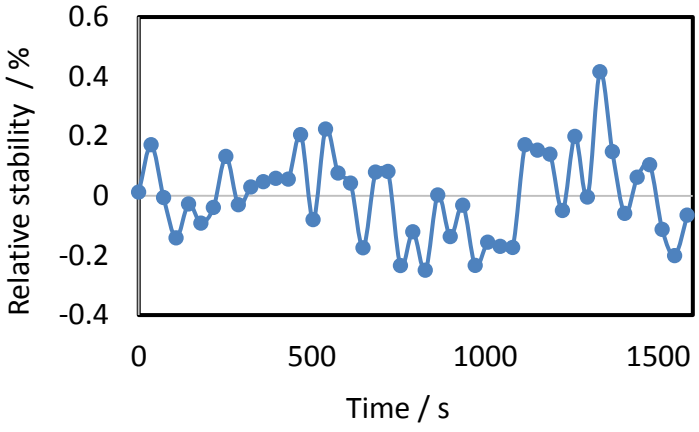

Figure 88: Stability of the generator at atmospheric pressure and x ≈ 0.2

The uncertainty elaboration will be discussed on page 83; this is worth mentioning that in the low range this is more crucial to minimize the pressure fluctuations, more rigorously, almost one-third of the uncertainty is contributed by pressure. In contrast, within the high humidity range Debye constants, i.e.

polarizability of water molecules, are the only governing contribution, and any meaningful mitigation of the uncertainty should be focused on that.

Pressure of the chamber has been gradually increased to 0.4 MPa and the equivalent mole fraction of the mass flow controllers has been compared - by using the molar mass of water and that of the carrier gas over the values of the microwave resonator. The fist expanded uncertainty levels remained constant and, as it was expected, that of the QSR increases by increasing the amount fraction and at the last points they exhibit almost the same uncertainty levels. The importance of the data fusion at the higher levels are highlighted in Figure 89.

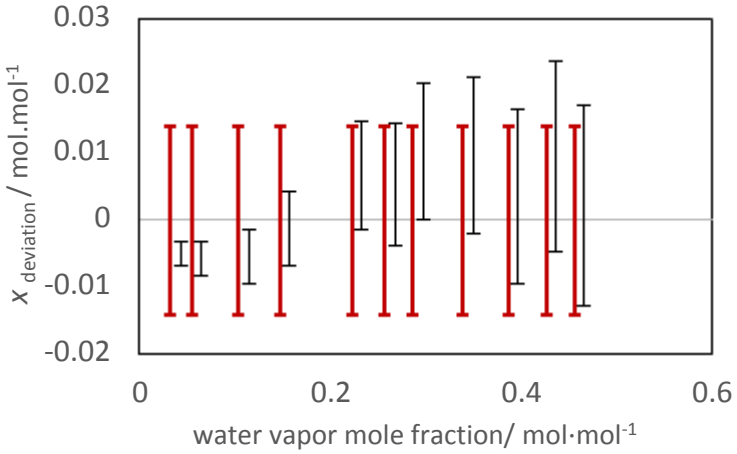

Figure 89: Consistency check at 0.4 MPa, conversion of the generated mixing ratio in red and QSR measurement in black, uncertainty bars are indicative of the expanded uncertainty (k=2) and shifted horizontally for the sake of visualization

Operation of the generator has been tested by automatically-controlled steps of humidity setpoint changes. This can be used in the calibration procedure without any assistance of the operators and can decrease the calibration cost price for calibration labs. Figure 90 shows the agreement between MFCs and QSR; likewise, uncertainty levels remain at the same level as targeted in previous sections. (i.e. Figure 91).

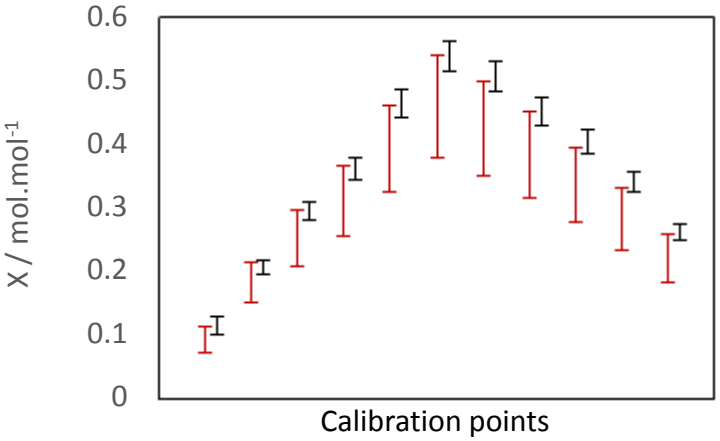

Figure 90: Automatic operation of the generator up to the highest dew-point temperature, conversion of the generated mixing ratio in red and QSR measurement in black, uncertainty bars are indicative of the expanded uncertainty and shifted horizontally for the sake of visualization, P= 0.6 MPa, T=160 °C.

The uncertainty at 0.6 MPa and 160 °C never exceeds 8 parts in 10^3 even at the highest target, i.e. x= 0.5. This is worth noticing that the generator operation challenges even saturation-based systems for its smooth operation, refer to Figure 92, besides its fast converge to the set-point and, thus, is ideal to be integrated with a chilled mirror hygrometer as it is very common in the humidity standard labs.

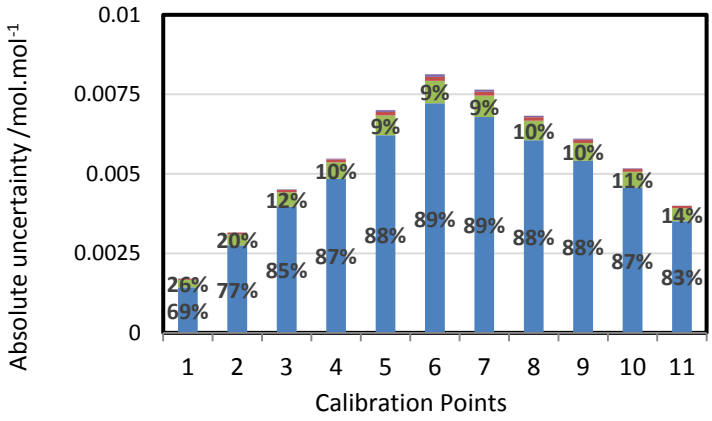

Figure 91: Uncertainty assessment of the QSR at the extreme temperature and pressure, blue stands for the contribution of the polarizability parameters in literature, green stands for the pressure uncertainty and red is indicative of that of the temperature.

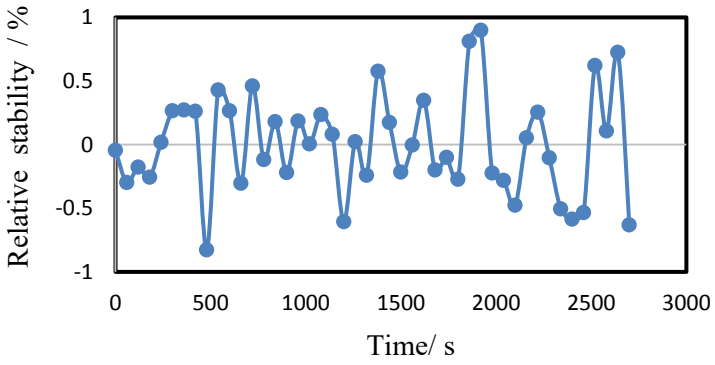

Figure 92: Stability at P=0.6MPa and T_{dp}=136℃

2.6 Performing humidity calibrations

A horizontal cylindrical sub-chamber has been designed, manufactured and accommodated inside the thermal chamber. The geometry of the sub-chamber is detailed in Figure 93. The calibration at high pressure, high temperature and high humidity yields to harsh conditions for the generator, the reference and the calibrants; thus, certain considerations should be taken into account. Initially, when calibrating at high pressures, the time needed to reach stability increases with pressure. Since more amount of water should be absorbed by the embedded polymer of the capacitive relative humidity sensors to get the equilibrium with humid media. When calibrating at high temperature and high humidity, particular care must be devoted to avoid the oxidation of cables.

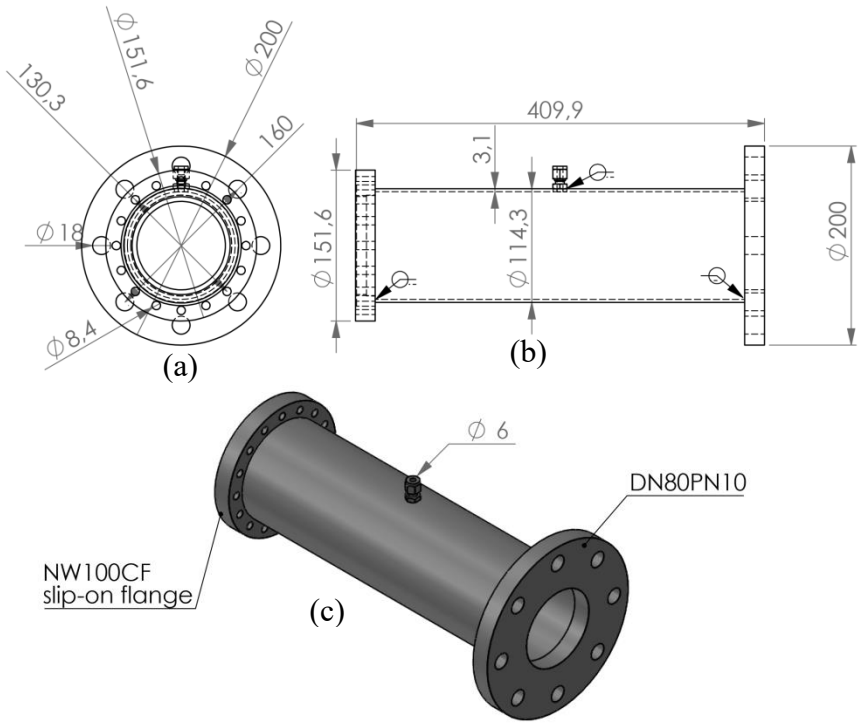

Figure 93: Mechanical design of the sub-chamber, (a) side view, (b) front view and (c) isometric view, all dimensions are reported in millimeters.

The temperature gradient within the humidity chamber should be minimised; for this purpose, the sub-chamber set inside a thermostatic chamber with the lowest possible volume is of importance. Likewise, it is highly recommended to start with the highest temperature and highest pressure calibration points and proceed then to lower temperatures and pressures. This is to minimize the drift of the sensor during the calibration for the RH sensors using a hygroscopic material. This is based on the common experience of the experts and may be linked to the absorption of water in the polymer sensing element. The initial drift of new sensors should also be considered, at the highest temperature and pressure of use for several hours.

As concerns the calibration procedure, the correct power supply is applied for checking the digital display the instrument is set in the testing chamber, as well as the temperature probe close enough to the sensing element of the DUC, through. The maximum immersion depth of DUC through bulkhead fittings is checked. Check for leaks and measurement of pressure drop is realized. The temperature of the thermostatic chamber is set at the desired value while the temperature of the heated hoses are adjusted in order to avoid unwanted condensation. As soon as the temperature stability is reached inside the testing chamber and the generator, a final check is performed with the DUC. If no instability is observed, the calibration can start for the level that has been set. The calibration lasts at least 20 minutes. A minimum of 20 readings on the DUC and 20 readings on the references, as required for the Gaussian distribution fitting, are recorded. Shorter acquisitions should be fitted to the student's t-distribution. At the end of the calibration, data processing is done by taking into account corrections from calibrations, pressure measurement and frequency shifts of the microwave resonator. The calibration set-up. sub-chamber is presented in Figure 94.

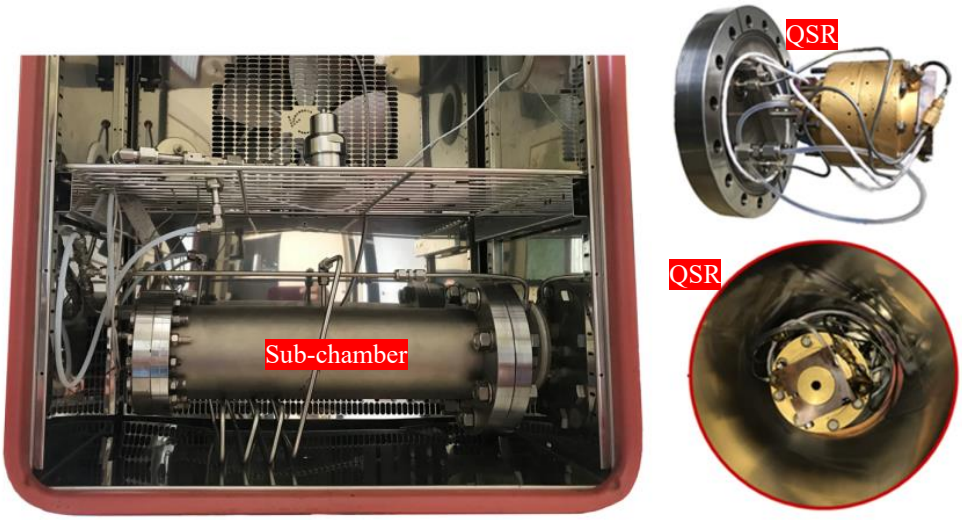

Figure 94: Calibration set-up. Sub-chamber hosted in a climatic chamber (left side) and microwave resonator hosted in the sub-chamber (right side).

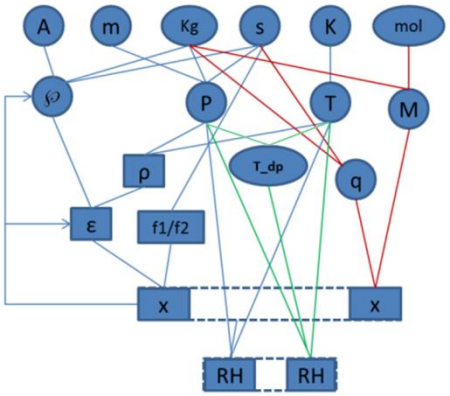

Figure 95: The traceability chain, RH is the relative humidity, x is the water vapor mole fraction, f_1 and f_2 are the resonance frequencies, $\boldsymbol{\varepsilon}$ is the relative dielectric constant, ρ is the density, $\wp$ is the polarizability, P is pressure, T is temperature, T_dp is the dew-point temperature, q is the specific humidity, M is the molar mass, A is ampere, m is meter, kg is kilogram, s is second, K is Kelvin and finally mol is mole.

Figure 95 shows the traceability tree of the relative humidity to the basic SI units. The dashed line is the place for the data fusion to minimize the uncertainty levels. Red lines show the traceability of the mixing ratio to SI basic units, green depicts that of employing the dew-point temperature measurements and blue indicates the traceability of the MW resonator measurements.

The humidity generator relies on the indirect gravimetric method, thus, the mass flow rate of the carrier gas(i.e .typically nitrogen) and that of water are measured in an SI-traceable manner, therefore, it provides an SI-traceable mixing-ratio (or specific humidity). Considering an SI-traceable pressure measurement, a traceable dew-point temperature is achieved and considering a calibrated SPRT for temperature measurements a traceable RH can be generated. However, this would provide significant uncertainty levels. In order to improve the uncertainty, the QSR has been integrated into the system which employs SI-traceable temperature and pressure measurements to single out the water mole fraction through the polarizability difference between water vapor and nitrogen. Considering the molar mass of water vapor and that of the nitrogen.

2.6.1 Discussion on the uncertainty associated with determination of the water molar fraction based on microwave hygrometry

The measurement model described by equations, presented in [59, 60] and [62], is an absolute scheme and is therefore affected by the accuracy of the pressure transducer. This issue can be overcome if a relative measurement model is implemented instead, measuring the resonance MW frequencies twice, in the dry carrier gas and the humid mixture at the same pressure and temperature. The working equation becomes

$$\varepsilon_{mix}(P,T) = \varepsilon_d(P,T)\left(\frac{f_d}{f_{mix}}\right)^2, \qquad (2\text{-}12)$$

where ε_{mix} and ε_d are the relative dielectric constant of the mixture and of the dry gas at the same thermodynamic state (P, T) respectively, while f_{mix} and f_d are the resonance frequencies measured in the same conditions.

The uncertainty budget for water mole fraction determination is listed in Table 72 for P=100 kPa, T=160 °C. The relative uncertainty, in the high mole fraction range exhibits a lower magnitude. Figure 96 clearly shows a slight decrease of the expanded uncertainty in the highest water vapor mole fractions.

Table 72 : Uncertainty budget for water mole fraction at 100 kPa and T=160 °C

x	0.2		0.5		0.8	
	u_i	$100.u_i/x$	u_i	$100.u_i/x$	u_i	$100.u_i/x$
$\wp_w$	1.03E-03	0.517	2.58E-03	0.515	4.12E-03	0.515
P	1.00E-04	0.050	2.50E-04	0.050	3.98E-04	0.050
T	4.60E-06	0.002	1.18E-05	0.002	1.85E-05	0.002
$\bar{f}$	5.00E-06	0.003	1.18E-05	0.002	1.87E-05	0.002
B_{mix}	4.00E-06	0.002	1.50E-05	0.003	4.04E-05	0.005
u_c	1.04E-03	0.519	2.59E-03	0.517	4.14E-03	0.517
U (k=2)	2.08E-03	1.038	5.17E-03	1.035	8.28E-03	1.035

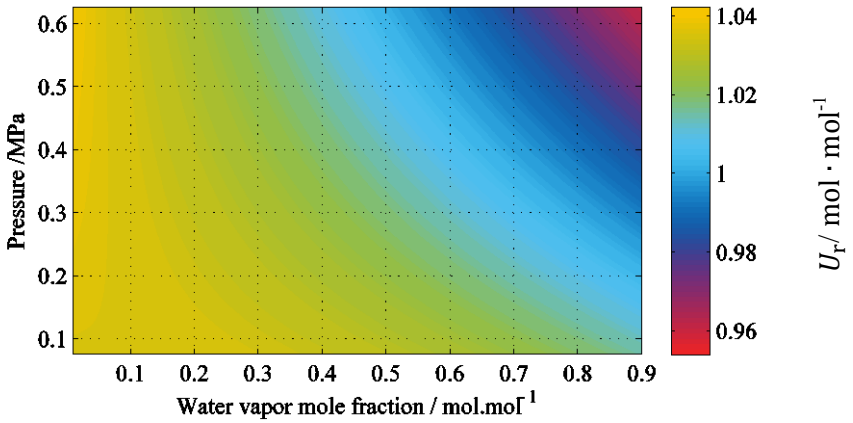

Figure 96: Pressure dependence of the relative expanded uncertainty (k=2)

2.6.2 Uncertainty associated with relative humidity calibration

The relative humidity as the ratio between the water vapor partial pressure and saturation water vapor pressure at the temperature corrected by the water vapor enhancement factor is given by,

$$RH = \frac{x \cdot p}{f \cdot P_{ws}(T)}, \qquad (2\text{-}13)$$

$$u_{RH} = \frac{1}{f \cdot P_{ws}(T)} \cdot \sqrt{(u_x \cdot P)^2 + (u_P \cdot X)^2 + \left(\frac{u_f}{f} \cdot X \cdot P\right)^2 + \left(\frac{u_{P_{WS}(T)}}{P_{ws}(T)} \cdot X \cdot P\right)^2}, \qquad (2\text{-}13\text{-}1)$$

where x is the water vapor mole fraction, p is the total pressure, f is the water vapor enhancement factor and $P_{ws}(T)$ is the saturation water vapor pressure. Considering the Equation (2-5) the propagation of u_T to e_w can be considered using ,

$$\frac{\partial P_{ws}}{\partial T} = \frac{P_{ws}}{T^2}\left[-T(a_1 + \frac{3}{2}a_2\tau^{\frac{1}{2}} + 3a_3\tau^2 + \frac{7}{2}a_4\tau^{\frac{5}{2}} + 4a_5\tau^3 + \frac{15}{2}a_6\tau^{\frac{1}{2}}) - T_C(a_1\tau + a_2\tau^{\frac{3}{2}} + a_3\tau^3 + a_4\tau^{\frac{7}{2}} + a_5\tau^4 + a_6\tau^{\frac{15}{2}})\right], \quad (2\text{-}14)$$

in which the expression inside the brackets can be simplified as $26420 \cdot T^{-0.282}$ with a relative mean squared error of 0.06 %, thus,

$$\frac{u_{P_{ws}}}{P_{ws}} = 26420 \cdot u_T \cdot T^{-2.282}, \quad (2\text{-}15)$$

and consequently,

$$\frac{\partial RH}{\partial T} = -26420 \cdot RH \cdot T^{-2.282}, \quad (2\text{-}16)$$

$$\frac{\partial RH}{\partial f} = -\frac{RH}{f}, \quad (2\text{-}17)$$

$$\frac{\partial RH}{\partial P} = \frac{RH}{P}, \quad (2\text{-}18)$$

$$\frac{\partial RH}{\partial X} = \frac{RH}{X}. \quad (2\text{-}19)$$

An example of the uncertainty budget follows:

Table 73: Example of the relative humidity uncertainty budget at x=0.8, P=100 kPa, and T=160 °C

Quantity	Brief description	Standard uncertainty	Distribution	Sensitivity coefficient	Uncertainty contribution [% rh]
TR_{stb}	Reference thermometer stability	**17 mK**	normal	0.00042	**7.1E-03**
TR_{cal}	Calibration PRT	**10 mK**	normal	0.00042	**4.2E-03**
TR_{drift}	Reference thermometer drift	**10 mK**	rectangular	0.00042	**4.2E-03**
TMR_{cal}	Multimeter calibration	**3.2 mΩ**	normal	0.00105	**3.4E-03**
TMR_{stb}	Multimeter time stability	**0.5mΩ**	rectangular	0.00105	**5.3E-04**
TMR_{res}	Multimeter resolution	**0.1mΩ**	rectangular	0.00105	**1.1E-04**
T_{AH}	Sub-chamber, Axial homogenity	**200 mK**	normal	0.00042	**8.4E-02**
T_{RH}	Sub-chamber, radial homogenity	**20 mK**	normal	0.00042	**4.2E-03**
P_{stb}	Pressure stability	**29 Pa**	normal	1.66E-04	**4.8E-03**

P_{cal}	Calibration of pressure transducer	**20 Pa**	normal	1.66E-04	**3.3E-03**
P_{TC}	Temperature correction of P	**33 Pa**	normal	1.66E-04	**5.5E-03**
P_{CF}	Pressure calibration fitting	**30 Pa**	normal	1.66E-04	**5.0E-03**
P_{res}	Pressure resolution	**1 Pa**	rectangular	1.66E-04	**1.7E-04**
P_{dft}	Pressure drift	**50 Pa**	normal	1.66E-04	**8.3E-03**
f_U	Enhancement Factor Uncertainty	**1.00E-04**	normal	16.38	**1.6E-03**
X_{WP}	Polarisability of water	**4.12E-03**	normal	20.81	**8.6E-02**
X_{PS}	pressure dependency of X	**4.00E-04**	normal	20.81	**8.3E-03**
X_{TS}	Temperature dependency of X	**1.60E-05**	normal	20.81	**3.3E-04**
X_B	Virial EoS	**1.60E-05**	normal	20.81	**3.3E-04**
X_{PDS}	Pressure of dry sample	**4.00E-05**	normal	20.81	**8.3E-04**
				u_c	**0.12**
				U (k=2)	**0.24**

The most significant contribution comes from the uncertainty of the temperature inhomogeneity and the water vapor polarizability equation u (x_{WP}), i.e. the Debye constants. Although this has been documented by a number of old publications dated back to 1935 to 1958, none of them can ensure a trustable result with low uncertainty levels. Essentially, Groves and Sugden [63], stranathan [64], Essen and Froome (1951) [65] and Essen(1953) [66] are among the most famous works. In this work, it has been decided to use a weighted average of the selected articles as discussed in [67]. This is worth mentioning that the contribution of the Debye constants increases with the relative humidity.

2.6.3 **Study of relative humidity sensors at high temperature**

The study has been carried out for two capacitive relative humidity sensors of the same type at elevated humidity and temperature levels. The first study point is set at 100.5 °C and 150 kPa. Figure 97 illustrates the calibration corrections. It is noticeable that the difference between sensors remains almost at the constant value of 0.53 %rh with the standard deviation of 0.03 %rh which remains below the reproducibility of the sensors.

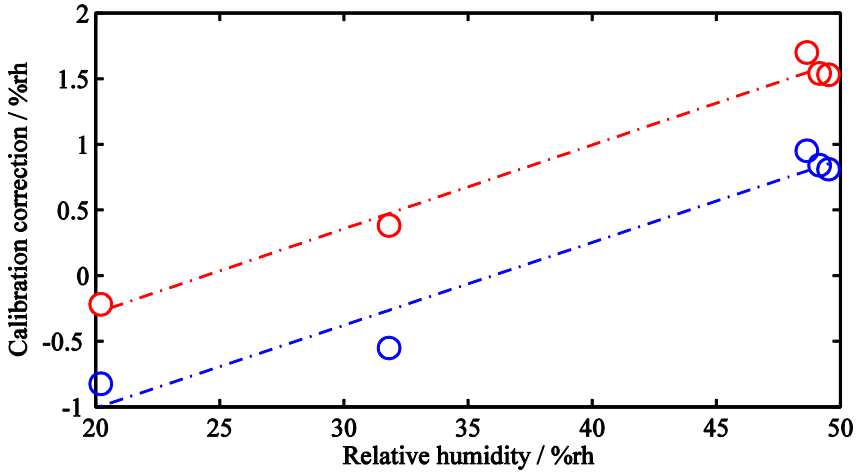

Figure 97: Study of capacitive humidity sensors, at nominal temperature 100.5 °C and 150 kPa, blue stands for sensor one and red for sensor two. The expanded uncertainty (k=2) is 0.42 %rh at 20 %rh growing to 1%rh at 50%rh.

The second set of calibration points were at nominal values of 115.5 °C and 145 kPa. According to Figure 98, the calibration correction of the two sensors remains proportional to the reference relative humidity with a non-linearity which could be estimated by the RMS error of about 0.17 %rh.

Table 74: Calibration correction of capacitive relative humidity sensors. The expanded uncertainty (k=2) is 0.26 %rh at 10 %rh growing to 1.32%rh at 70%rh.

h_{ref} / %rh	T / °C	P / kPa	$h_{IUT1} - h_{ref}$ / %rh	$h_{IUT2} - h_{ref}$ / %rh
70.35	115.8	144	1.45	2.45
63.61	115.8	143	1.09	1.89
46.71	115.5	143	0.39	1.04
46.71	115.5	147	0.39	1.04
30.1	115.5	145	-0.1	0.6
30.03	115.8	146	-0.03	0.77
29.79	115.8	146	0.01	0.71
25.93	115.8	147	-0.13	0.57
25.87	115.8	147	-0.17	0.53
20.43	115.5	144	-0.43	0.13
12.12	115.5	144	-1.12	-0.74
9.12	115.5	142	-1.22	-0.95

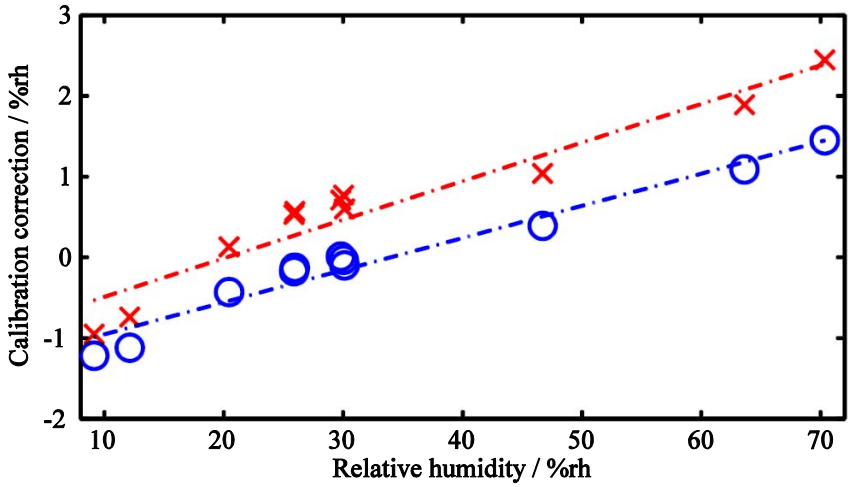

Figure 98: Study of capacitive humidity sensors, at nominal temperature 115 °C and 150 kPa, blue stands for sensor one and red for sensor two. The expanded uncertainty (k=2) is 0.26 %rh at 10 %rh growing to 1.32%rh at 70%rh.

2.6.4 **Pressure dependency**

The experiment has been repeated at the neighboring test pressure points and a considerable shift in the calibration correction has been observed, thus, a certain care should be taken to perform any calibration at the exact pressure of interest.

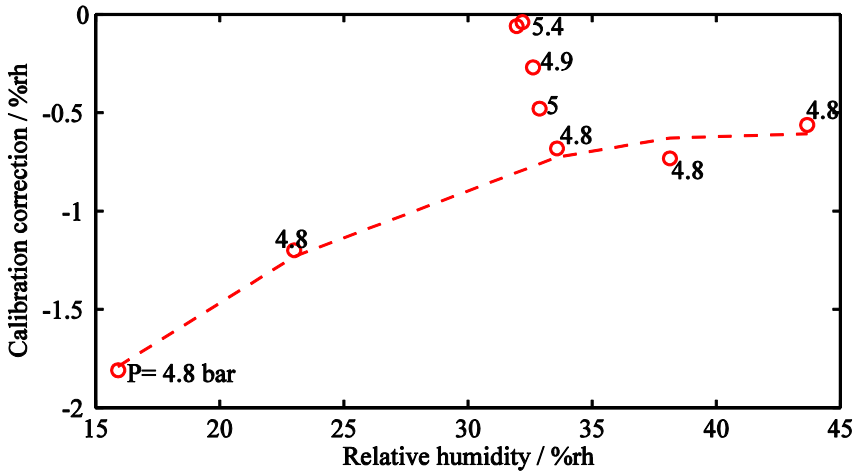

Figure 99: Pressure dependency of RH sensors

2.6.5 **Reproducibility**

Reproducibility of the relative humidity sensors at high temperatures is considered having a successive repetition of the experiment by considering different approaching history, as well as, performing the measurements at the neighboring pressure and temperature values. Results of such tests are summarized in Figure 100 and Figure 101.

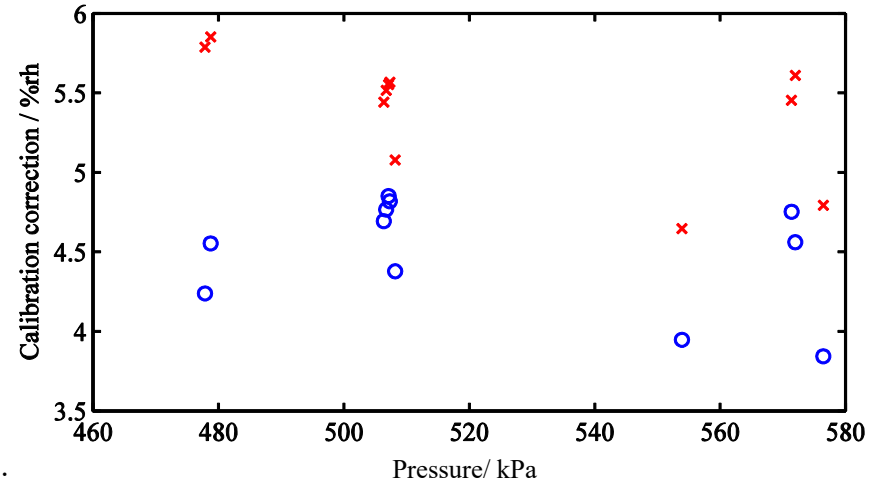

Figure 100: Pressure dependency of the calibration correction for RH sensors

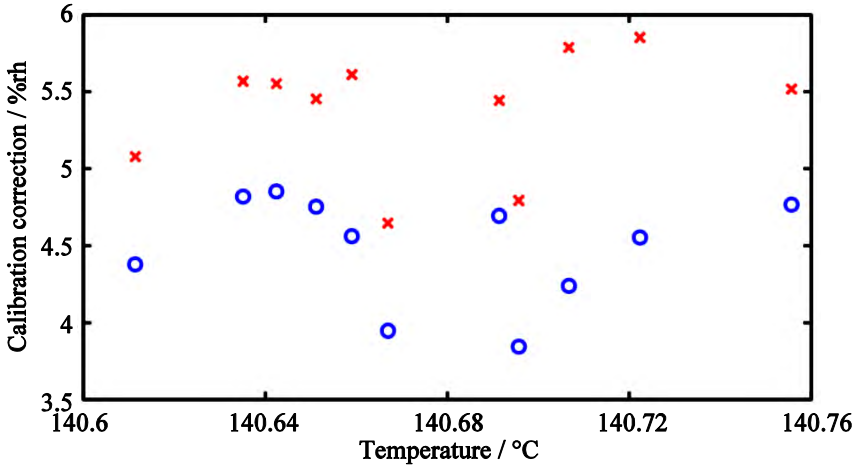

Figure 101: Temperature dependency of the calibration correction for RH sensors

The water mole fraction calculations, as described in Sec.2.4, are following the relative method and, inevitably, the deviation between the dry and wet sample, even if compensated for small changes, may result in wrong measurements. In order to investigate this effect, the calibration correction is plotted against the deviations of pressure and temperature, refer to Figure 102 and Figure 103.

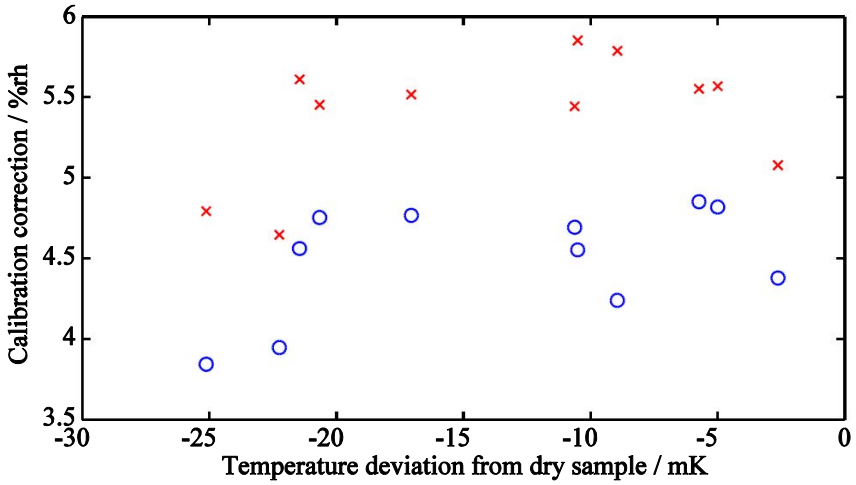

Figure 102: Deviations from dry samples, temperature dependency

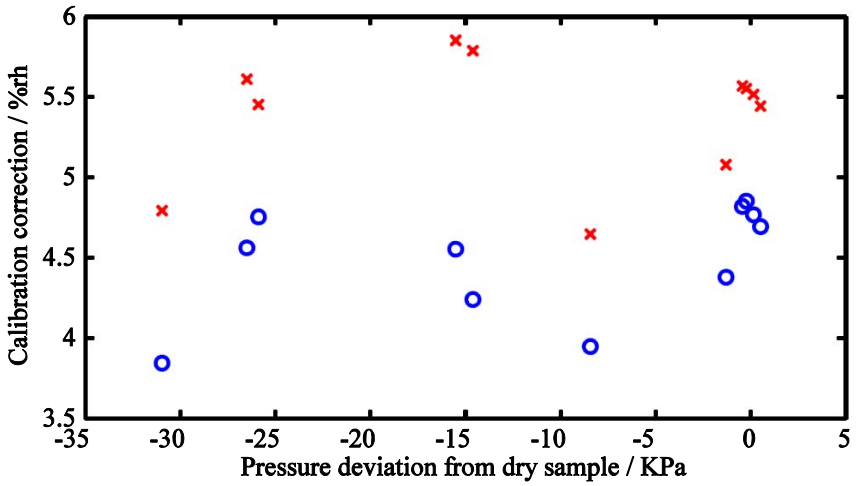

Figure 103: Deviations from dry samples, pressure dependency

The calibration correction exhibits a random variation against small changes of pressure and temperature as well as deviations from the dry reference samples. The calibration data has been fitted in the Gaussian probability distribution. The probability plot, as depicted in Figure 104, shows some deviations from the normal distribution; however, this seems reasonable enough to estimate the reproducibility of RH sensors.

The variances of the calibration corrections are 0.12 %rh and 0.15 %rh for first and second sensors respectively. Considering the confidence interval as 95 %, with the degree of freedom of 10, thus t=2.228, the reproducibility estimated to be about 0.7 %rh and 0.8 %rh respectively for the sensors. It considers small differences in the pressure, temperature and significant variations in the flow-rate and approaching history as well.

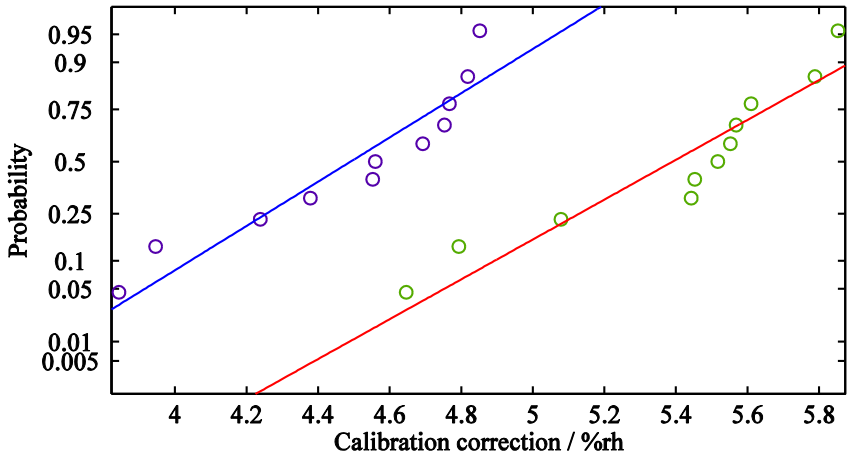

Figure 104: Probability plot representing the reproducibility of the sensors

2.7 Operation at extreme temperature and pressure

The generator, MW-based hygrometer and the capacitive humidity sensors have been challenged at the extreme operating range of the system. The generator exhibited a very fast and stable operation. This should be highlighted that the saturation-based systems suffer from incomplete saturations at high dew-point temperatures, however, gravimetric approaches are the best options for such high humidity levels. Furthermore, MW resonator was also tested for the extreme target point at T= 180.5 °C, P =615.738 kPa and RH=24.93 %rh, i.e. Figure 105.

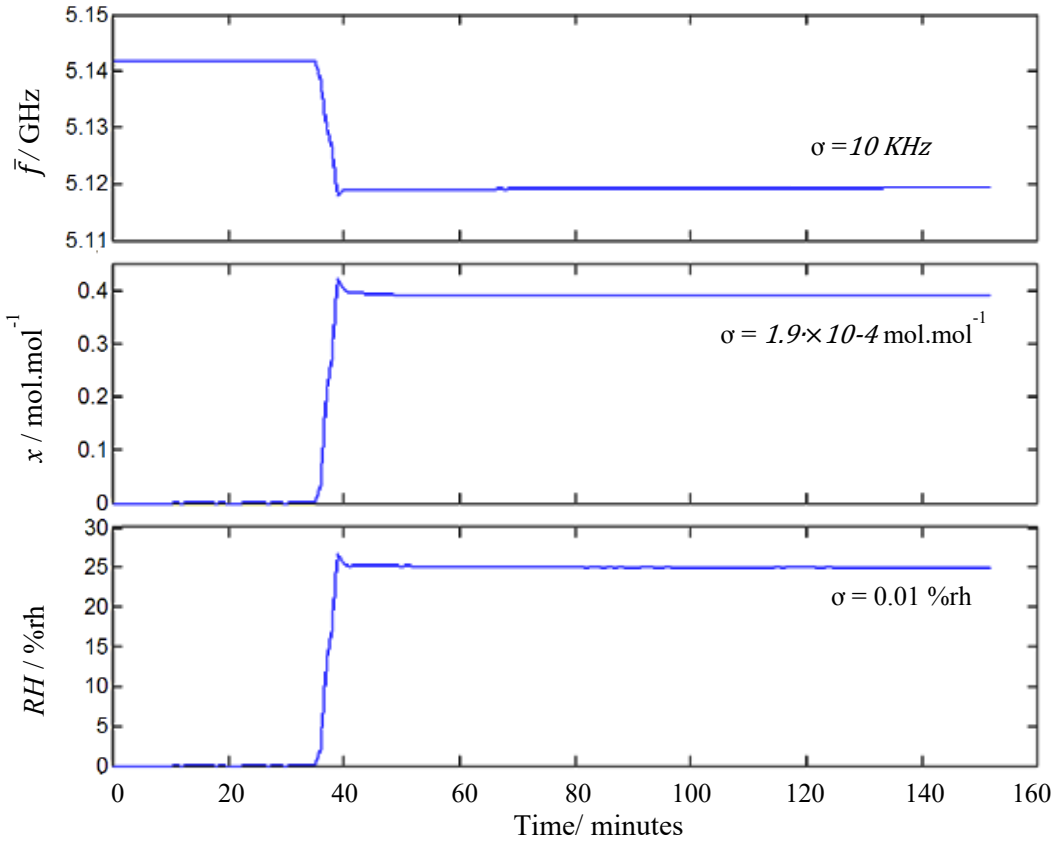

Figure 105: Operation at extreme conditions

Generator shows a short settling time and it gets a stability of $1.9 \cdot 10^{-4}$ of water mole fraction at x=0.391, i.e. $4.8 \cdot 10^{-4}$in terms of relative stability, which yields to a relative humidity stability of about 0.01 %rh. The temperature stability is 1.7 mK , pressure stability is 174 Pa and the readout of the sensors are 24.2 %rh and 25 %rh respectively.

2.7.1 Comparison against a saturation-based humidity generator

Within the framework of a European metrology project, i.e. Metrology for Humidity at High temperatures and Transient Conditions 14IND11 HIT, a preliminary comparison has been carried out using the same humidity sensors as reported in the previous section against a humidity generator which has been designed and developed at VSL (i.e. Dutch National Metrology Institute) [27]. Figure 106 and Figure 107 illustrate the comparison results and the agreement between the calibration corrections within the uncertainty levels of both measurements. The calibration corrections of the current work shows a much more reproducible result and it is hard to judge the agreement between that and those other diverse results at high range of relative humidity (i.e. Figure 106), however, at the lower range of relative humidity(i.e. Figure 107) even if the temperature is higher, different sets of data match ideally.

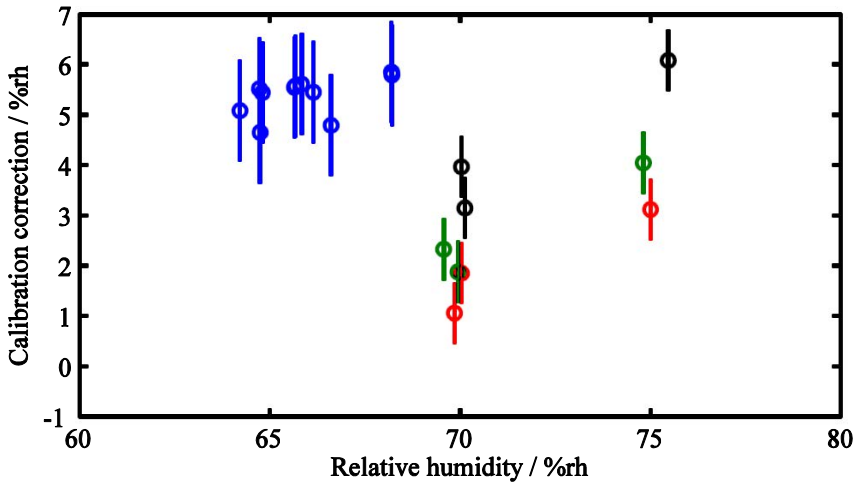

Figure 106: Calibration of a capacitive humidity sensor at 140 °C and 500 kPa: blue for this work, black for VSL first cycle, red for VSL second cycle and green for VSL last cycle, error bars are indicative of the expanded uncertainty (k=2).

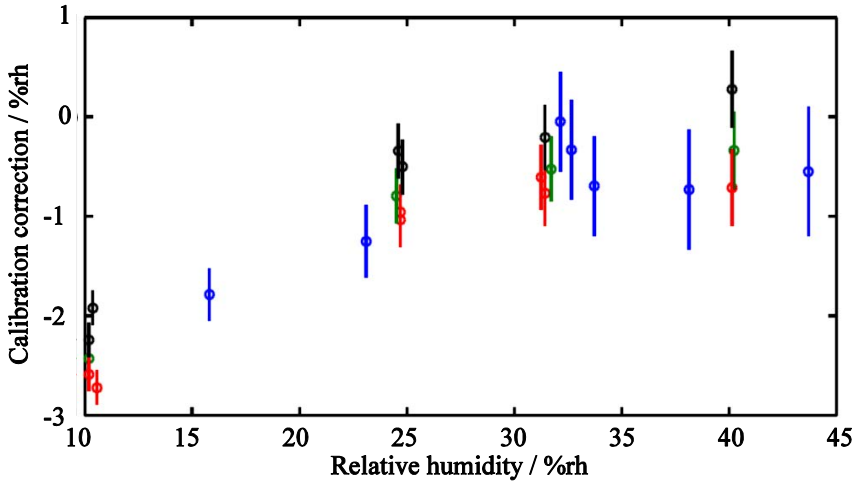

Figure 107: Calibration of a capacitive humidity sensor at 170 °C and 500 kPa :blue for this work, black for VSL first cycle, red for VSL second cycle and green for VSL last cycle, error bars are indicative of the expanded uncertainty (k=2).

2.8 Concluding remarks

This chapter concludes with specifications of the generator and a summary on consistency checks and validations. One of the most outstanding characteristics of this generator is its fast response both in the generation phase and in the measurement phase. Figure 108 shows the fast track of changes using QSR. It is noticeable that the differences are within the uncertainty as reported in the previous section. Basically, conventional humidity generators are built on the saturation of a carrier gas over a water pool and an inherently slow operation by their nature. This generator can be used as a transient profile maker with relatively sharp ramps.

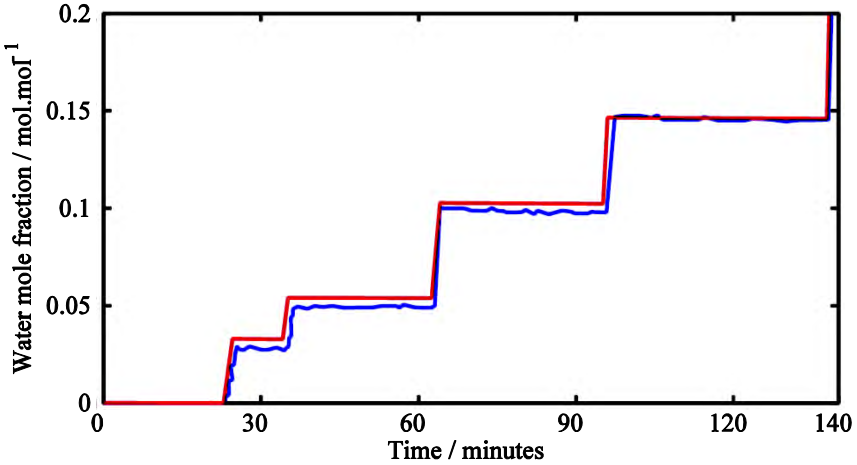

Figure 108: Transient study of the system, QSR in blue and conversion of the generated mixing ratio in red.

The generator is accommodated in a climatic chamber which is operatable up to +180 °C. Moreover, the humidity generator itself is capable of generating

humid gas in the equivalent dew-point temperature range of 35 °C to 140 °C. Pressure is limited to 0.6 MPa by the high-temperature pressure transducer, and the minimum should be slightly higher than that of the environment. Specific humidity is restricted by the limitations of the MFCs. The lowest stable point can be reached in about 0.07 kg/kg, and the maximum is slightly higher than 0.646 kg/kg. The equivalent dew-point temperature for the parameters mentioned above is the range from 35 °C to more than 142 °C. MFCs can operate in high flow rates up to 40 l/m, and a significant portion may be bypassed. The minimum flow that can guarantee a good pressure stability is recommended to be not lower than 1 $l \cdot m^{-1}$.

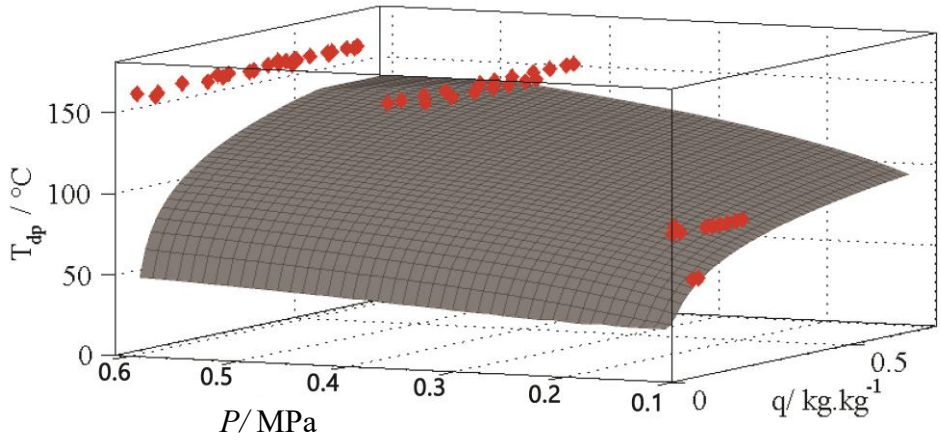

Figure 109: Validation points of the generator, the surface is indicative of the dew-point temperature

The surface depicted in Figure 109 is indicative of the dew-point temperature as a function of specific humidity and pressure and red points are presenting the validation and consistency checkpoints against chilled mirror hygrometers and a gold-plated quasi-spherical microwave resonator. A relative method has been employed to calculate the water mole fraction of the mixture. The uncertainty budget has been assessed to the measurements and the most significant contribution, especially in higher water concentrations, appeared to be the constants of the polarizability of water. A reasonably good agreement has been observed in the validations by confronting the generated mixing ratio of the mass flow controllers either to the quasi-spherical resonator or to the chilled mirror hygrometer for a selected sub-range. As the next step, the generator has been integrated into a sub-chamber for calibrations of RH sensors. These results showed fairly good agreements with that of a saturation-based humidity generator.

Chapter 3

Non-static Calibration of RH Sensors

3.1 Introduction

The calibration time directly affects the cost price of the sensors. “It can be estimated that by saving only 1.5 hours of the calibration time for 1000 units, one man-year of costs can be cut” [68]. In this chapter, a novel approach is discussed to calibrate generic second order probes which are able to model RH sensors as well since their experimental response to the stepwise changes can be fitted to that of a second-order transfer function.

3.2 Theory

In principle, the classical calibration by comparison is performed in static conditions after thermal and chemical equilibria of the sensor-calibrator system and finally making the ratio between the readout of the sensor in calibration over that of the reference. Let *F (S)* be the transfer function of any second order system in the Laplace domain

$$F\,(S) = \frac{q_0 \cdot (S - Z_1) \cdot (S - Z_2)}{(S - P_1) \cdot (S - P_2)}, \qquad (3\text{-}1)$$

in which Z_1 and Z_2 are the zeros, q_0 is the constant and P_1 and P_2 are the poles of the sensor. By imposing the unit step to this transfer function and applying the inverse transform the output can be expressed by the summation of three terms in the time domain [69] as

$$Y(t) = y_1^s + y_2^s + y_\infty^s, \qquad (3\text{-}2)$$

$$y_1^s = \frac{q_0 e^{P_1 t}}{P_1(P_1 - P_2)} \cdot ({P_1}^2 - P_1 Z_1 - P_1 Z_2 + Z_1 Z_2), \qquad (3\text{-}2\text{-}1)$$

$$y_2^s = -\frac{q_0 e^{P_2 t}}{P_2(P_1 - P_2)} \cdot ({P_2}^2 - P_2 Z_1 - P_2 Z_2 + Z_1 Z_2), \qquad (3\text{-}2\text{-}2)$$

$$y_{\infty}^{s} = \frac{q_0 Z_1 Z_2}{P_1 P_2}, \qquad (3\text{-}2\text{-}3)$$

y_1^s and y_1^s are mathematical terms governing the double exponential form of the transient and y_{∞}^s is the horizontal asymptote, thus, the calibration correction for the RH sensors can be expressed as the ratio of the asymptotes as illustrated in Figure 110,

$$C = \frac{RH^c}{RH^r} = \frac{y_{\infty}^{s,c}}{y_{\infty}^{s,r}} = \frac{\frac{q^c Z_1^c Z_2^c}{P_1^c \cdot P_2^c}}{\frac{q^r Z_1^r Z_2^r}{P_1^r \cdot P_2^r}}, \qquad (3\text{-}3)$$

in which *c* stands for the calibrant and r stands for the reference. This method requires a considerable amount of time, mainly, due to the stabilization time of the humidity generators and, later, to the stability of the relative humidity.

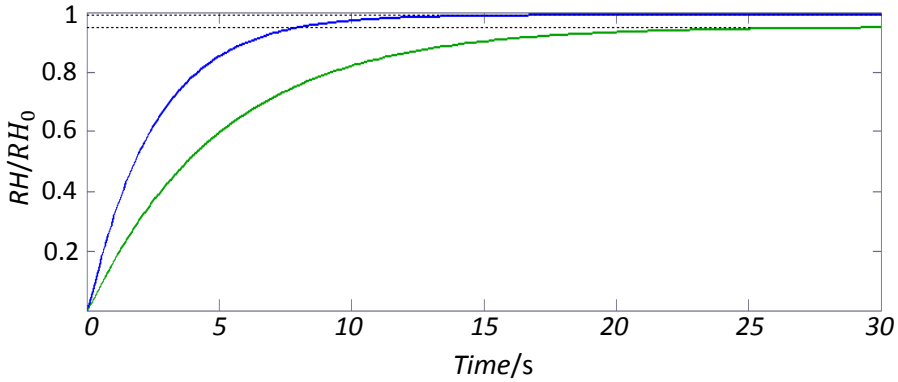

Figure 110: Classical calibration by comparison approach. Solid lines are indicative of the RH sensor readouts and dotted lines stand for their asymptotes

In order to retain the same definition for non-static conditions, considering a second order system, the response of the relative humidity sensor to a pure ramp might be estimated by the four terms of the Equation (3-4) as

$$Y^{r,c} = \sum_{y=1}^{4} y_i \,, \qquad (3\text{-}4)$$

$$y_1^{r,c} = \frac{\alpha q_0 e^{p_1 t}}{P_1^2 \cdot (P_1 - P_2)} \cdot (P_1^2 - P_1 Z_1 - P_1 Z_2 + Z_1 Z_2) \,, \qquad (3\text{-}4\text{-}1)$$

$$y_2^{r,c} = -\frac{\alpha q_0 e^{p_2 t}}{P_2^2 \cdot (P_1 - P_2)} \cdot (P_2^2 - P_2 Z_1 - P_2 Z_2 + Z_1 Z_2) \,, \qquad (3\text{-}4\text{-}2)$$

$$y_3^{r,c} = -\frac{\alpha q_0}{P_1^2 \cdot P_2^2} \cdot (P_1 P_2 (Z_1 + Z_2) - Z_1 Z_2 (P_1 + P_2)), \qquad (3\text{-}4\text{-}3)$$

$$y_4^{r,c} = -\frac{\alpha q_0 Z_1 Z_2 t}{P_1 \cdot P_2}, \qquad (3\text{-}4\text{-}4)$$

in which α is the input slope. y_1 describes the initial curved part due to the first pole for either reference or calibrant, y_2 describes the initial curved part due to the second pole, y_3 stands for the constant bias due to the time delay and y_4 is the major component and shows the ramp.

The ratio between the fourth terms yields the same definition of the calibration coefficient

$$C = \frac{y_\infty^{s,c}}{y_\infty^{s,r}} = \frac{y_4^c}{y_4^r}. \qquad (3\text{-}5)$$

The term $y_4^{r,c}$ is not available explicitly; however, it can be estimated by $Y^{r,c}$-$y_1^{r,c} - y_2^{r,c} - y_3^{r,c}$ and since poles and constant of a sensor is not known during the calibration, the error term, i.e. $E=\sum_{i=1}^{3} y_i^{r,c}$, can be considered as an uncertainty source by probabilistic assumption of the unknown transient terms, refer to Figure 111.

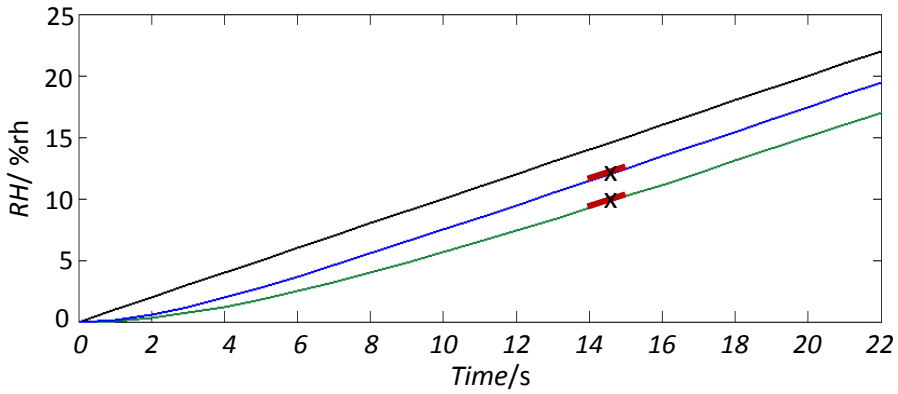

Figure 111: Example of the response to the ramp of second order sensors, black stands for the input and blue and green for two different RH sensors while x is indicative of the discrete readout and red is indicative of its first time derivative.

In order to mitigate the uncertainty levels for fast ramps, this is worth to consider also a complementary approach of having the first time derivatives of $Y^{r,c}$ to reconstruct Equation (3-3) by,

$$C = \frac{A^C}{A^r} = \frac{\dot{y}_4^c}{\dot{y}_4^r} = \frac{\dot{Y}^c - \dot{y}_1^c - \dot{y}_2^c}{\alpha}, \qquad (3\text{-}6)$$

in which $\dot{y}_1^{c,r} = P_1 \cdot y_1^{c,r}$ and $\dot{y}_2^{c,r} = P_2 \cdot y_2^{c,r}$, thus, the second approach gives lower levels of uncertainty when $P_1^C < \frac{\alpha}{Y^r}$ and $P_2^C < \frac{\alpha}{Y^r}$, however, in any case the data fusion between the two approaches can minimize the uncertainty.

3.2.1 **Generalization to arbitrary RH profiles**

The formulations discussed above can be generalized to any randomly shaped humidity profile as discussed in [70]. Figure 113 depicts the first time derivative of the arbitrary curve of Figure 112.

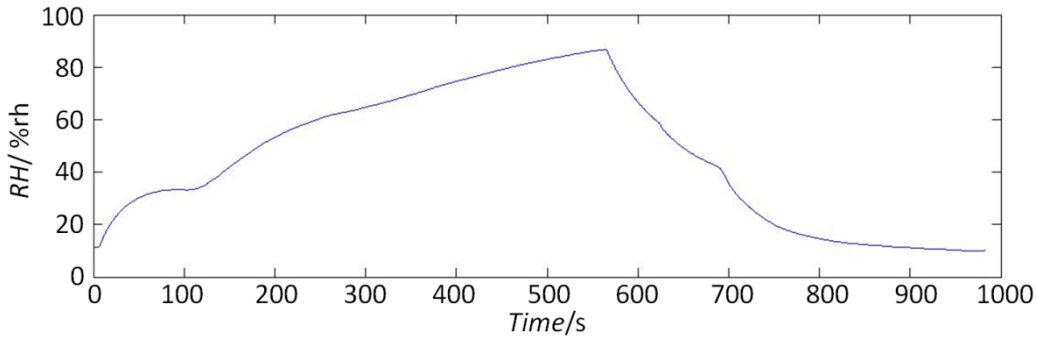

Figure 112: Arbitrary humidity profile

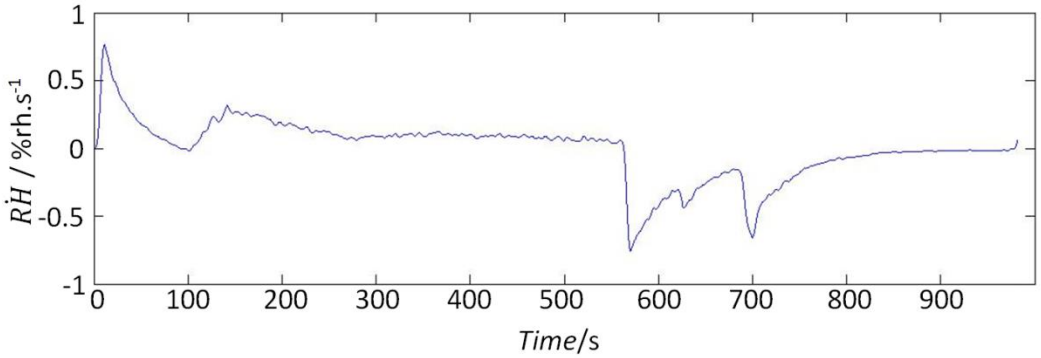

Figure 113: First time-derivative of the humidity profile

Eventually, the profile of Figure 113 can be interpreted as the superposition of the ramps starting from each time epoch with a slope equals to the second time derivative of the original discrete signal, i.e. Figure 114.

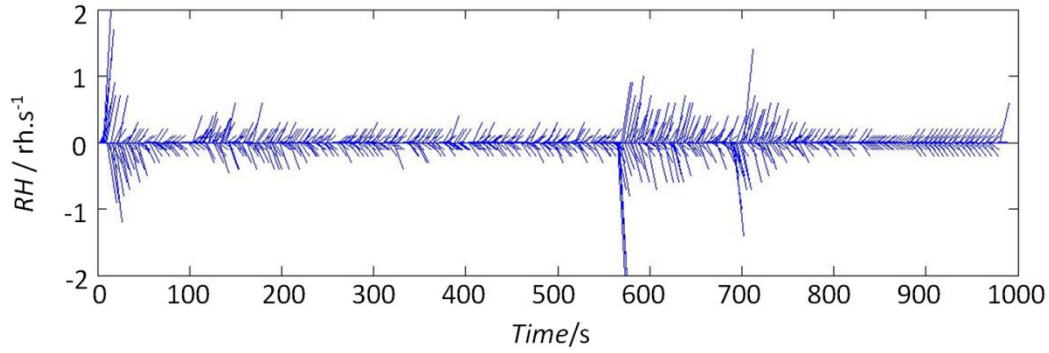

Figure 114: Splitting the original signal into the ramps, only a few first seconds are plotted for the sake of visualization.

Assuming a uniform probability distribution for $P_1$and P_2 the nonlinearity uncertainty contribution can be estimated as the accumulation of the terms described by Equations (3-4-1) and (3-4-2). This is illustrated in Figure 115.

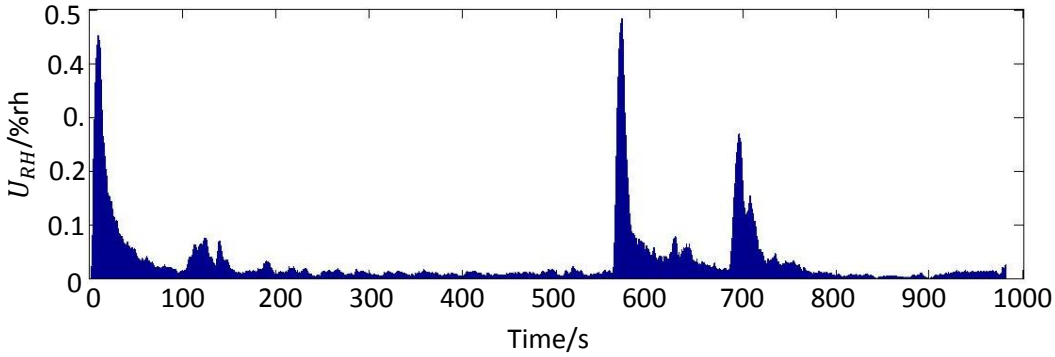

Figure 115: The uncertainty contributions due to the non-linearity term for the arbitrary curve of Figure 112

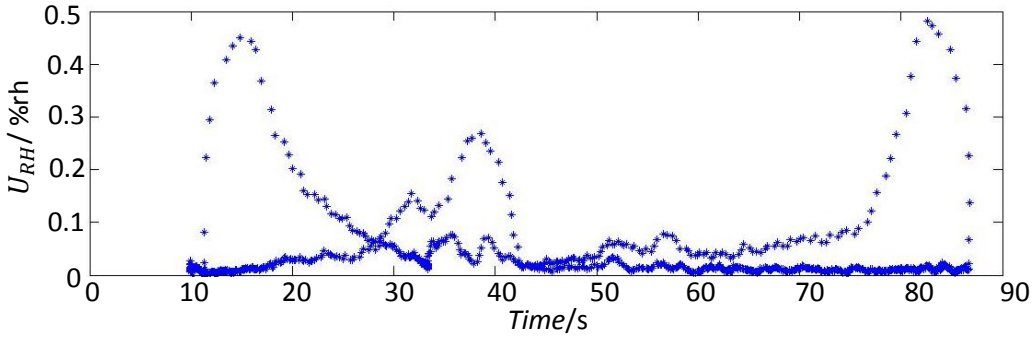

Figure 116: Relative humidity non-linearity contribution to the uncertainty at each relative humidity value.

As discussed in the real cases, input RH profile deviates from linearity and the accumulation of the mathematical terms $y_1^{r,c}$ and $y_2^{r,c}$ over the time should be considered. The uncertainty contribution dedicated to non-linearity of the humidity profile, as plotted in Figure 116, should be considered in accordance with the data fusion of the two available sets of information which, obviously, gives an uncertainty lower than each one.

3.2.2 **Contribution of the temperature**

The sensing element (polymer) of relative humidity capacitive sensor shows a well-known temperature dependence; temperature compensation is usually performed; however, under the transient conditions, the temperature measured by the sensor is not necessarily equal to the actual temperature of the polymer. In order to propagate the uncertainty towards the calibration results, firstly, it is necessary to find out the uncertainty of the temperature itself having the same approach described in Sec. 3.2.1 and, secondly, to consider the sensitivity of the temperature correction formula of the sensor.

Considering the arbitrary temperature profile of Figure 117 and assuming a random variable for the typical time constant of the embedded temperature sensor, Equation (3-4-3) can be solved. The non-linearity uncertainty contribution, as illustrated in Figure 118, can be interpreted as the accumulation of this term over the time.

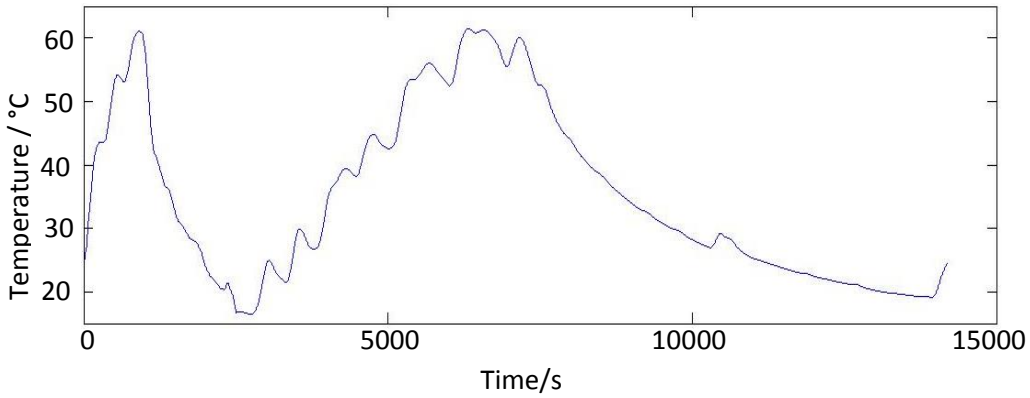

Figure 117: Randomly shaped temperature profile

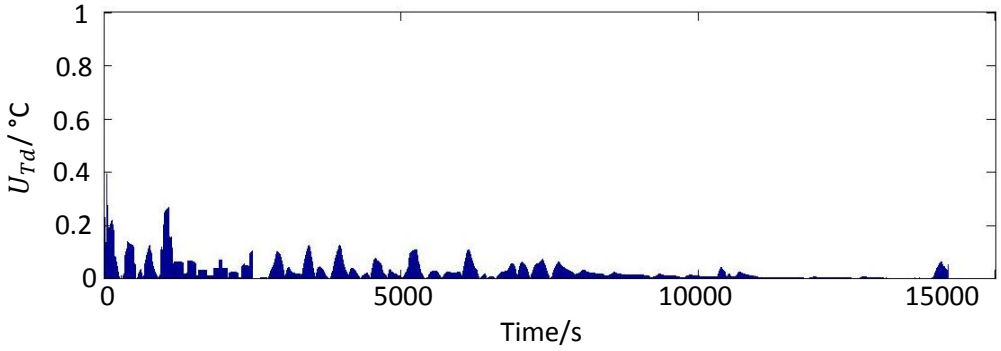

Figure 118: Uncertainty contribution of temperature sensing delay

Likewise, by employing Equations (3-4-1) and (3-4-2) the non-linearity terms are estimated and reported in Figure 119. Eventually, the two terms can be propagated through the temperature correction of the capacitive sensor which is plotted in Figure 120.

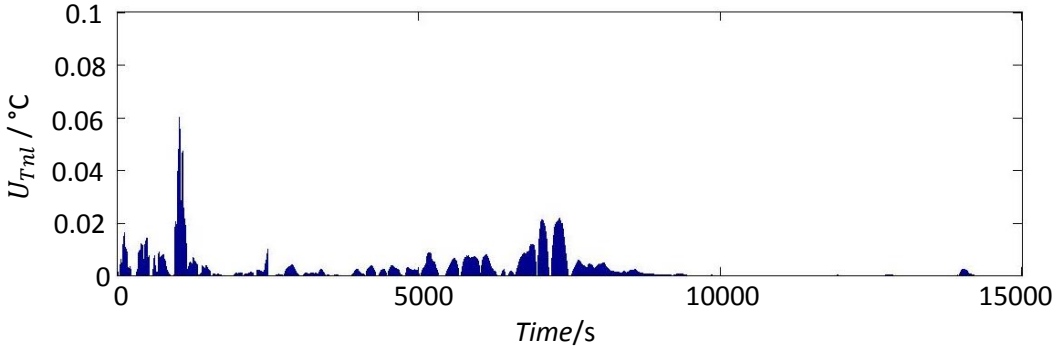

Figure 119: Uncertainty contribution of temperature non-linearity term

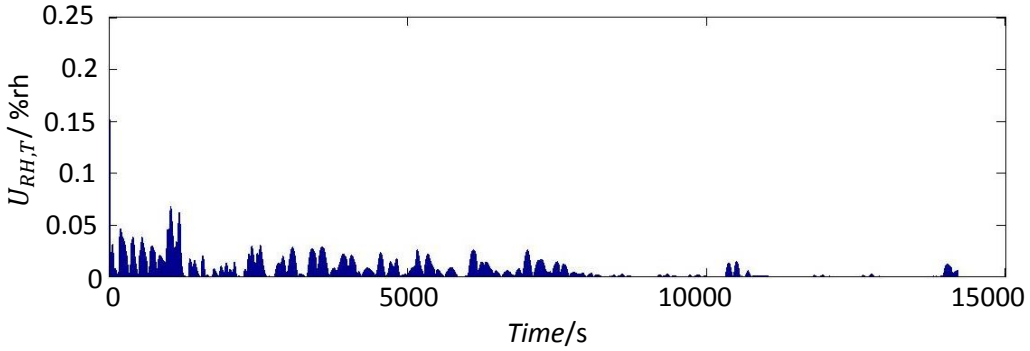

Figure 120: Total temperature contribution to the uncertainty of relative humidity measurement

3.3 Design and prototyping of a field humidity calibrator

In order to design a calibrator for a set of target specifications, this is crucial to design the calibrator considering different aspects including the kinetic and dynamic design of the system.

The kinetic design of the system is considered by obtaining the flow coefficients of valves, air passage channels and the pressure drop through the desiccant which has been evaluated by Ergun equation [71] and double checked by the CFD models. The CFD modeling shows relatively higher pressure drops than that of the Ergun equation. Thus, the values of the Ergun equation is corrected by about 30 % at the design stage. Ergun equation is given by,

$$\frac{dP}{dx} = \frac{150\mu\cdot\nu}{l^2} + \frac{1.75\cdot\rho_{air}\cdot\nu^2}{l}, \qquad (3\text{-}7)$$

in which the characteristic velocity is

$$\nu = \frac{\dot{M}_{air}}{\rho_{air}\cdot\varepsilon_{air}\cdot A_s}, \qquad (3\text{-}8)$$

and the characteristic length is

$$l = d_p\left(\frac{\varepsilon_v}{1-\varepsilon_v}\right), \qquad (3\text{-}9)$$

where $\dot{M}_{air}$ is the mass flow rate in kg/s, A_s is the cross section area of the bed in m^2, ε_v is the void fraction, ρ_{air} is the air density in Kg/m^3, μ is the air viscosity in Kg/m·s, and d_p is the effective particle diameter in meters.

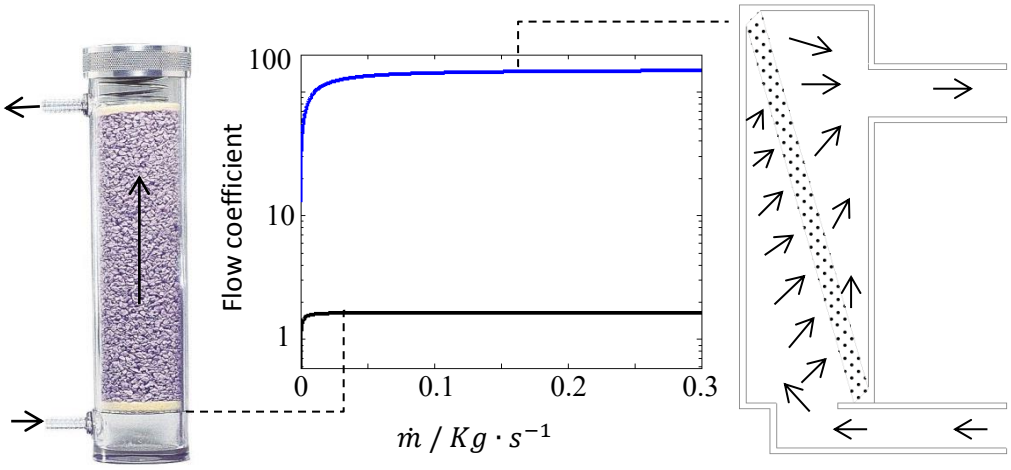

Figure 121: Dehumidifier design of the field humidity calibrator

By employing Equation (3-7) and ρ_{air} and μ values for the standard dry air, a typical silica gel diameter of 3 mm and the void fraction of 0.32 a first-order approximation of the pressure drop can be achieved. This is reported in Figure 121. Besides, the pressure drop is estimated using different geometries for air channels, by considering CFD models and valves by taking to account the values of the flow coefficients reported in the specifications. The schematic of the humidifier is also presented in Figure 122.

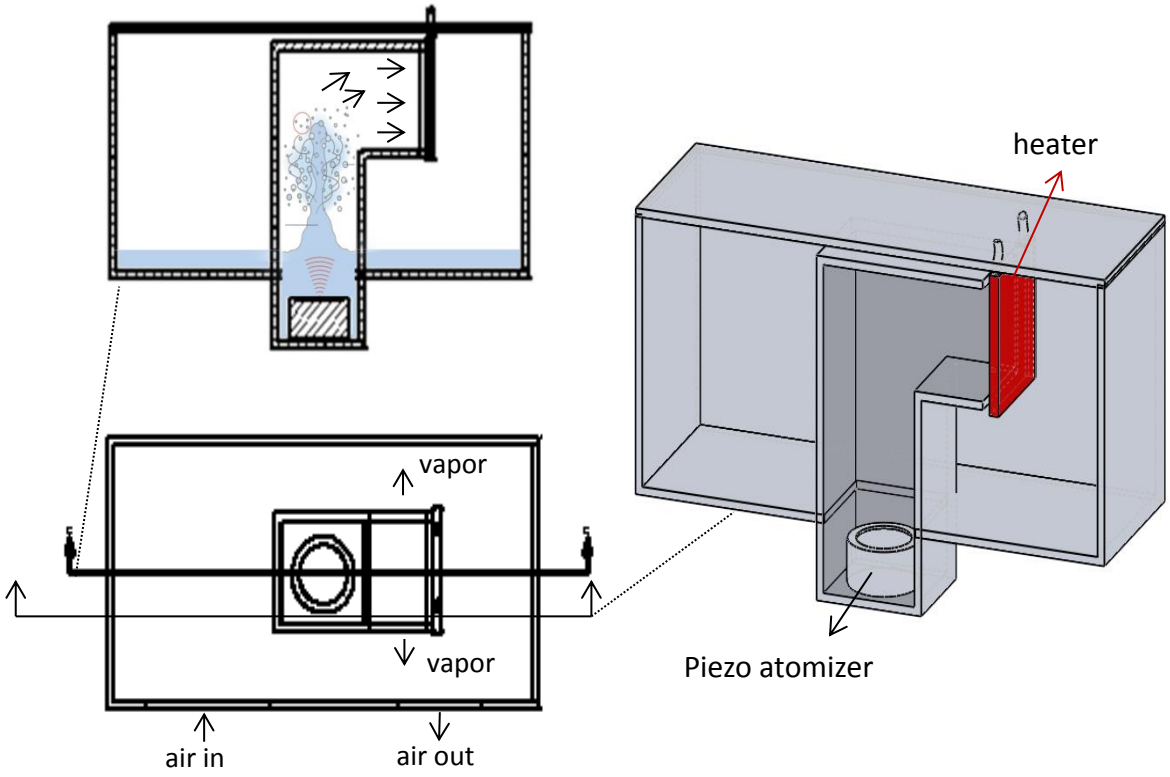

Figure 122: Humidifier design

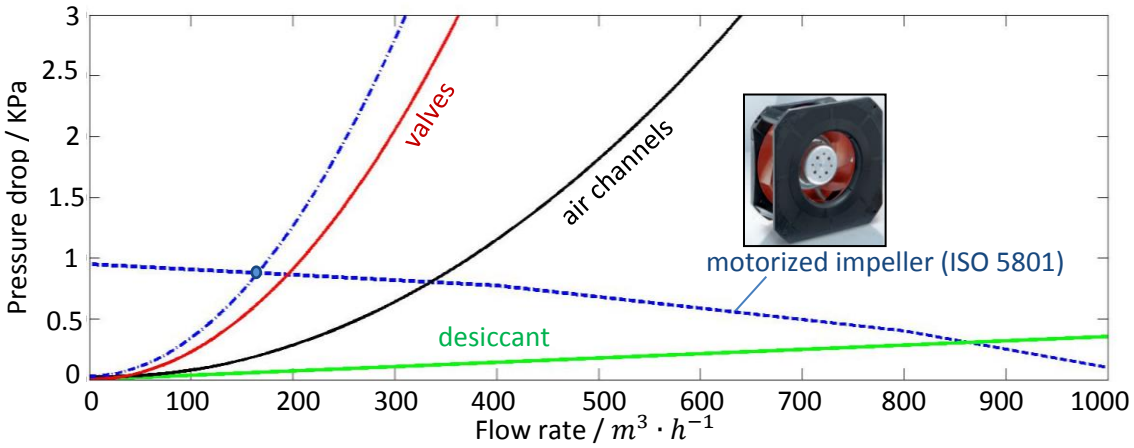

Figure 123: Design criteria, dashed line for the fan curve and dash-dot line for the total pressure drop of the system

The possibility of having different impellers has been studied and the best-fitted one resulted in the operation point of 2.7 m^3/min which guarantees a fast and homogeneous temperature and humidity changes. Accordingly, low pressure drop (i.e. below 900 Pa) gives the opportunity of having a light and cheap impeller, refer to Figure 123.

3.3.1 Dynamic design of the system

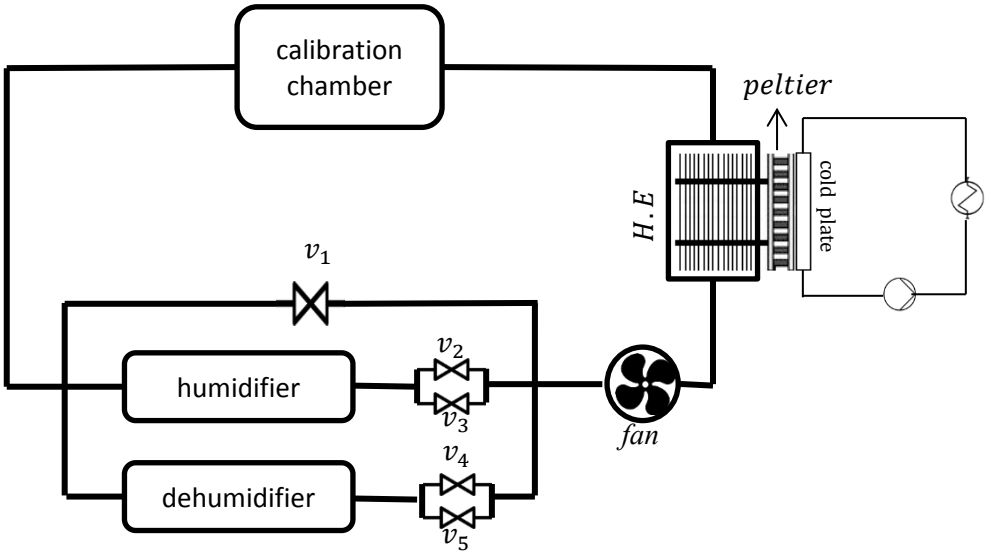

Figure 124: Working principle of the humidity calibrator

Considering the relative humidity of the calibration chamber, refer to Figure 124, at the time epoch t+Δt as the volumetric weighted average of the calibration chamber and the upstream relative humidity, i.e. Equation (3-10), and the time derivative of the relative humidity in the calibration chamber can be estimated by applying the definition in Equation (3-11) as

$$RH(\ t+\Delta t\ )=\frac{(V-Q_v\Delta t)RH+(Q_v\Delta t)RH_{up}}{V}, \quad (3\text{-}10)$$

$$\dot{RH} = \lim_{\Delta t\to 0}\frac{RH(t+\Delta t)-RH(t)}{\Delta t} = \frac{Q_v}{V}\left(RH_{UP}-RH(t)\right), \quad (3\text{-}11)$$

The integrator of the Equation (3-11) can be depicted in the form of a block diagram, see Figure 125, in which the flow rate of any valve, Q_v, is calculated for different combinations of the candidate valves and tabulated in Table 75

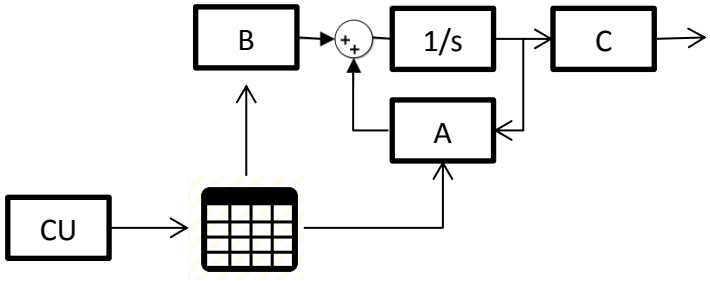

Figure 125: Block diagram of Equation (3-11).

A and B, as indicated in the block diagram, can be calculated by employing the equations

$$A=\frac{-Q_v}{V*3.6}, \quad (3\text{-}12)$$

$$B=\frac{RH_{up}*Q_v}{V*3.6}, \quad (3\text{-}13)$$

where Q_v is the flow rate through the valve, RH_{up} is the upstream relative humidity and V is the total air volume of the closed system.

Table 75: Valve positioning: -4 stands for maximum dehumidification and +4 stands for maximum humidification

Position of the valves	Qv of V_2 [m3/h]	Qv of V_3 [m3/h]	Qv of V_4 [m3/h]	Qv of V_5 [m3/h]
-4	28.18	0	0	0
-3	2.295	0.19	0	0
-2	2.295	0	0	0
-1	0	0.19	0	0
0	0	0	0	0
+1	0	0	0.19	0

+2	0	0	0	2.295
+3	0	0	0.19	2.295
+4	0	0	0	28.18

In order to design the controller, the first step is to identify the relative humidity sensors. The easiest way should be considered by monitoring the response of a sensor to a step input, i.e. a sudden stepwise change in the humidity, to obtain the constants of the transfer function and, consequently, poles of the system, e.g. Figure 126.

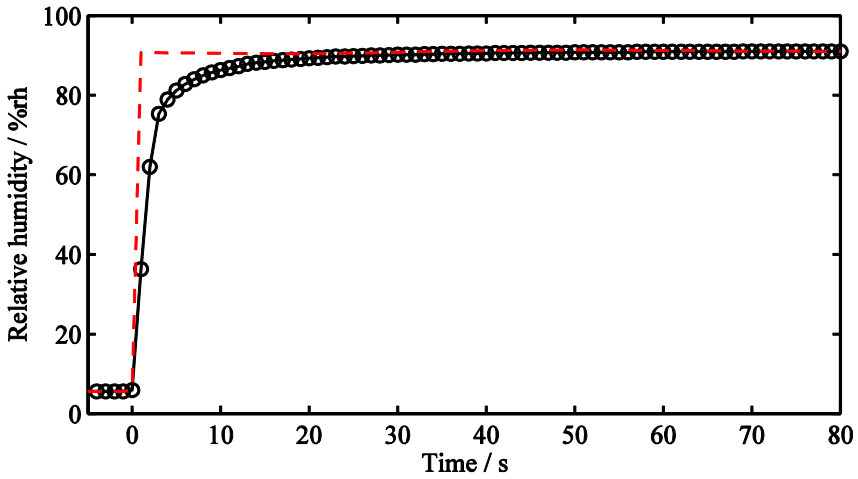

Figure 126: Example of the RH sensor response to the step changes of humidity, the input step is illustrated in red and the response signal in black.

Step response of four different capacitive relative humidity sensors are illustrated in Figure 127 and important fitted parameters are detailed in Table 76.

Table 76: Transient parameters of four capacitive relative humidity sensors under study.

	Rise time	Settling time	Z_1	Z_2	P_1	P_2
Sensor 1	14.148	87.13	10.05	-0.025	-0.36	-0.022
Sensor 2	13.9052	26.28	2.81	-0.0022	-0.162	-0.0022
Sensor 3	11.434	20.84	2.286	-4.115	-0.772	-0.203
Sensor 4	11.036	29.51	6.175	-0.114	-0.55	-0.087

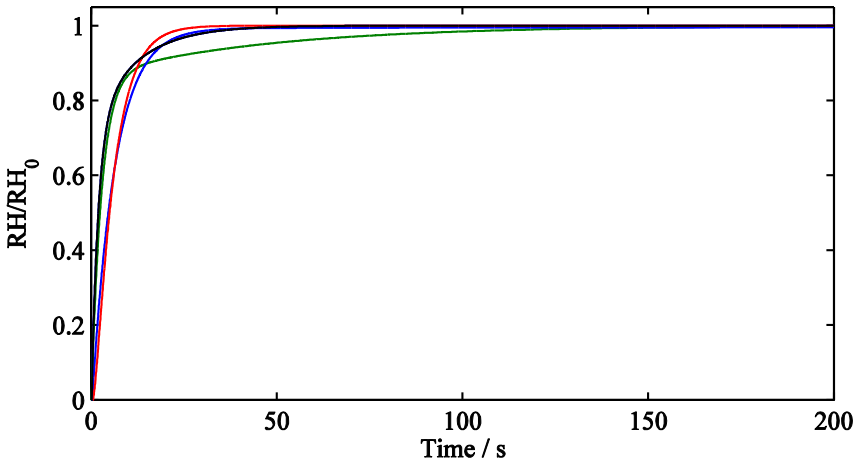

Figure 127: Step responses of four capacitive relative humidity sensors under study. Different colors stand for different sensors.

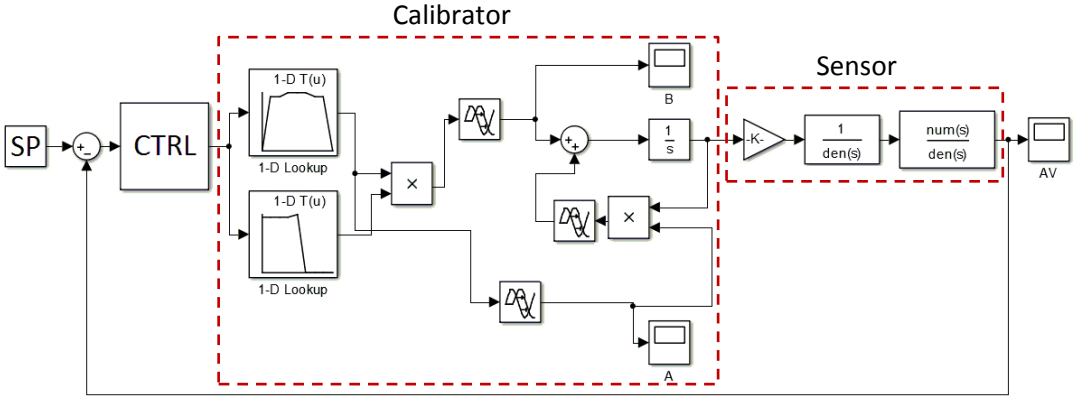

Figure 128: Block diagram of the system

In order to investigate the operation of the system at the design phase, this is necessary to evaluate the transfer function of the sensors, as already discussed above, followed by the block diagram of Figure 125. The transporting delay should also be considered according to the air velocity through the channels. Later, a numerical simulation, in the Laplace domain, can cast light to understand the problem in a more realistic way, refer to Figure 128. Likewise, an appropriate controller can also be designed and optimized to consider the operation of the system in a control loop. A few controllers have been investigated and the best controller turned to be a combination of different controllers (i.e. summation of a relay controller for significant differences of the actual value and the set-point, PID controller for the middle range and a D controller for deviations within the uncertainty levels.)

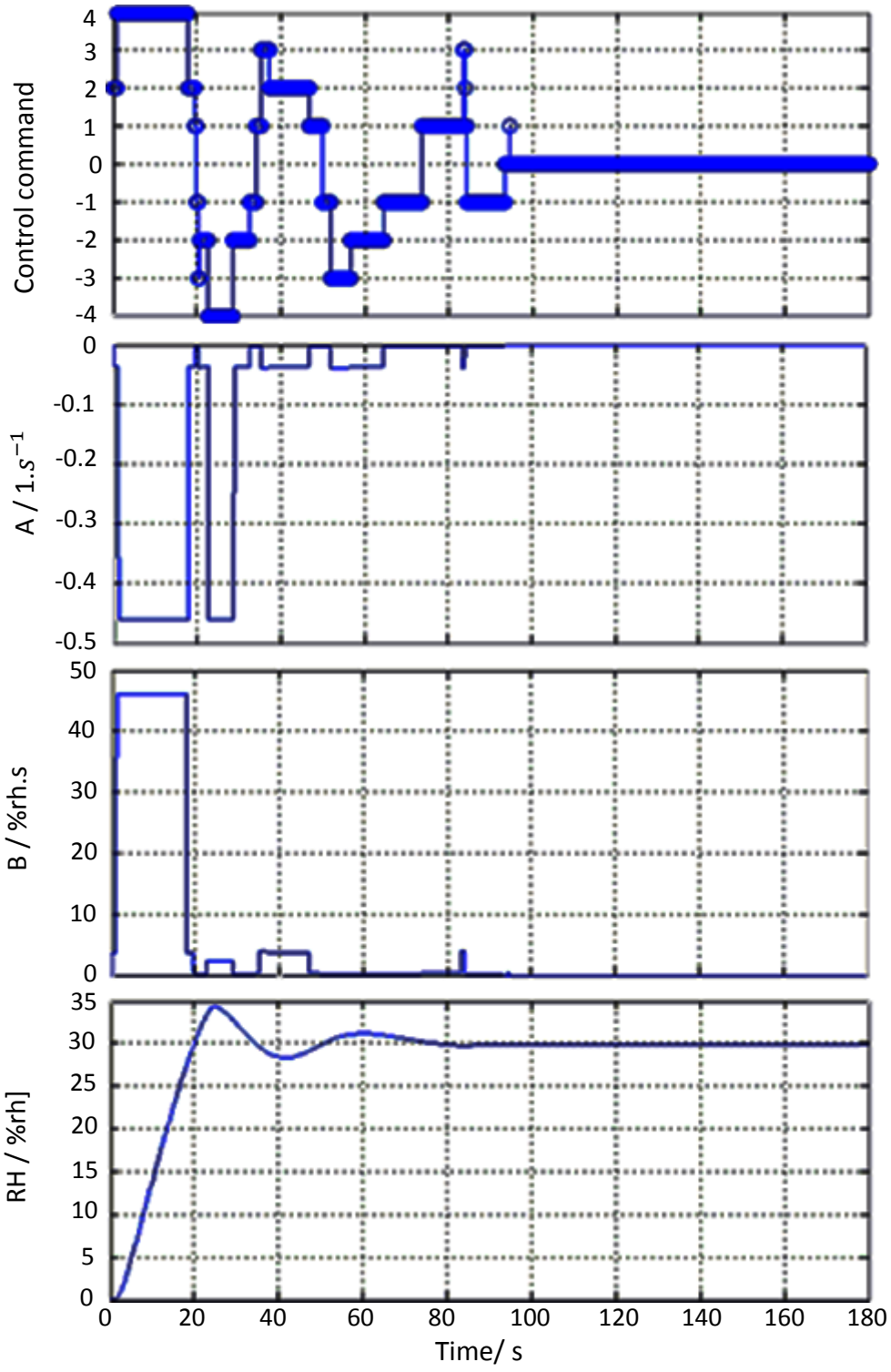

Figure 129: Operation of the system based on the Laplace-domain simulations

Figure 129 shows the numerical simulation of the controller. The command signals are sent from the controller to the actuators (i.e. valves and heaters) according to Table 75, i.e. an integer between -4 and +4. The A and B values are calculated by employing Equations (3-12) and (3-13) and, eventually, by solving the block diagram of Figure 130, the relative humidity inside the calibration chamber is estimated and depicted in the last part of Figure 131.

3.4 Conceptual prototyping

In order to prototype the calibrator with the lowest cost price, the geometrical design of the passages, as examined by CFD models, have been sized and manufactured out of Acrylonitrile Butadiene Styrene (ABS) and Polyvinyl Chloride (PVC). The gate-valve, i.e. v_1 in Figure 124, and the solenoid valves, i.e. v_2 to v_5 of the same figuer, has been chosen to assure the favorable flow coefficients which guarantee the target operation speed. Moreover, in order to control and stabilize the chamber temperature, a planar heat exchanger has been manufactured in copper and has been coated by chromium for corrosion resistance. The heat exchanger is integrated with a Peltier element which exchanges heat, from its other side, with a water cooling system through a copper-made cold plate. The most important elements are reported in Figure 130 and Figure 131.

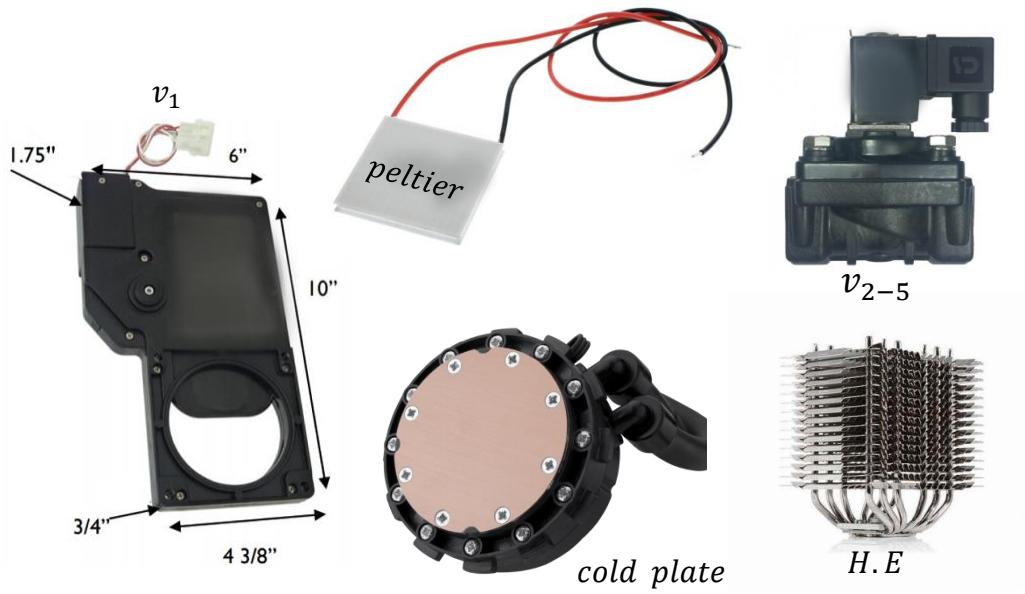

Figure 130: Prototype elements

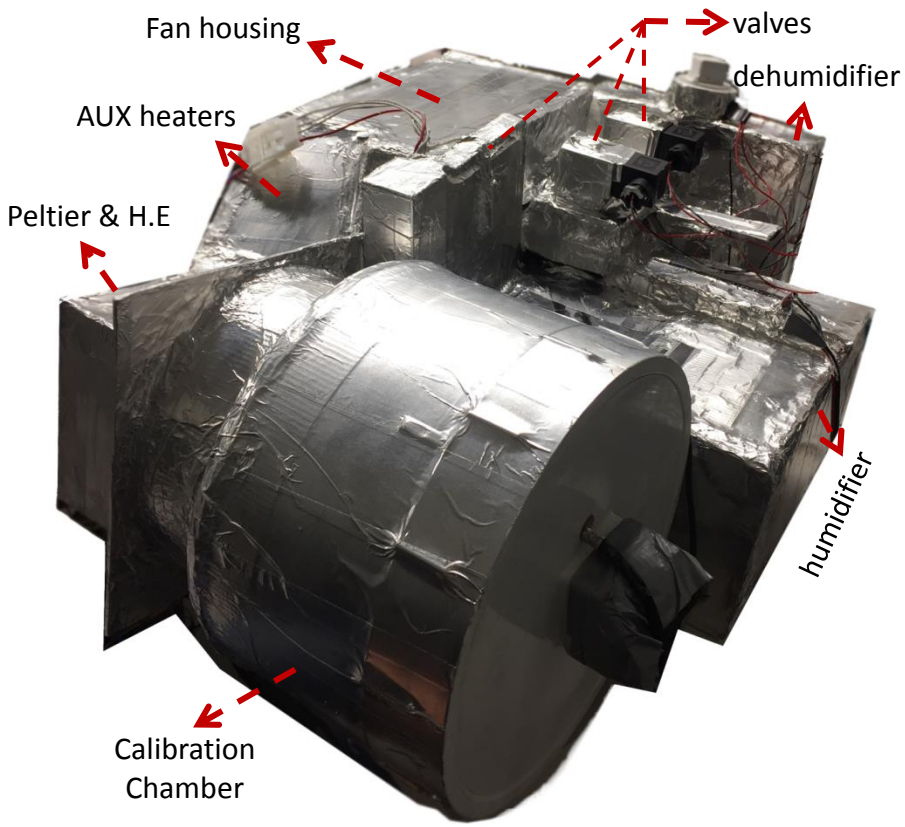

Figure 131: Calibrator prototype

The prototype has been tested and characterized by a capacitive relative humidity sensor. Figure 132 together with Figure 133 are examples of such investigation. This calibrator exhibits outstanding specifications beyond state of the art such as fast humidification and dehumidification rates of about 60 %rh·min^{-1} and relative stability of about 0.8 %. Table 77 details a list of specifications and compares them over the most similar one in the market as reported in its specifications.

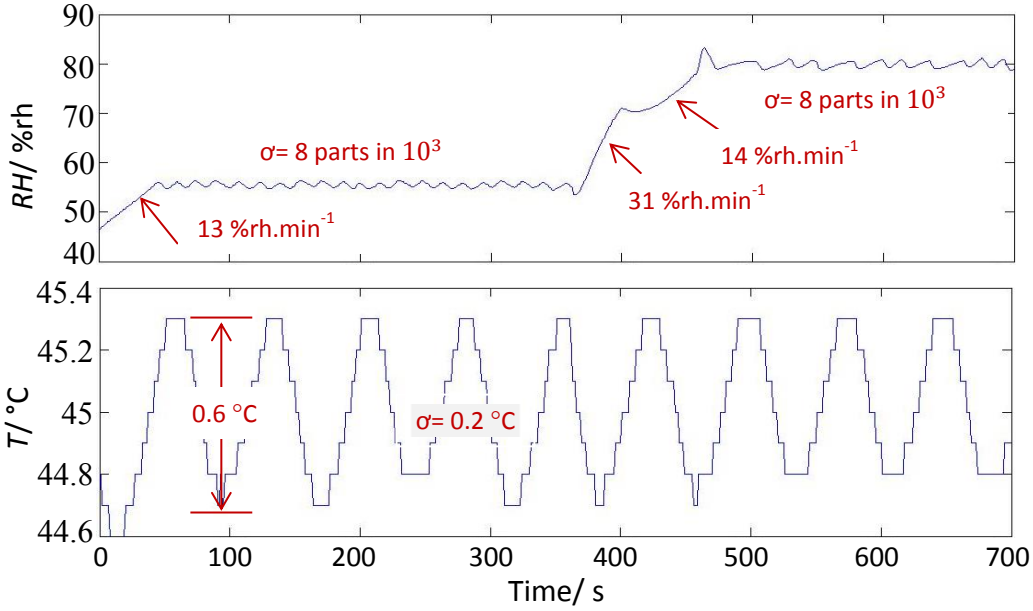

Figure 132: Stability and rate of changes

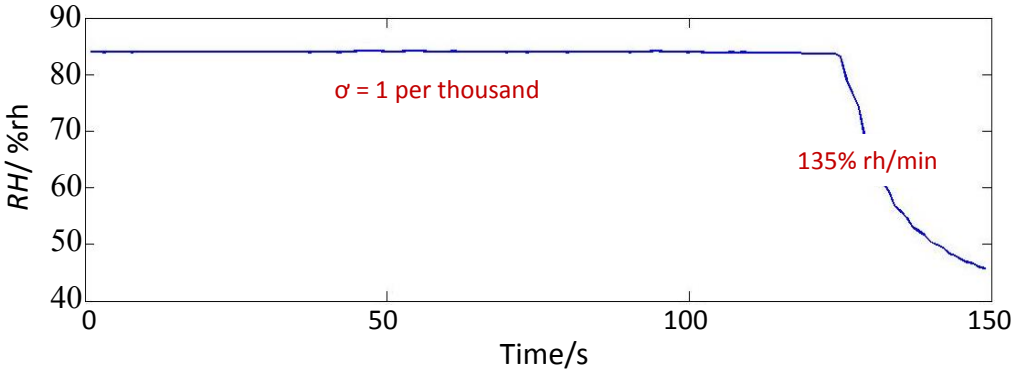

Figure 133: Operation of the calibrator

Table 77: Specifications of the calibrator

	SoA in the market [72]	**This work**
Cooling rate	1.5 °C/min (Typical)	1.5 to 2.2 °C /min
Heating rate	10 °C /min (Typical)	10 °C /min (Avg)
Dehumidification rate	5 % rh/min (Typical)	60% rh/min(Avg)
Humidification rate	10 % rh/min (Typical)	63 % rh/min(Avg)
Max T_{dp}	32 °C	59 °C
Min T_{dp}	Not reported	3 °C
RH time stability	2-7% of Reading	0.8% of Reading
T time stability	1% of Reading	0.4% of Reading

3.5 Results

3.5.1 Calibration at lower temperatures

The prototype of Sec.3.4 has been used to calibrate a relative humidity sensor against a calibrated reference capacitive RH sensor. The calibrant and the reference, despite having the same brand, have very different time constants causing different transient behaviors. In order to cope with this issue, the data should be analyzed according to the theories developed in Sec.3.2. Obviously, the uncertainty associated with each point is not only affecting the calibration uncertainty, but also the calibration correction.

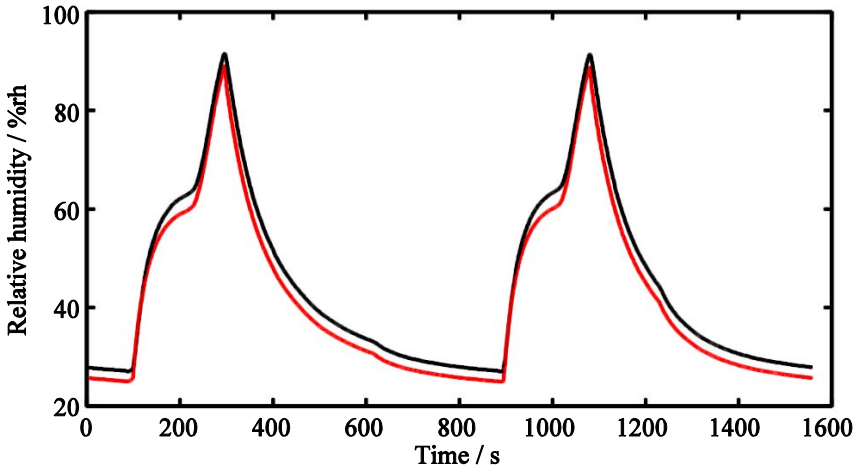

Figure 134: Humidity profile, reference in black and calibrant in red

Considering the first time derivative of the signals, by employing Equation (3-4-3), the time delay between the sensors is achievable having a type-B uncertainty of the transient parameters. Time-delay uncertainty contribution, according to Figure 134, is reported in Figure 135.

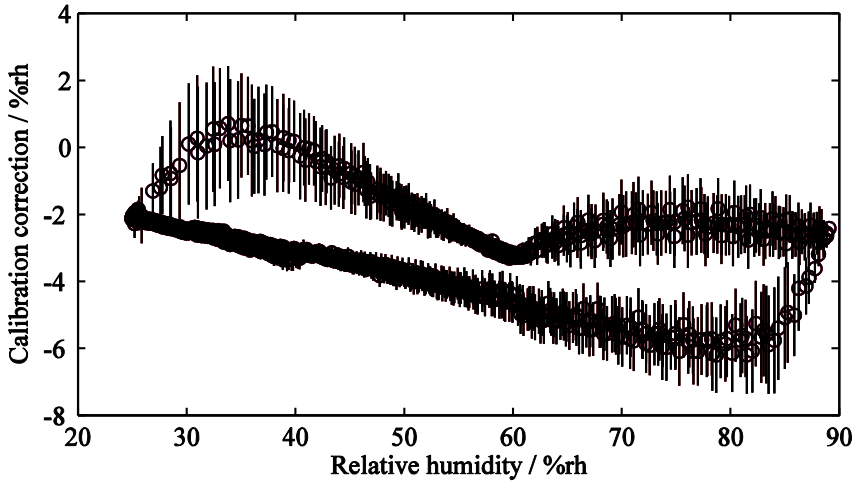

Figure 135: Calibration by comparison of points, error bars are indicative of the uncertainty contribution of the Time delay

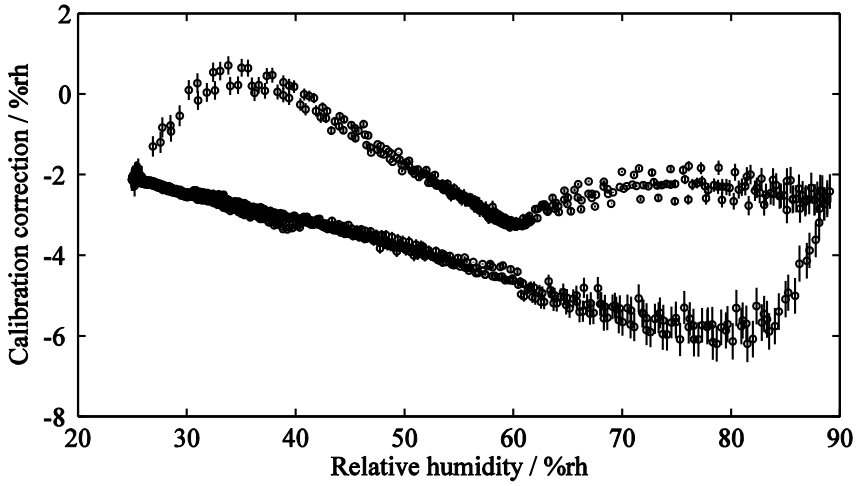

Figure 136: Calibration by comparison of points, error bars are indicative of the uncertainty contribution of the profile non-linearity

Non-linearity of any profile is contributing to the uncertainty budget which is estimated by calculating the slope deviations, refer to page 98, by substituting these deviations in Equations (3-4-1) and (3-4-2) and accumulating them over the time, the non-linearity uncertainty contributions are calculated and reported in Figure 136.

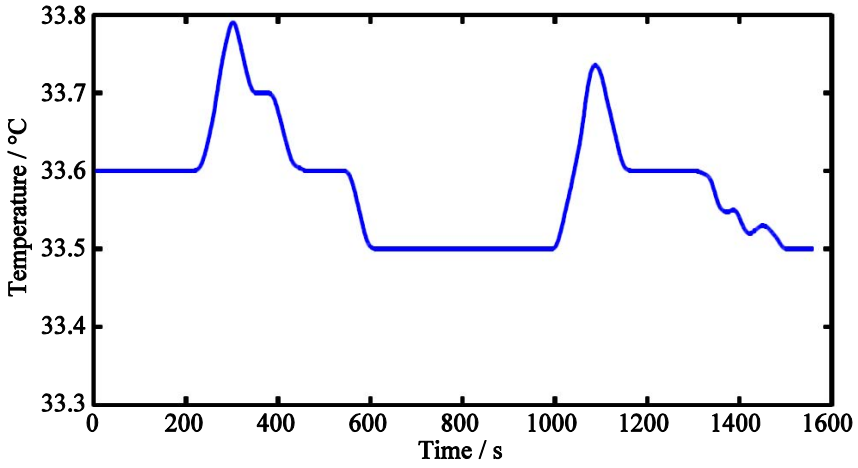

Figure 137: Temperature profile

The temperature non-stability is also contributing to the uncertainty budget, mainly because the temperature compensation of the relative humidity is performed by a value which differs with the real one. In order to estimate these contributions, the temperature profile of Figure 137 should, firstly, be split into the ramps. Later, the time delay and non-linearity effects should be considered by employing Equations (3-4-1) to (3-4-3) and considering the typical time constants of the embedded temperature sensors. Eventually, the temperature uncertainty terms should be converted into the humidity uncertainty terms having

the sensitivity analysis of the temperature correction formula of the DUC (i.e. Figure 138).

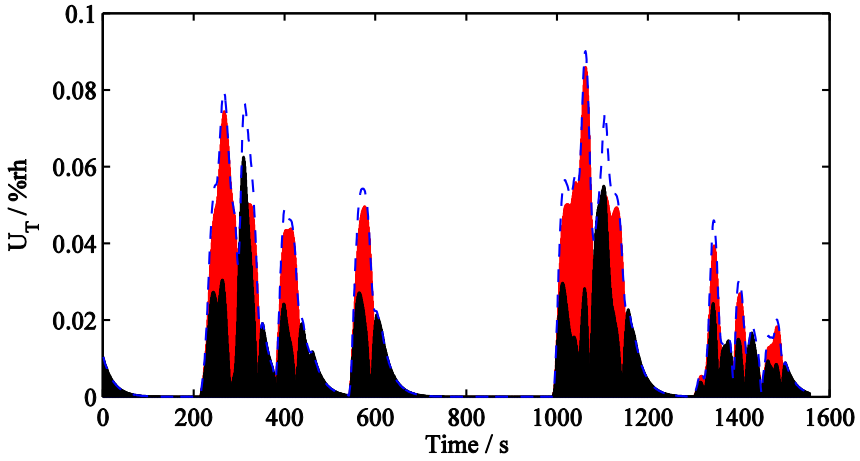

Figure 138: Temperature contribution to the uncertainty, red stands for the time delay, black for the nonlinearity and dashed-line for the overall contribution

Additional calibration information can be extracted by the comparison of slopes, as already discussed by Equation (3-6), the non-linearity uncertainty contribution of these points should be taken into account by ${P_1}^{c,r} \cdot y_1^{c,r}(Y^{c,r}/\dot{Y}^{c,r})$ and ${P_2}^{c,r} \cdot y_2^{c,r}(Y^{c,r}/\dot{Y}^{c,r})$, such elaboration is detailed in Figure 139. The time delay contribution in this case will be zero and it can mitigate the uncertainty levels, especially, in the presence of the sharp ramps. However, the differentiation uncertainty contribution should be estimated by considering the fitting mean squared error of the first order polynomial. The fitting has included the data starting from three time epochs before the point and ending at three time epochs after the point under study. This uncertainty contribution, i.e. the line's slope fitting uncertainty in practice, is reported in Figure 140.

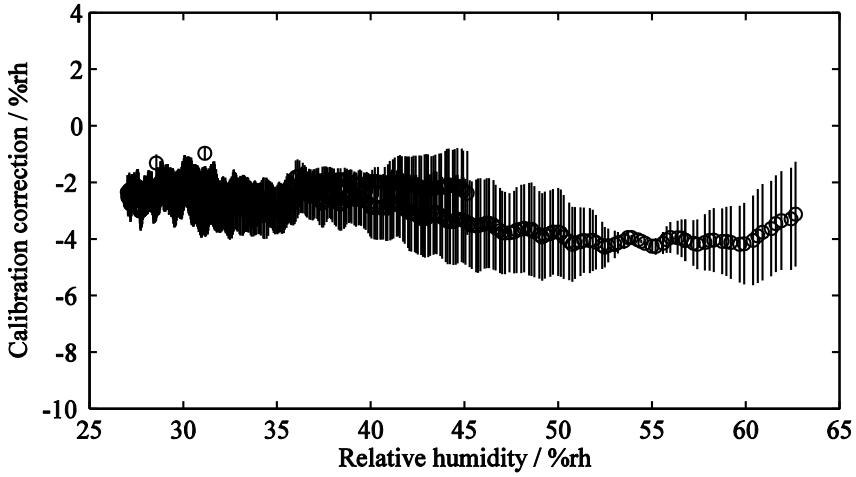

Figure 139: Non-linearity uncertainty contribution by exploiting the comparison of slopes

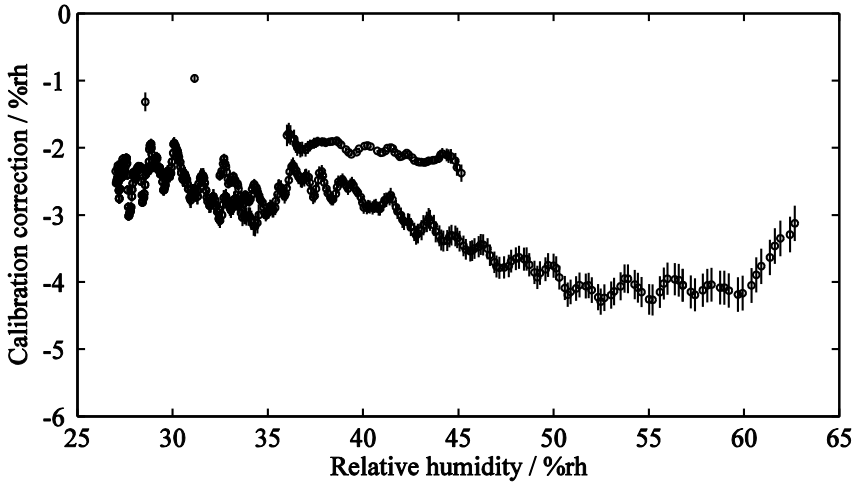

Figure 140: Calibration by comparison of slopes, error bars are indicative of the uncertainty contribution of the differentiation

As a final stage, the uncertainty of each point should be combined by the law of propagation of the uncertainty. These results yield different PDFs that should be collected in different sets. For instance, one can cluster the PDFs which belong to the range between two successive integer numbers (e.g. 23 %rh and 24 %rh). This is worth mentioning that sequential epochs exhibit similar PDFs and, since they are not providing additional information, they cannot be used for the data fusion. On the other hand, by switching the positive slopes to negative slopes, or by switching from comparison of points to comparison of slopes, independent PDFs can be obtained and, later, be employed for the data fusion.

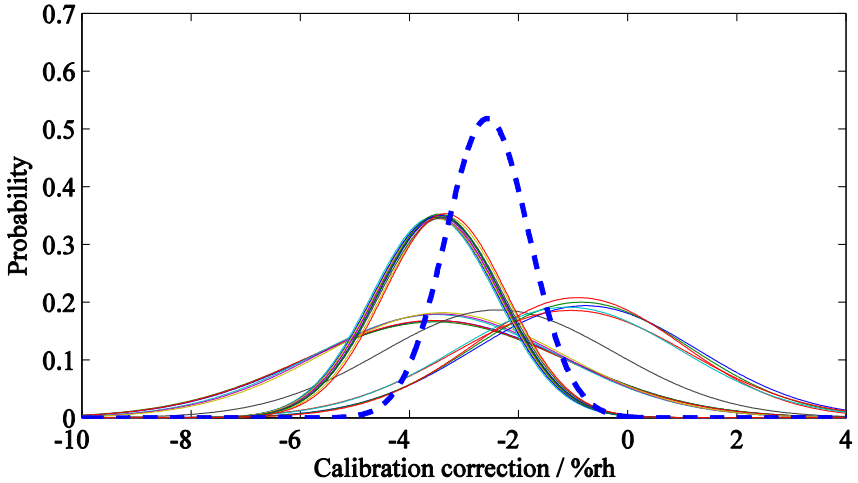

Figure 141: Example of the data fusion, solid lines for individual PDFs and dashed line for the result

The data reduction, as illustrated in Figure 141, consists of five main steps:

- Averaging the input PDFs of the same group (i.e. sequential epochs)
- Allocate an interval of interest (e.g. -10 %rh to +4 %rh)
- Discretize each input PDF, a typical grid should be 0.01 %rh
- Take the product of each input PDF

- Normalize the output PDF and calculate the best estimate and the confidence interval

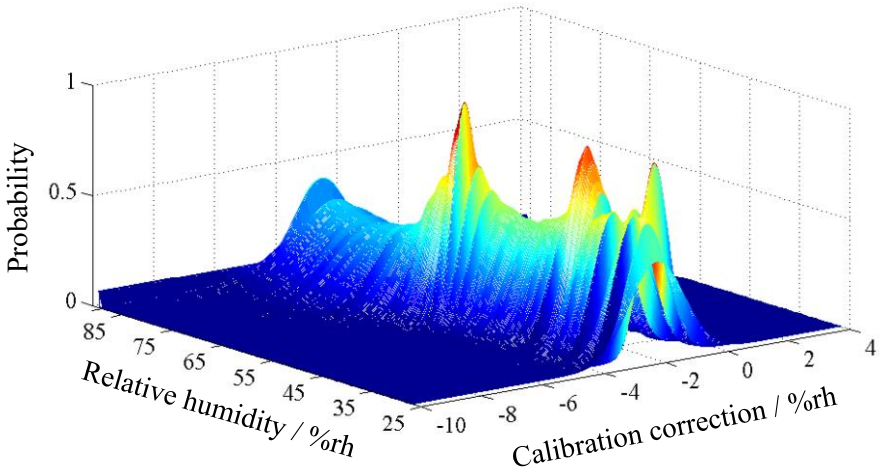

Figure 142: Data fusion along the calibration range

By merging the chain of PDFs along the entire range of calibration, a three-dimensional probability is calculated and illustrated in Figure 142. Thus, the best estimate and confidence interval can be obtained as continuous curves.

Figure 143 reports the calibration corrections, comparison of points in red and comparison of slopes in black, vertical lines are indicative of the expanded uncertainty and circles stand for the best estimates. Eventually, the final result of this calibration, as estimated by the data fusion of each point, and its confidence interval is depicted in blue.

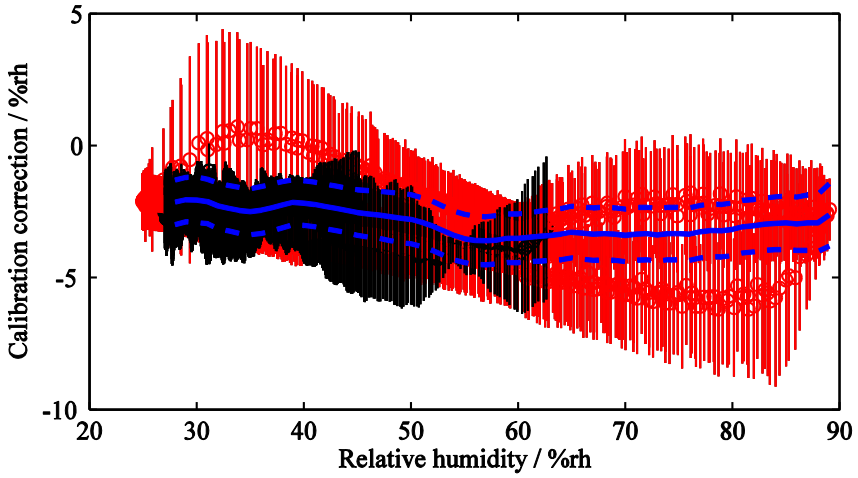

Figure 143: Non-static calibration results of RH sensors. Red stands for comparison of points, black for comparison of slopes and blue for the final results. Dashed lines are indicative of the confidence interval.

3.5.2 Calibration at higher temperatures

The same relative humidity sensors of Sec.2.6.3 have been used for non-static calibrations using the generator of Sec.2.2. The temperature is fixed at $T = 115$ °C

and the dew-point is changing proportional to the time from -15 °C to 99.7 °C at 140 kPa. The humidity profile, as plotted in Figure 144, reports the humidity changes for 7 cycles. The humidity changing rate differs from 0.06 %rh.s^{-1} (i.e. cycle 3) to 1 %rh.s^{-1} (i.e. cycle 7). This is worth mentioning that faster ramps, even if practically possible for the generator, yield to unacceptable uncertainty levels and are not recommended

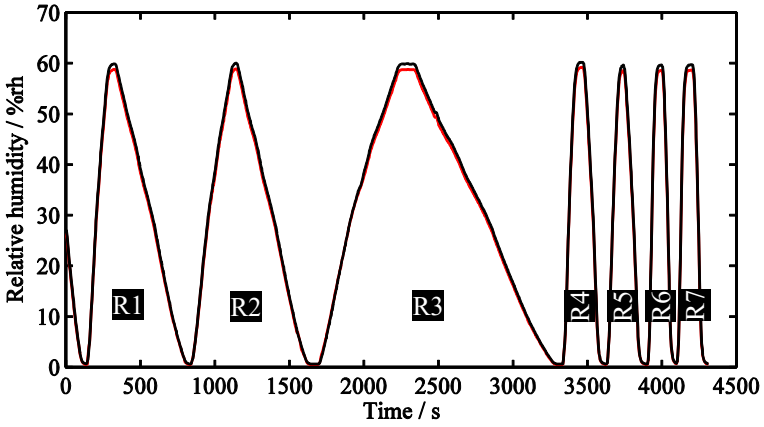

Figure 144: Humidity profile at 140 kPa and 115 °C

By following a similar approach, calibration correction points have been calculated. The data reduction procedure provides the calibration line and the confidence intervals. The black solid circles are the results of static calibration and, as it is evident in Figure 145, are in a fairly good agreement with the non-static calibration line.

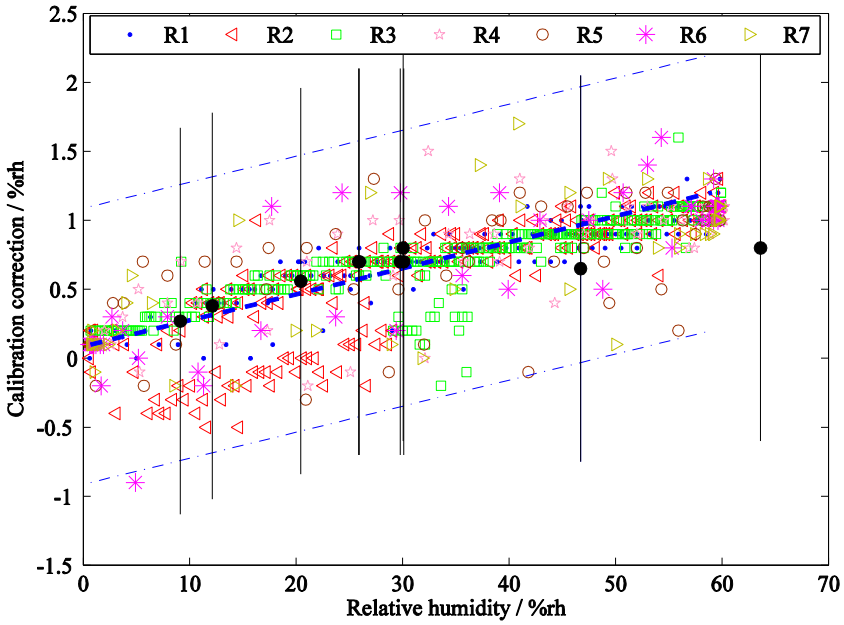

Figure 145: Calibration line, different symbols stand for different ramps and black circles for steady-state calibrations. The dashed blue line indicate the confidence interval of the non-static calibration (k=2) and error bars are the expanded uncertainty of the steady-state calibrations.

3.5.3 Calibration at dew-points above 100 °C

By increasing the chamber pressure to 600 kPa this is possible to have very high dew-point temperatures. In this section, this is aimed to see whether single ramps are trustable for RH sensor calibrations for the sake of time and simplicity. The calibration correction and associated uncertainties can be obtained by having a stable chamber temperature at 140 °C and decreasing the dew-point temperature proportionally from 138 °C down to 46 °C and elaborating the data. These results are depicted in Figure 146 in which comparison of slopes are in blue and comparison of points are in red, in addition, outputs of the data fusion, refer to page114, are plotted in green.

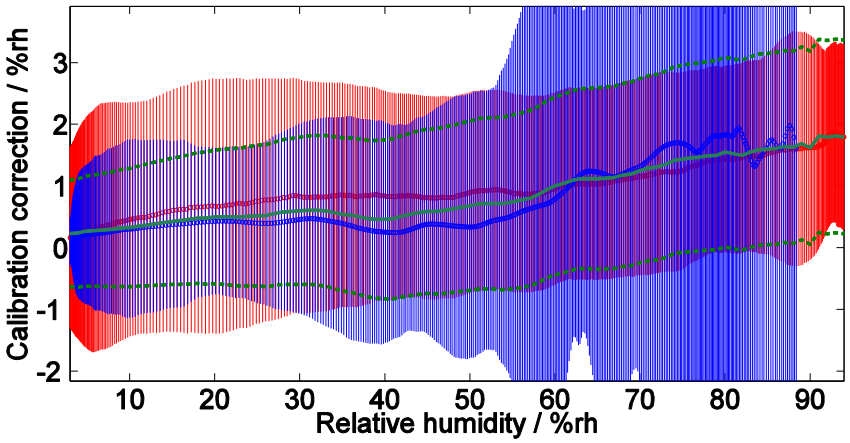

Figure 146: Non-static calibration of RH sensors using a single ramp at 140 °C, red bars for the expanded uncertainty of calibration by comparison of points and blue for comparison of slopes, final calibration curve in solid green and confidence interval in dashed green.

In order to check the validity of the calibration curve of the previous figure, another ramp, with the average slope of +0.75 %rh.s^{-1}, has been studied. The humidity profile is depicted in Figure 147 in which the dew-point temperature starts from 34 °C and increases up to 140 °C.

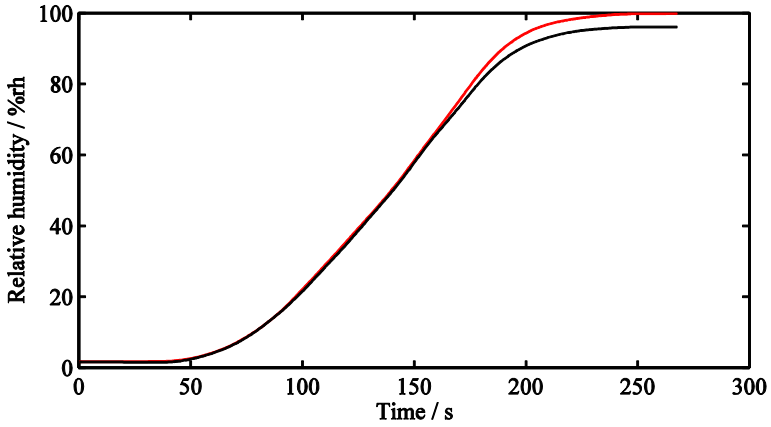

Figure 147: Humidity ramp up to dew-point temperature of 140 °C, reference in black and calibrant in red

Figure 148 compares the results of Figure 146 with the new results obtained from Figure 147, in which a fairly good agreement is evident in the range lower

than 70 %rh and small discrepancies in the higher range, however, the deviation is within the uncertainty. This is noticeable that sensors exhibit, considerably, high reproducibility values and this is the main reason for the deviations. The results of steady-state calibrations lie in the middle of the confidence interval.

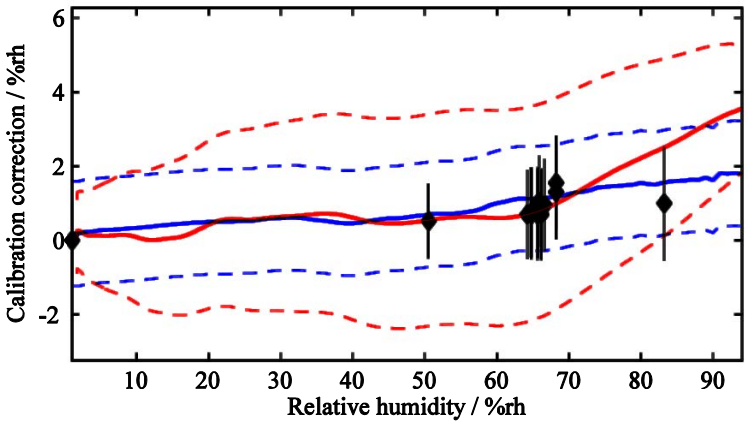

Figure 148: Comparison of two non-static calibration curves against the steady-state calibrations, black diamonds for the steady-state calibrations, error bar for expanded uncertainty and dashed lines for non-static calibration confidence intervals.

3.5.4 Calibration at the extreme conditions

By increasing the temperature to 170 °C, and pressure at 600 kPa, and by changing the dew-point temperature from zero to 130 °C, this is possible to cover the main range of interest for industrial dryers. Figure 149 summarizes the calibration corrections and highlights a fairly good agreement between non-static measurements and that of the steady-state. The probability density function along the calibration range is also illustrated in Figure 150.

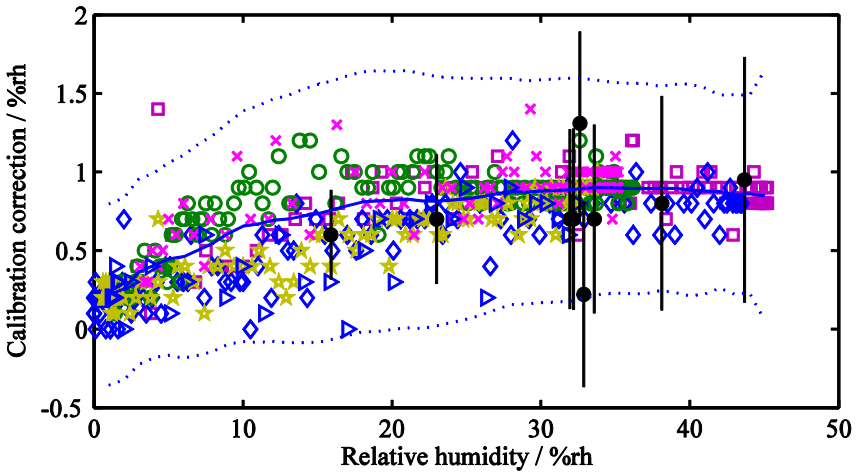

Figure 149: Calibration of RH sensors by employing multiple ramps, different symbols stand for different ramps and black circles for steady-state calibrations, error bars show the expanded uncertainty (k=2) and dashed line the confidence interval.

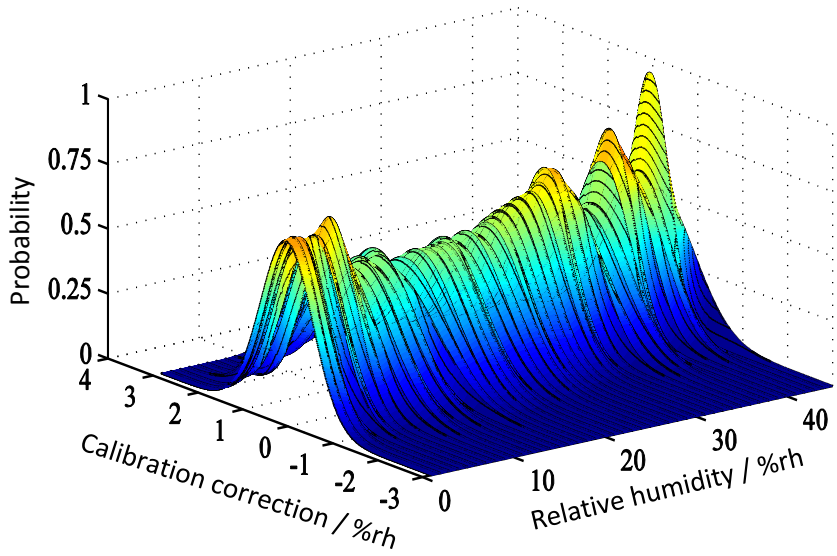

Figure 150: Probability density function along the calibration range

3.6 Two-dimensional calibration

Based on the theories developed at Sec.3.2.2, the simultaneous change of temperature and humidity became possible during the calibration. In order to examine the theory, the calibrator of Sec.3.4 has been exploited to generate randomly-shaped profiles covering the range of interest for humidity and temperature. Figure 151 and Figure 152 are illustrating the humidity and temperature profiles respectively.

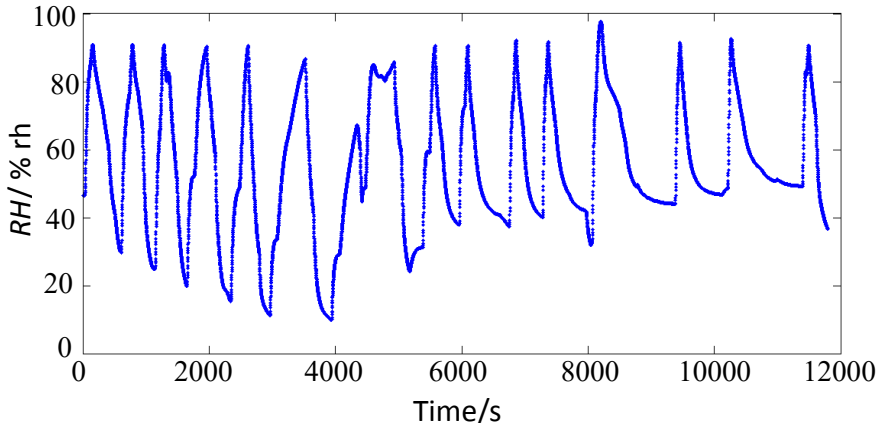

Figure 151: Randomly-shaped humidity profile

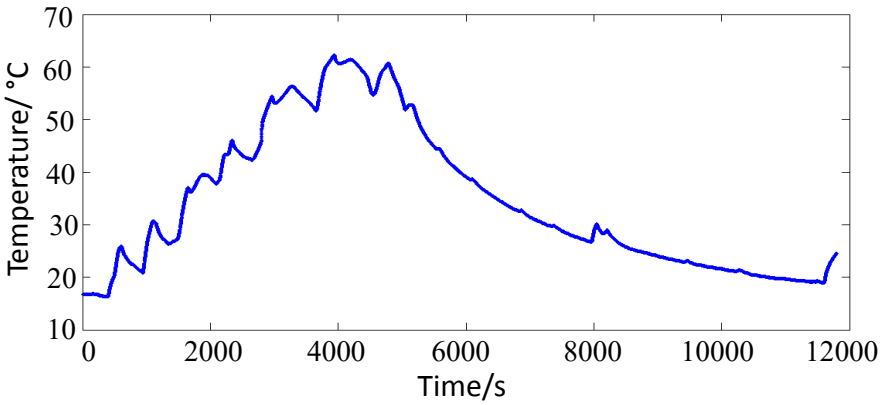

Figure 152: Randomly-shaped temperature profile

By considering the calibration correction by comparison of points, as well as, comparison of slopes, and weight them by their inverted variance, the most probable plane can be determined. This method has been double checked with a three-dimensional data fusion of page115. And the deviation between the two methods remains negligible. This plane has been illustrated in Figure 153 together with the calibration points. This is noticeable that the gap between the points and the plane is within the expanded uncertainty levels. The uncertainty bars are not reported for the sake of visualization; meanwhile, expanded uncertainty of the calibration correction points are illustrated in Figure 154. From the graph, this is observable that the comparison of the slopes provides much lower expanded uncertainty levels in contrast with that of the comparison of points. The main reason for this superiority is mainly due to the reproducibility of the capacitive relative humidity sensors which can be neglected in the second case.

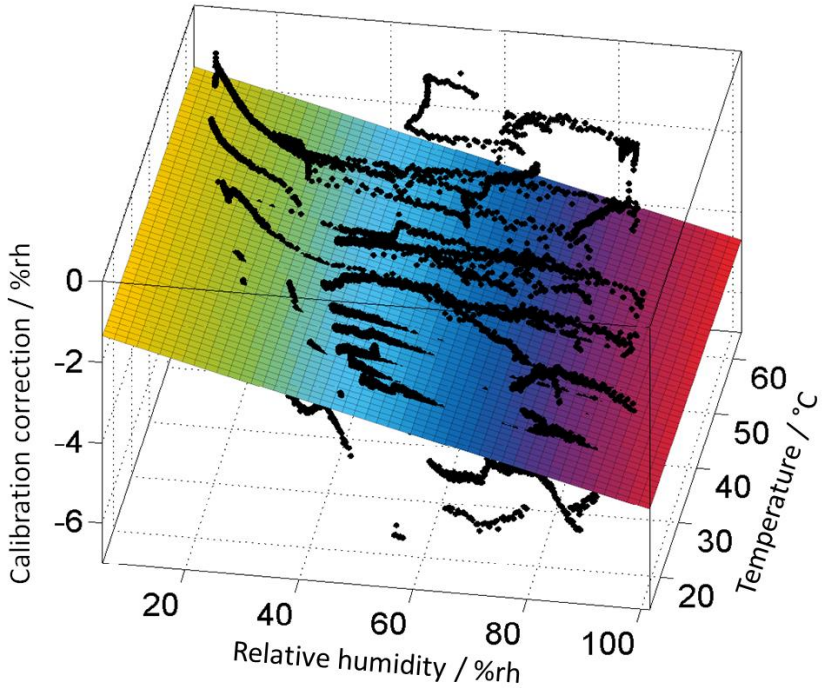

Figure 153: Calibration plane

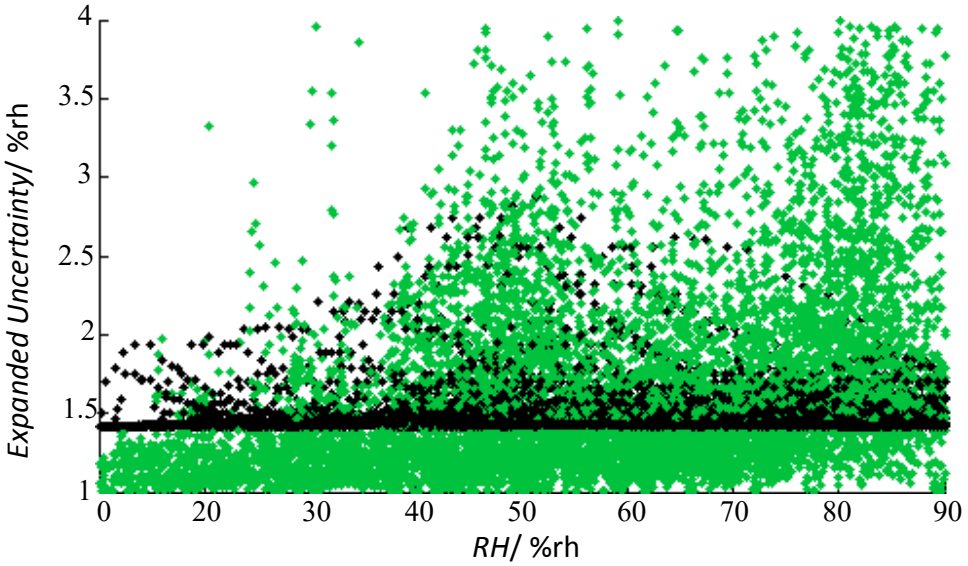

Figure 154: Uncertainty of each point, black stands for comparison of points and green stands for the comparison of the slopes

Taking into account the result of Figure 153, the two-dimensional calibration map can be reported as the final calibration correction of the entire range. From this graph, we can note that the calibration correction depends gently on the temperature, which may differ from a case to the other. Finally, the expanded uncertainty map can be examined by considering the uncertainty of each point and the local fitting residuals. This has been calculated and summarized in Figure 155.

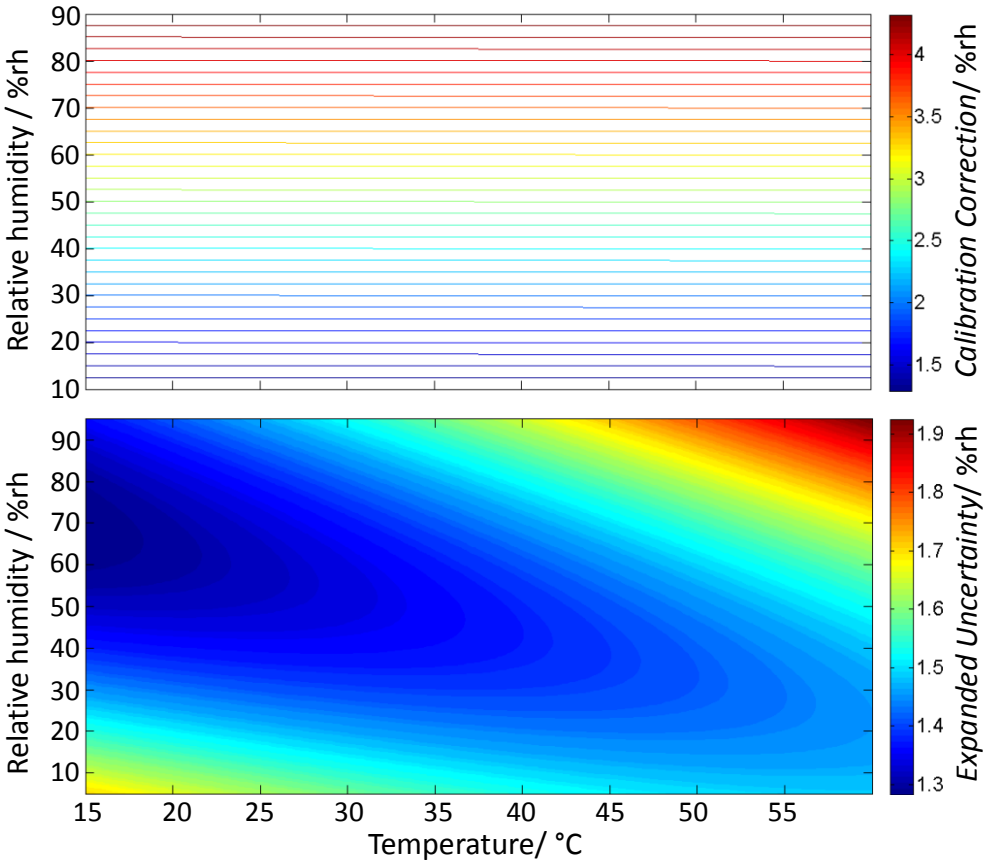

Figure 155: 2D calibration results and its expanded uncertainty

The two RH sensors are from the same manufacturer and they exhibit similar temperature dependency; therefore, the temperature dependence of the RH calibration corrections contributes negligibly to the calibration by comparison. However, the current method is able to consider the contribution in the case of its presence.

3.7 Concluding remarks

This chapter has investigated the possibility of the non-static calibration for RH sensors based on Laplace-domain studies as well as addressing a method to elaborate the data and extract the calibration correction and associate its uncertainty. The method has been founded on the response of the sensor to an ideal ramp and, later, has been generalized to any arbitrary profile.

Different sources of the uncertainty have been discussed step-by-step for several non-static calibrations under different conditions and in different ranges. A data fusion technique has been introduced to single out the calibration correction and the associated confidence interval. Results show a fairly good agreement between this method and the conventional method under steady state conditions. In addition, this method has also been adopted for two-dimensional calibrations.

In order to examine the theory, an in-situ humidity calibrator has been designed, simulated, optimized and conceptually prototyped. The prototype exhibits unique features, especially, in humidification and dehumidification rates, i.e. roughly 1 %rh.s^{-1}. This field humidity calibrator has been employed to perform a set of calibration in this chapter.

Chapter 4

A Neural Network-based Uncertainty Algorithm

The statistical simulation of the probability density functions and their propagation through the mathematical models turned to be a widely-accepted method and is recommended by the first Supplement of the guide to the expression of uncertainty in measurement (GUM) in which propagation of distributions using a Monte-Carlo method (MCM) has been discussed [33]. These simulations can cast light in cases in which the linearization is inadequate and/or the PDFs differ from the Gaussian distribution. Likewise, they can validate the uncertainty assessments employed by GUM uncertainty framework (GUF) and remain trustable also in the case of deviations. However, a good MCM is achievable, typically, when it relies on a few million points causing a slow operation in the case of having mathematically expensive models. This chapter is aimed to introduce a general purpose uncertainty algorithm that guarantees the same results of adaptive Monte-Carlo method (AMCM) with much higher efficiency. The conceptual idea, mathematical derivation, algorithm, software implementation, test and validation of the NNUA has been performed by the author.

4.1 Theory

Neural Network-based Uncertainty Algorithm (NNUA) is an iterative algorithm aimed at propagating uncertainty and/or Probability Density Functions in Multi Input Multi Output nonlinear mathematical models and this is of greater value when the computation cost is relatively high. This is worth mentioning that any mathematical model can be employed by this algorithm. Moreover, this could be easily applied when an explicit form of a mathematical model is not available or when the measurements are interpreted in a procedure and the evaluation of a mathematical model is time-consuming.

NNUA consists of three main steps:

Step I: to generate uniformly distributed random (i.e. practically pseudo-random) samples in the range $\pm\bar{k}\sigma$ applied for each input variable. Followed by substitution in the mathematical model to have the target sets allocated to each output variable. The extreme points of the range are added to have a symmetric set which yields to a better mapping in the next step. The sample sets are

extremely smaller than the sample size needed for MCM. This is worth noticing that the training interval $\overline{k}$, is not necessarily equal to the coverage factor (i.e. indicated by k) and the recommended value is 10 which helps to simplify equation X in step III.

Step II: Artificial Neural Network training using the data sets of step-I. The ANN is architected with I_n input nodes, one hidden layer of H_n nodes with a tangent hyperbolic function and O_n output nodes. Input data sets are linearly mapped to the ±1 interval. Thanks to the data sampling strategy, the best estimate and variance could be expressed as,

$$\mathrm{E}[\bar{I}_n] = 0, \qquad (4\text{-}1)$$

and,

$$\mathrm{E}[\bar{I}_n{}^2] = (\frac{1}{\bar{k}})^2, \qquad (4\text{-}2)$$

where $\bar{I}_n$ is the n^{th} mapped input.

The ANN is trained based on the Levenberg-Marquardt back-propagation algorithm that employs the Jacobian matrix of errors with respect to the weights and biases and is computationally efficient and straightforward. As a final stage of this step the ANN should be validated in a more rigorous way than the typical validation of neural networks. A new set of input and target points are generated as described in step-I to check the error level, the mean squared errors and the variance of errors are calculated and compared to the numerical tolerance D, i.e. Equation (4-3), which guarantees the required number of significant digits,

$$\mathrm{D} = \frac{10^{-2(\mathrm{N_d}+2.3979)}}{4\cdot\bar{d}}, \qquad (4\text{-}3)$$

where $N_d$is the required number of significant digits and $\bar{d}$ is the tolerance divisor.

Step III- Sensitivity analysis of the ANN and estimating the output variances.

The first derivative of O_{ml} with respect to $n_l{}^{th}$ mapped input at $\bar{I}$ could be written as,

$$O^{(n_1,m_1)} = \Delta\mathrm{T}\sum_{n=1}^{H_n} 4a^{(n1,m1)} \odot \mathrm{Z} \oslash (Z+1)^{\odot 2}, \qquad (4\text{-}4)$$

the second derivative of O_{ml} with respect to n_1 and n_2 at $\bar{I}$,

$$O^{([n_1,n2],m_1)} = \Delta\mathrm{T}\sum_{n=1}^{H_n} 8b^{([n1,n2],m1)} \odot (2Z^{\odot 2} \oslash (Z+1)^{\odot 3} - \mathrm{Z} \oslash (Z+1)^{\odot 2}), \qquad (4\text{-}5)$$

and the third one

$$O^{([n_1,n2,n3],m_1)} = \Delta\mathrm{T}\sum_{n=1}^{H_n} c^{([n1,n2,n3],m1)} \odot (16\mathrm{Z} \oslash (Z+1)^{\odot 2} - 96Z^{\odot 2} \oslash (Z+1)^{\odot 3}) \qquad (4\text{-}6)$$

$$+96z \oslash (Z+1)^{\odot 4}),$$

where,

$$\begin{aligned} a^{(n1,m1)} &= I_w\,(n1) \odot L_w\,(m1), \\ b^{([n1,n2],m1)} &= I_w\,(n1) \odot I_w\,(n2) \odot L_w\,(m1), \\ c^{([n1,n2,n3],m1)} &= I_w\,(n1) \odot I_w\,(n2) \odot I_w\,(n3) \odot L_w\,(m1), \end{aligned} \quad (4\text{-}7)$$

and

$$Z = e^{-2X*I_W-2B}, \quad (4\text{-}8)$$

where $\odot$ is the Hadamard product and $\oslash$ is the Hadamard division.

The maximum third derivative, M, in the range $|\bar{I}(n)| < \frac{1}{k}$ for n=1,2,...,$I_N$in a computationally cheap method can be written as follows.

Let $\bar{M}\{2^{I_n}, I_n\}$ be the matrix of any combination of $\pm\frac{1}{K}$ for the input variables and $\bar{B}\{H_o, 2^{I_n}\}$=[B,B,..,B], thus,

$$\bar{Z} = \{\bar{z}\} = e^{-2\bar{M}*I_W-2\bar{B}}. \quad (4\text{-}9)$$

Let $\hat{z}$ be the closest point of $\bar{z}$ in the aforementioned range to $z^* \approx 0.23065$. The maximum third derivative could be over-estimated by substituting $\hat{Z} = \{\hat{z}\}$ in Equation(4-6).

Let us write the Taylor expansion of Fat $\bar{I} = 0$ as,

$$F(\bar{I}) = \sum_{n=0}^{\infty} \frac{1}{n!} ((€.\nabla)^n F(\bar{I}))\Big|_{\bar{I}=0}. \quad (4\text{-}10)$$

By considering the first three terms of the Equation (4-10) we can rewrite it as

$$\begin{aligned} &E[(F(\bar{I}) - F_0(\bar{I}))^2] = \\ &E[(€.\nabla F(0) + \tfrac{1}{2}€^2.\nabla^2 F(0) + R_2)^2], \end{aligned} \quad (4\text{-}11)$$

in which R_2 is the remainder of the second order Taylor expansion and could be estimated using the Taylor's inequality,

$$R_2 = [R_{2,1}\ R_{2,2}\ \dots\ R_{2,n}]^T \ and\ |R_{2,n}| < \frac{\partial^3 F(0)}{3!\partial {x_n}^3} €^3. \quad (4\text{-}12)$$

Let's consider P_R as the difference between $var(F(0))_{n=\infty}$ and $var(F(0))_{n=2}$, thus,

$$\begin{aligned} P_R = E[&\left(\frac{\partial^3 F(0)}{3!\partial {x_n}^3}\right)^2 €^6 + €.\nabla F(0)\frac{\partial^3 F(0)}{3\partial {x_n}^3}€^3 + \\ &€^2.\nabla^2 F(0)\frac{\partial^3 F(0)}{3\partial {x_n}^3}€^3]. \end{aligned} \quad (4\text{-}13)$$

The first term has a lower order of magnitude and could be estimated as

$$P_{R,1} = E\left(\frac{€^6 {M_3}^2}{36}\right), \quad (4\text{-}14)$$

where M_3 is the summation of the third partial derivative tensor elements,

$$M_3 = \sum_{i,j,k=1}^{I_n} \left(\frac{\partial^3 f(\hat{z}_3)}{\partial x_i \partial x_j \partial x_k}\right). \quad (4\text{-}15)$$

For normal distributions $P_{R,1}$ is estimated to be $\frac{5{M_3}^2}{12\bar{K}^6}$ and the second term has the magnitude of,

$$P_{R,2} = E\left(\frac{€^4 M_1 M_3}{6}\right), \quad (4\text{-}16)$$

where M_1 is the summation of the Jacobian matrix at zero

$$M_1 = \sum_{i1}^{I_n} \left(\frac{\partial f(0)}{\partial x_i}\right). \quad (4\text{-}17)$$

For normal distributions $P_{R,2}$ is estimated to be $\frac{M_1 M_3}{2\bar{K}^4}$ and the last term of Equation (4-13) is zero for symmetric input PDFs. Thus P_R could be estimated as,

$$P_R = \frac{M_1 M_3}{2\bar{K}^4} + \frac{5{M_3}^2}{12\bar{K}^6}, \quad (4\text{-}18)$$

in which $\sqrt{P_R}$ is the maximum deviation due to the propagation of the Taylor's expansion truncation. Considering the rectangular distribution, the variance would be $\frac{P_R}{3}$.

The converging criterion for the variance could be presented as,

$$\left|\frac{P_R}{3} + Var(\hat{E})\right| < D = \frac{10^{-2(N_d+2.3979)}}{4\bar{d}}, \quad (4\text{-}19)$$

where $\hat{E}$ is the error vector of the ANN, N_d is the number of significant digits and $\bar{d}$ is the tolerance devisor. This is recommended to use $\bar{d}$ greater than 3. Likewise, for the mean value, we can write,

$$E[F(\bar{I}) - F_0(\bar{I})] = E[€.\nabla F(0) + \frac{1}{2}€^2.\nabla^2 F(0) + R_2], \quad (4\text{-}20)$$

and

$$E(F(0))|_{n=\infty} - E(F(0))|_{n=2} = E\left(\sum_{i,j,k=1}^{I_n} \frac{\partial^3 F(0)}{3!\partial {x_n}^3} €^3\right), \quad (4\text{-}21)$$

which is zero for any symmetric PDF, therefore, the second converging criterion is

$$|MSE_{ANN}| < D = \frac{10^{-2(N_d+2.3979)}}{4d}. \quad (4\text{-}22)$$

For the upper and lower ranges of the confidence interval, the following condition should be satisfied as

$$\left|MSE_{ANN} + \frac{K^2 P_R}{3}\right| < D = \frac{10^{-2(N_d+2.3979)}}{4d}. \quad (4\text{-}23)$$

Let us rewrite the Equation (4-11) for the unmapped inputs as,

$$\begin{aligned} &\mathrm{E}[(\mathrm{F}(I) - \mathrm{F}_0(I)^2] = \mathrm{E}[(€.\nabla \mathrm{F}(\mathrm{I}) + \tfrac{1}{2}€^T Hf(I)€)^2] \\ &= \mathrm{E}\,[J\,€€^T J^T + \tfrac{1}{4}€^T Hf(I)€€^T Hf(I)^T € + \tfrac{1}{2} J.€€^T Hf(I)€]. \end{aligned} \quad (4\text{-}24)$$

The last term is zero for symmetric PDFs and the second term is a scalar and therefore is equal to its trace, considering tr(A*B) = tr(B*A). Thus,

$$\mathrm{Var(O)} = \mathrm{diag}(\mathrm{J}\sum \mathrm{J}^{\mathrm{T}}) + \mathrm{S}, \quad (4\text{-}25)$$

where $\sum$ is the variance-covariance matrix and S is the second order correction which equals to

$$\mathrm{S} = [tr(\textstyle\sum * H^T_{On=1})^2, tr(\sum * H^T_{On=2})^2, \dots, tr(\sum * H^T_{On=ON})^2]^T. \quad (4\text{-}26)$$

The Jacobian matrix can be written as,

$$\mathrm{J} = 4(\Delta \mathrm{T}/\Delta x^T) \odot \mathrm{A}^*(\,\mathrm{Z} \oslash (Z+1)^{\odot 2})^{\mathrm{T}}, \quad (4\text{-}27)$$

where

$$\mathrm{A}(\mathrm{I_n}, \mathrm{O_n}, \mathrm{H_n}) = \begin{bmatrix} a(1,1) & \cdots & a(I_n, 1) \\ \vdots & \ddots & \vdots \\ a(1, o_n) & \cdots & a(I_n, o_n) \end{bmatrix}. \quad (4\text{-}28)$$

A is a three-dimensional tensor containing all of the "a" values, refer to Equation (4-7), for different Input-output combinations. And similarly for the Hessian matrix,

$$\begin{aligned} \mathrm{H_{on}}(I_{n1}, I_{n2}) = 8 \cdot \frac{\Delta \mathrm{T}_{on}}{\Delta \mathrm{x}_{n1} \cdot \Delta \mathrm{x}_{n2}} \cdot b^T([n_1, n_2], m_1)^* \\ [2Z^{\odot 2} \oslash (Z+1)^{\odot 3} - \mathrm{Z} \oslash (Z+1)^{\odot 2}], \end{aligned} \quad (4\text{-}29)$$

where the mean squared error and the variance of error are lower than D but $\left|\frac{P_R}{3} + Var(E)\right|$ does not satisfy the condition or when this is requested for double checking, NNUA would be merged with AMCM in the third step. The trained ANN is used instead of the computationally expensive mathematical models using the vector data inputs (i.e. recommended size is one million points rather than ten thousand points which is recommended by GUM [33]), however, classical converging thresholds of AMCM must be modified in the form of Equations (4-30) to (4-33). The input PDFs are generated based on the Cholesky factorization [73] as suggested by supplement-II of GUM [74] using the upper triangle of ∑ matrix. The conversion criteria are then,

$$\sqrt{var(\bar{y}) + {E^2}_{ANN}} < D/2, \qquad (4\text{-}30)$$

$$\sqrt{var(\sigma_y) + var(E_{ANN})} < D/2, \qquad (4\text{-}31)$$

$$\sqrt{var(y_{low}) + {E^2}_{ANN}} < D/2, \qquad (4\text{-}32)$$

and

$$\sqrt{var(y_{high}) + {E^2}_{ANN}} < D/2. \qquad (4\text{-}33)$$

4.2 Worked example: calculating dew-point temperature from mole fraction and pressure

Thermodynamic equation of seawater-2010 (TEOS-10) is based on a Gibbs function formulation from which all thermodynamic properties of seawater, water and air (density, enthalpy, entropy sound speed, etc.) can be derived in a thermodynamically consistent manner [37].

By recalling Equations (1-10) to (1-12), Equilibrium between liquid water and vapor in the air can be written as

$$\left(f_\rho^{AV} + f_{q\rho}^{AV} - \frac{P}{(\rho^{AV})^2}\right)\Delta\rho^{AV} - \left(f_\rho^{W} - \frac{P}{(\rho^{W})^2}\right)\Delta\rho^{W} = P\left(\frac{1}{\rho^{W}} - \frac{1}{\rho^{AV}}\right) + f^{W}\text{-}f^{AV} + (q-1)f_q^{AV}, \qquad \text{R(1-10)}$$

$$\left(2f_\rho^{AV} + \rho^{AV} f_{\rho\rho}^{AV}\right)\Delta\rho^{AV} = \frac{P}{\rho^{AV}} - \rho^{AV} f_\rho^{AV}, \qquad \text{R(1-11)}$$

$$\left(2f_\rho^{W} + \rho^{W} f_{\rho\rho}^{W}\right)\Delta\rho^{W} = \frac{P}{\rho^{W}} - \rho^{W} f_\rho^{W}. \qquad \text{R(1-12)}$$

Considering a given specific humidity and a given total pressure system of equations can be solved simultaneously and iteratively. The calculated temperature is the dew-point temperature.

This mathematical model exhibits some particular characteristics:

1) There is a system of equations

2) It should be solved iteratively

3) Considering the physical problem, the Input uncertainties are not necessarily Gaussian

4) Some other thermodynamic properties are needed (i.e. independent equations) including partial pressure, amount fraction, boiling temperature, the density of liquid water, the density of humid air and Gibbs functions.

The Seawater-Ice-Air (SIA) library [38] contains the TEOS-10 subroutines for evaluating a wide range of thermodynamic properties of pure water (using IAPWS-95 [75]) and for the moist air. This library also provides a solver for the system of equations above [76].

The sensitivity analysis of GUF, i.e. GUM framework, cannot be considered for the system of equations and MCM, as an alternative, remains the best solution. MC is a method for propagation of distributions by employing random sampling from probability distributions. MC simulations of this mathematical model have been detailed in [77].

We can apply NNUA and compare the results with AMCM.

INRIM high-humidity generator, refer to chapter-2, is depicted in Figure 156. To evaluate the dew-point temperature three main methods are available.

1) Conversion of specific humidity calculated from mass flow meter readings.

2) Direct measurements with a chilled mirror hygrometer.

3) Conversion of the amount fraction measured by a resonant cavity hygrometer.

Simultaneous measurements of the methods, if available, can also be employed by a data fusion algorithm which has also been discussed in [77].

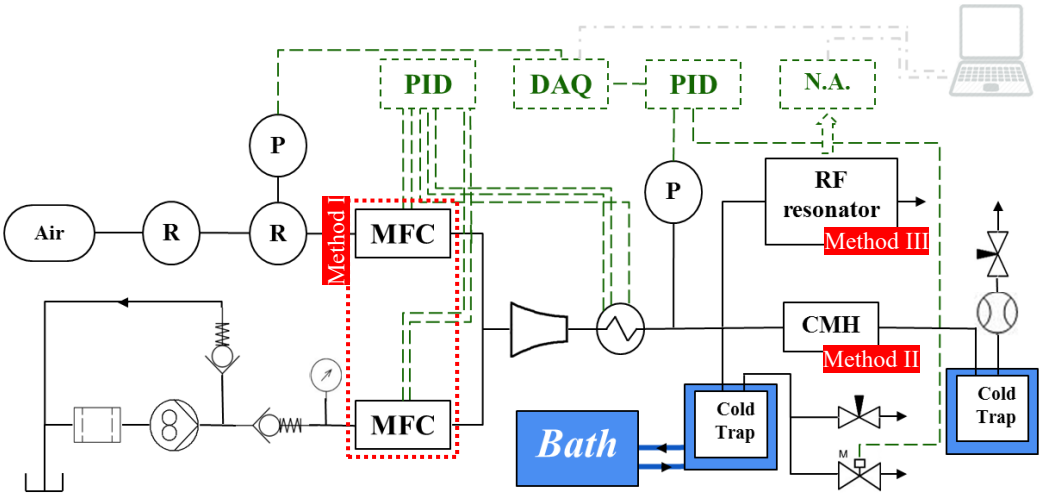

Figure 156: INRIM high-humidity generator

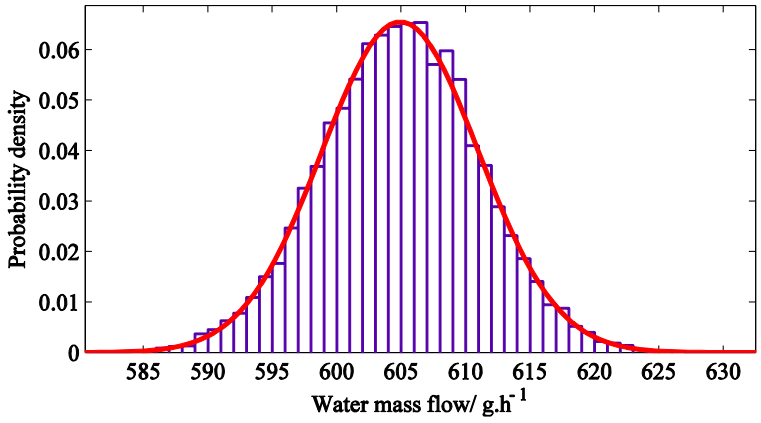

Figure 157: Input PDF for *l*-MFC

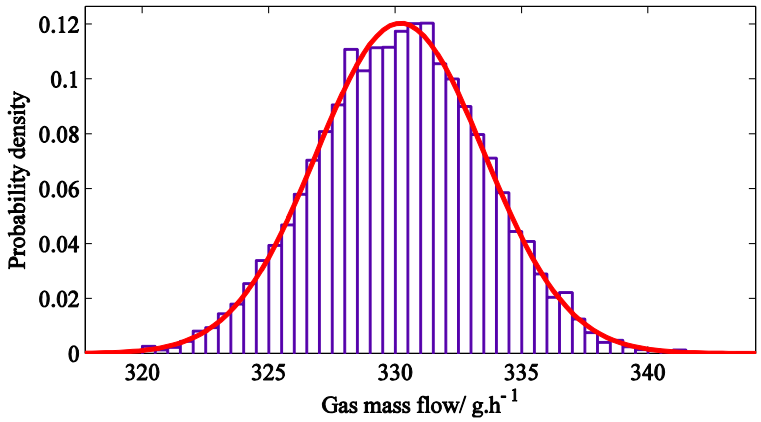

Figure 158: Input PDF for *g*-MFC

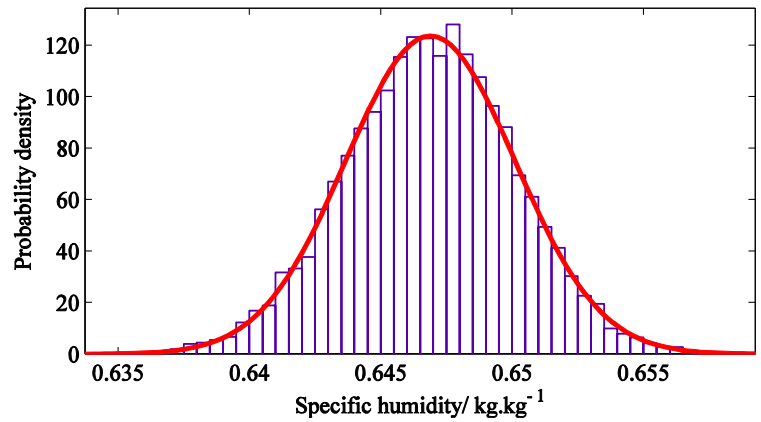

Figure 159: Resulting input PDF for specific humidity

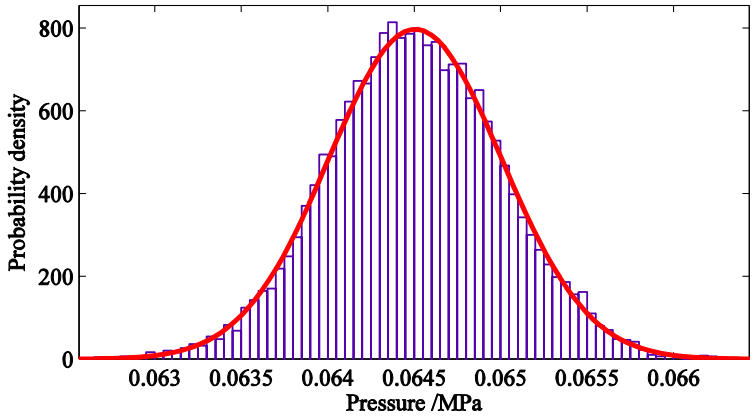

Figure 160: Input PDF for the total pressure

The probability density functions of each input variable have been estimated by generating random numbers in accordance with the input uncertainties; they have been merged to allocate a final PDF to each input variable out of all the contributions as depicted by Figure 157 to Figure 160.

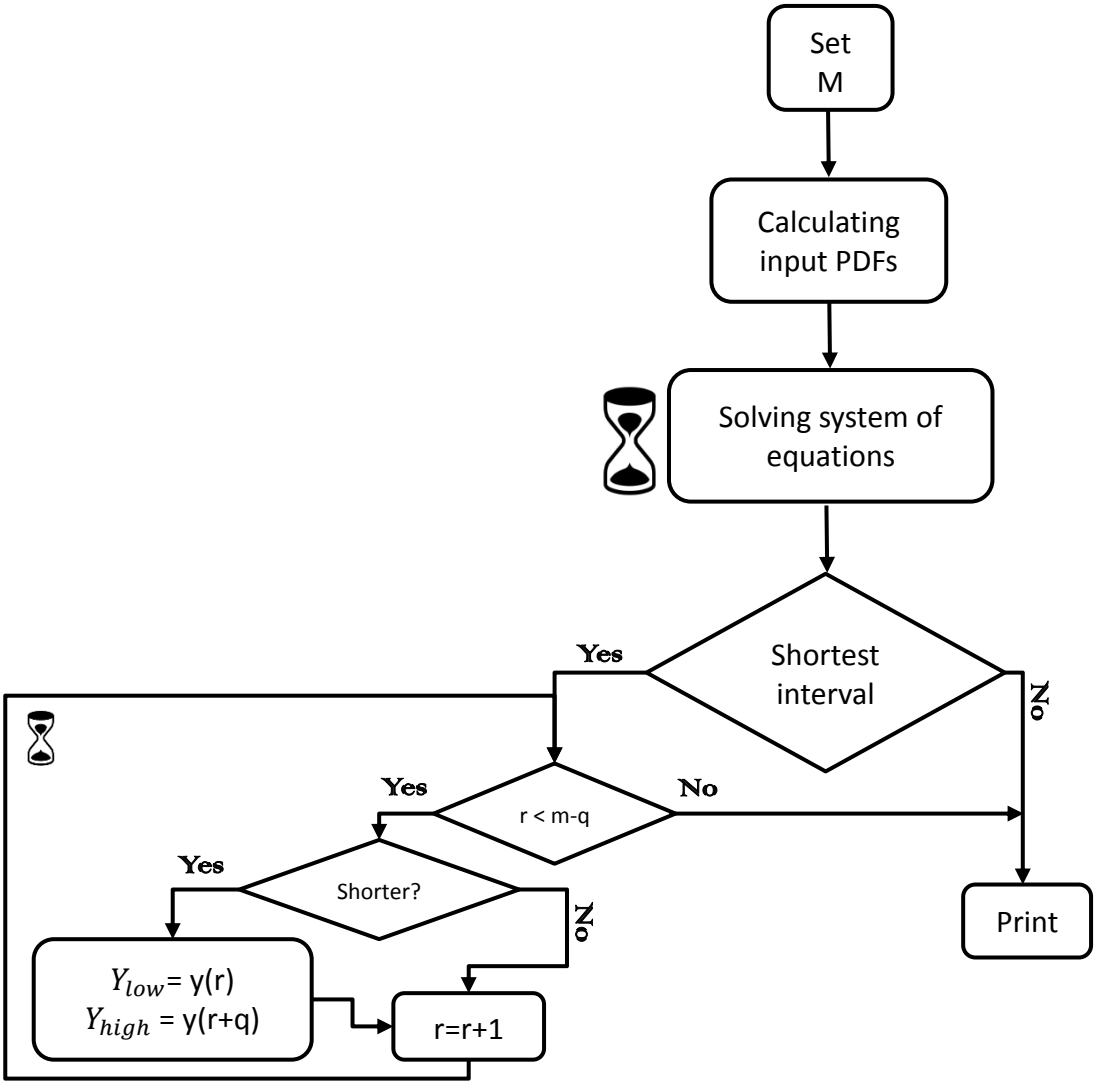

Figure 161: Monte-Carlo algorithm

The MC algorithm, as detailed in Figure 161, can be simply exploited to perform the simulations and single out the best estimate, standard deviation and the confidence interval by considering either the shortest or the symmetric interval. The main challenge of the MC algorithm is the number of sample points. In order to ensure an adequate number of points, AMCM can be employed [78]. The flowchart of this algorithm is depicted in Figure 162, considering 47 iterations and having 4.7×10^{7} points stability of 5×10^{-4} can be reached to guarantee three significant digits. In all cases, it is computationally more expensive to reach the stability for the coverage intervals rather than for the best estimation and the standard deviation.

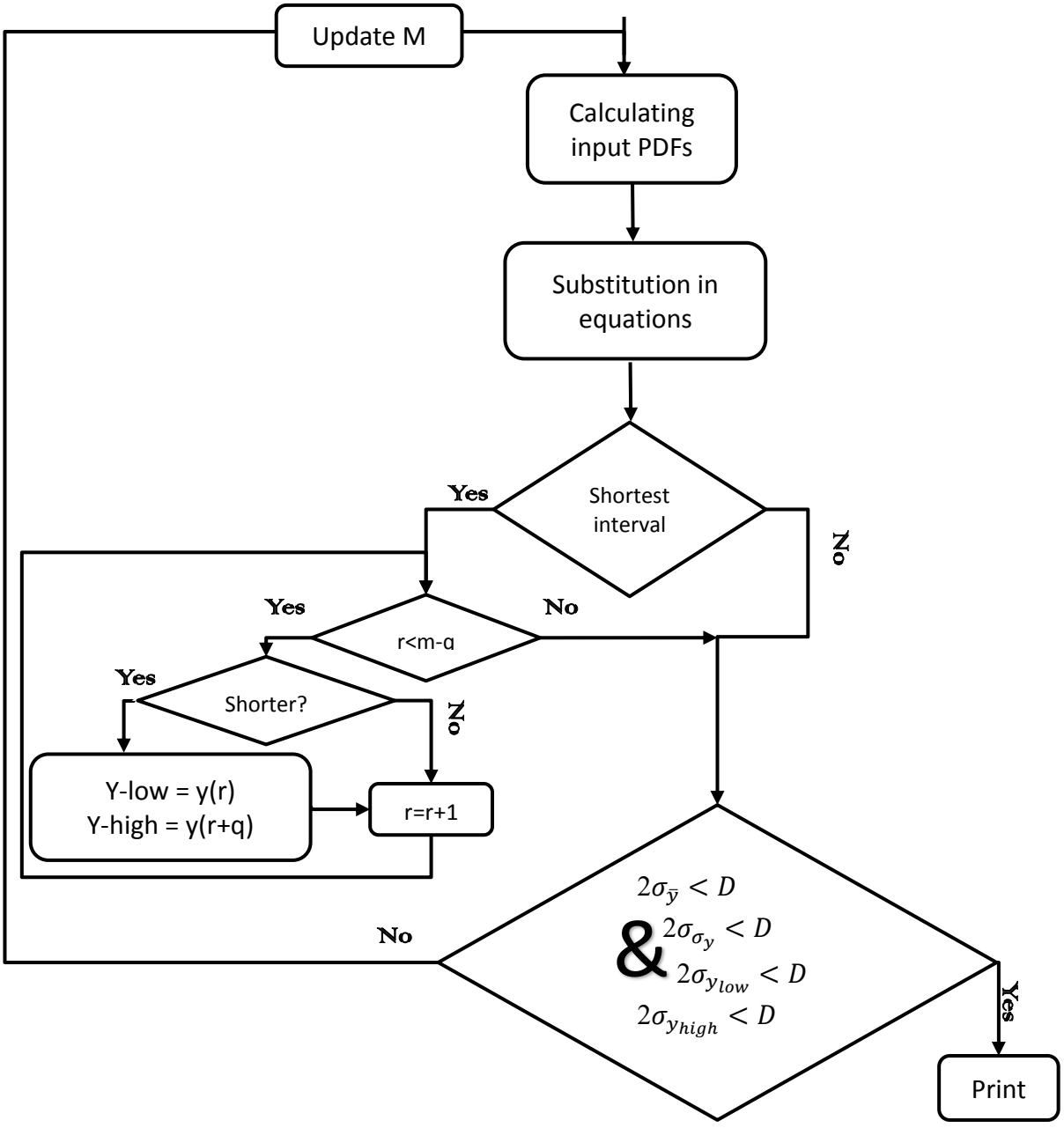

Figure 162: Numerical implementation of adaptive Monte-Carlo method similar to that of [79]

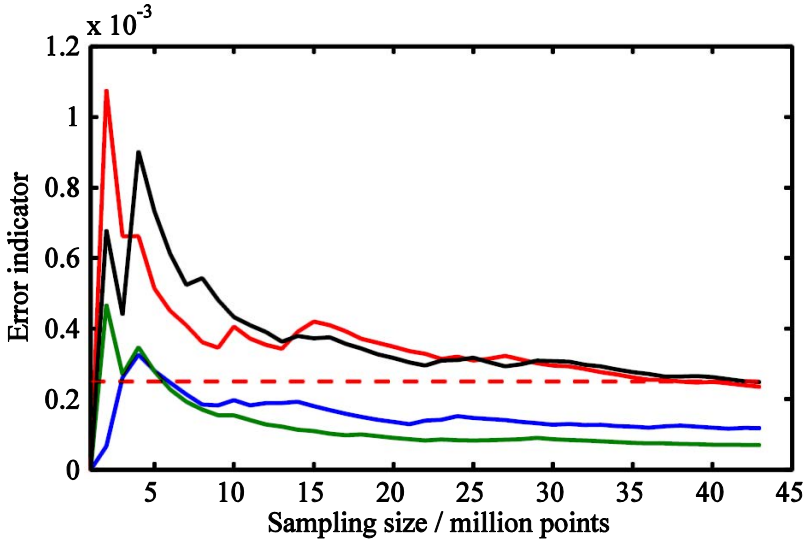

Figure 163: Adaptive Monte-Carlo converging iteration, green stands for mean, blue for the standard deviation, black and red for the upper and lower confidence levels

The output of the AMCM after the convergence, Figure 163, results in the PDF of the dew-point temperature and is illustrated in Figure 164. Statistical parameters of this PDF is also detailed in Table 78.

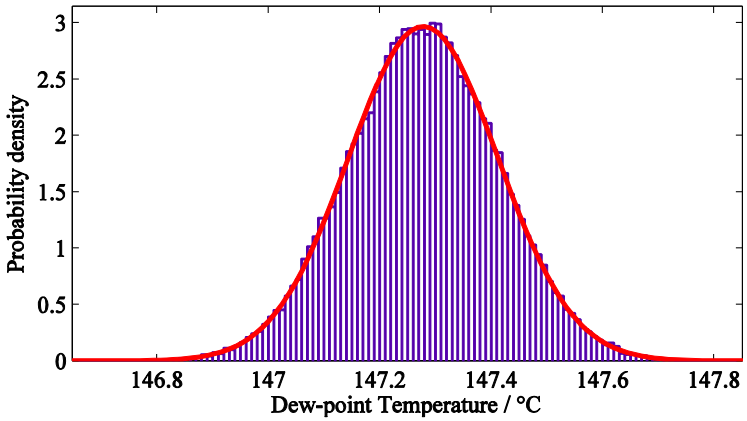

Figure 164: The output PDF for the dew point temperature calculation

Table 78: Statistical parameters of the output variable by employing AMCM

$\bar{Y}$	σ_Y	Y_{low}	Y_{high}	Converging time
147.2778	0.1345	147.0133	147.5405	78 hours

The problem can also be solved by following the theoretical approach of Sec.4.1. in order to train the network, the algorithm applies the back-propagation algorithm for either maximum 100 epochs or the minimum error gradient of 10^{-10} continued by intaking 100 more randomly picked sample points which, obviously, provides a sudden increase in the training error indication. However,

when the network is well-trained, the mean squared error becomes less sensitive to the fresh samples. The converging criteria have been satisfied in the sixth step however the numerical indication is plotted for a few more iterations for the sake of control, i.e. Figure 165.

Table 79: Statistical parameters of the output variable by employing NNUA method

$\bar{Y}$	σ_Y	Y_{low}	Y_{high}	**Converging time**
147.277	0.134	147.009	147.545	30 s

The final result is converged after only 30 seconds, refer to Figure 166, in a perfect agreement with that of the Monte-Carlo after 67 hours of calculation considering the same hardware.

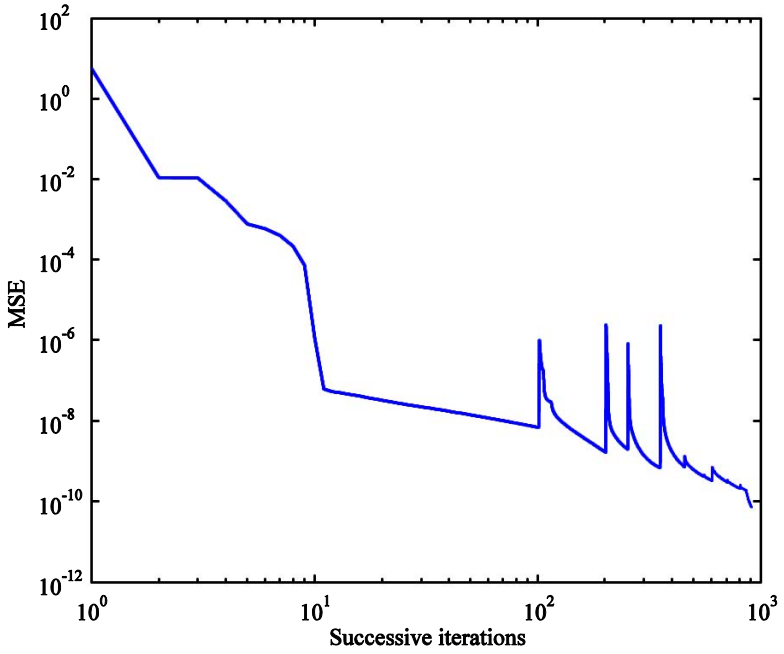

Figure 165: Performance indication of the NNUA

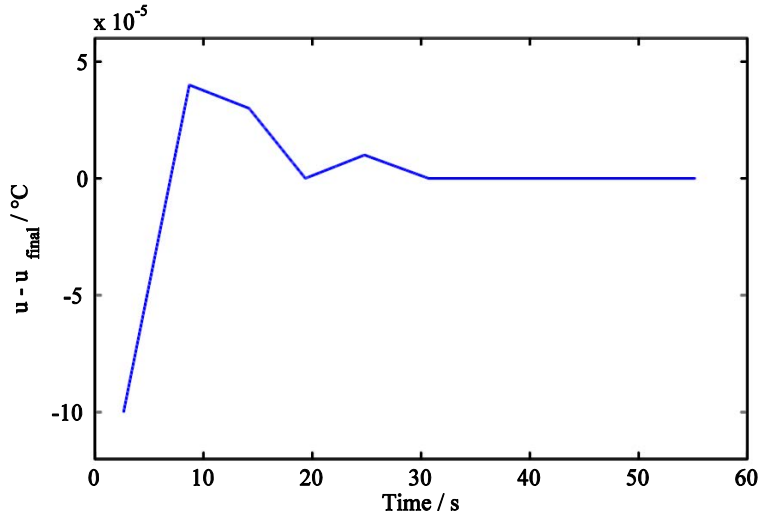

Figure 166: Output standard uncertainty convergence against the total calculation time

4.3 Concluding remarks

This chapter introduced a general-purpose algorithm for the propagation of the input uncertainties and PDFs through the MIMO mathematical models. The best estimation, variance and confidence interval of this artificial neural network-based algorithm are guaranteed to be similar to that of AMCM for the required number of significant digits much more cost-efficiently. The algorithm can figure out the nonlinearity of the mathematical model and if needed it merges itself with AMCM time-efficiently

A system of equations has been employed from TEOS-10 set of equations to study the operation of the algorithm. It consists of a system of differential equations which should be solved simultaneously and iteratively; besides, a few variables should also be defined considering independent equations. The output of NNUA confirmed a complete agreement with AMCM up to the millikelvin level with 6800 times faster operation in terms of the computation time.

Conclusions

Humidity is a fundamental parameter in controlling drying processes in many industrial applications. The accuracy of humidity measurements directly affects the productivity through the efficiency of energy and material usage, the time taken for the process and the quality of the product. Drying and baking are key processes in the food industry and humidity control is an essential parameter in controlling product quality; similar needs also exist in various other industries such as paper production [80], ceramic manufacturing, wood drying and tile production. These sectors will specifically benefit from the study of a new high-humidity generator.

High-temperature and high-pressure standards need a careful study of the humid gas mixture non-idealities. The enhancement factor is attracting widespread interest in the humidity metrology area since reference values should be converted from one parameter to the other one where non-ideality of the mixture plays a crucial role. The enhancement factor estimation is typically based on complex experiments, however, inevitably, either there is a lack of experimental data, or the information is incomplete in many cases. The most widely used formulation is a functional equation published by Greenspan in 1975 [31] and is, non-efficiently, based on the temperature, pressure and the saturation vapor pressure. Chapter-1 presents the numerical implementation of different methods to estimate the water vapor enhancement factor as well as a new functional equation for metrological applications.

In the first chapter, the possibility of using the Helmholtz-based calculations has been studied and the numerical implementation of this approach has been presented. The water vapor enhancement factor has been estimated using the virial equation of estate by introducing the sub-enhancement factors and their magnitude analysis for mixtures with adequate experimental knowledge of their second virial cross coefficients. Sec.1.7 reports such calculations for air. Moreover, for polar gases, e.g. ammonia, the experimental results of the excess parameters, e.g. excess enthalpy, have been considered for calculating the enhancement factor.

Likewise, the mixing rules of the Lennard-Jones potential have been employed to calculate B_{aw} of other gas-water vapor mixtures. Such calculations have been presented in other subsections of sec 1.5. An alternative method has also been discussed for applying the direct numerical integration over the Lennard-Jones parameters of the carrier gas and that of the mixture in Sec.1.7.

Besides, the enhancement factor of air components have been studied based on available second virial cross coefficients, B_{aw}, calculated by quantum

chemistry. Such calculations of first-principals are valid in a wider range of temperature with competitive uncertainty levels. Results have been compared over the estimated values of Sec.1.4 for each component and the air-water vapor mixture. These calculations are also confronted with the results of Sections 1.2 1.4.1 and the method of sec.1.7.

A new functional formula has been introduced and its coefficients were discussed in different sections. The formula is founded on two factors, F_1which is called the atmospheric factor and F_P which is the pressure factor. These factors are functions of the water vapor mole fraction. Eventually, as a result of this chapter, these factors are available for helium, nitrogen, oxygen, ammonia, hydrogen, argon and methane in a wide range of operation.

In the second chapter, the development of a mass fraction humidity generator has been reported to provide traceable calibrations of humidity sensors at temperatures above 100 °C. The principle of operation is based on mixing and evaporating a known mass of water into a known mass of dry air. The generator operates up to 180 °C, with dew-point temperatures up to 140 °C and pressures up to 0.6 MPa.

The vapor generator has been thoroughly validated at 55 different operation points against chilled mirror hygrometers and a gold-plated quasi-spherical microwave resonator. The cavity has been well characterized in terms of Isothermal compressibility, thermal expansion coefficient and resonance frequencies in the vacuum. Alongside that, a relative method has been used to calculate the water mole fraction of the mixture. The uncertainty budget has been assessed to the measurements and the most significant contribution, especially in higher water concentrations, appeared to be the constants of polarizability of water, i.e. the so-called Debye constants. A reasonably good agreement has been observed in the validations by confronting the mixing ratio of the mass flow controllers either to the quasi-spherical resonator or to the chilled mirror hygrometer for a selected sub-range.

Later, a horizontal sub-chamber has been integrated into the generator for the calibration of the relative humidity sensors. Besides, two relative humidity sensors were calibrated to perform a set of preliminary inter-laboratory comparison to a saturation-based generator at VSL [81]. The repeatability of the relative humidity sensors shows a great dependency on the measurement value caused mainly by the absorption of water into the polymer. Results of such comparisons report good agreements, especially in the higher temperature range. The uncertainty increases with the increase of relative humidity, for instance at *RH*= 10 %rh, *P*=0.1 MPa and *T*=100 °C the uncertainty is estimated to be 0.2 %rh growing to about 1.5% at *RH*= 90 %rh at the same pressure and temperature, in contrast, it decreases by the increase of the temperature, for instance, a reduction to 0.1% at *RH*= 10 %rh was observable at *P*=0.1 MPa and *T*=180 °C.

Calibration of humidity sensors at the industrial level, currently, is performed at discrete set-points, by imposing steady-state conditions [82]. Likewise, at the primary standard laboratories, a specific water-gas mixture realized and measured

in the most stable conditions. Chapter 3 has underlined the importance of non-static humidity calibrations as well as addressing a method to elaborate the data and extract the calibration correction and associate the uncertainty.

Initially, the response of capacitive relative humidity sensors has been studied in the Laplace domain and the definition of the calibration coefficient has been established based on the results of the step response of the same sensors. This consideration helps to figure out the calibration corrections as well as the associated uncertainty contributions due to the time delay and non-linearity of both humidity and temperature profiles. Later, the idea has been generalized for any arbitrary curve interpreted as a superposition of ramps starting from each time epoch.

In order to examine the theory, an in-situ humidity calibrator has been designed, simulated, optimized and, eventually, conceptually prototyped. The prototype exhibits unique features, especially, in humidification and dehumidification rates, i.e. roughly 1 $\%rh.s^{-1}$, which are respectively 12 and 6 times greater than that of state of the art in the market. However, considering the nature of the conceptual prototypes, the air leakage turned to be inevitable. Therefore, the minimum dew-point temperatures lower than 3 °C were not achievable.

The third chapter confronts the results of non-static calibration with that of the static calibration for a wide range of temperature and pressure and has obtained comprehensive finding demonstrating that the method is able to provide the calibration in a reasonably good agreement with steady-state calibrations in only a few minutes for the whole range of interest. Besides, this method has also been adopted for two-dimensional calibrations.

The uncertainty levels achievable by the non-static method depend significantly on the slope of the imposed ramp as well as its linearity. In addition to that, similarity of the time constants of RH sensors plays a crucial role; however, the uncertainty can be improved by employing multiple ramps. In the cases under study, it has been shown that the final calibration uncertainties are comparable with that of the static calibrations which are limited mainly by the contribution of reproducibility of the RH sensors to their associated uncertainty.

Scientist, engineers and, especially, metrologists repeatedly face questions like how good is a measurement or how reliable are the numerical simulations and the uncertainty estimation gives the answer. The Guides to the expression of Uncertainty in Measurement (GUM)[32] is the most widely accepted document among all and suggests AMC as the most trustable method which guarantees a given number of the significant digits. However, the most critical drawback of such methods appears to be the time-efficiency.[33]

Chapter-4 succeeded in introducing a general purpose uncertainty algorithm which guarantees to reproduce the results of MCM, in a much cost-efficient way, within a numerical tolerance that does not affect the significant digits of interest. The algorithm evaluates the level of nonlinearity and if needed it merges itself

with AMCM time-efficiently. NNUA provides propagation of the uncertainty and/or PDFs in MIMO models.

A mathematical model has been employed from TEOS-10 set of equations in order to examine the operation of the algorithm. It consists of a system of differential equations which should be solved simultaneously and iteratively; besides, a few variables should also be defined considering independent equations. The output of NNUA remained in a perfect agreement with AMCM up to the millikelvin level and 6800 times faster in terms of the computation time.

NNUA, as discussed in the last chapter, can be exploited in several fields. The current work can benefit not only the computational fluid dynamics and its everyday increasing applications, but also propagation of the PDFs through the image processing, system of equations and any other case in which the mathematical model is not explicitly available or is computationally expensive.

References

1. Heinonen M, Cavallarin L, Dell'Isola M, et al. Metrology for humidity at high temperatures and transient conditions. In: *17th International Congress of Metrology*. EDP Sciences; 2015:15015.
2. O'grady PF. *Thales of Miletus: The Beginnings of Western Science and Philosophy*. Routledge; 2017.
3. Ronan CA. *The Shorter Science and Civilisation in China*. Vol 2. Cambridge University Press; 1985.
4. Bellitto CM, Izbicki TM, Christianson G. *Introducing Nicholas of Cusa: A Guide to a Renaissance Man*. Paulist Press; 2004.
5. Teague KA, Gallicchio N. *The Evolution of Meteorology: A Look Into the Past, Present, and Future of Weather Forecasting*. John Wiley & Sons; 2017.
6. Mölders N, Kramm G. *Lectures in Meteorology*. Springer; 2014.
7. Korotcenkov G. *Handbook of Humidity Measurement, Volume 2: Electronic and Electrical Humidity Sensors*. CRC Press; 2019.
8. Brande WT. *A Dictionary of Science, Literature, & Art: Comprising the History, Description, and Scientific Principles of Every Branch of Human Knowledge; with the Derivation and Definition of All the Terms in General Use*. Longman, Brown, Green, and Longmans; 1842.
9. Museo Galileo - Institute and Museum of the History of Science. online. https://catalogue.museogalileo.it/object/CondensationHygrometer.html.
10. Mildred Geshwiler. *Psychrometrics Theory and Practice*. Atlanta; 1996.
11. Cuccaro R, Rosso L, Smorgon D, Beltramino G, Tabandeh S, Fernicola V. Development of a low frost-point generator operating at sub-atmospheric pressure. *Meas Sci Technol*. 2018;29(5):54002.
12. Heinonen M. The CMA humidity standard. *Measurement*. 1996;17(3):183-188.
13. Zvizdić D, Kolobarić V, Galaso I, Šerfezi D. A new two temperature humidity generator as a primary standard for measuring humidity in Croatia. In: *The 7th International Symposium on Temperature and Thermal Measurements in Industry and Science TEMPMEKO'99*. ; 1999.
14. Choi BI, Nham HS, Woo SB, Kim JC, Kwon SY. The new KRISS low frost-point humidity generator. *Int J Thermophys*. 2008;29(5):1578-1588.
15. Hasegawa S, Little JW. The NBS two-pressure humidity generator, mark 2. *Jour Res NBS A*. 1977;81:81-88.
16. Kitano H, Niwa T, Ochi N, Takahashi C. Saturator efficiency and uncertainty of NMIJ two-pressure two-temperature humidity generator. *Int J Thermophys*. 2008;29(5):1615-1622.
17. Venzke H, Schirmer B, Still M, Melling A, Durst F. Fast trace humidity generation in the 0.1 ppm to 1000 ppm range with a two-stage dilution and mixing generator. *Meas Sci Technol*. 2000;11(12):1732-1743. doi:10.1088/0957-0233/11/12/313
18. Abe H, Kitano H. Development of humidity standard in trace-moisture region: Characteristics of humidity generation of diffusion tube humidity generator. *Sensors Actuators A Phys*. 2006;128(1):202-208.

19. Bell SA. Validation of the NPL gravimetric hygrometer. 1995.
20. Wiederhold PR. *Water Vapor Measurement: Methods and Instrumentation*. CRC Press; 2012.
21. Folland CK, Sparks WR. A two-pressure humidity generator for calibrating electrical hygrometers used in meteorology. *J Phys E*. 1976;9(2):112.
22. Crovini L. A HUMIDITY GENERATOR FOR-150 ^{0}C TO 90 ^{0}C DEW POINTS. In: *Proceedings of Congres International de Metrologie*. Vol 58. ; 1989.
23. Heinonen M. A humidity generator with a test chamber system. *Measurement*. 1999;25(4):307-313.
24. Benyon R, Mitter H. The new INTA high-range standard humidity generator and its comparison with the Austrian national humidity standard maintained at BEV/E+ E. *Int J Thermophys*. 2008;29(5):1623-1631.
25. Vega-Maza D, Miller WW, Ripple DC, Scace GE. A Humidity Generator for Temperatures up to 200° C and Pressures up to 1.6 MPa. *Int J Thermophys*. 2012;33(8-9):1477-1487.
26. Tabandeh S, Fernicola V. A Mass fraction 0.5, humidity generator for specific humidity up to kg/kg and pressure up to 0.6 MPa. In: INTiBS, Kraków: XIII Thermal, Int. Symposium on Temperature and Science, Measurements in Industry (TEMPMEKO); :124.
27. Bosma R, Pouw RJ, van Schaik W, Peruzzi A. Climatic chamber for dew-point temperatures up to 150° C. *Metrologia*. 2018;55(4):597.
28. Hyland RW, Wexler A. The enhancement of water vapor in carbon dioxide-free air at 30, 40, and 50 C. *J Res Natl Bur Stand A*. 1973;77:115-131.
29. Gavioso RM, Ripa DM, Benyon R, et al. Measuring humidity in methane and natural gas with a microwave technique. *Int J Thermophys*. 2014;35(3-4):748-766.
30. Sairanen H, Heinonen M. Validation for a new apparatus measuring water vapour enhancement factors up to 6 MPa. *Meas Sci Technol*. 2014;25(3):35301. doi:10.1088/0957-0233/25/3/035301
31. Greenspan L. Functional equations for the enhancement factors for CO2-free moist air. *J Res Natl Bur Stand Phys Chem*. 1976;80(1):41-44.
32. JCGM J. Evaluation of measurement data—Guide to the expression of uncertainty in measurement. *Int Organ Stand Geneva ISBN*. 2008;50:134.
33. Bipm I, IFCC I, ISO I. IUPAP, and OIML, 2008,"Evaluation of Measurement Data—Supplement 1 to the Guide to the Expression of Uncertainty in Measurement," Propagation of Distributions Using a Monte Carlo Method, Joint Committee for Guides in Metrology. *Bur Int des Poids Mes JCGM*. 2008;101.
34. Hyland RW. A Correlation for the Second Interaction Virial Coefficients and Enhancement Factors for Moist Air *. 1975;79(4):551-560.
35. Goff JA. Standardization of thermodynamic properties of moist air. *Heat Piping Air Cond*. 1949;21(11):118.
36. Hardy B. ITS-90 formulations for vapor pressure, frostpoint temperature, dewpoint temperature, and enhancement factors in the range–100 to+ 100 C. In: *The Proceedings of the Third International Symposium on Humidity & Moisture, Teddington, London, England*. ; 1998:1-8.
37. Commission IO. The International thermodynamic equation of seawater–2010: calculation and use of thermodynamic properties.[includes

corrections up to 31st October 2015], UNESCO, Paris, France. 2010.
38. Feistel R, Wright DG, Jackett DR, et al. Numerical implementation and oceanographic application of the thermodynamic potentials of liquid water , water vapour , ice , seawater and humid air – Part 1 : Background and equations. 2010:633-677. doi:10.5194/os-6-633-2010
39. Hyland RW, Wexler A. The Second Interaction (Cross) Virial Coefficient for Moist Air. 1973;77(1):133-147, JOURNAL OF RESEARCH of the Notional Bureau of Standards - A. Physics and Chemistry
40. Montgomery R, McDowall R. *Fundamentals of HVAC Control Systems*. Elsevier; 2008.
41. Ahrens CD. *Essentials of Meteorology: An Invitation to the Atmosphere*. Cengage Learning; 2011.
42. Laurendeau NM. *Statistical Thermodynamics: Fundamentals and Applications*. Cambridge University Press; 2005.
43. Rabinovich VA, Beketov VG. *Moist Gases: Thermodynamic Properties*. Begell House New York; 1995.
44. Wormald CJ, Wurzberger B. Second virial cross coefficients for (ammonia+ water) derived from gas phase excess enthalpy measurements. *J Chem Thermodyn*. 2001;33(9):1193-1210.
45. García Gallegos J. A comparative study of traditional and novel humidity sensing technologies in natural gas. Universidad de Valladolid. Escuela de Ingenierías Industriales, 2017.
46. Meyer CW, Harvey AH. Dew-Point Measurements for Water in Compressed Carbon Dioxide, American Institute of Chemical Engineers, 2015;61(9). doi:10.1002/aic
47. Hodges MP, Wheatley RJ, Harvey AH. Intermolecular potential and second virial coefficient of the water-helium complex. *J Chem Phys*. 2002;116(4):1397-1405. doi:10.1063/1.1421065
48. Harvey AH, Huang PH. First-Principles Calculation of the Air – Water Second Virial Coefficient, Int J Thermophys, 2007;28(2):556-565. doi:10.1007/s10765-007-0197-8
49. International Association for the Properties of Water and Steam, Guideline on a Virial Equation for the Fugacity of H_2O in Humid Air. 2015.
50. Jumah RY, Mujumdar A, Raghavan VGS. Control of Industrial Dryers, CRC Press, Boca Raton, USA 2007;(January). doi:10.1201 /9781420017618.ch49
51. Directive EE. Directive 2012/27/EU of the European Parliament and of the Council of 25 October 2012 on energy efficiency, amending Directives 2009/125/EC and 2010/30/EU and repealing Directives 2004/8/EC and 2006/32. *Off Journal, L*. 2012;315:1-56.
52. Industry C. Characterizing Ceramics During the Drying Process. www.ceramicindustry.com/articles/84768-characterizing-ceramics-during-the-drying-process.
53. Gard W. Wood-Drying-Centre Europe. 2016;(June).
54. Saklar S, Katnas S, Ungan S. Determination of optimum hazelnut roasting conditions. *Int J food Sci Technol*. 2001;36(3):271-281.
55. Heinonen M, Arpino F, Bosma R, et al. Towards improved humidity measurements at high temperatures and transient conditions. In: *18th International Congress of Metrology*. EDP Sciences; 2017:6002.
56. Sonntag D. The history of formulations and measurements of saturation

water vapour pressure. In: *Third International Symposium on Humidity & Moisture, NPL, London, England*. ; 1998:93-102.
57. Hyland RW. Formulations for Thermodymnamic Properties of the Saturated Phases Of H2O from 173.15 K to 473.15 K. *Ashrae Trans A*. 1983;2:500-513.
58. Wagner W, Pruss A. International equations for the saturation properties of ordinary water substance. Revised according to the international temperature scale of 1990. Addendum to J. Phys. Chem. Ref. Data 16, 893 (1987). *J Phys Chem Ref Data*. 1993;22(3):783-787.
59. Cuccaro R, Gavioso RM, Benedetto G, Ripa DM, Fernicola V, Guianvarc'h C. Microwave determination of water mole fraction in humid gas mixtures. *Int J Thermophys*. 2012;33(8-9):1352-1362.
60. May EF, Pitre L, Mehl JB, Moldover MR, Schmidt JW. Quasi-spherical cavity resonators for metrology based on the relative dielectric permittivity of gases. *Rev Sci Instrum*. 2004;75(10):3307-3317.
61. Underwood RJ, Cuccaro R, Bell S, et al. A microwave resonance dew-point hygrometer. *Meas Sci Technol*. 2012;23(8):85905. doi:10.1088/0957-0233/23/8/085905
62. á Jackson JD. Classical electrodynamics, Wiley, New York, 1975.
63. Groves LG, Sugden S. 221. The dipole moments of vapours. Part II. *J Chem Soc*. 1935:971-974.
64. Stranathan JD. Dielectric constant of water vapor. *Phys Rev*. 1935;48(6):538.
65. Essen L, Froome KD. The refractive indices and dielectric constants of air and its principal constituents at 24,000 Mc/s. *Proc Phys Soc Sect B*. 1951;64(10):862.
66. Essen L. The refractive indices of water vapour, air, oxygen, nitrogen, hydrogen, deuterium and helium. *Proc Phys Soc Sect B*. 1953;66(3):189.
67. Cuccaro R. Hygrometric applications of microwave quasi-spherical resonators. 2012. doi:10.6092/polito/porto/2502548
68. Pietari Tomi. Calibrations in LEAN manufacturing environment. 2017, online: https://www.empir-hit.eu/?action=home:_first.getDoc&idDoc=67.
69. Burns R. *Advanced Control Engineering*. Elsevier; 2001.
70. Tabandeh S, Heinonen M. New approach to calibrate a RH probe and its application to field calibrations. 2017, online: https://www.empir-hit.eu/?action=home:_first.getDoc&idDoc=70.
71. Ergun S. Fluid flow through packed columns. *Chem Eng Prog*. 1952;48:89-94.
72. Fast RHG. RHapid-Cal Humidity Generator Fast, portable humidity probe and logger calibration with accredited 1 % RH system accuracy. :1-8.
73. Gentle JE. Matrix algebra. *Springer texts Stat Springer, New York, NY, doi*. 2007;10:970-978.
74. Committee J. JCGM 102 : 2011 Evaluation of measurement data – Supplement 2 to the " Guide to the expression of uncertainty in measurement " – Extension to any number of output quantities. 2011;(October).
75. Wagner W, Pruß A. The IAPWS formulation 1995 for the thermodynamic properties of ordinary water substance for general and scientific use. *J Phys Chem Ref data*. 2002;31(2):387-535.
76. McDougall T Barker P. Getting started with TEOS-10 and the Gibbs

Seawater (GSW) Oceanographic Toolbox. Trevor J McDougall. www.teos-10.org/software.htm. Published 2011.

77. Tabandeh S, Fernicola V. Uncertainty evaluation of a humidity calibrator using Monte-Carlo method, ANN and data fusion. In: *Abstracts. XIII Int. Symposium on Temperature and Thermal Measurements in Industry and Science TEMPMEKO 2016 (INTiBS, Kraków, 2016)*. ; 2016.
78. Marti K, Ermoliev Y, Makowski M, Pflug G. *Coping with Uncertainty: Modeling and Policy Issues*. Vol 581. Springer Science & Business Media; 2006.
79. Ferna MS. Implementation in MATLAB of the adaptive Monte Carlo method for the evaluation of measurement uncertainties. Accreditation and Quality Assurance 2009:95-106. doi:10.1007/s00769-008-0475-6
80. Valeriani R. The value of humidity measurement in paper manufacturing. 2018. https://www.empir-hit.eu/?action=home:_first.getDoc&idDoc=107.
81. Peruzzi A, Bosma R, Tabandeh S, Fernicola V, Georgin E, Pietari T. An informal comparison of calibration facilities for relative humidity at temperatures up to 180 ^{0}C. 2018. https://www.empir-hit.eu/?action=home:_first.getDoc&idDoc=111.
82. Heinonen M, Högström R. Calibration of humidity sensors at non-static conditions. 2017. https://www.empir-hit.eu/?action=home:_first.getDoc&idDoc=64.

Appendix I

Report on the water vapor enhancement factor as a function of temperature and pressure

The water vapor enhancement factor has been discussed in the first chapter. These results are reported by F_1 and F_P . In contrast, this appendix is aimed to provide the same information based on the temperature and pressure to be in line with the conventional methods.

I.I: The water vapor enhancement factor for air as a function of temperature and pressure.

Equilibrium over a planar pool of liquid water based on the calculations of Sec.1.2.

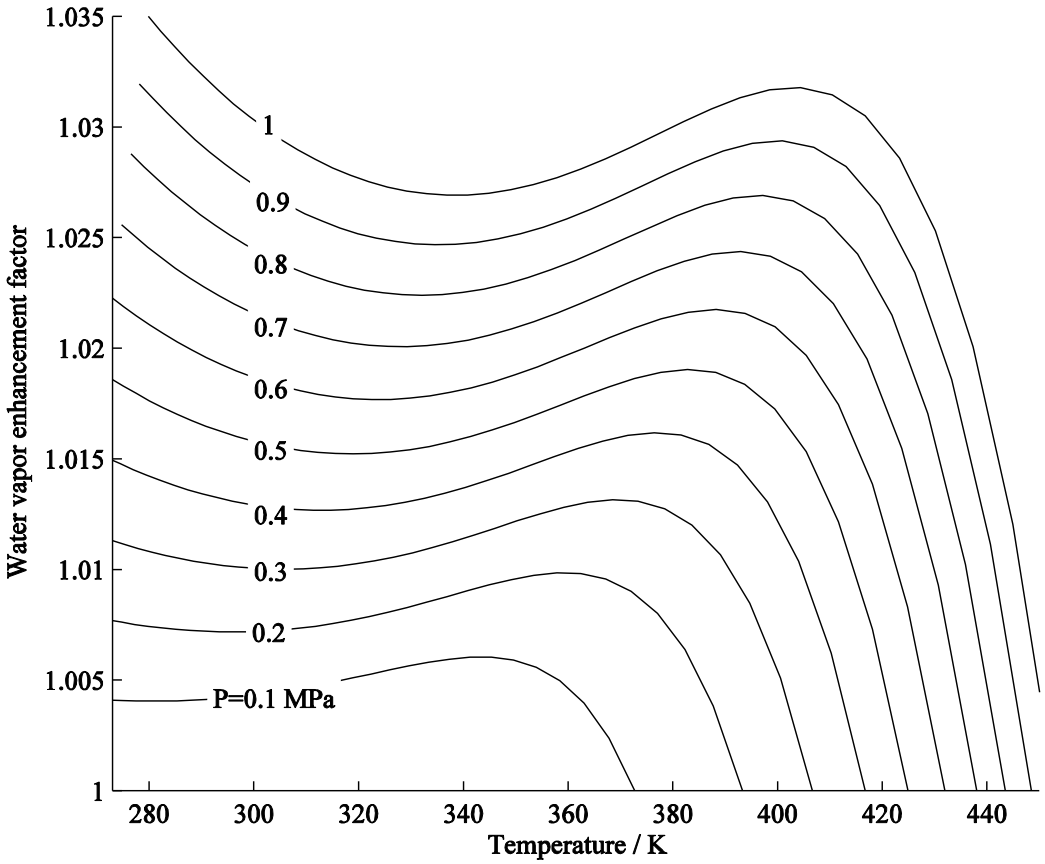

Figure I: Results of Sec.1.2 as a function of temperature and pressure

I.II: The water vapor enhancement factor for air as a function of temperature and pressure

Equilibrium over a planar pool of liquid water:

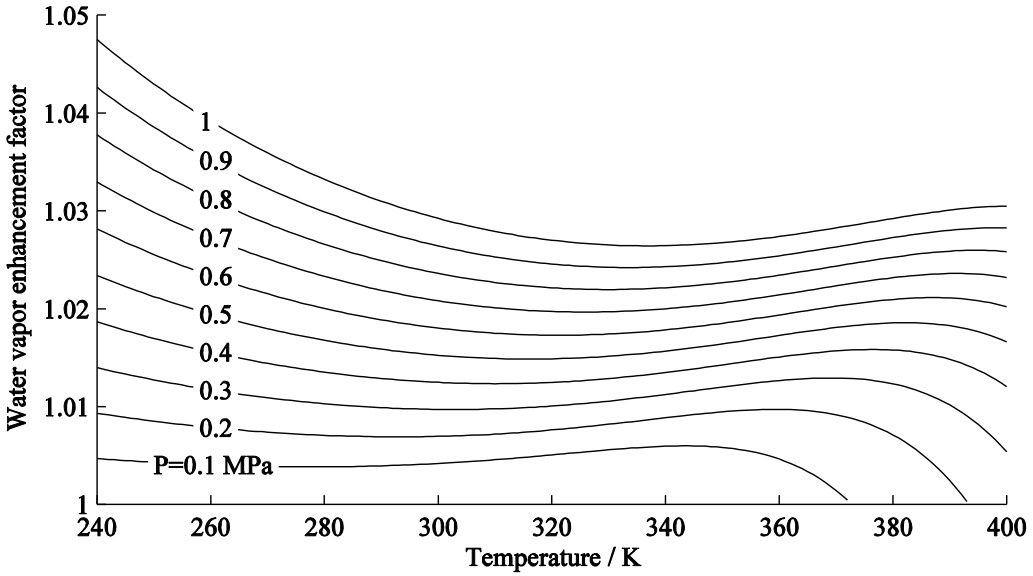

Figure II: Results of Sec.1.4.1 for equilibrium over liquid water as a function of temperature and pressure

Equilibrium over ice plane:

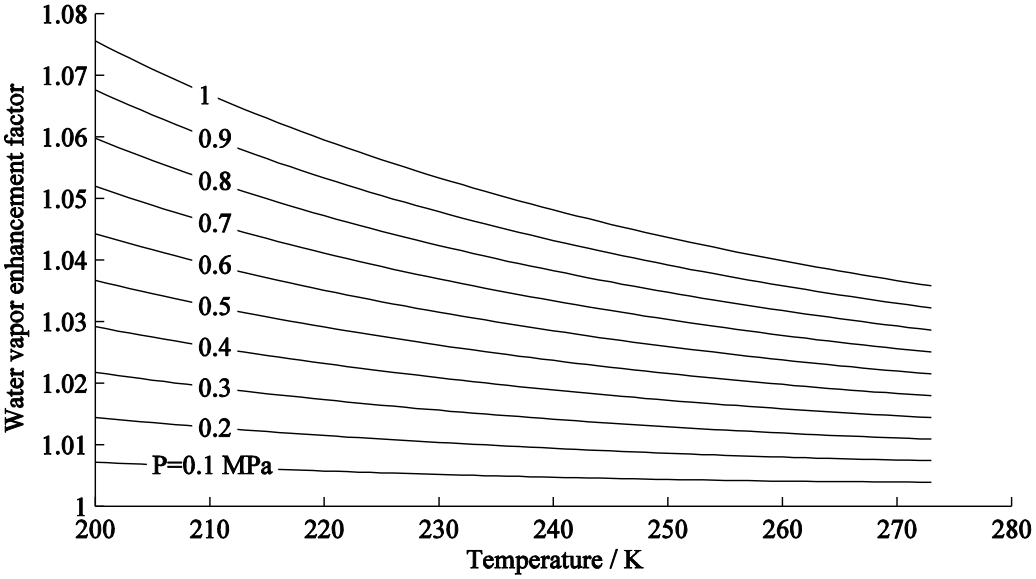

Figure III: Results of Sec.1.4.1 for equilibrium over solid water as a function of temperature and pressure

I.III: The water vapor enhancement factor for nitrogen as a function of temperature and pressure

Equilibrium over a planar pool of liquid water:

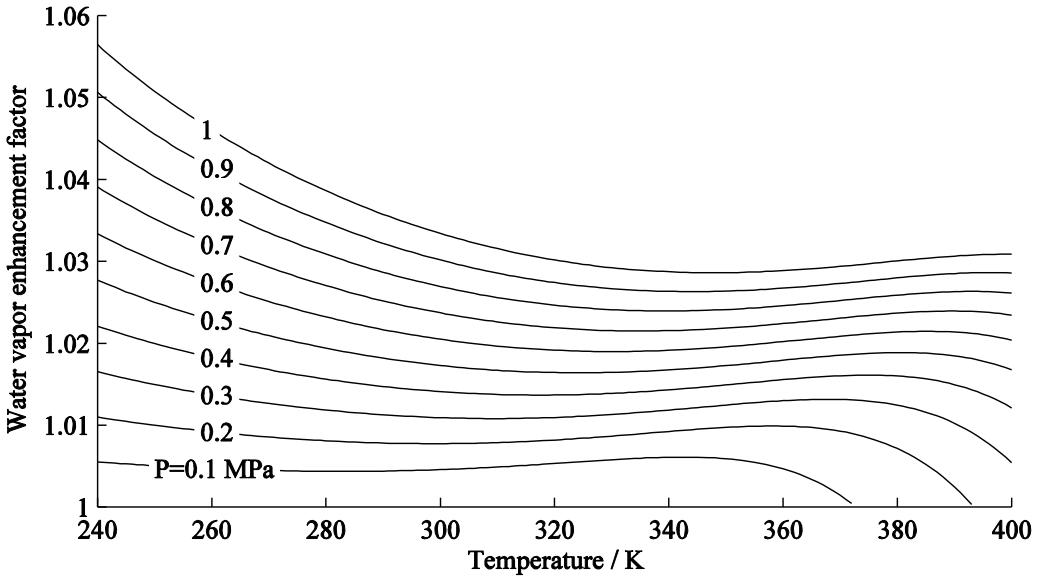

Figure IV: Results of Sec.1.4.2 for equilibrium over liquid water as a function of temperature and pressure

Equilibrium over ice plane:

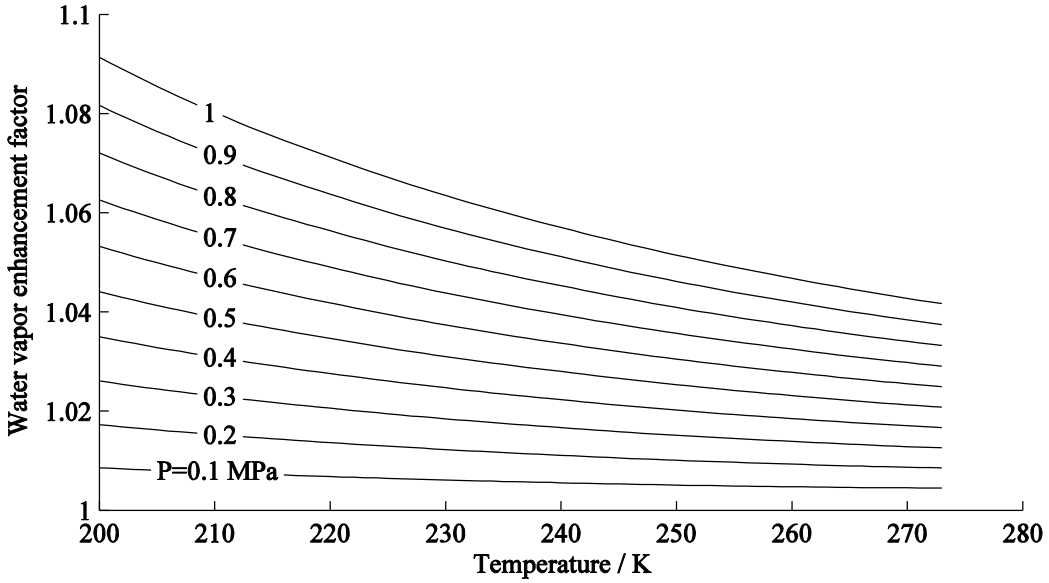

Figure V: Results of Sec.1.4.2 for equilibrium over solid water as a function of temperature and pressure

I.IV: The water vapor enhancement factor for oxygen as a function of temperature and pressure

Equilibrium over a planar pool of liquid water:

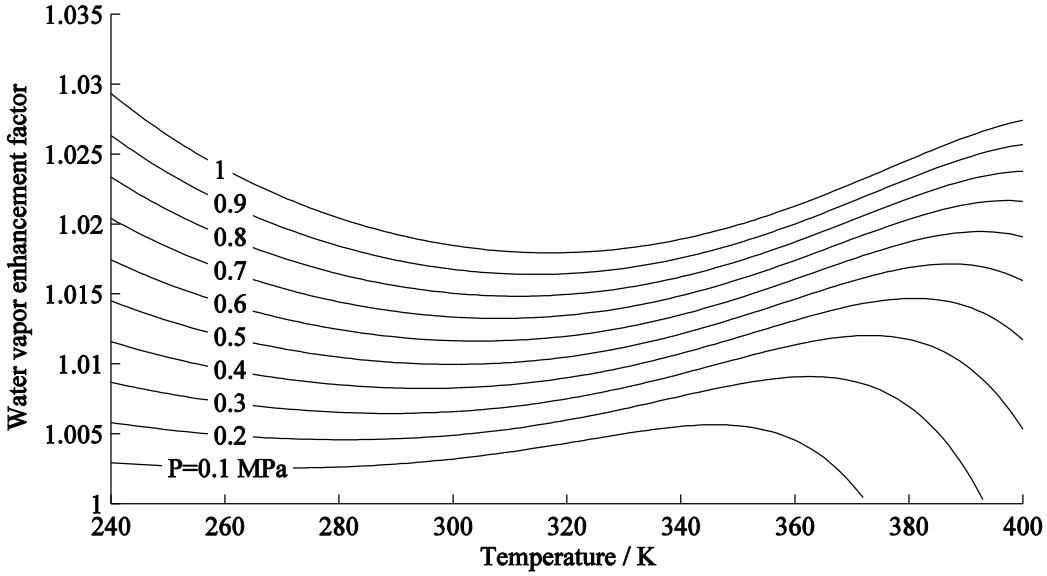

Figure VI: Results of Sec.1.4.3 for equilibrium over liquid water as a function of temperature and pressure

Equilibrium over ice plane:

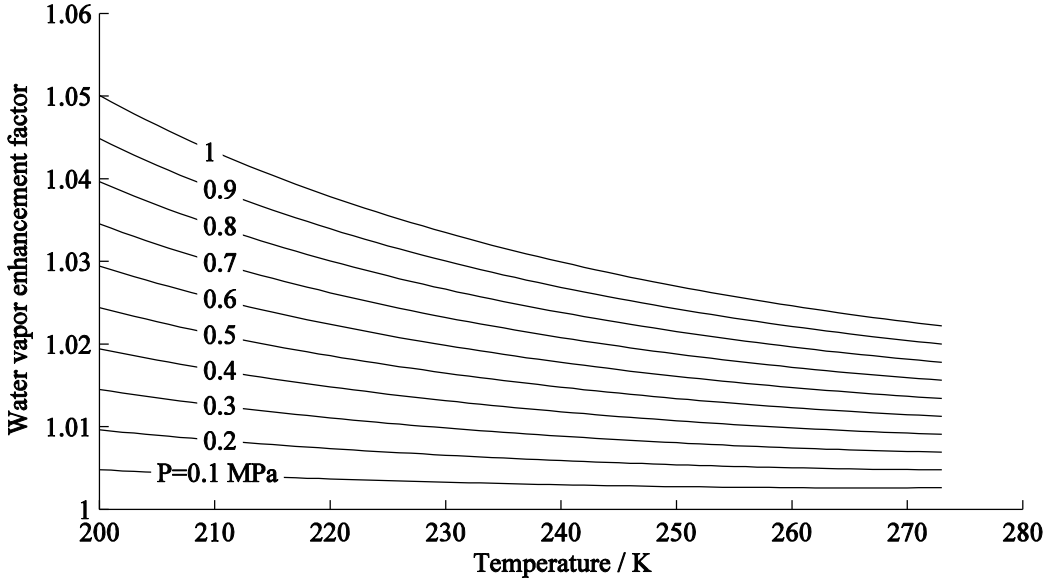

Figure VII: Results of Sec.1.4.3 for equilibrium over liquid water as a function of temperature and pressure

I.V: The water vapor enhancement factor for argon as a function of temperature and pressure

Equilibrium over a planar pool of liquid water:

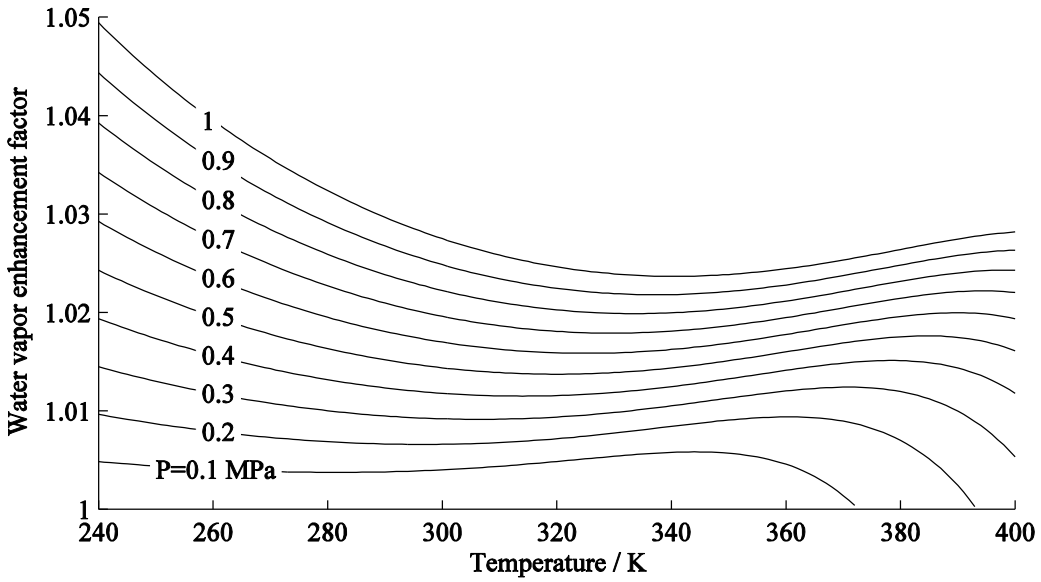

Figure VIII: Results of Sec.1.4.7 for equilibrium over liquid water as a function of temperature and pressure

Equilibrium over ice plane:

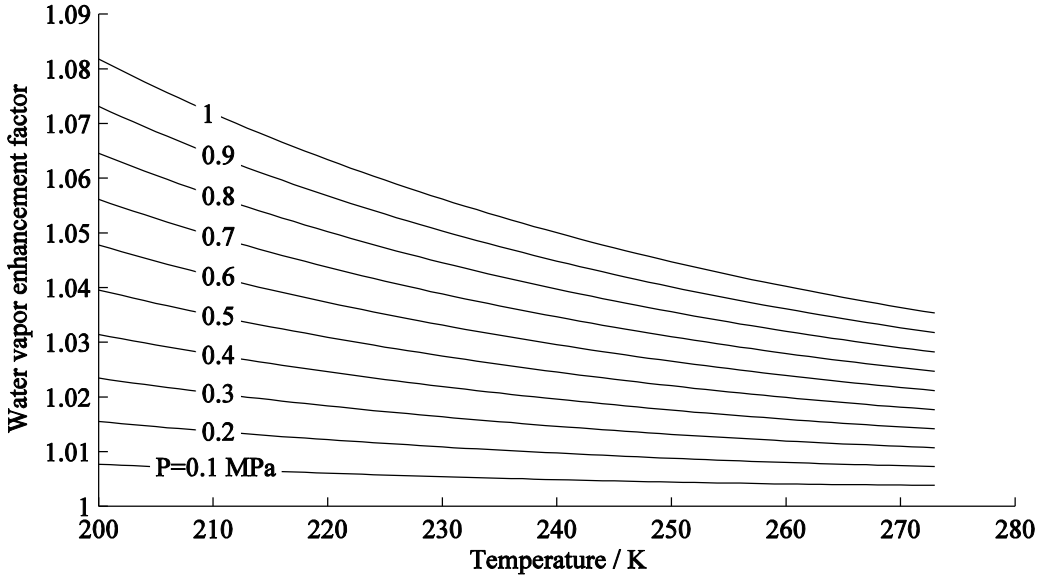

Figure IX: Results of Sec.1.4.7 for equilibrium over solid water as a function of temperature and pressure

I.VI: The water vapor enhancement factor for hydrogen as a function of temperature and pressure

Equilibrium over a planar pool of liquid water:

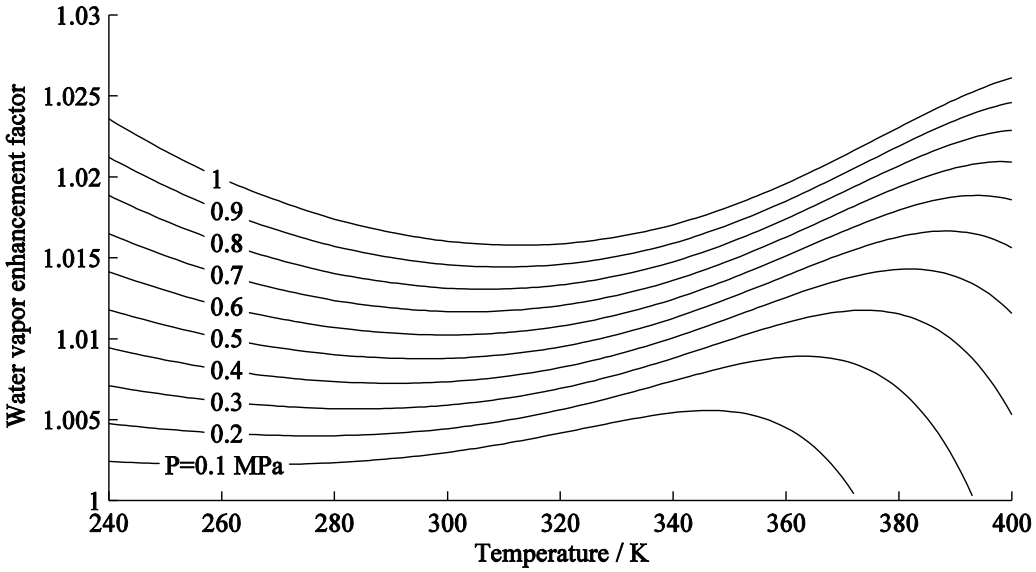

Figure X: Results of Sec.1.4.5 for equilibrium over liquid water as a function of temperature and pressure

Equilibrium over ice plane:

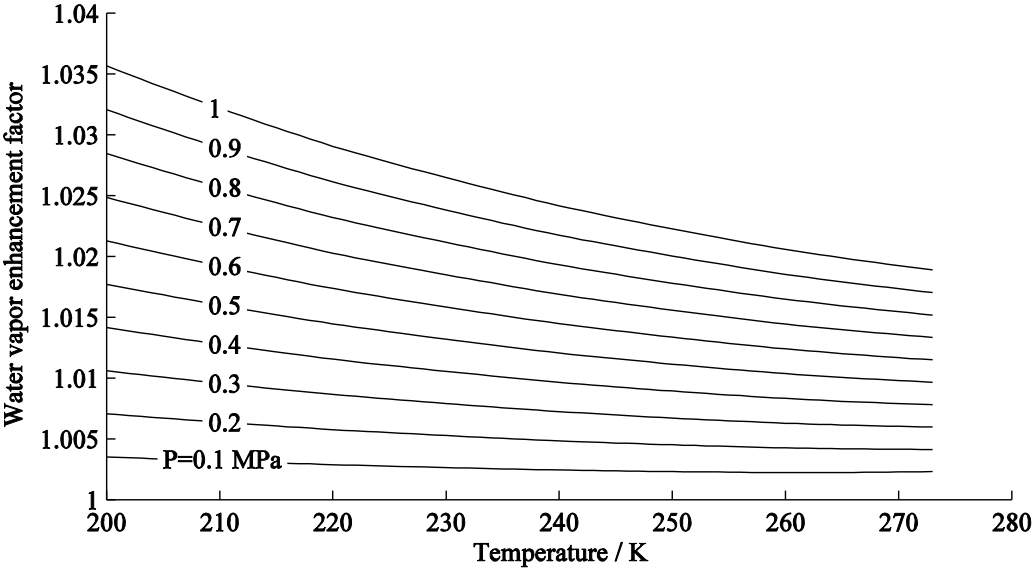

Figure XI: Results of Sec.1.4.5 for equilibrium over solid water as a function of temperature and pressure

I.VII: The water vapor enhancement factor for carbon dioxide as a function of temperature and pressure

Equilibrium over a planar pool of liquid water:

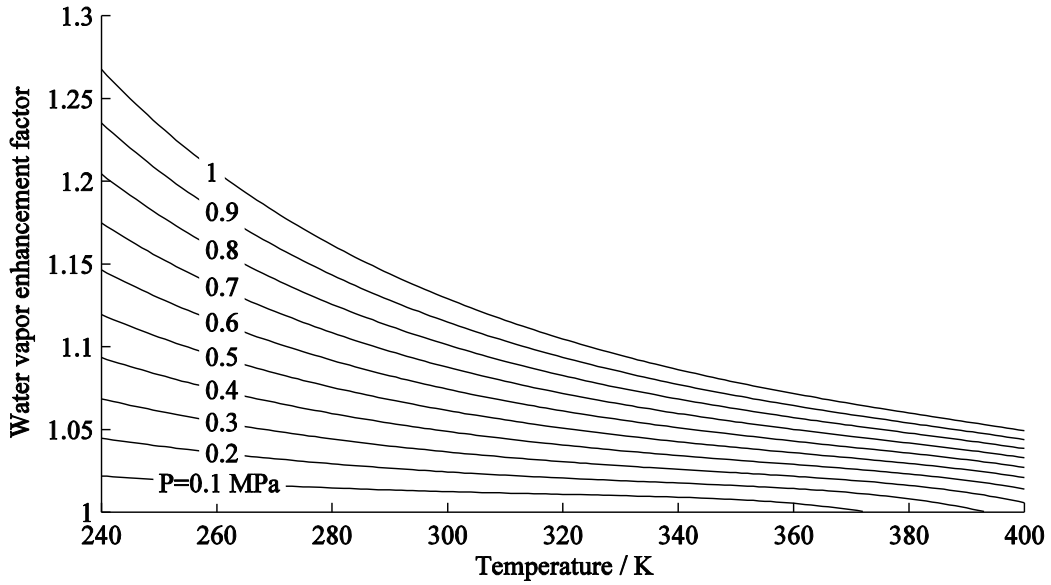

Figure XII: Results of Sec.1.4.8 for equilibrium over liquid water as a function of temperature and pressure

Equilibrium over ice plane:

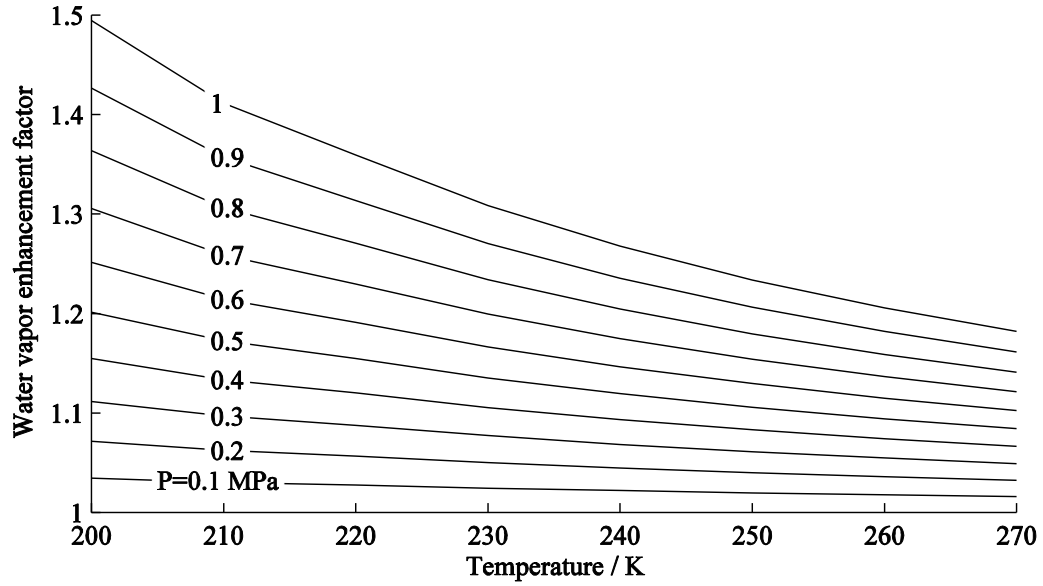

Figure XIII: Results of Sec.1.4.8 for equilibrium over solid water as a function of temperature and pressure

I.VIII: The water vapor enhancement factor for methane as a function of temperature and pressure

Equilibrium over a planar pool of liquid water:

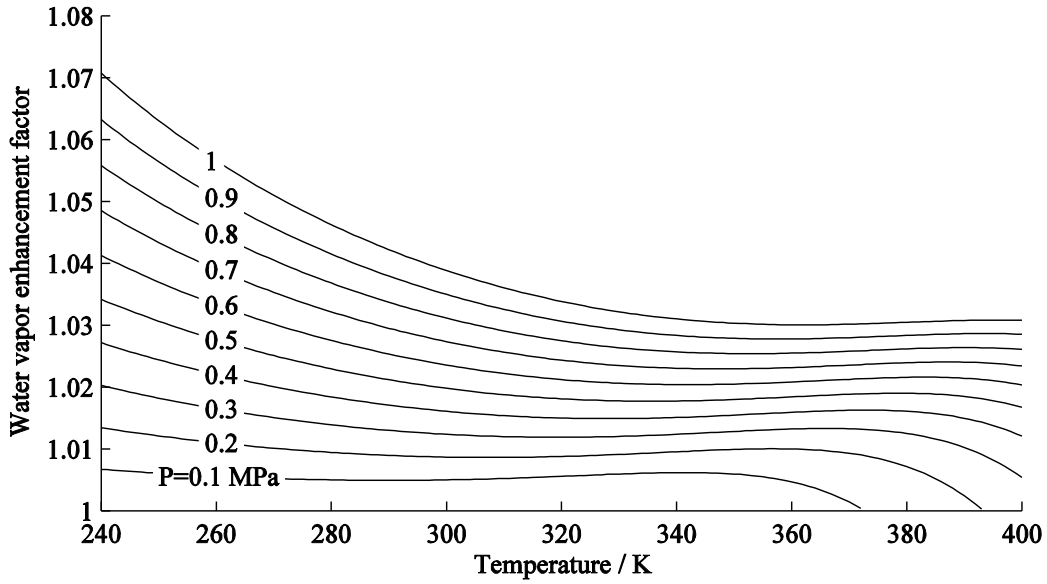

Figure XIV: Results of Sec.1.4.6 for equilibrium over liquid water as a function of temperature and pressure

Equilibrium over ice plane:

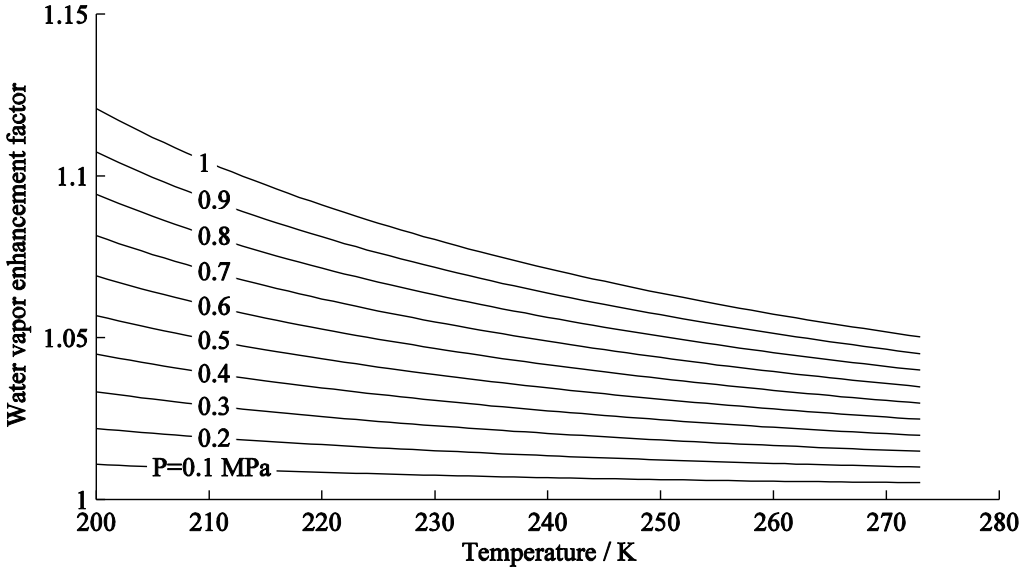

Figure XV: Results of Sec.1.4.6 for equilibrium over solid water as a function of temperature and pressure

I.IX: The water vapor enhancement factor for nitrogen as a function of temperature and pressure based on first-principles calculations

Equilibrium over a planar pool of liquid water:

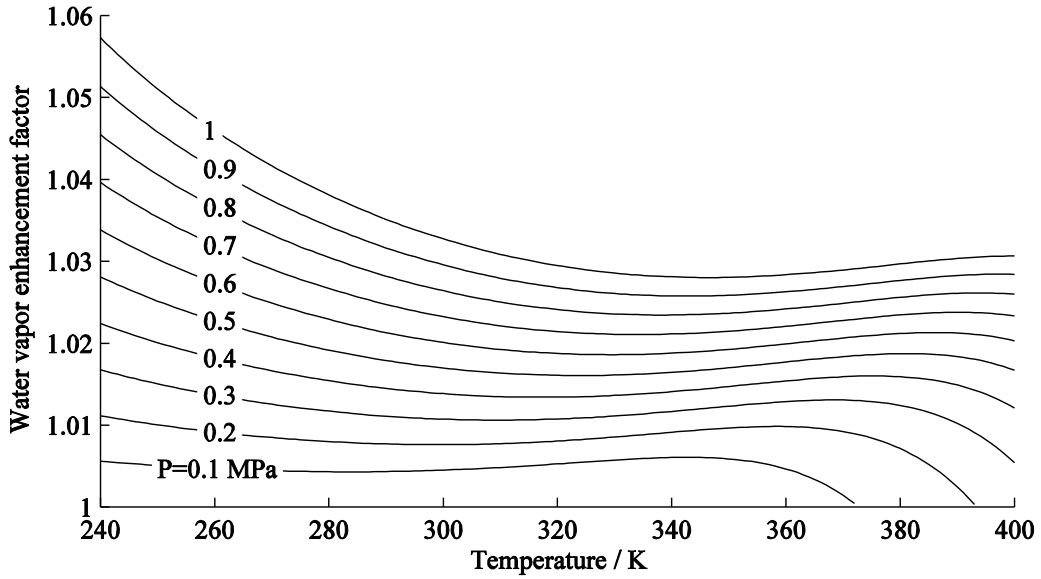

Figure XVI: Results of Sec.1.5.1 for equilibrium over liquid water as a function of temperature and pressure

Equilibrium over ice plane:

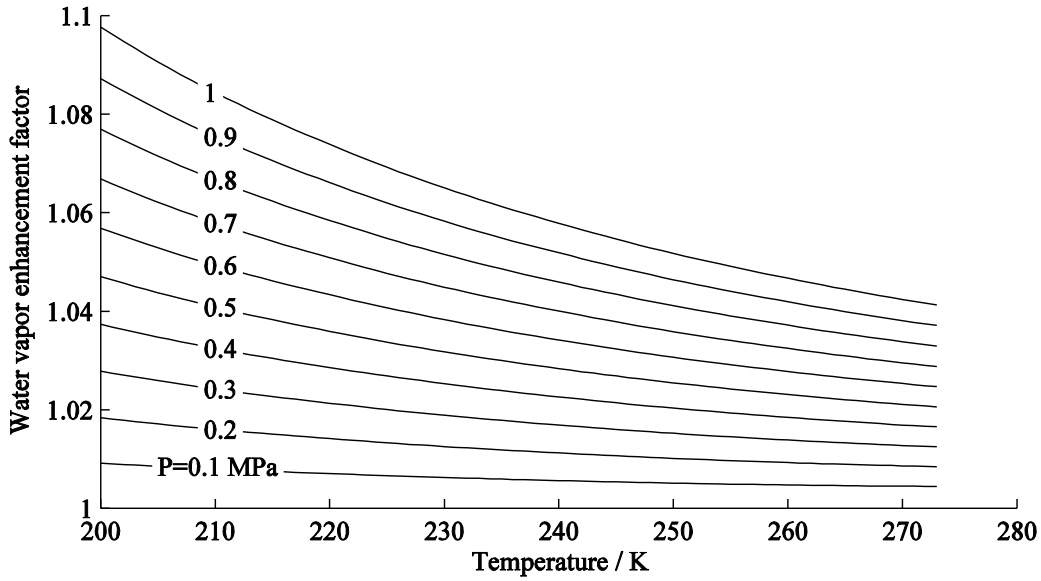

Figure XVII: Results of Sec.1.5.1 for equilibrium over liquid water as a function of temperature and pressure

I.X: The water vapor enhancement factor for argon as a function of temperature and pressure based on first-principles calculations

Equilibrium over a planar pool of liquid water:

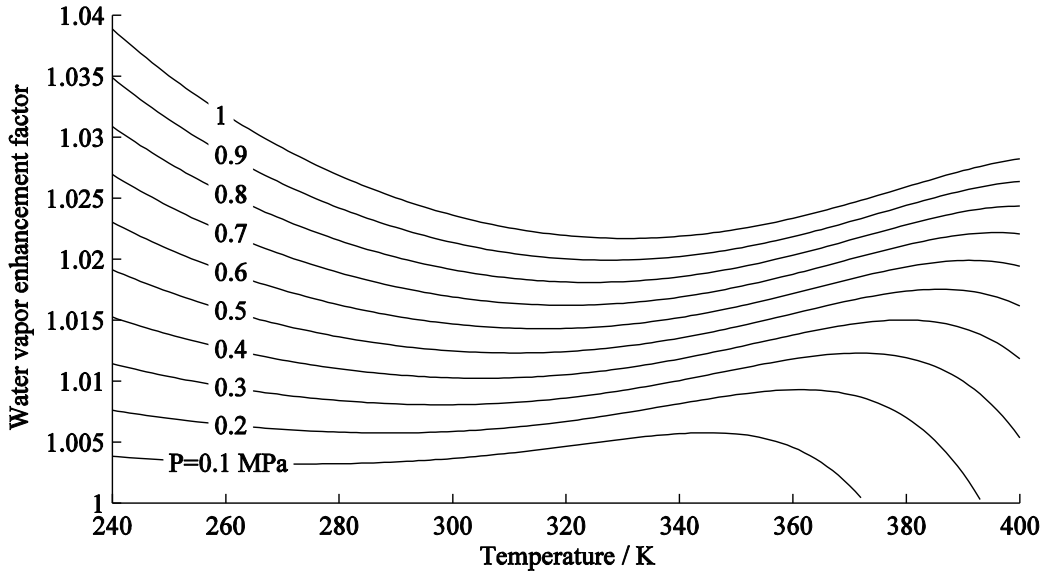

Figure XVIII: Results of Sec.1.5.2 for equilibrium over liquid water as a function of temperature and pressure

Equilibrium over ice plane:

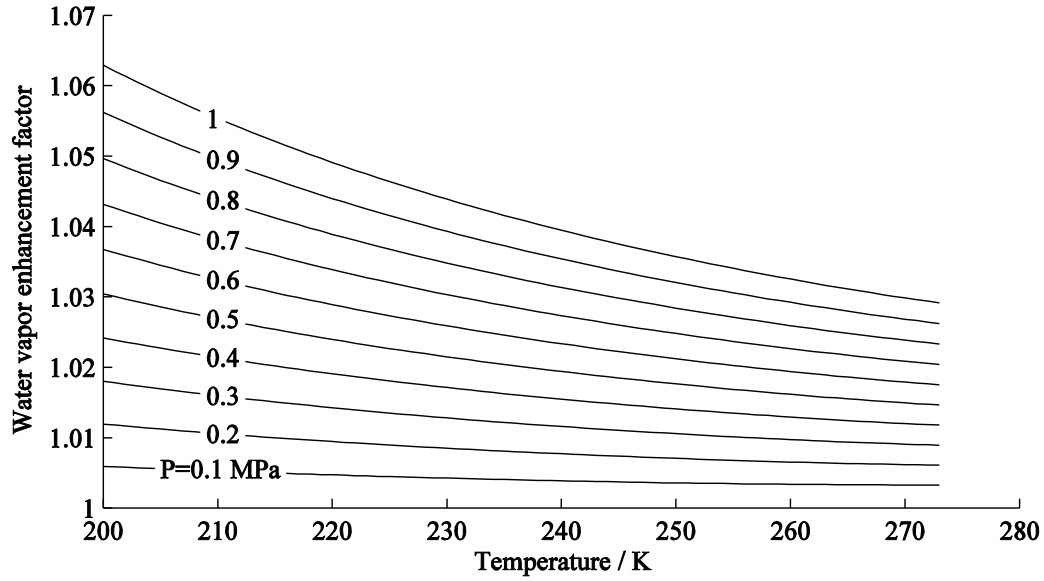

Figure XIX: Results of Sec.1.5.2 for equilibrium over solid water as a function of temperature and pressure

I.XI: The water vapor enhancement factor for oxygen as a function of temperature and pressure based on first-principles calculations

Equilibrium over a planar pool of liquid water:

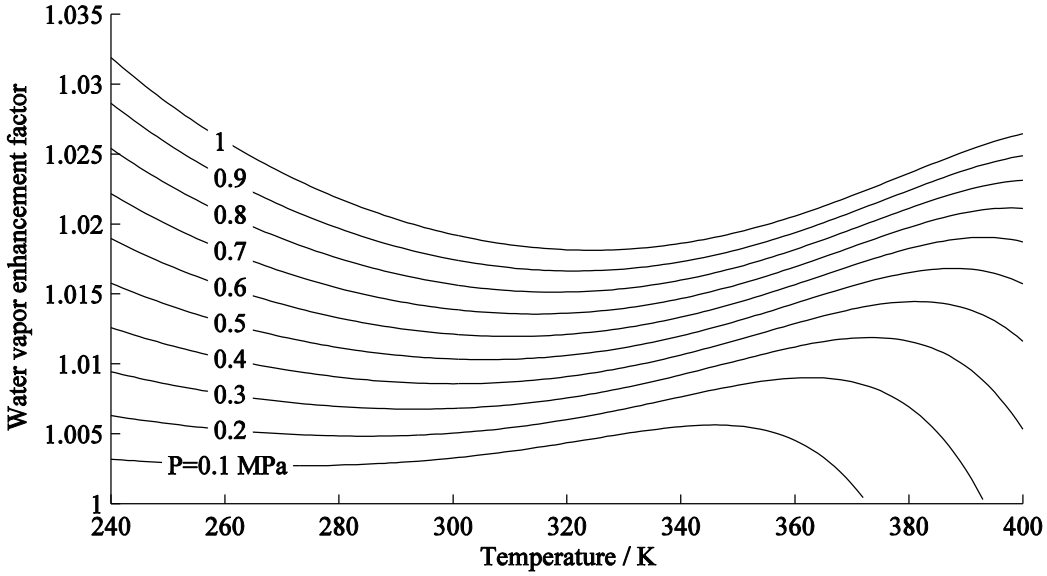

Figure XX: Results of Sec.1.5.3 for equilibrium over liquid water as a function of temperature and pressure

Equilibrium over ice plane:

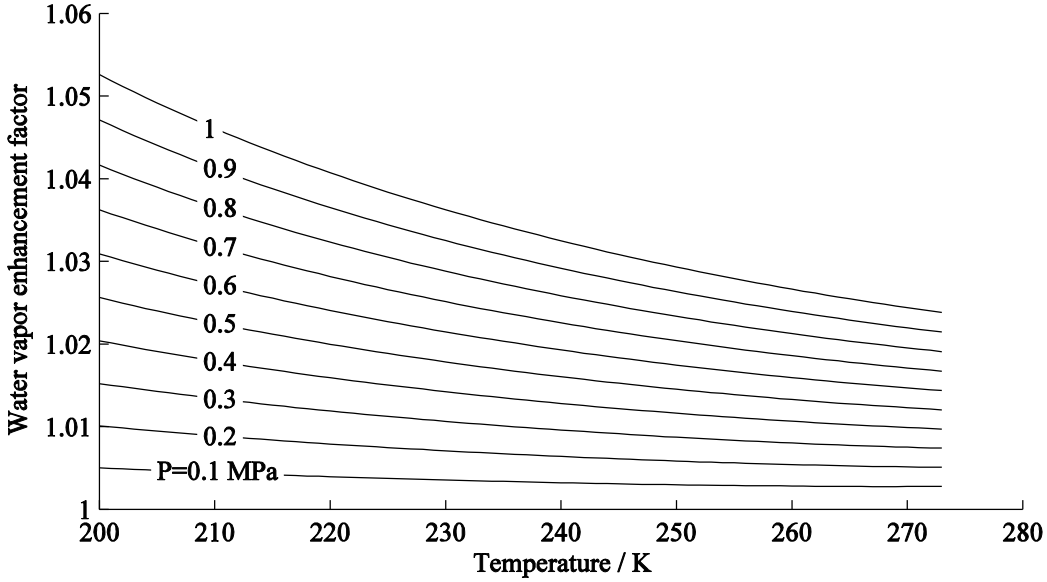

Figure XXI: Results of Sec.1.5.3 for equilibrium over solid water as a function of temperature and pressure

I.XII: The water vapor enhancement factor for standard air as a function of temperature and pressure based on first-principles calculations

Equilibrium over a planar pool of liquid water:

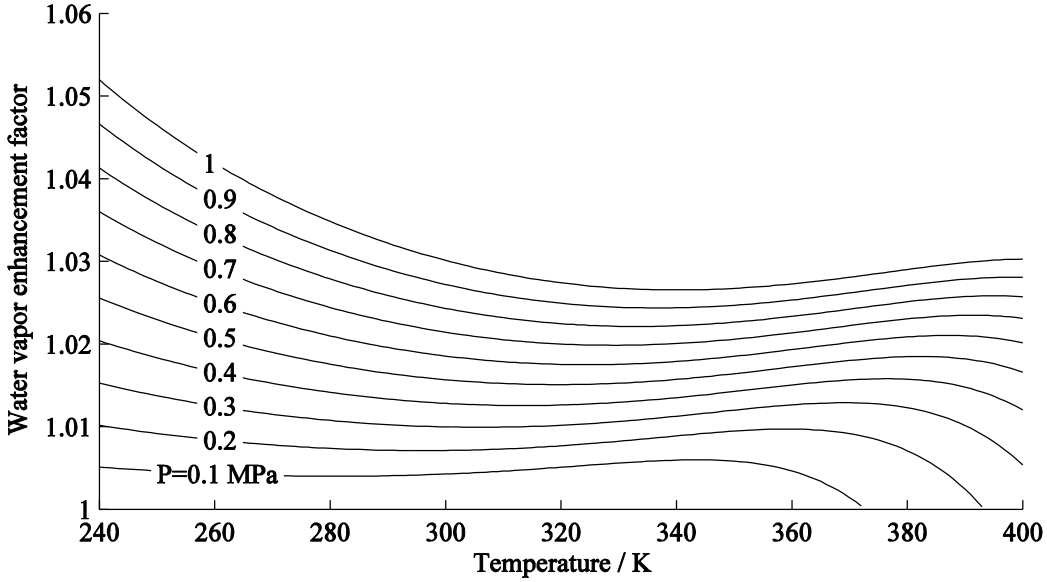

Figure XXII: Results of Sec.1.5.4 for equilibrium over liquid water as a function of temperature and pressure

Equilibrium over ice plane:

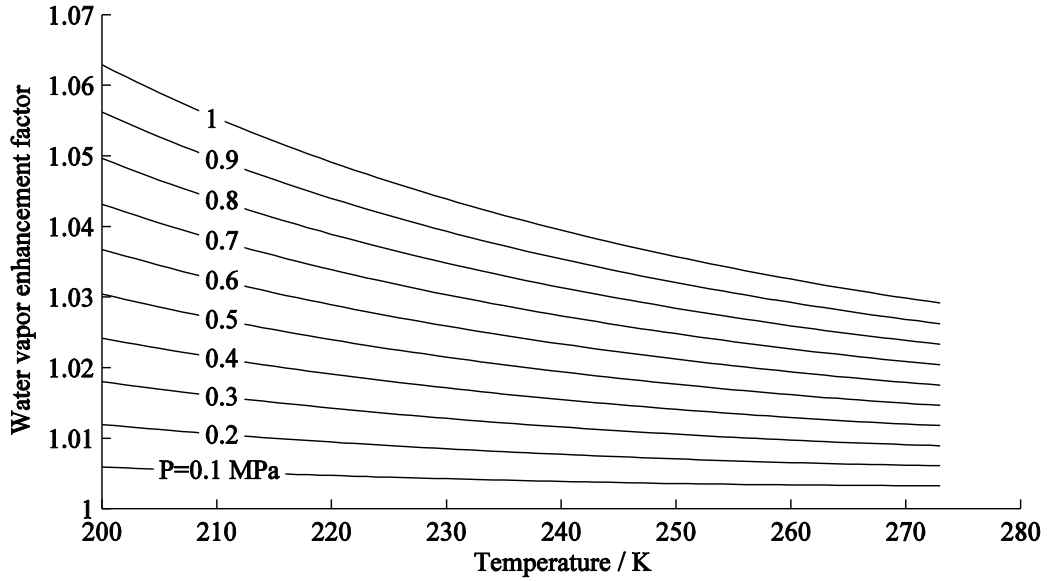

Figure XXIII: Results of Sec.1.5.4 for equilibrium over solid water as a function of temperature and pressure